UNIVERSITY OF CALIFORNIA, SAN DIEGO

Numerical Simulations of the Stratified Oceanic Bottom Boundary Layer

A dissertation submitted in partial satisfaction of the
requirements for the degree Doctor of Philosophy
in
Engineering Sciences (Mechanical Engineering)

by

John R. Taylor

Committee in charge:

Sutanu Sarkar, Chair
Thomas Bewley
Paul Linden
Robert Pinkel
William Young

2008

The dissertation of John R. Taylor is approved, and it is acceptable in quality and form for publication on microfilm:

Chair

University of California, San Diego

2008

To Erin and my family with love

TABLE OF CONTENTS

LIST OF SYMBOLS

$\mathbf{u}$	Velocity
u_*	Friction velocity
U_∞	Free stream velocity
z_0	Roughness length
κ	Von Karman's constant
α	Ekman veering angle
θ	Potential temperature
Ri	Richardson number
Re	Reynolds number
Fr	Froude number
Pr	Prandtl number
$< \cdot >$	Reynolds average
f	Coriolis parameter
g	Gravitational acceleration
ω	Wave frequency
ρ	Density
Θ	Wave propagation direction
N	Buoyancy frequency
δ	Ekman layer depth
h	Channel height

LIST OF FIGURES

LIST OF TABLES

ACKNOWLEDGMENTS

I would like to acknowledge Professor Sutanu Sarkar for invaluable support and guidance and for making graduate school an enjoyable and rewarding experience. I would like to thank the members of my committee for many helpful suggestions and encouragement. Professors Vincenzo Armenio and Thomas Bewely are gratefully acknowledged for their assistance learning and developing the numerical methods used in this thesis and described in Chapter VI. I would also like to acknowledge the students of the CFD lab for their help and camaraderie.

Chapter II is a reprint of material published in *Physics of Fluids*, 2005, co-authored by Professors Sutanu Sarkar and Vincenzo Armenio.

Chapter V is a reprint of material published in the *Journal of Fluid Mechanics*, 2007, co-authored by Professor Sutanu Sarkar.

Chapter VI, in part, contains material developed while co-lecturing a graduate level course in computational fluid dynamics at the University of California San Diego with Professor Thomas Bewley.

VITA

2001	B.S., Engineering Physics, Santa Clara University.
2004	M.S., Engineering Sciences (Mechanical Engineering), University of California, San Diego.
2008	Ph.D., Engineering Sciences (Mechanical Engineering), University of California, San Diego.

PUBLICATIONS

Taylor J.R., and S. Sarkar, 2007: Stratification effects in a bottom Ekman layer. *Journal of Physical Oceanography*, *submitted*.

Taylor J.R., and S. Sarkar, 2007: Internal gravity waves generated by a turbulent bottom Ekman Layer. *Journal of Fluid Mechanics*, **590**, 1, 331–354.

Taylor J.R., S. Sarkar, and V. Armenio, 2005: Large eddy simulation of stably stratified open channel flow. *Physics of Fluids*, **17**, 116602.

Taylor J.R, and S. Sarkar, 2007: Near-wall modeling for large eddy simulation of an oceanic bottom boundary layer (Invited), *Proceedings of the Fifth International Symposium on Environmental Hydraulics*, Tempe, AZ.

Taylor J.R, and S. Sarkar, 2007: Internal wave generation by a turbulent bottom boundary layer, *Proceedings of the Fifth International Symposium on Environmental Hydraulics*, Tempe, AZ.

Taylor J.R, and S. Sarkar, 2007: Large eddy simulation of a stratified benthic boundary layer, *Turbulence and Shear Flow Phenomena - V*, Garching, Germany.

Taylor J.R., and S. Sarkar, 2007: Direct and large eddy simulations of a bottom Ekman layer under an external stratification. *International Journal of Heat and Fluid Flow*, *submitted*.

Taylor J.R, S. Sarkar, and V. Armenio, 2005: Open channel flow stratified by a surface heat flux, *Turbulence and Shear Flow Phenomena - IV*, Williamsburg, VA.

Bennett A.F., J.R. Taylor, and B.S. Chua, 2005: Lattice Boltzmann open boundaries for hydrodynamic models. *Journal of Computational Physics*, **203**, 89–111.

Taylor J.R., K.K. Falkner, U. Schauer, and M. Meridith, 2003: Quantitative considerations of dissolved Barium as a tracer in the Arctic Ocean. *Journal of Geophysical Research*, **108**, C12, 3374.

ABSTRACT OF THE DISSERTATION

Numerical Simulations of the Stratified Oceanic Bottom Boundary Layer

by

John R. Taylor
Doctor of Philosophy in Engineering Sciences (Mechanical Engineering)
University of California, San Diego, 2008
Professor Sutanu Sarkar, Chair

Numerical simulations are used to consider several problems relevant to the turbulent oceanic bottom boundary layer. In the first study, stratified open channel flow is considered with thermal boundary conditions chosen to approximate a shallow sea. Specifically, a constant heat flux is applied at the free surface and the lower wall is assumed to be adiabatic. When the surface heat flux is strong, turbulent upwellings of low speed fluid from near the lower wall are inhibited by the stable stratification. Subsequent studies consider a stratified bottom Ekman layer over a non-sloping lower wall. The influence of the free surface is removed by using an open boundary condition at the top of the computational domain. Particular attention is paid to the influence of the outer layer stratification on the boundary layer structure. When the density field is initialized with a linear profile, a turbulent mixed layer forms near the wall, which is separated from the outer layer by a strongly stable pycnocline. It is found that the bottom stress is not strongly affected by the outer layer stratification. However, stratification reduces turbulent transport to the outer layer and strongly limits the boundary layer height. The mean shear at the top of the boundary layer is enhanced when the outer layer is stratified, and this shear is strong enough to cause intermittent instabilities above the pycnocline. Turbulence-generated internal gravity waves are observed in the outer layer with a relatively narrow frequency range. An

explanation for frequency content of these waves is proposed, starting with an observed broad-banded turbulent spectrum and invoking linear viscous decay to explain the preferential damping of low and high frequency waves. During the course of this work, an open-source computational fluid dynamics code has been developed with a number of advanced features including scalar advection, subgrid-scale models for large-eddy simulation, and distributed memory parallelism.

I Introduction

At the bottom of the ocean, the stress exerted by the seafloor against the near-bottom currents creates a layer of enhanced shear and turbulence. The turbulence produced in the bottom boundary layer is strong enough to overcome the local stratification and create a nearly ubiquitous mixed layer near the seafloor. In this sense, the bottom boundary layer is analagous to the surface mixed layer, where turbulence is produced by wind, waves, and surface heat fluxes. The bottom boundary layer is an important source of drag on mean currents and mesoscale eddies, and is a location where diapycnal mixing of the density field is large. In order to quantify the momentum and buoyancy fluxes associated with the bottom boundary layer, it is important to accurately represent the turbulent motions responsible for these fluxes. Understanding the physics of the turbulent bottom boundary layer, therefore, is an important step towards improving the dynamical description of large-scale motions.

Unfortunately, the deep ocean is a notoriously difficult location to directly observe. It is difficult to sample near the seafloor using ship-lowered instruments without hitting the seafloor and potentially damaging delicate sensors. In addition, measurements using acoustic doppler current profilers (ADCPs) can be corrupted in the bottom boundary layer due to the rebound of the acoustic signals off the seafloor. In order develop a fundamental understanding of the physics of the bottom boundary layer, we will turn to turbulence-resolving numerical simulations.

The turbulent mixed layer at the bottom of the ocean is relatively thin, typically extending $O(10m)$ from the seafloor. Above the mixed layer the density

profile is stable. In fact, a strong pycnocline is sometimes observed just above the mixed layer (Armi (1978); D'Asaro (1982)). As we will see, in order to accurately simulate important processes such as the boundary layer growth, the turbulent eddies responsible for entrainment of stratified fluid into the boundary layer must be resolved. The lengthscale of these eddies is typically $O(1m)$ or less and is limited by the strength of the stratification outside of the mixed layer. Unlike many of the motions in the stratified interior of the ocean, the horizontal length scale associated with the turbulent eddies in the bottom mixed layer is the same order as the vertical length scale. Therefore, to resolve the eddies responsible for entrainment, a numerical model would require horizontal resolutions $O(1m)$. However, even high resolution regional ocean models typically need to resolve much larger horizontal structures such as mesoscale eddies with lengthscales $O(100km)$. This scale separation makes it impractical to resolve the turbulent boundary layer in ocean circulation models with the available present-day computational resources.

Since motions in the bottom boundary layer cannot be resolved by large-scale ocean models, the influence of the bottom boundary layer on the ocean circulation must be parameterized. However, since observations of the bottom boundary layer are relatively scarce, it is not clear how to determine if a given parameterization is successful. One of the goals of this study is to produce a database from simulations of the bottom boundary layer in idealized conditions that could be used to test the performance of new parameterizations.

Compared to the oceanic bottom boundary layer, the atmospheric boundary layer is relatively well sampled and studied. One important difference between the oceanic and atmospheric boundary layers is the surface boundary condition on the temperature field. Turbulence in the atmospheric boundary layer is often driven by thermal convection caused by solar heating at the ground. However, it is also possible for a stabilizing heat flux to occur at the ground, a situation common in nocturnal and marine atmospheric boundary layers.

Unlike the atmospheric boundary layer, the oceanic bottom boundary

layer is unaffected by solar radiation. There is a geothermal heat flux at the seafloor that at times can be large enough to drive convective plumes, such as those observed at hydrothermal vents. However, the geothermal heat flux is typically much smaller than at these hotspots, and the seafloor can be assumed to be adiabatic. In order to verify this assumption, we can follow the procedure used for Monin-Obukhov scaling in the atmospheric boundary layer. The Obukhov length is defined by:

$$L = \frac{-u_*^3}{\kappa B_0} = \frac{-u_*^3 c_p \rho T}{kgQ_0}, \tag{I.1}$$

where u_* is the friction velocity, c_p is the specific heat, $k = 0.41$ is the von Karman constant, Q_0 is the surface heat flux, and B_0 is the corresponding surface buoyancy flux. Under unstable conditions the Obukhov length is negative and provides a measure of the relative importance of turbulent production by surface stress and convection. When $z < |L|$ production dominates over buoyancy effects and the reverse is true for $z > |L|$. A typical value of the heat flux at the seafloor is

$$Q_0 = 50\frac{mW}{m^2}. \tag{I.2}$$

Since the seafloor heat flux distribution is skewed towards high values, the mean seafloor heat flux is about twice this value, but $50mw/m^2$ is the most *common* value (Hofmeister and Criss (2005)). Using Q_0, we can estimate the Obukhov length with the following physical parameters: $c_p = 4.2J/gm^\circ K$, $\rho = 1000kg/m^3$, and $T = 275^\circ K$. It is then left to estimate the friction velocity. If we consider a tidal channel, we can use the friction velocity, $u_* = 0.024m/s$ observed by Sanford and Lien (1999). This gives an Obukhov length of $L = 79km$. Under these conditions $z << L$ in the boundary layer and the heat flux does not play a significant dynamical role. In a less turbulent abyssal ocean, if we crudely estimate u_* to be about 1/20 of the velocity external to the boundary layer, then a value of $u_* = 0.0012m/s$ corresponding to an outer velocity of $2cm/s$ seems reasonable. Using this friction velocity and the same parameters as before gives $L = 39.5m$. Under these conditions Monin-Obukhov scaling would likely break down before

$z = |L|$ since the interior stratification will likely be felt below this height. This suggests that the assumption of zero surface heat flux is a reasonable approximation.

One feature of stable atmospheric boundary layers that is not typically seen in the ocean is 'global intermittency' of the boundary layer turbulence. Intermitency can occur in stable atmospheric boundary layers when the surface buoyancy flux becomes large enough to increase the gradient Richardson number beyond a critical value, at which point turbulent production in the boundary layer is reduced (Armenio and Sarkar (2002); Mahrt (1999); Coleman et al. (1992)). In contrast, since the surface heat flux is nearly zero in the benthic boundary layer, even under relatively quiescent conditions, a mixed layer can be expected sufficiently close to the seafloor.

It can be shown using scaling arguments that the bottom boundary layer can be expected to remain turbulent. Direct numerical simulations by Coleman et al. (1990) found that an unstratified Ekman layer was turbulent at a friction Reynolds number of $Re_* = u_*^2/\nu f = 340$. If we take $\nu = 10^{-6} m^2/s$ and $f = 10^{-4} s^{-1}$, this Reynolds number corresponds to a friction velocity of $u_* = 1.84 * 10^{-4} m/s$. The geostrophic drag coefficient observed in the simulations was $u_*/U_\infty = 0.0652$ (Coleman et al. (1990)). Therefore, this Reynolds number corresponds to an Ekman layer formed as a steady current with a speed of $U_\infty = 0.28 cm/s$ flows over the seafloor. If we take this Reynolds number to be the minimum for a turbulent Ekman layer, we can expect turbulence as long as the mean flow outside of the boundary layer is in excess of $2.8 mm/s$.

Since the oceanic bottom boundary layer is primarily distinguished from its atmospheric counterpart by the thermal boundary conditions, one of the primary goals of this study will be to examine the effects of stratification on the boundary layer structure. Density variations affect the bottom boundary layer through the external stratification. As the density gradient associated with the outer layer fluid increases, so does the potential energy required to create a mixed

layer of a given height. The outer layer stratification may therefore be able to affect the thickness of the bottom mixed layer. In a stable atmospheric boundary layer, the stable surface heat flux can reduce the near-wall turbulent production. Since the seafloor is nearly adiabatic, this effect is not expected in the oceanic bottom boundary layer. However, as we will see, stratification can still affect turbulent motions by limiting the turbulent transport from the near-wall region to the outer layer.

To our knowledge, these are the first turbulence-resolving simulations of a stratified oceanic bottom boundary layer over a non-sloping seafloor. In order to systematically study the physics of this flow, we will begin with an idealized study in a simple geometry and progressively increase the degree of complexity by increasing the Reynolds number, including effects owing to the Earth's rotation, and modeling the bottom roughness. It is hoped that this study will provide a framework for interpreting future simulations and field data that contain more of the complexities that are found in the oceanic bottom boundary layer.

This dissertation is organized as follows. Chapter II will present simulations of stratified open channel flow with a uniform heat flux at the free surface and an adiabatic lower wall. Although the geometry is relatively simple, this allows us to compare directly with previous numerical simulations that used thermal boundary conditions more akin to the stable atmospheric boundary layer. Chapter III presents validations of the large-eddy simulations and the near-wall model that will be used in subsequent chapters to simulate flow at much higher Reynolds numbers. Chapter IV considers the influence of the outer layer stratification on the structure and turbulence in a bottom Ekman layer. Chapter V examines the internal gravity waves that are generated by the boundary layer turbulence. Finally, Chapter VI presents the numerical methods that are used throughout the thesis.

II Large Eddy Simulation of Stably Stratified Open Channel Flow

II.1 Introduction

As a model problem to study the influence of thermal boundary conditions consistent with a stratified bottom boundary layer, a large eddy simulation (LES) is used to study flow through an open channel driven by a steady pressure gradient. The lower boundary is a flat, no-slip, insulating wall, and the top of the domain is bounded by an undeformed stress-free surface where a constant heat flux is applied. The choice of boundary conditions is intended to approximate a shallow sea or estuary heated from above without wind forcing and allows us to compare directly with previous studies with buoyancy effects present at the turbulence generation site.

Open channel flow is an important model problem with relevance to many environmental and industrial applications. In many cases, temperature gradients are large enough for buoyancy effects to become dynamically important. The present study considers open channel flow with stable stratification imposed by a constant heat flux at the free surface and an adiabatic lower wall. This choice of boundary conditions allows us to contrast the flow behavior when buoyancy effects are present at the turbulence generation site, with the present case where such

effects are absent. Specifically, since the near wall region remains unstratified, the interaction between wall-generated turbulence and an external stable stratification is examined. In addition, the influence of stratification on the well-known characteristics of unstratified turbulence near the free surface are also considered.

Several previous studies have considered stratified channel flow, but in each case stratification was applied with fixed temperature boundaries. Armenio and Sarkar (2002) used a large eddy simulation (LES) to study stratified closed channel flow with a fixed temperature difference ΔT across the channel. In that study, the authors found that the turbulent momentum and buoyancy fluxes and the turbulent Froude number can be well described as functions of the gradient Richardson number, Ri_g. For large ΔT, they observed a buoyancy affected region near the walls and a buoyancy dominated region near the centerline. In contrast, the present study considers open channel flow and a larger Reynolds number, $Re_\tau = 400$ versus 180, but as will be seen the largest difference is due to the choice of temperature boundary conditions that qualitatively changes the profile of N, the buoyancy frequency.

Komori et al. (1983) used steam to heat the surface of water in an inclined open channel at relatively low Reynolds number. Similar to the later results of Armenio and Sarkar (2002), it was found by Komori et al. (Komori et al. (1983)) that Ri_g governs the effect of buoyancy on the local turbulence. When the fluid became sufficiently stratified, they also observed wavelike motion in the interior accompanied by countergradient heat and momentum fluxes. Although the mathematical representation of the boundary conditions for this experiment are likely to be complicated, it has been argued that they are best approximated by a fixed temperature difference across the channel (Garg et al. (2000)). Nagaosa and Saito (1997) reach similar conclusions from a DNS of open channel flow with fixed ΔT across the channel. They considered a friction Reynolds number of 150, a Prandtl number of 1, and friction Richardson numbers of 0, 10, and 20. When the Richardson number is nonzero, turbulence is affected throughout the channel. They also

show that stratification is effective in reducing the skin friction.

Since all previous studies of open channel flow have considered fixed temperature walls, the near-wall region became stratified, and hence one of the major influences of stratification was a reduction of the near-wall turbulence production. When considering environmental flows, the results of these studies may be analogous to the atmospheric surface boundary layer under conditions of strong surface cooling where a stably stratifying heat flux at the ground can lower turbulent production in the surface layer (Mahrt (1999)). In contrast, our proposed boundary conditions are more relevant to the oceanic bottom boundary layer where the bounding surface is adiabatic. See Lien and Sanford (2004) for a good explanation of the differences between atmospheric and oceanic boundary layers.

The choice of the free surface boundary condition has been shown to be important even when applied to a passive scalar. Handler et al. (1999) compared the behavior of open channel flow with Neumann and Dirichlet boundary conditions on a passive scalar at the free surface. They found that variations of the surface flux in the Dirichlet case were much larger than variations of surface concentration when a Neumann condition was used. The structure of the scalar field at the free surface was also considerably different between the two cases.

A number of studies have focused on the turbulent statistics and coherent structures at the free surface in unstratified open channel flow. It was originally conjectured that the dynamics of free surface turbulence would be quasi two-dimensional. However, Walker et al. (Walker et al. (1996)) asserted that turbulence is three-dimensional up to the surface, and even at the surface does not conform to two-dimensional dynamics. In support of this, they demonstrated that vortex stretching is maximal at the free surface, and the tangential vorticity vanishes only in a very thin layer. This conclusion was supported by Nagaosa (1999) who cited the non-vanishing streamwise wall-normal velocity correlation coefficient, R_{uw} as evidence for the three-dimensionality of free surface turbulence.

The dominant structures at a free surface have been identified as up-

wellings (fluid impinging on the free surface), downdrafts, and spiral eddies (see Pan and Banerjee (1995) and Perot and Moin (1995)). Pan and Banerjee (1995) demonstrated that the upwellings and downdrafts are driven by active turbulence generated at the bottom of the channel. In numerical simulations at $Re_\tau = 171$, after allowing the open channel flow to fully develop, they replaced the no-slip bottom wall with a rigid, no-stress surface, and observed that the upwellings and downdrafts near the upper free surface quickly decay leaving the surface attached spiral eddies. Since the spiral eddies are predominantly two-dimensional, they suggest that the three-dimensionality and anisotropy observed in free surface turbulence is caused by impinging patches of three-dimensional turbulence. Calhoun and Street (2002) conducted a computational study of turbulence at a free surface with and without density stratification. They found that with stable stratification the upwellings seen at the surface are less frequent and weaker relative to an unstratified case.

Two analogies are suggested between the present study and environmental situations. The first is a bottom boundary layer in the deep ocean subject to stable stratification imposed from above. In that problem, as in the present study, a mean flow drives turbulence which creates a well-mixed layer beneath an external stratification. In this analogy, the free surface is an artificial representation of an open boundary. Despite the simplified dynamics considered here compared to an oceanographic setting, we hope to gain fundamental insights into the interaction between wall-generated turbulence and an imposed stable stratification. This should then provide a basis for comparison with studies that include additional physical processes.

The second analogy is an ocean thermocline formed by surface heating in shallow water of nearly uniform depth. In order to eliminate processes beyond the scope of this study, the surface is assumed to be undeformed (the external Froude number is small) and stress free. Therefore, features common to oceanographic flows such as surface waves, Langmuir cells, and a mixed layer are excluded. The

Coriolis parameter is also neglected, corresponding to a small Rossby number valid for the small scale motions of interest here. It should also be noted that this study does not attempt to model the open ocean thermocline which may be dominated by large scale horizontal inhomogeneities and along-isopycnal transport. It is believed that in the open ocean many of the isopycnals outcrop to the surface (are 'ventilated'), where mixing can readily occur via the wind stress (Luyten et al. (1983)). The present study only considers the situation of a heated free surface, radiative and evaporative heat transfer from the ocean to the atmosphere is not accounted for, and therefore the thin thermal sublayer (or 'cool skin') where stratification can be unstable (Paulson and Simpson (1981)) is not considered.

II.2 Formulation

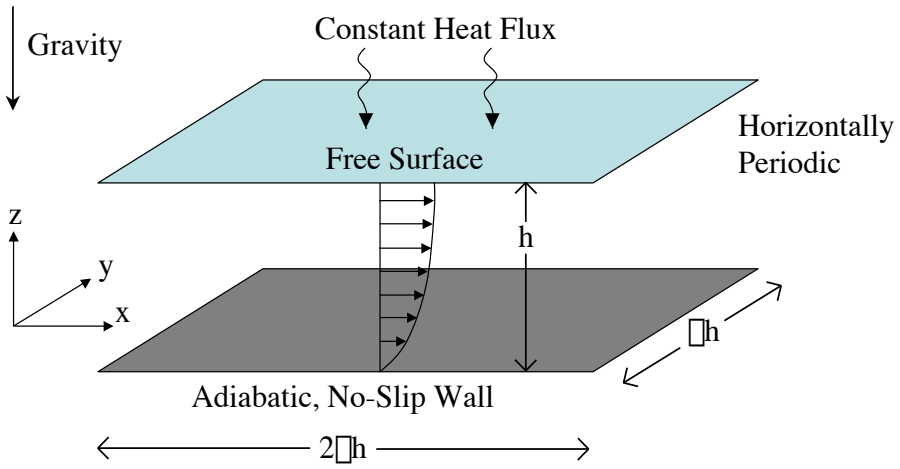

Figure II.1: Model Domain

The geometry of the open channel considered here is shown in Figure IV.1. Flow is driven by a uniform pressure gradient aligned with the x-axis, and periodicity is applied in both horizontal directions while flat no-slip and no-stress

surfaces bound the bottom and top respectively. The y-axis is aligned with the cross-stream direction, and the z-axis is normal to the wall. The velocities in the x, y, and z directions are denoted by u, v, and w. The domain size in the x and y directions is $2\pi h$ and πh respectively, where h is the channel depth. The constant, negative density gradient imposed at the free surface can be thought of as surface heating with a constant heat flux if density changes are linearly related to temperature changes. The total density is given by $\rho_T = \rho_0 + \rho^*(\mathbf{x}, t)$, with $\rho^* << \rho_0$, allowing the Boussinesq approximation known to be appropriate for stratified water.

II.2.A Governing Equations

The governing equations are nondimensionalized with the channel height h, friction velocity $u_\tau = (\tau_w/\rho_0)^{\frac{1}{2}}$, and the absolute value of the imposed free surface gradient $|\partial\rho^*/\partial z|_s$. The shear stress, τ_w used to define the friction velocity is the horizontally averaged value at the wall which must balance the vertically integrated pressure gradient for steady state ($\Pi h =< \tau_w >$). With these choices, the nondimensional governing equations can be written:

$$\frac{D\mathbf{u}}{Dt} = -\nabla p^* + \frac{\nabla^2 \mathbf{u}}{Re_\tau} - Ri_\tau \rho^* \hat{\mathbf{k}} + \Pi \hat{\mathbf{i}}, \tag{II.1}$$

$$\frac{D\rho^*}{Dt} = \frac{\nabla^2 \rho^*}{Re_\tau Pr}, \tag{II.2}$$

$$\nabla \cdot \mathbf{u} = 0, \tag{II.3}$$

$$z = 0: \quad u = v = w = 0, \quad \frac{d\rho^*}{dz} = 0 \tag{II.4}$$

$$z = 1: \quad \frac{\partial u}{\partial z} = \frac{\partial v}{\partial z} = w = 0, \quad \frac{d\rho^*}{dz} = -1, \tag{II.5}$$

where Π is the imposed pressure gradient equal to unity with the present nondimensionalization, p^* is the deviation from the hydrostatic pressure, and the hydrostatic pressure gradient has been canceled with the nominal gravitational force in the usual way. The nondimensional Reynolds, Richardson, and Prandtl numbers

are defined as:

$$Re_\tau = \frac{u_\tau h}{\nu}, \quad Ri_\tau = -\frac{g}{\rho_0}\frac{\partial \rho^*}{\partial z}|_s \frac{h^2}{u_\tau^2}, \quad Pr = \frac{\nu}{\kappa}, \tag{II.6}$$

where κ is the molecular diffusivity. The bulk Richardson number is defined by:

$$Ri_b = \frac{\Delta \rho g h}{\rho_0 U_b^2}, \tag{II.7}$$

where U_b is the bulk (volume-averaged) velocity through the channel. The parameters used for this study are listed in Table I.

Table II.1: Physical Parameters

Ri_τ	$Ri_b * 10^{-3}$	Re_τ	Re_b	Pr
0	0	400	6967	5
25	1.84		6976	
100	8.80		7002	
250	34.3		7071	
400	76.9		7195	
500	117.8		7310	

Notice that since the imposed surface density gradient is used to make the density nondimensional, it appears in the Richardson number defined in Eq. (II.6). This is the only variable quantity in the definition of Ri_τ; since we are considering a fixed forcing pressure gradient Π, the quantities τ_w and u_τ are also fixed. Therefore, increasing Ri_τ is physically equivalent to increasing the imposed surface stratification. When $Ri_\tau = 0$, density acts as a passive scalar and the velocity field can be checked against previous unstratified open channel studies. When $Ri_\tau > 0$, a negative density gradient is imposed at the free surface, corresponding to stable stratification.

II.2.B Laminar Solution

We will briefly examine the properties of the laminar solution, found by neglecting changes in the horizontal directions, assuming that the velocity profile

is independent of time, and solving the nondimensional equations. The laminar velocity is then given by:

$$u = \Pi Re_\tau(\frac{z^2}{2} - z), \quad v, w = 0. \tag{II.8}$$

The density profile is unsteady owing to the surface heat flux. The laminar form of Eq. (II.2) is:

$$\frac{\partial \rho^*}{\partial t} = \frac{1}{Re_\tau Pr}\frac{\partial^2 \rho^*}{\partial z^2}. \tag{II.9}$$

The density profile may be divided into the following components:

$$\rho^*(z,t) = f(z) + g(t) + H(z,t), \tag{II.10}$$

where $H(z,t)$ is the solution to Eq. (II.9) with homogeneous (zero gradient) boundary conditions, $g(t)$ is the term owing to surface heating, and $f(z)$ satisfies the inhomogeneous boundary conditions given in Eq. (II.4) and Eq. (II.5). The inhomogeneous problem is then

$$g_t = \frac{1}{Re_\tau Pr} f_{zz}, \tag{II.11}$$

with

$$f_z(z=1) = \frac{-1}{Re_\tau Pr}, \quad f_z(z=0) = 0, \quad g(t=0) = 0, \tag{II.12}$$

and the homogeneous problem is:

$$H_t = \frac{H_{zz}}{Re_\tau Pr}, \quad H_z(z=0,1) = 0, \quad H(t=0) = \rho_0(z). \tag{II.13}$$

Solving Eq. (II.11) and Eq. (II.12) first for $f(z)$ and $g(t)$:

$$g(t) = \frac{-t}{Re_\tau Pr}, \tag{II.14}$$

and

$$f(z) = \frac{-z^2}{2} + B. \tag{II.15}$$

Eq. (II.13) is solved using separation of variables with $H(z,t) = \phi(z)\psi(t)$. Using this form and the appropriate boundary conditions gives:

$$\psi(t) = e^{-\lambda_n^2 t}, \quad \phi(z) = B_n cos(\lambda_n z), \tag{II.16}$$

with

$$\lambda_n = n\pi, \quad n = 0, 1, 2, 3, ... \tag{II.17}$$

so the homogeneous solution takes the form:

$$H(z,t) = \sum_{n=0}^{\infty} B_n cos(\lambda_n z) e^{-\lambda_n^2 t}. \tag{II.18}$$

The constant can be found from the initial condition:

$$\rho^*(t=0) = \rho_0(z) = \frac{-z^2}{2} + \sum_{n=0}^{\infty} B_n cos(\lambda_n z). \tag{II.19}$$

Multiplying by $cos(\lambda_n z)$ and integrating gives:

$$B_n = 2\int_0^1 (\rho_0(z) + \frac{z^2}{2}) cos(\lambda_n z) dz. \tag{II.20}$$

The general laminar solution for the density is then:

$$\rho^*(z,t) = \frac{-t}{Re_\tau Pr} - \frac{z^2}{2} + \sum_{n=0}^{\infty} B_n e^{-\lambda_n^2 t} cos(\lambda_n z). \tag{II.21}$$

Notice that when $t >> 1$ (and the dimensional time $>> h/u_\tau$) the last term becomes small compared to the first two when $n \neq 0$. The choice of $B_0 = 0$ is made implying that ρ^* (a negative quantity) is the nondimensional density departure from the value at the bottom wall. Therefore, after sufficient time, there is a linear (in time) heating trend which is *uniform* in space and the solution reduces to:

$$\rho^*(z,t) = \frac{-t}{Re_\tau Pr} - \frac{z^2}{2}. \tag{II.22}$$

The value of $\Delta\rho = \rho^*(z=0) - \rho^*(z=1) = 1/2$; i.e., in the laminar case, the dimensional value of the density difference is $|d\rho/dz|_s h/2$ for a given surface flux and channel height.

II.2.C Density Flux Balance

In view of the preceding discussion of the laminar density profile, we can separate the unsteady part from the density field as follows. Let

$$\rho^* = \rho_1(t) + \rho(\mathbf{x}, t), \tag{II.23}$$

where $\rho^* = \rho_T(\mathbf{x}, t) - \rho_0$, the variable ρ_1 denotes the deterministic field that decreases in time owing to the imposed surface heating, and $\rho(\mathbf{x}, t)$ is the turbulent density field that is *statistically steady*. Substituting Eq. (II.23) into Eq. (II.2) gives

$$\frac{d\rho_1}{dt} + \frac{\partial \rho}{\partial t} = -u_j \frac{\partial \rho}{\partial x_j} + \frac{1}{Re_\tau Pr} \frac{\partial^2 \rho}{\partial x_j^2}. \tag{II.24}$$

Taking the Reynolds average of Eq. (II.24),

$$\frac{d\rho_1}{dt} = -\frac{\partial}{\partial z} < \rho' w' > + \frac{1}{Re_\tau Pr} \frac{\partial^2 < \rho >}{\partial z^2}. \tag{II.25}$$

The r.h.s. is a function of space only (recall that $\rho(\mathbf{x}, t)$ is a statistically steady field) while the l.h.s. is a function of time only so that, for Eq. (II.25) to hold, both sides must be constant. In order to evaluate the constant, integrate Eq. (II.25) from $z = 0$ to $z = 1$

$$\int_0^1 \frac{d\rho_1}{dt} dz = \frac{1}{Re_\tau Pr} [\frac{\partial < \rho >}{\partial z}|_{z=1} - \frac{\partial < \rho >}{\partial z}|_{z=0}]. \tag{II.26}$$

Using the flux boundary conditions, Eq. (II.4) and Eq. (II.5), leads to

$$\frac{d\rho_1}{dt} = -\frac{1}{Re_\tau Pr}, \tag{II.27}$$

so,

$$\rho_1(t) = -\frac{t}{Re_\tau Pr} + C, \tag{II.28}$$

and the final constant can be absorbed into ρ_0. Inserting Eq. (II.27) into Eq. (II.25) and integrating from $z = 0$, a useful equation that represents a local balance between turbulent and viscous fluxes is obtained:

$$Re_\tau Pr < \rho' w' > - \frac{\partial < \rho >}{\partial z} = z. \tag{II.29}$$

We will come back to the interpretation of this equation later. Henceforth we will present results concerning $\rho(\mathbf{x}, t)$, the statistically steady turbulent field. After each time integration of Eq. (IV.6) - Eq. (II.3), the density change owing to $\rho_1(t)$ is subtracted, and the resulting density field becomes statistically steady after an initial transient, at which point statistics are collected.

II.3 Computational Methods

In order to study the flow in the open channel described above, we use a large eddy simulation (LES). The LES used here is the same used by Armenio and Sarkar (2002) and the numerical methods are described in detail by Armenio and Piomelli (2000). Since the computational model has already been extensively validated, this is not done here. The filtered equations are integrated using a version of the fractional-step method of Zang et al. (1994), which is second order accurate in space and time. The spatial derivatives are computed with central finite difference. The convective terms are time-stepped with the Adams-Bashforth scheme, and the diffusive terms are stepped with the implicit Crank-Nicolson scheme. The multigrid method is used to solve the Poisson equation for the pressure.

The subgrid-scale (SGS) stresses are modeled with a dynamic mixed model:

$$\tau_{ij} = \overline{\overline{u_i}\,\overline{u_j}} - \overline{\overline{u_i}}\,\overline{\overline{u_j}} - 2C\,\overline{\Delta}^2\,\overline{|S|}\,\overline{S_{ij}}, \tag{II.30}$$

where the overbar denotes the filtering operation, $\overline{\Delta}$ is related to the transformation Jacobian J by $\overline{\Delta} = 2J^{-1/3}$, and S_{ij} is the rate of strain tensor. The model coefficient C is determined using a dynamic eddy-viscosity model. The first two terms in Eq. (II.30) represent the scale-similar part of the model. To model the subgrid density flux, a dynamic eddy diffusivity model is used:

$$\lambda_i = -C_\rho \overline{\Delta}^2 |\overline{S}| \frac{\partial \overline{\rho}}{\partial x_i}, \tag{II.31}$$

where the constant C_ρ is evaluated dynamically (see Armenio and Sarkar (2002) for more details).

For simplicity, the free surface is assumed to be undeformed, an approximation good for low Froude number. In a DNS of unstratified open channel flow with a deformable free surface, Komori et al. (1993) found that at $Re_\tau = 160$, the surface is displaced by about 0.01% of the channel depth. Although we are considering a larger Reynolds number, it is expected that any displacements would remain small. Indeed, when $Re_b = 7550$, its maximum value here, the external

Froude number,

$$Fr = \frac{U_b}{\sqrt{gh}}, \tag{II.32}$$

is less than 0.1 as long as the dimensional channel height is greater than 8.3cm, which is the case for all applications considered here.

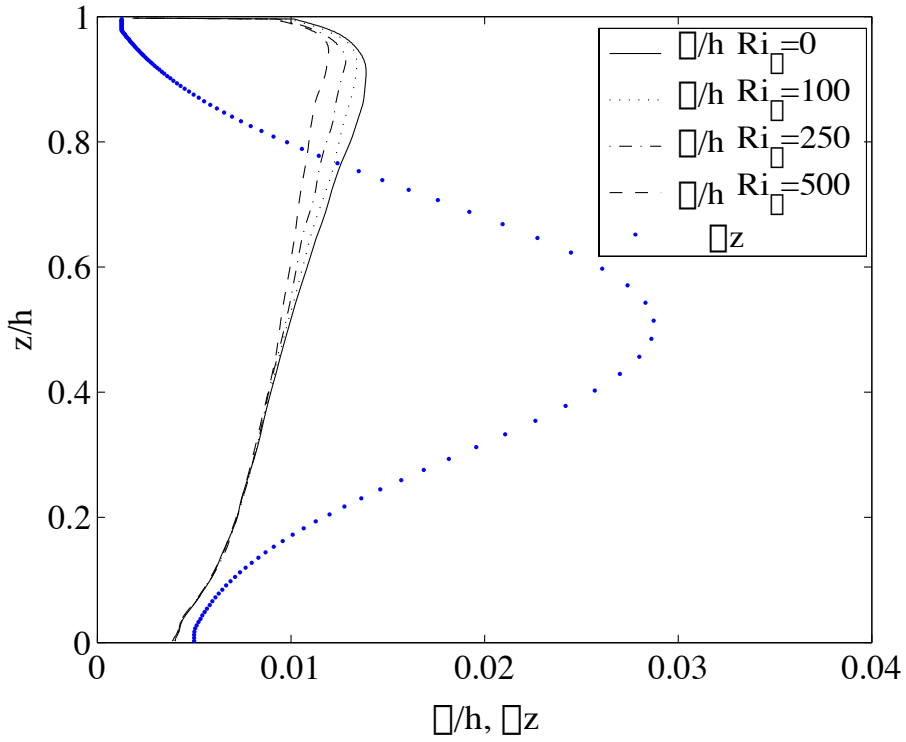

Figure II.2: Kolmogorov scale and vertical grid spacing

Free surface flow presents a number of challenges for turbulence modeling. It has been shown that the flow at the free surface is highly anisotropic (Shen and Yue (2001)). Also, as mentioned in the introduction, Walker et al. (1996) found that the vertical gradient of the horizontal velocity vanished only in a very thin layer near the free surface, requiring a fine grid to resolve the mean profile. Shen and Yue (2001) show that the energy backscatter (transfer from subgrid scales to larger scales) is maximal at the free surface. It can be expected that these unique factors would make it difficult to apply a generic turbulence model to the free surface region. Indeed, as shown by Salvetti and Banerjee (1995) using

DNS data for open channel flow, the dynamic Smagorinsky model performs quite poorly. They find that a dynamic mixed model (the class used here) is a significant improvement, but is not perfect. We attempt to bypass these concerns by using a stretched grid in the vertical with very high resolution at the free surface. As shown in Figure II.2, the vertical grid spacing in the top 20% of the channel is smaller than the Kolmogorov scale. It should be noted that even in the upper region the model cannot be considered a DNS since the horizontal grid spacing, $\Delta x^+ = 40$ and $\Delta y^+ = 20$, is much larger than the vertical.

Stratification presents another difficulty in numerical modeling since it acts to decrease the vertical length scales of motion, requiring higher resolution. The density microscale (Batchelor (1959)) is,

$$\eta_\rho = \frac{\eta}{\sqrt{Pr}}, \tag{II.33}$$

where again η is the Kolmogorov length. This scale sets the distance over which density fluctuations can be expected in a turbulent flow and therefore is the limiting resolution for a DNS with $Pr > 1$. Since we are not attempting to fully resolve the diffusive scales of motion, this requirement does not strictly apply here. However, for accuracy of the LES results, the direct effect of stratification on the subgrid scales is limited here by ensuring a sufficiently small grid spacing. The smallest scale at which buoyancy effects are felt is the Ozmidov scale, defined as

$$L_{oz} = (\frac{\epsilon}{N^3})^{\frac{1}{2}}, \tag{II.34}$$

where ϵ is the dissipation rate and N is the Brunt-Väisälä (buoyancy) frequency. In all of the cases presented here, the vertical grid spacing is kept smaller than L_{oz}, although since they are of the same order near the free surface when $Ri_\tau = 500$, we cannot increase Ri_τ further with computational resources available to us.

In order to resolve the details of the turbulence at the free surface, a fine grid must be used in the vertical direction. The grid spacing used here at the top and bottom walls is $\Delta z^+ = 1/2$ and $\Delta z^+ = 2$, respectively. The present numerical method solves the equations with second-order accuracy on a uniform

computational grid. In order for the discretization scheme to be second-order accurate on the physical grid, the vertical grid stretching parameter, r_z, must obey (Fletcher (1991)):

$$r_z \equiv \frac{z_{j+1}}{z_j} = 1 + O(\Delta z). \tag{II.35}$$

The restriction on the grid stretching factor is therefore more stringent at the boundaries where Δz is very small. In order to account for this, an exponential function is used to set the vertical grid spacing so that the grid stretching is maximum in the center of the domain where the Δz is large. In addition, five uniformly spaced grid points are placed at the lower wall and 16 are placed near the free surface. With these restrictions, more points are needed in the vertical direction, and the grid size is 64 x 64 x 128 in the x, y, and z directions, respectively. The maximum vertical grid spacing is $\Delta z^+ = 11.5$. In order to ensure that the anisotropy of the grid does not introduce numerical errors, a case with more points in the horizontal was run and no significant differences were found.

The bulk Reynolds number after spinup for each case is listed in Table I, where Re_b is defined as:

$$Re_b \equiv \frac{u_b h}{\nu}, \qquad u_b \equiv \frac{1}{h}\int_0^h < u > dh, \tag{II.36}$$

and nondimensional time:

$$t_\tau = \frac{t u_\tau}{h}. \tag{II.37}$$

The case with $Ri_\tau = 0$ is started by interpolating from the velocity and density fields in half of the full-channel simulations of Armenio and Sarkar (2002). The first two stratified cases, $Ri_\tau = 25$ and 100 are both initialized with the $Ri_\tau = 0$ fields at $t_\tau = 4.4$, while the latter two, $Ri_\tau = 250$ and 500 are both initialized with the $Ri_\tau = 100$ data at $t_\tau = 51.8$. Each case has a spinup period where Re_b increases, indicating that the mean flow initially accelerates owing to an initial imbalance between the wall shear stress, reduced by stratification, and the driving pressure gradient. Eventually all cases tend to an equilibrium where $Re_\tau \simeq 400$, the mean wall shear stress and $\partial p/\partial x$ are in balance, and Re_b is steady in time.

Once a statistically steady state is reached (at $t_\tau \simeq 45$ for the $Ri_\tau = 500$ case), each simulation is continued for at least $50t_\tau$ to obtain a sample size sufficiently large to obtain converged statistics.

II.4 Results

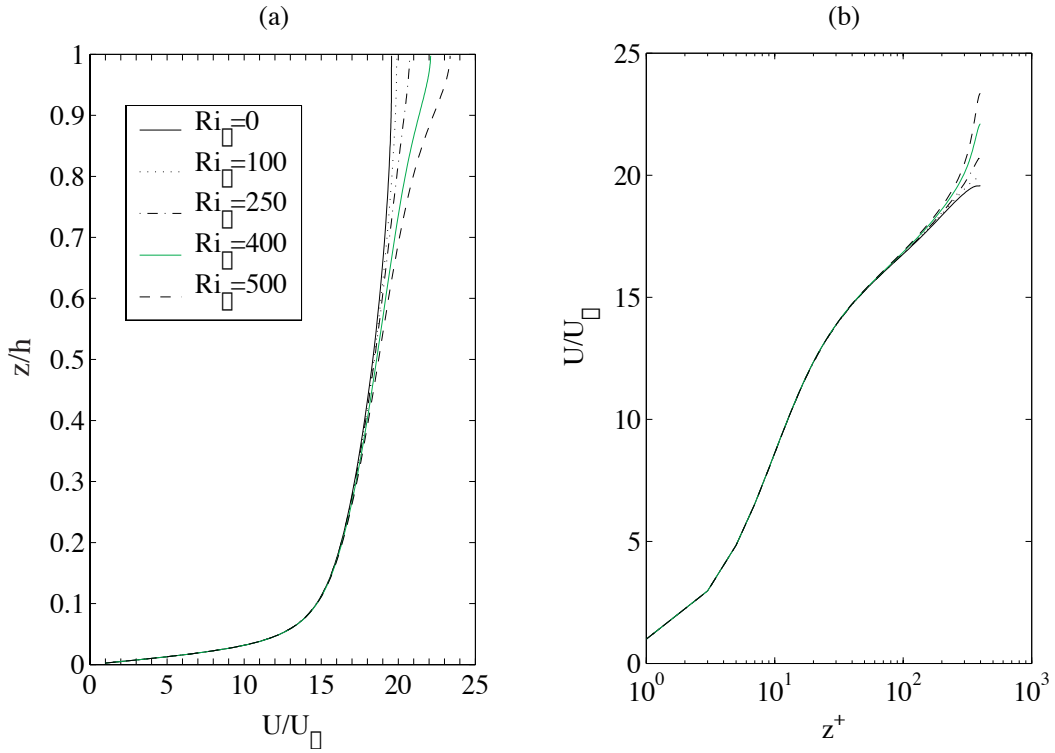

Figure II.3: Mean Velocity Profile

II.4.A Mean Profiles

We begin by describing some mean flow properties. Averages over the horizontal plane and time are denoted by $< \cdot >$. The average streamwise velocity profile, nondimensionalized by u_τ is shown versus z/h in Figure II.3(a). It has already been seen that u_b, the bulk-mean velocity defined by:

$$u_b = (1/h) \int_0^h < u > dz, \tag{II.38}$$

increases with Ri_τ. This increase of $< u >$ is seen to occur only in the region near the free surface. Note also that the mean shear in the pycnocline increases with Ri_τ. The spanwise and wall-normal velocities (not shown) are nominally zero. The log-law behavior is shown in Figure II.3(b). A log profile exists in the passive scalar case from $z^+ \simeq 40$ to near the free surface. Increasing Ri_τ causes the profile to deviate from the log law in the upper portion of the channel. The location of the deviation from the log-law correlates well with the location where the density gradient begins to diverge from the case of $Ri_\tau = 0$. For example, the location where $< U >$ becomes 1% larger than when $Ri_\tau = 0$ is very close to the location where $d < \rho > /dz$ is twice the passive scalar value. When $Ri_\tau = 500$ the region of log-law validity is relatively small, approximately 50 wall units.

Table II.2: Friction Coefficient: The present study has an imposed surface heat flux at the upper surface and an adiabatic lower wall. Nagaosa and Saito have an upper free surface and a lower wall, both being isothermal. Armenio and Sarkar have upper and lower walls, both being isothermal.

Taylor et al.

Ri_τ	$Ri_{\tau,\Delta}$	$C_f * 10^3$
0	0	6.593
25	0.56	6.579
100	2.7	6.535
250	10.7	6.397
400	24.8	6.183
500	39.4	5.989

Nagaosa and Saito

$Ri_{\tau,\Delta}$	$C_f * 10^3$
0	8.71
10	7.06
20	6.03

Armenio and Sarkar

$Ri_{\tau,\Delta}$	$C_f * 10^3$
0	8.18
18	6.37
60	4.99
120	3.71
240	3.19
480	240

Nagaosa and Saito (1997) also observe an increase in the streamwise velocity when they apply a fixed temperature difference across the channel to produce stable stratification. The region of increased velocity in their case extends from the surface to about 10 wall units from the lower wall, a much thicker region than is seen here. A convenient measure of the bulk change in streamwise velocity is

the skin friction coefficient:

$$C_f = 2\tau_w/\rho U_b^2. \tag{II.39}$$

Table II.2 gives C_f for each case of Ri_τ. For comparison, the values found by Nagaosa and Saito (1997) and Armenio and Sarkar (2002) are also shown. $Ri_{\tau,\Delta}$ defined with the density difference across the channel,

$$Ri_{\tau,\Delta} = \frac{gh\Delta\rho}{\rho_0 u_\tau^2}, \tag{II.40}$$

is introduced to measure stratification on a similar basis in all studies. Clearly C_f decreases with $Ri_{\tau,\Delta}$ in all studies, but the dependence observed here is much weaker than the 31% decrease between $Ri_{\tau,\Delta} = 0$ and 20 observed by Nagaosa and Saito (1997) and the 22% decrease between $Ri_{\tau,\Delta} = 0$ and 18 observed by Armenio and Sarkar (2002). This can be explained by the relatively limited region affected by stratification in the present study, a qualitative difference with respect to the previous fixed ΔT cases.

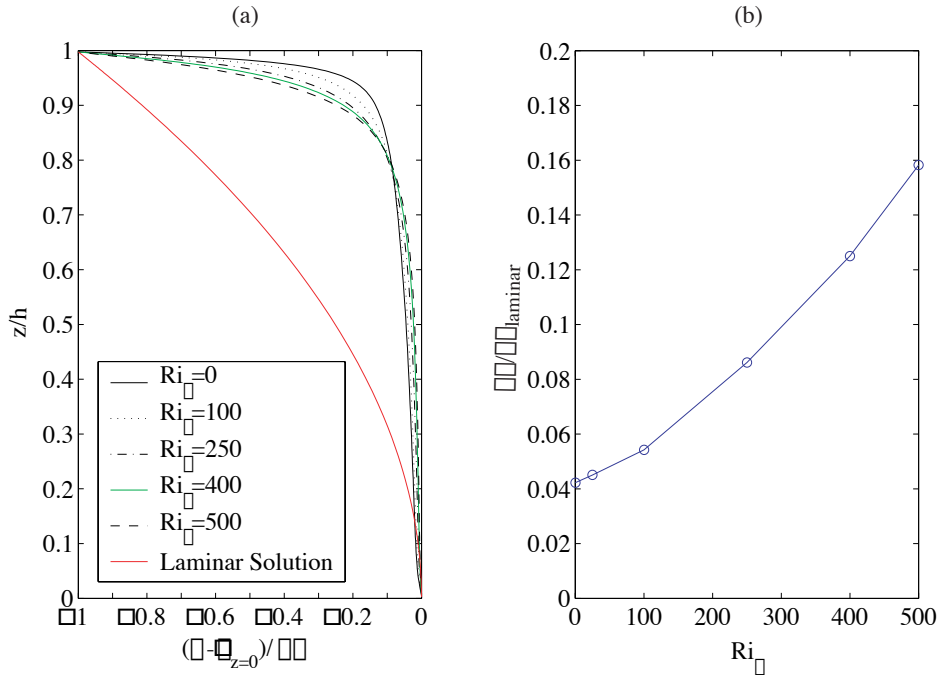

Figure II.4: Mean density profiles and density difference across the channel

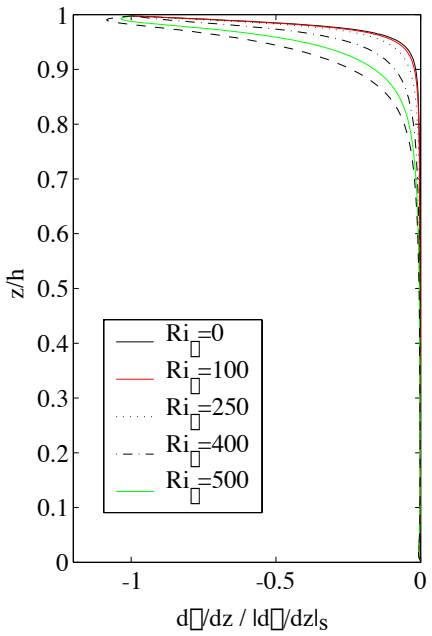

Figure II.5: Mean Density Gradient

The averaged density profile for each case is plotted as a function of nondimensional height in Figure IV.7(a) where the density is made nondimensional by $\Delta\rho$, the difference between wall and surface values as in Komori (1983). The laminar solution, the term $-z^2/2$ in Eq. (II.22), is also shown. Unlike the gradual variation of $\rho(z)$ in the laminar case, the turbulent flow exhibits a strongly stratified region, or pycnocline, near the free surface that overlies a relatively well-mixed region near the lower wall. The presence of the mixed region must depend on the existence of active turbulence since the density gradient of the laminar solution vanishes only near the wall. The thickness of the pycnocline increases with Ri_τ, implying that the turbulence generated near the lower wall is less effective at mixing for large Ri_τ. It should be noted that the density gradient is small but nonzero and nearly constant in the lower portion of the channel and only vanishes in a very thin layer within about 5 wall units from the wall. Figure IV.7(b) shows the variation of $\Delta\rho$ between cases. $\Delta\rho$ tends to increase with increasing Ri_τ (increasing stabilization) but, even for the largest $Ri_\tau = 500$ considered here, $\Delta\rho$

is much smaller than in the laminar case, another indication that the bottom wall continues to strongly generate turbulence.

The scaling of the pycnocline thickness as a function of the imposed stratification can be seen by considering a simple model. From Figure IV.7(a) it might be expected that an exponential function will provide a good first order representation to the density profile. First, for convenience, a nondimensional vertical coordinate is defined from the free surface: $z^* = 1 - z/h$. Then, the density gradient is approximated with an exponential:

$$\frac{d\rho}{dz^*} \simeq Ae^{-z^*/L}, \tag{II.41}$$

with the boundary conditions

$$\frac{d\rho}{dz^*}(z^* = 0) = 1, \quad \frac{d\rho}{dz^*}(z^* \to \infty) = 0. \tag{II.42}$$

The characteristic lengthscale of the pycnocline is L. Applying the boundary condition at the free surface gives $A = 1$. Figure II.5 shows that the density gradient vanishes well before the wall, so the zero flux boundary condition at $z^* = 1$ can be approximated to occur at $z^* \to \infty$, which is satisfied by Eq. (II.41). Integrating Eq. (II.41) gives

$$\rho(z^*) - \rho(0) = L(1 - e^{-z^*/L}). \tag{II.43}$$

Evaluating as $z^* \to \infty$:

$$\rho(\infty) - \rho(0) \simeq \rho(1) - \rho(0) = \frac{\Delta\rho}{\frac{d\rho}{dz}|_s h} = L. \tag{II.44}$$

Therefore the nondimensional characteristic length of the pycnocline is

$$L = \Delta\rho/(d\rho/dz|_s h). \tag{II.45}$$

Since $\Delta\rho$ increases with Ri_τ, the model correctly predicts the same to be true for L. The model fit to the density profiles is shown in Figure II.6. The model captures the qualitative behavior of the data, however the decay of $d\rho/dz$ is overestimated for small Ri_τ.

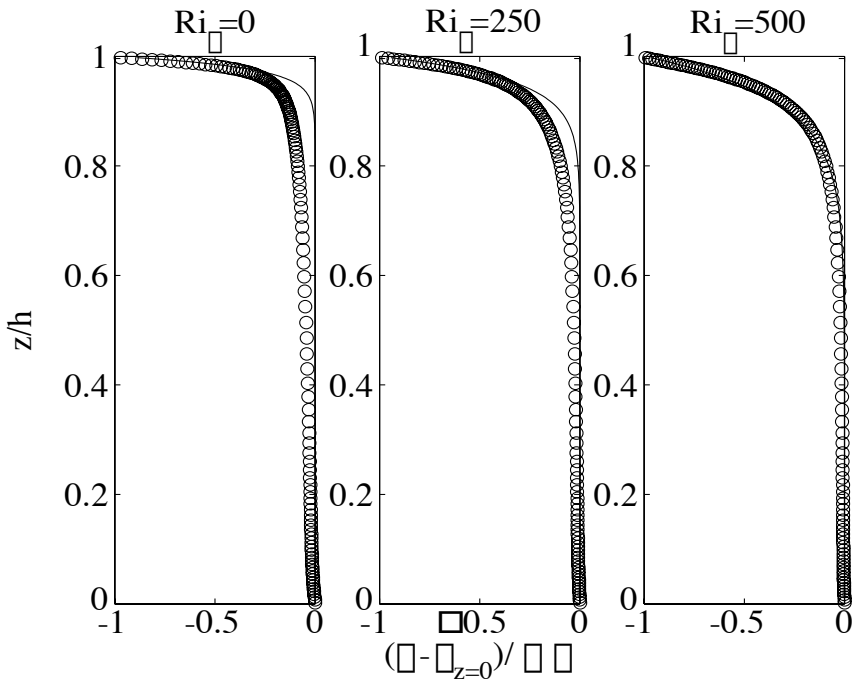

Figure II.6: LES data (circles) with an exponential model for the density profiles (lines)

II.4.B Turbulence Characteristics

Figure II.7(a) shows ρ_{rms} nondimensionalized with the surface gradient and the channel height. In all cases, the maximum occurs in the pycnocline where the density gradient is largest. Nondimensionalized in this way, the magnitude of ρ_{rms} increases with Ri_τ, and the location of the maximum is very close to the free surface in all cases but deepens slightly with Ri_τ. However, from Figure II.7(b), it is apparent that the magnitude of ρ_{rms} decreases with respect to $\Delta\rho$ with increasing Ri_τ. This is a sign that turbulence is somewhat suppressed by the stable stratification when Ri_τ is large.

Figure II.8 shows the profile of the *rms* vertical velocity components. In the lower portion of the channel, the profiles collapse and are consistent with unstratified closed channel flow. In the upper region, w_{rms} decreases monotonically with increasing Ri_τ. Since w_{rms} corresponds to the vertical turbulent kinetic energy, and Ri_τ is linked to the size of the buoyancy suppression term in the

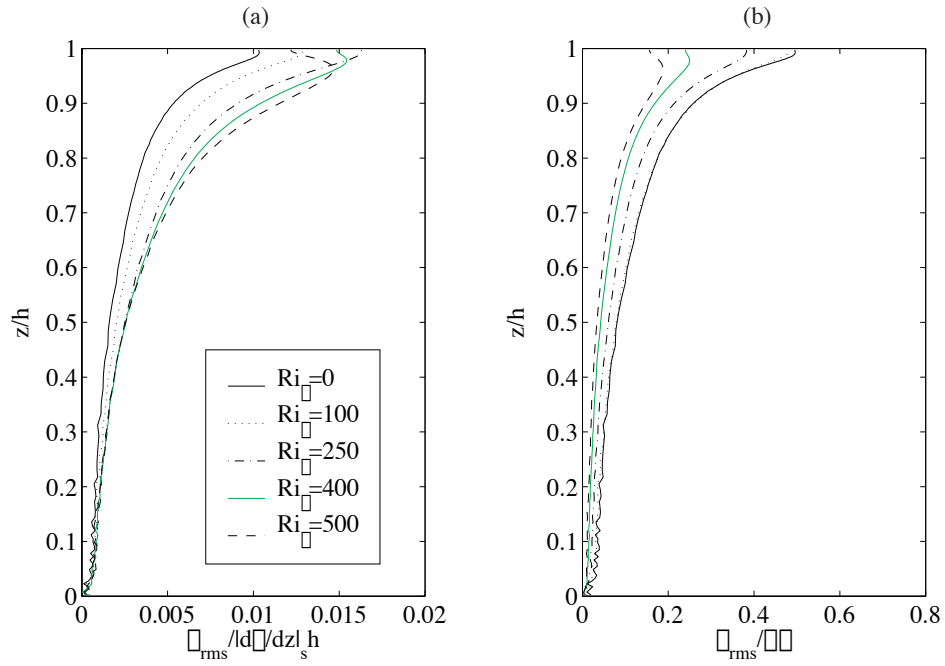

Figure II.7: *rms* density profiles normalized by (a) free surface gradient and (b) density jump across channel

TKE budget, the observed decrease might be expected. Interestingly, near the free surface where w_{rms} is suppressed by the geometry in the unstratified case, the dependence on Ri_τ is lost. The profiles of u_{rms} and v_{rms} are more complicated. In the region between about $0.5 < z/h < 0.85$, the horizontal *rms* velocity increases with Ri_τ, consistent with the increase of mean shear in that region. Then, in the near surface region, the horizontal *rms* first increases from $Ri_\tau = 0$ to $Ri_\tau = 250$, then decreases sharply in the most stratified cases.

We can begin to trace the cause of the increase in $< u >$ with Ri_τ by looking at the Reynolds shear stress, $< u'w' >$ shown in Figure II.9(b). Also shown is the total shear stress, $\tau(z) = \tau_{wall}(1 - z/h)$. It can be shown (eg. Pope (2000)) that the viscous shear stress is the difference between this line and $< u'w' >$. Thus, the increase in the mean vertical shear (equivalently viscous shear stress) in the pycnocline, and therefore $< u >$ at the free surface, occurs because of the stratification induced decrease in the magnitude of $< u'w' >$, which is especially

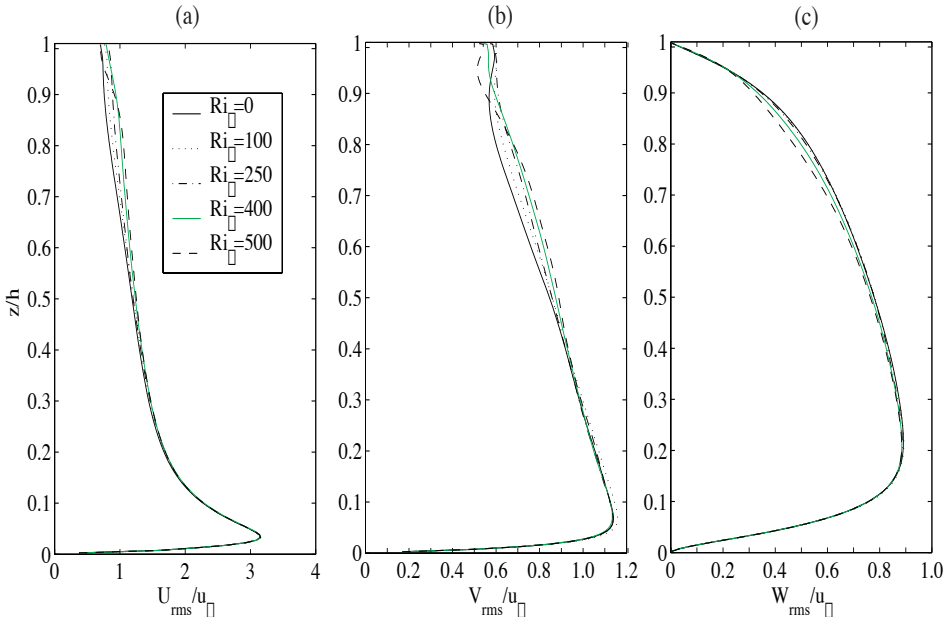

Figure II.8: *rms* velocity profiles

strong when $Ri_\tau = 500$. The drop in $< u'w' >$ magnitude will be explained using energy arguments in section IV (C).

Contributions to the Reynolds stress can be seen by plotting u' vs. w' as shown in Figure II.10 for $z/h = 0.84$. In each quadrant of the plots is a label showing its contribution to $< u'w' > /u_\tau^2$. The upwelling events can be clearly seen for $Ri_\tau = 0$ by an anisotropic tail extending to the upper left. When $Ri_\tau = 500$ the strength of the upwellings is diminished, and the distribution becomes more isotropic. In both cases, downwelling events are not as energetic as upwelling bursts, and contribute less to $< u'w' >$.

The buoyancy flux, $B = -g/\rho_0 < \rho'w' >$, couples the vertical component of turbulent kinetic energy and the turbulent potential energy. Figure II.9(b) shows the mass flux, $< \rho'w' >$ nondimensionalized by the free surface density gradient, the channel height, and u_τ. Vertical motion under the negative mean density gradient implies a positive mass flux (negative buoyancy flux) for the usual case of co-gradient transport. The mass flux decreases everywhere with increasing Ri_τ and has a small countergradient value near the surface when $Ri_\tau = 500$. Coun-

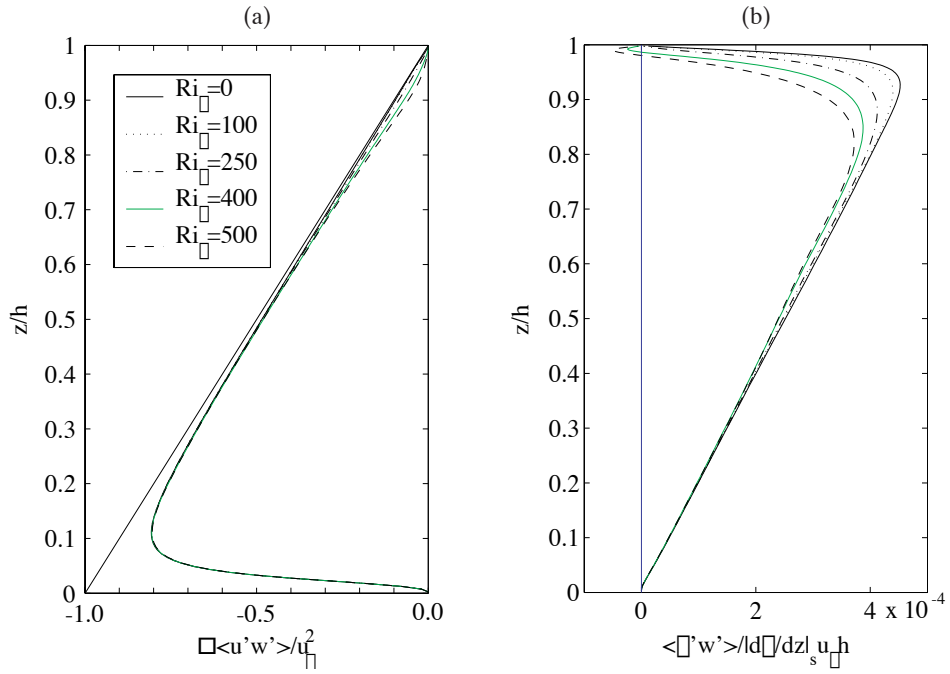

Figure II.9: Reynolds shear stress and mass flux

tergradient transport is associated with falling heavy fluid that releases potential energy to kinetic energy. Komori et al. (1983) also find a countergradient heat flux, although they report it being much larger and appearing at lower Ri_τ than in the present simulations. The difference is presumably due to the boundary conditions, since in the Komori et al. (1983) experiments, the wall and free surface were roughly held at fixed temperature. Large countergradient buoyancy fluxes were also seen in the study by Armenio and Sarkar (2002) in a closed channel with fixed temperature boundary conditions at the walls.

The source of the countergradient buoyancy flux can be seen by examining the phase angle of the velocity-density spectra. By defining the co-spectrum, $Co_{\rho w}(\kappa_x, z)$ and quadrature spectrum, $Qu_{\rho w}(\kappa_x, z)$ as the real and imaginary parts, respectively, of:

$$\sum_{\kappa_y} \hat{w}(\kappa_x, \kappa_y, z)\hat{\rho}^*(\kappa_x, \kappa_y, z), \tag{II.46}$$

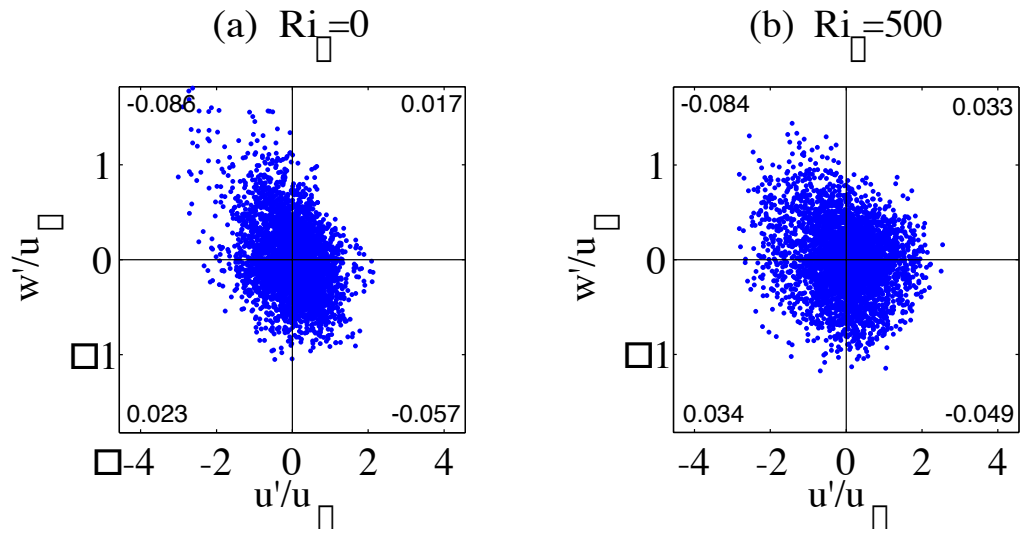

Figure II.10: u' vs w' at z/h=0.84

the phase angle, $\phi(\kappa_x, z)$ can be defined by:

$$tan(\phi) = \frac{Qu_{\rho w}}{Co_{\rho w}}. \tag{II.47}$$

The absolute value of the phase angle is shown for $Ri_\tau = 0$ and $Ri_\tau = 500$ in figure V.6. The phase angle is averaged over data at several time instants and linearly weighted by the absolute value of the energy at the corresponding k_x and t,

$$E_{\rho w}(\kappa_x, z, t) = \sum_{\kappa_y} \hat{\rho}\hat{w}^* + \hat{\rho}^*\hat{w}, \tag{II.48}$$

which is shown in figure II.12. When $0 \leq |\phi| < \pi/2$ the flow acts to mix the density field, $< \rho' w' >$ is positive, and energy is extracted from the turbulent kinetic energy by buoyancy. When $\pi/2 < |\phi| \leq \pi$, the value of $< \rho' w' >$ is negative, and buoyancy is a source of turbulent kinetic energy since, on average, heavy fluid is falling and light fluid is rising. It is known that linear internal waves are associated with a phase angle $|\phi| = \pi/2$ (Gill (1982).) The horizontal wave number κ_x in figure V.6 has been nondimensionalized by the channel height. For all cases, most of the energy is contained in wavenumbers $\kappa_x < 15$ as seen in figure II.12. Figure V.6 (a)-(b) show that when $Ri_\tau = 0$, all wavenumbers are in the range of active mixing as would be expected for a passive scalar. When

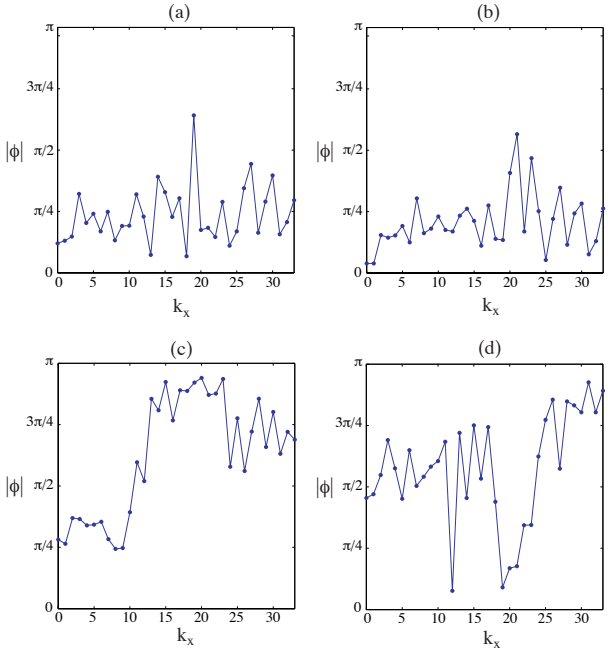

Figure II.11: Absolute value of the velocity-density phase angle, (a): $Ri_\tau = 0$, $z/h = 0.927$ where $< \rho' w' >$ is maximum, (b): $Ri_\tau = 0$, $z/h = 0.99$ near the free surface (c): $Ri_\tau = 500$, $z/h = 0.825$ where $< \rho' w' >$ is maximum (d): $Ri_\tau = 500$, $z/h = 0.99$ where $< \rho' w' >$ is minimum and negative

$Ri_\tau = 500$, and at the location of maximum buoyancy flux, $z/h = 0.825$ (see figure V.6(c)), the large energy-containing scales have $|\phi| < \pi/2$ indicating mixing, while the small scales exhibit a counter-gradient buoyancy flux of small magnitude, see figure II.12(c). Near the free surface where the buoyancy flux is minimum and negative, most of the energy containing scales appear to be associated with linear internal waves ($|\phi| \simeq \pi/2$) or mild counter-gradient fluxes, while the small scales are more strongly counter gradient but of small magnitude. From figure II.12(d) it can be seen that the dominant contribution to the countergradient buoyancy flux comes generally from the large scales of motion.

Although the influence of Ri_τ on the bulk Reynolds stress is rather small as also reflected in small changes to the friction coefficient, the *local* turbulent diffusion is strongly affected in a significant portion of the channel, as can be seen

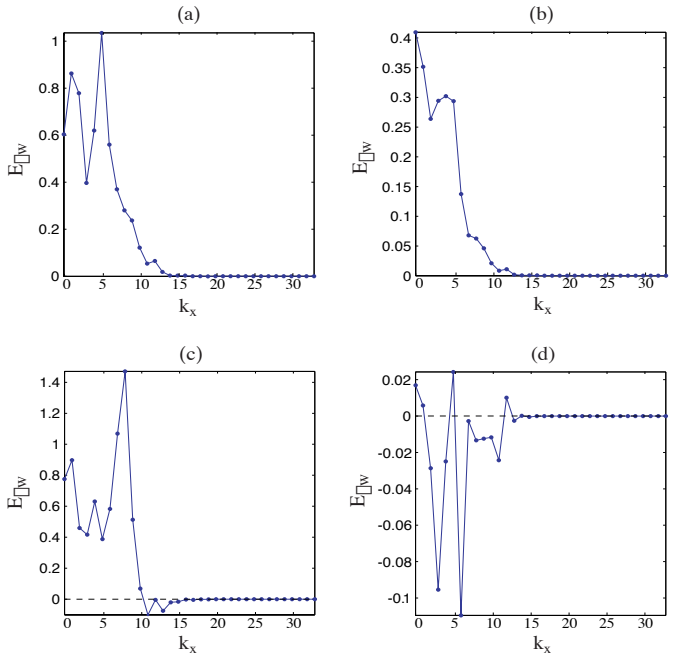

Figure II.12: Energy of the velocity-density co-spectrum at, (a): $Ri_\tau = 0$, $z/h = 0.927$ (b): $Ri_\tau = 0$, $z/h = 0.99$ (c): $Ri_\tau = 500$, $z/h = 0.825$ (d): $Ri_\tau = 500$, $z/h = 0.99$

by defining the eddy viscosity, ν_T:

$$- < u'w' >= \nu_T \frac{d < u >}{dz}. \tag{II.49}$$

The mean streamwise stress balance can then be written:

$$\tau_w(1 - \frac{z}{h}) = \frac{d < u >}{dz}(\frac{1}{Re_\tau} + \nu_T), \tag{II.50}$$

so any change in the mean shear between cases must also be reflected in the eddy viscosity, plotted in Figure II.13(a). Eddy viscosity decreases very significantly with Ri_τ, even in the interior of the open channel where stratification is relatively low. The mass diffusivity, κ_T defined as:

$$< w'\rho' >= -\kappa_T \frac{d\rho}{dz}, \tag{II.51}$$

also decreases very significantly with Ri_τ at nearly every vertical level as shown in figure II.13(b).

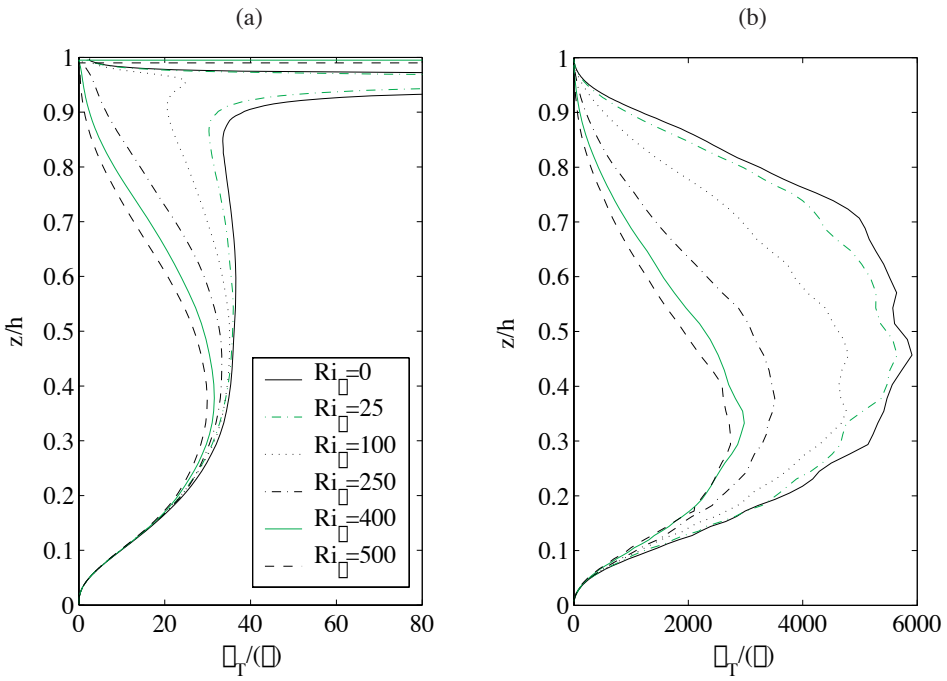

Figure II.13: Eddy viscosity and Eddy diffusivity

The buoyancy or Brunt-V*äisälä* frequency, N defined as:

$$N^2 = \frac{-g}{\rho_0}\frac{\partial < \rho >}{\partial z}, \tag{II.52}$$

is shown in the left panel of figure II.14. This plot makes clear the deepening and strengthening of the pycnocline with increasing Ri_τ. A local measure of the relative importance of stratification and shear, the gradient Richardson number can be defined using N and the mean shear, $S = d < u > /dz$ so that $Ri_g = N^2/S^2$, also shown in figure II.14. The gradient Richardson number measures the relative importance of turbulent production by the mean shear, and suppression by the stable stratification. As such, it is associated with the stability of the flow, with linear instability possible only if $Ri_g < 1/4$ somewhere in the domain. Since N increases with Ri_τ, it is surprising that above the linear stability threshold, Ri_g tends to decrease with Ri_τ. Evidently an increase in mean shear more than compensates for the increase in N.

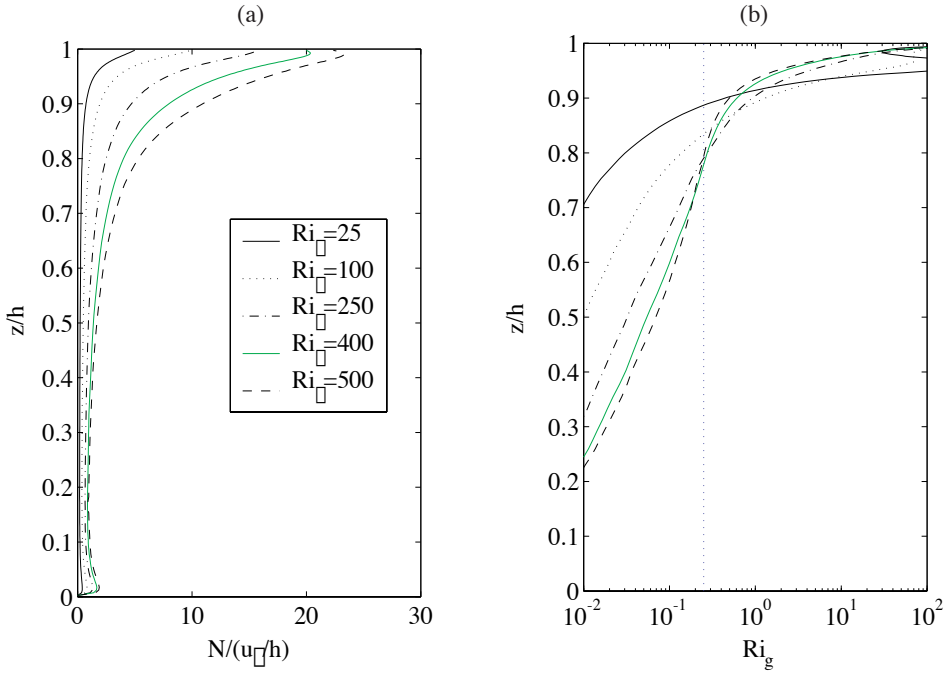

Figure II.14: Brunt-Vaisala Frequency and Gradient Richardson number

II.4.C Turbulence-surface interactions

The increase in $< u >$ seen near the free surface in the highly stratified cases can be attributed to a potential energy barrier created by the presence of the pycnocline. It has been shown previously (Pan and Banerjee (1995)) that a large portion of the Reynolds stress near an unstratified free surface in open channel flow is due to impinging of low-speed fluid advected from the near wall region. While the wall generated low speed streaks do not maintain coherence over distances comparable to the channel height in this study, low-speed ejections from the wall boundary layer are observed to directly impact the free surface in the low stratification cases.

That the upward advection of low speed fluid to the surface is inhibited for large Ri_τ is implied by the drop in correlation between u' and w' in the Reynolds stress of figure II.9(b). To determine the fate of turbulence generated near the lower wall more directly, it is useful to consider an energy balance. Traditionally, the buoyancy scale w_{rms}/N gives a measure of how far a fluid parcel would travel

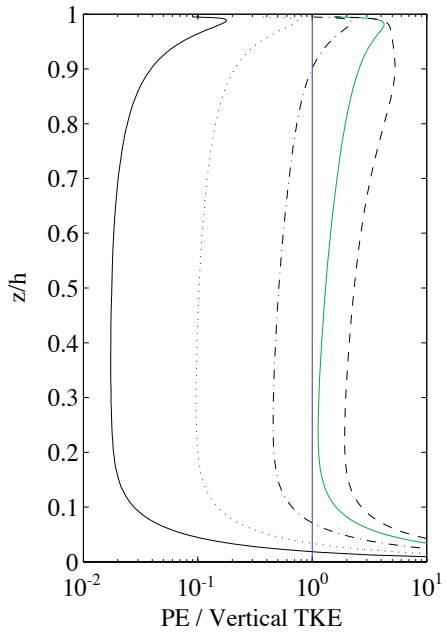

Figure II.15: Ratio of potential energy needed to reach the upper surface from a given location to the vertical TKE at that location

vertically if all of its vertical turbulent kinetic energy were converted to potential energy. For the situation considered here, this is not accurate since N is highly variable in the vertical direction. For instance, in the highly active region near the lower wall, w_{rms} is large while N is small, so the buoyancy scale may be very large. However, the presence of a strong pycnocline near the surface adds to the potential energy barrier, and may prevent direct interaction with the surface.

As a more accurate measure of the ability of local turbulence to reach the free surface, we compare the vertical turbulent kinetic energy to the potential energy deficit relative to the free surface. This ratio, shown in figure II.15 is:

$$\frac{g\int_z^h (<\rho>(z') - <\rho>(z'))dz'}{\frac{1}{2}<w'w'>}. \tag{II.53}$$

As expected, this ratio is largest when $Ri_\tau = 500$ since this case has a stronger, deeper pycnocline, requiring more energy to reach the free surface. The cases with the lowest stratification, namely $Ri_\tau = 25$ and $Ri_\tau = 100$, have small values of this

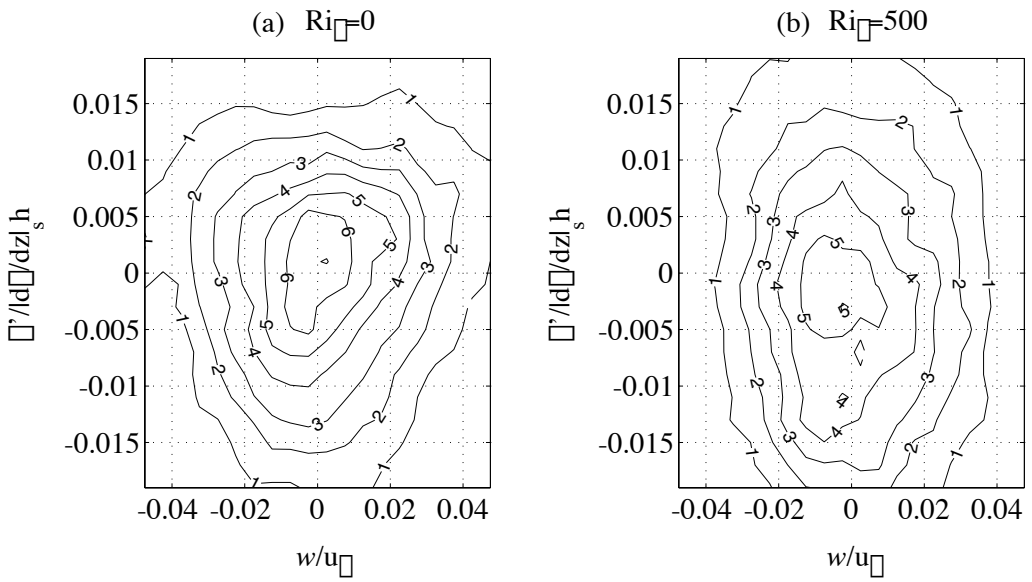

Figure II.16: Joint PDF between vertical velocity, w and density anomaly, $\rho'(\mathbf{x},t) = \rho(\mathbf{x},t) - <\rho>(z)$ at z/h=0.975 for (a) $Ri_\tau = 0$, (b) $Ri_\tau = 500$. The density anomalies corresponding to $<\rho>$ at the top and bottom respectively are -0.013 and 0.008 for $Ri_\tau = 0$, and -0.023 and 0.056 for $Ri_\tau = 500$.

ratio. Since the pycnocline is weak in relation to the vertical TKE, the cases with $Ri_\tau = 25$ and $Ri_\tau = 100$ are quite similar to the passive scalar case, $Ri_\tau = 0$. The strength of the pycnocline dominates over the vertical TKE when $Ri_\tau = 500$. As the low-speed fluid near the wall, on average, does not have sufficient energy to reach the surface in the latter case, a drop in $<u'w'>$ is observed near the surface and, correspondingly, there is an increase in $<u>$. It should be noted that, since this ratio is an *average* measure, it does not preclude the instantaneous advection of bottom fluid to the surface, but does indicate that it is much less likely when a strong pycnocline exists.

The strength and frequency of upwelling events can be quantified with a joint probability density function (PDF) of the vertical velocity, w, and density anomaly, $\rho'(\mathbf{x},t) = \rho(\mathbf{x},t) - <\rho>(z)$ as shown in Figure II.16 for $Ri_\tau = 0$ and

500 at $z/h = 0.975$. The figure caption lists the values of ρ' corresponding to the mean density at the top and bottom for comparison. The plot indicates that when $Ri_\tau = 500$, it is very rare for fluid with density equal to the mean at $z = 0$ (corresponding to $\rho' = 0.056$ and well out of the plotted region) to be seen at this height. In the case of $Ri_\tau = 0$ it is common to see $\rho' = 0.008$, the mean at $z = 0$, and the free surface value $\rho' = -0.013$ is somewhat less likely. The tails of the w distribution are wider when $Ri_\tau = 0$ and $\rho' > 0$; a large w and $\rho' > 0.008$ is associated with the strong upwelling events seen when $Ri_\tau = 0$ and mentioned previously. For the case of $Ri_\tau = 0$ large w events of both signs are associated with positive density anomaly and the distribution is nearly symmetric about $w = 0$. Evidently, at this location, the downwellings of dense fluid are as strong and frequent as the upwellings. When $Ri_\tau = 500$, the largest vertical velocities are no more likely to be associated preferentially with either heavy or light fluid, indicating that events with upwelling of dense fluid are not dominant.

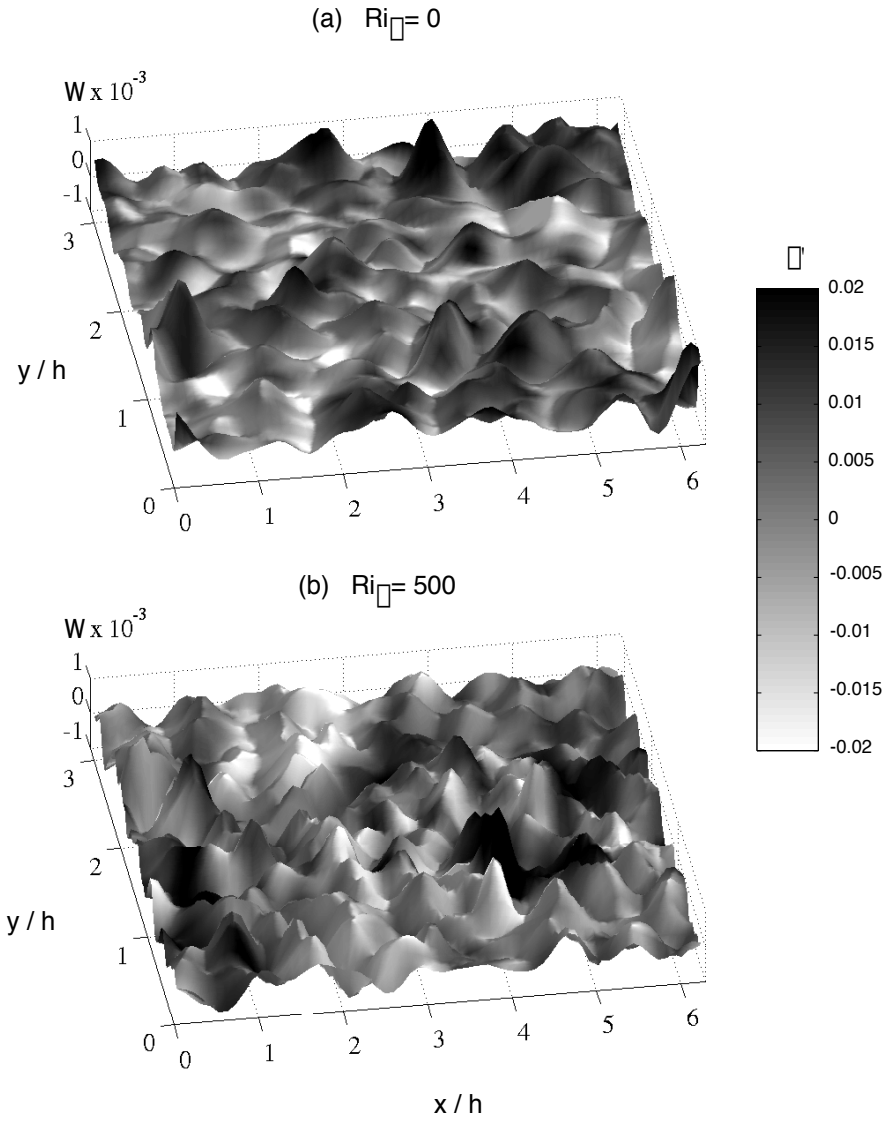

Figure II.17: Instantaneous height maps of vertical velocity with density perturbation in grayscale

The effect of stratification on dense fluid upwellings at the free surface can also be clearly seen by examining the instantaneous property distributions. Figure II.17 shows ρ' and w', the deviation from the horizontal mean, at $z/h = 0.999$ for $Ri_\tau = 0$ and $Ri_\tau = 500$ at the last simulation time in both cases. The height of the surface mesh denotes the vertical velocity with the tall peaks indicating rising fluid ($w' > 0$). The corresponding grayscale shows ρ' with dark gray denoting heavy fluid with positive ρ'. Notice that for $Ri_\tau = 0$, each region of upwelling is associated with a positive density anomaly indicating an upwelling of dense fluid from the bottom. When $Ri_\tau = 500$ none of the positive w' patches at this particular time are associated with large positive ρ'. These snapshots are typical of those seen throughout the simulation; while the existence of dense fluid upwellings cannot be precluded for the strongest stratification cases, they are much less common than when $Ri_\tau = 0$.

II.4.D Classification of Buoyancy Effects

It will be useful for the remaining discussion to precisely define regimes according to the relative influence of stratification. Since part of our flow remains unstratified, a local measure of buoyancy effects is desired. It would be possible to follow Armenio and Sarkar (2002) who, based on qualitative changes in mean flow profiles, correlation coefficients and buoyancy flux at $Ri_g \approx 0.25$, defined a buoyancy dominated region in the outer flow where $Ri_g(z) > 0.25$, and a buoyancy affected region near the wall where $Ri_g(z) < 0.25$. From an examination of mixing diagnostics as a function of Ri_g presented later in section IV F, it is clear that classification based on Ri_g would not work in the present case. Instead, it is suggested that the stratification may be classified by comparing turbulent length scales with the Ozmidov scale as reported in Itsweire et al. (1993). They use the Ellison length scale, L_E, to characterize the large scales of turbulence and the Kolmogorov scale, η, to characterize small scales, and find that the buoyancy affected region (the beginning of departure from passive scalar behavior also called buoyancy control

by these authors) begins when $L_O \approx L_E$, and buoyancy domination begins when $L_O \approx 9 * \eta$, where η is the Kolmogorov scale. We find that L_E overestimates the large scale of turbulence and propose that, for the bounded flow considered here, use of the distance to the nearest boundary gives a more direct estimate of the length characterizing the large vertical scales of turbulence. We define this geometric scale by $L_z = min[2z, 2(h-z)]$, the factors of two have been added to give a peak to crest overturning scale.

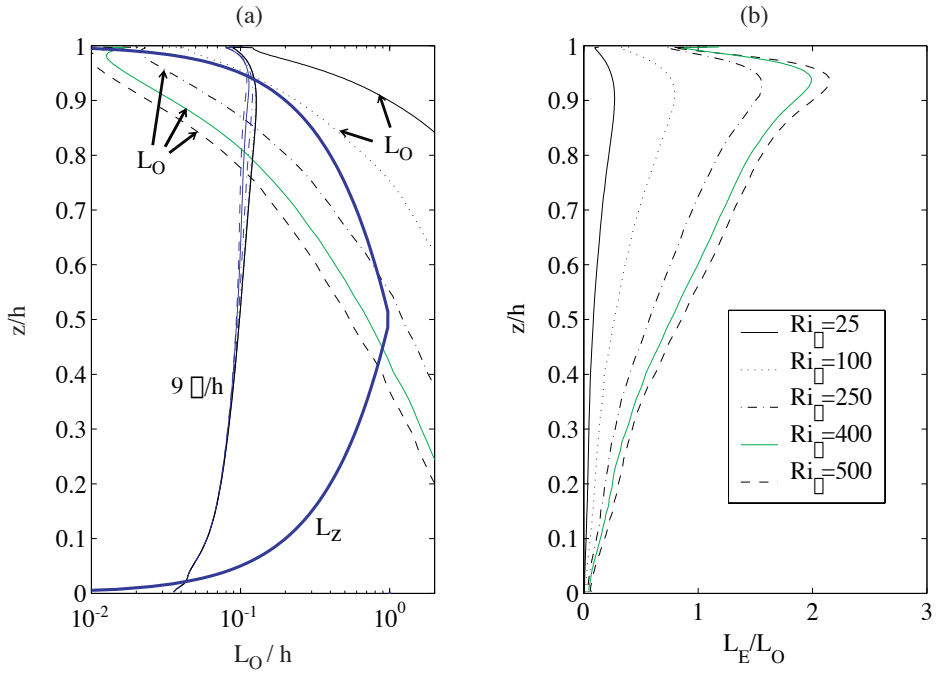

Figure II.18: (a) Ozmidov scale with Kolmogorov scale and geometric constraints, (b) Ratio of Ellison to Ozmidov scales

Figure II.18(a) shows profiles of the Ozmidov scale along with 9 times the Kolmogorov scale, and the geometric scale, L_z. This figure can be used to classify the relative importance of buoyancy. When $L_O > L_z$ and $> 9\eta$ the departure from unstratified flow is expected to be small. When $L_O < L_z$ but $> 9\eta$ the flow is buoyancy affected, and when $L_O < 9\eta$ the flow is buoyancy dominated. It should be stressed that that the demarcation between regimes is not sharp and that the definition of the length scales is only approximate. For instance the geometric

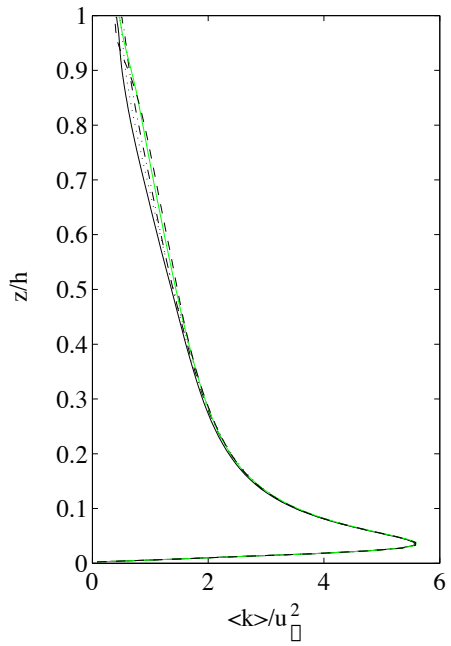

Figure II.19: Nondimensional turbulent kinetic energy

constraints on the upper and lower walls clearly should not be symmetric, and large eddies will not be isotropic. Nevertheless, the flow does appear to be qualitatively different in each regime. In particular, notice that $Ri_\tau = 25$ would be classified as unstratified, and $Ri_\tau = 100$ is only marginally buoyancy affected in the pycnocline, and we will see that these cases are qualitatively different than the others.

It is evident by re-examining the turbulent profiles that the flow behaves qualitatively different in each buoyancy regime. In each case, in the region with $L_z < L_0$, the profiles of rms velocity, Reynolds stress, and buoyancy flux collapse to the unstratified case, $Ri_\tau = 0$. For $Ri_\tau = 500$, this corresponds to $z/h < 0.4$. Note that, in this region, N and ρ_{rms} remain dependent on Ri_τ indicating that, although density changes remain, they are too weak for buoyancy to significantly influence the turbulence. Stratification starts to play a dynamical role in the buoyancy affected regime when $9\eta < L_O < L_z$. This regime applies to the flow region generally below the pycnocline, and the strength of buoyancy effects additionally depends on Ri_τ, e.g. the horizontal rms velocity increases and w_{rms} decreases

with increasing Ri_τ. As will be shown, the turbulent kinetic energy budget also changes significantly with Ri_τ. The location when L_O becomes less than 9η roughly corresponds to the start of the pycnocline, except in the cases with $Ri_\tau = 0$ and 25 where L_O is never a limiting lengthscale. In the buoyancy dominated regime, the dependence of u_{rms}, v_{rms}, and Ri_g on Ri_τ reverses compared to that of buoyancy affected flow. We will see that this is also true for the mixing efficiency and the turbulent Prandtl number.

II.4.E Turbulent Energy Budgets

The profiles of the Reynolds averaged turbulent kinetic energy,

$$< k >= \frac{1}{2} < u_i' u_i' >, \tag{II.54}$$

are shown in figure II.19. Several regions with distinct behavior can be identified. First, below $z/h \approx 0.4$ all cases behave like the passive scalar case, $Ri_\tau = 0$, and stratification is not felt. Then in the region $0.4 \leq z/h \leq 0.85$, the value of $< k >$ increases with increasing Ri_τ. Finally, in the near surface region where the more stratified cases become buoyancy dominated, the behavior is more complicated, first increasing with Ri_τ when $Ri_\tau \leq 250$ and then decreasing in the largest stratification cases.

At statistical steady state, the Reynolds averaged turbulent kinetic energy budget can be written:

$$\begin{aligned} -\frac{1}{2}\frac{\partial}{\partial z} < w' u_i' u_i' > -\frac{\partial}{\partial z} < w' p' > + \frac{1}{Re_\tau}\frac{\partial^2 k}{\partial z^2} - < S_{ij} >< u_i' u_i' > \\ -\frac{1}{Re_\tau} < \frac{\partial u_i'}{\partial x_j}\frac{\partial u_i'}{\partial x_j} > - Ri_\tau < w' \rho' > - \frac{\partial}{\partial z} < u_i' \tau_{31} > + < \tau_{ji}\frac{\partial u_i'}{\partial x_j} > = \frac{\partial k}{\partial t} = 0, \end{aligned} \tag{II.55}$$

where all terms are made nondimensional with u_τ, $d\rho/dz|_s$ and h. The terms are the turbulent transport, pressure transport, viscous diffusion, production, dissipation, buoyancy flux, subgrid transport and subgrid dissipation, respectively. These terms are shown in figure III.4 in the upper portion of the channel, and

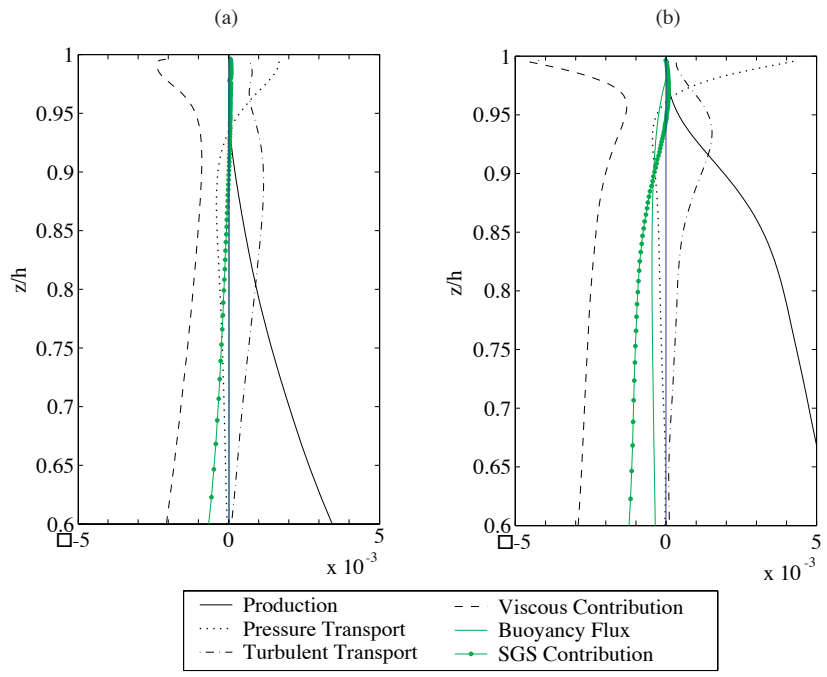

Figure II.20: Turbulent kinetic energy budgets for (a) $Ri_\tau = 0$, and (b) $Ri_\tau = 500$, normalized by u_τ^4/ν

normalized by u_τ^4/ν as per Calmet and Magnaudet (2003). Near the free surface, the production decreases while the turbulent and pressure transport increase to balance the viscous loss. Such behavior is similar to that shown by Calmet and Magnaudet (2003) for an LES of unstratified open channel flow at $Re_\tau = 1280$. In the lower portion of the channel the dominant balance is between production and dissipation, and this behavior can be still be seen in the lower portion of figure III.4.

The diagonal components of the pressure-strain tensor are shown in figure II.21 where:

$$\Pi_{ij} = < \frac{p}{\rho}(\frac{\partial u_i}{\partial x_j} + \frac{\partial u_j}{\partial x_i}) > . \tag{II.56}$$

Since the trace of the tensor, $\Pi_{ii} = 0$, it does not contribute to the budget for k, but is important for the redistribution of energy among the rms velocity components. For example, as is well-known and seen in figure II.21(a), near the wall Π_{11} is a large sink for u_{rms} and a source for v_{rms} and w_{rms}. In this region, the

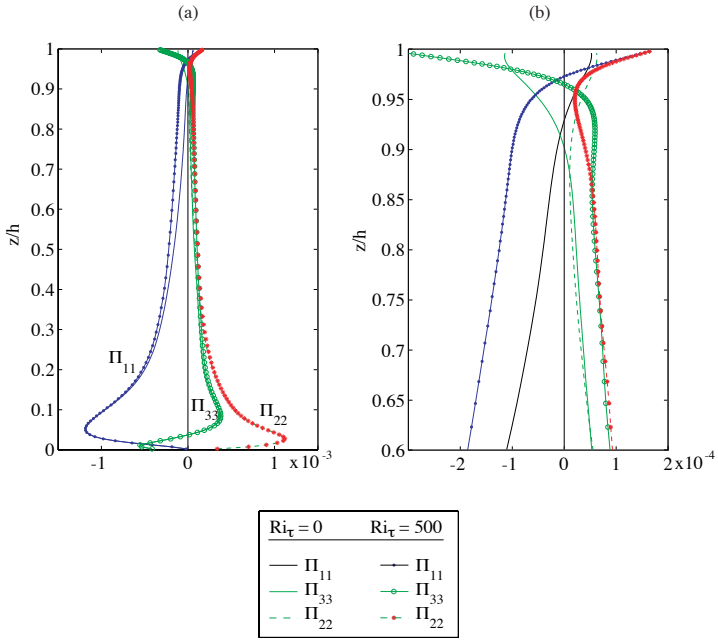

Figure II.21: Pressure-strain correlations over (a) whole channel and (b) near surface region. Lines denote $Ri_\tau = 0$, symbols denote $Ri_\tau = 500$

pressure-strain terms act to isotropize the Reynolds stresses. This behavior holds until about $z/h = 0.9$. Figure II.21(b) shows the upper portion of the channel in more detail. Again, solid lines denote $Ri_\tau = 0$ and lines with symbols denote $Ri_\tau = 500$. In both cases, near the free surface Π_{33} becomes negative and Π_{11} and Π_{22} become positive, indicating energy transfer from the wall-normal component to the horizontal directions. Since u_{rms} and v_{rms} are larger than w_{rms} in this area, this transfer promotes anisotropy, a behavior that has been associated with the 'splatting' of fluid on the free surface (Nagaosa and Saito (1997); Walker et al. (1996); Handler et al. (1999); Nagaosa (1999)). Nagaosa and Saito (1997) report that increasing the fixed temperature difference between the top and bottom of open channel flow decreases the transfer from vertical to spanwise directions through the pressure-strain. Interestingly, here with a fixed temperature gradient at the free surface we find the opposite effect. Increasing Ri_τ increases the energy transfer from the vertical to horizontal directions. One explanation for the reduc-

tion of Π_{ij} with increasing stratification found by Nagaosa and Saito is the partial relaminarization of the near-wall turbulence in their simulations, which results in a drop in each rms velocity component throughout the channel. The level of turbulent kinetic energy impacting the surface is therefore significantly smaller, as is the pressure-strain correlation. The effect on pressure-strain need not be the same as in Nagaosa and Saito in the present study where the turbulent production at the lower wall is unaffected by stratification.

As was mentioned in the introduction, previous studies (Walker et al. (1996); Nagaosa (1999)) have shown that turbulence at a free surface without the presence of stratification cannot be well represented by two-dimensional dynamics. It is generally thought that stratification tends to make turbulence more two-dimensional, so it might be anticipated that, with sufficient stratification, the dynamics at the free surface might be approximated by a two-dimensional model. However, the turbulent kinetic energy budget at the free surface shows that vertical gradients are important. It is therefore apparent that knowledge about the subsurface three-dimensional turbulence is necessary to model the dynamics at the free surface.

Although the pressure-strain transfer from w to u and v becomes larger with increasing Ri_τ, it is interesting that the x-z velocity correlation coefficient defined as

$$R_{uw} = -\frac{< u'w' >}{u_{rms} w_{rms}}, \tag{II.57}$$

decreases with increasing Ri_τ, dropping to zero at the free surface in the case with $Ri_\tau = 500$, as seen in figure II.22(a). Our results with $Ri_\tau = 0$ compare well to those of Nagaosa (1999) in unstratified open channel flow, except for a few minor differences that can be explained by the fact that we use a larger friction Reynolds number, $Re_\tau = 400$ compared to $Re_\tau = 150$. When $Ri_\tau = 0$, the value of R_{uw} at the free surface is nearly half of the maximum value. However, we see that R_{uw} decreases at the surface with increasing Ri_τ, and when $Ri_\tau = 500$, it becomes very small. When plotted as a function of Ri_g as in II.22(b), it appears that the

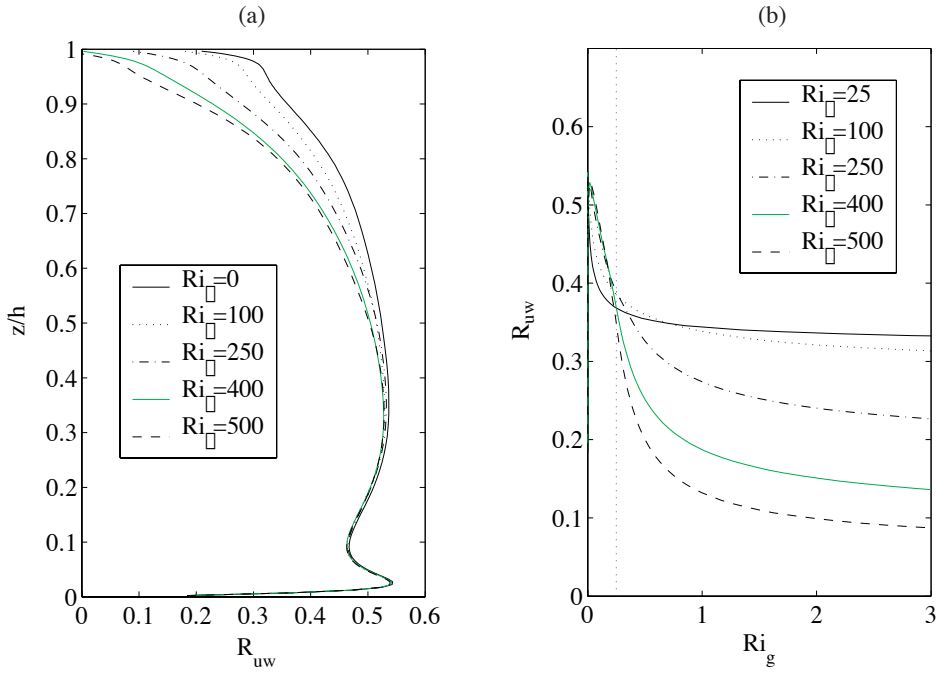

Figure II.22: Streamwise, wall-normal velocity correlation coefficient

behavior is well separated into two regions by $Ri_g = 0.25$. When $Ri_g < 0.25$, the buoyancy affected cases ($Ri_\tau \geq 250$) appear to collapse to one function of Ri_g. For $Ri_g > 0.25$, R_{uw} decreases with increasing Ri_τ.

II.4.F Mixing Diagnostics

The mass flux is plotted as a function of Ri_g in figure II.23(a). The maximum occurs near $Ri_g = 0.25$, and the cases with larger Ri_τ exhibit a decrease of mass flux with increasing Ri_g. Although the above mentioned dependence on Ri_g is consistent with Armenio and Sarkar (2002), it should be emphasized that there is an important difference: when plotted as a function of Ri_g, the buoyancy flux is still strongly dependent on Ri_τ. An alternate stratification parameter is the vertical Froude number,

$$Fr_v = \frac{w_{rms}}{NL_E}, \tag{II.58}$$

where $L_E =< \rho_{rms} > /d < \rho > /dz$ is the Ellison scale, and II.23(b) gives the mass flux, replotted as a function of Fr_v. The three largest Ri_τ cases, where buoyancy

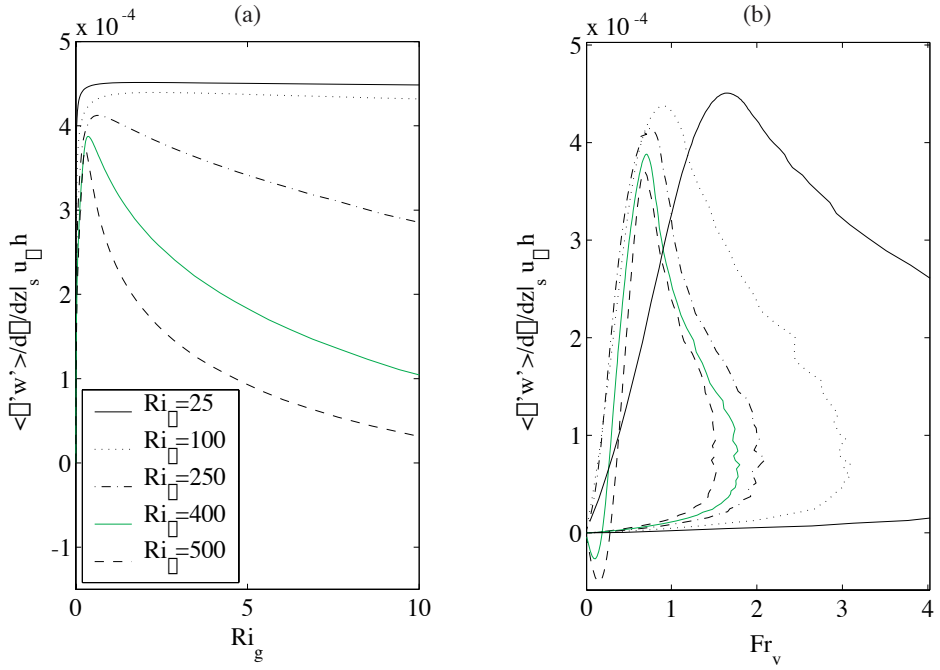

Figure II.23: Nondimensional mass flux vs. (a) Ri_g and (b) vertical Froude number

has been seen to play an important role, show much less dependence on Ri_τ when plotted against Fr_v compared to Ri_g. The parameter, Fr_v, is a direct measure of the state of stratification of the turbulence itself and collapse between cases using Fr_v indicates that the primary buoyancy effect in this problem is not on shear production (measured by Ri_g) but on turbulent transport. The vertical Froude number has been used here instead of the isotropic turbulent Froude number, $Fr_T = \sqrt{(2* < k >)}/(NL_E)$, since a better collapse of the data is obtained using only the component of the TKE directly responsible for vertical mixing. A vertical profile of Fr_v in figure II.24(a) reveals that it is largest near the bottom wall and decreases monotonically with Ri_τ. At any given z, the value of $Fr(z)$ decreases with increasing Ri_τ, and it is this decrease in $Fr(z)$ between cases which is responsible in part for the observed buoyancy effects. From figure II.24(b) it can be seen that the peak in Fr_v occurs at very small Ri_g, about $10^{-2} - 10^{-4}$, although Fr_v is still $O(1)$ near the linear stability threshold, $Ri_g = 0.25$.

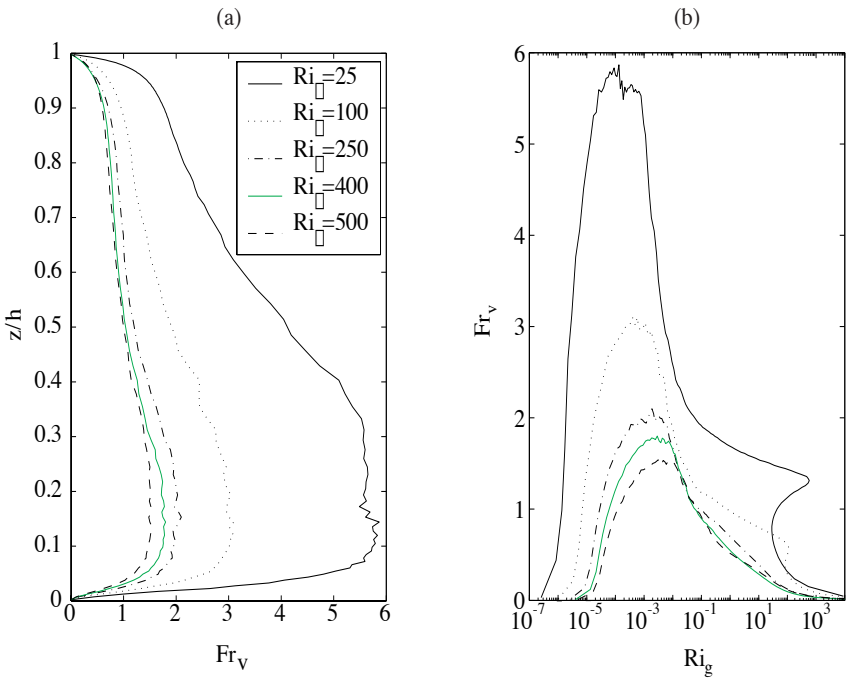

Figure II.24: Vertical Froude number vs. (a) z/h and (b) Ri_g

Ivey and Imberger, (1991) define a "generalized flux Richardson number",

$$R_f = \frac{-B}{-B+\epsilon} \tag{II.59}$$

where $B = -(g/\rho_0) < \rho' w' >= -Ri_\tau < \rho' w' >$ is the buoyancy flux seen in Eq. (IV.19) and ϵ is the viscous dissipation. This definition is generalized from the definition $R_f = -B/P$ to be useful for flow regions where shear production is not the dominant source of local turbulence. This quantity, limited to be between 0 and 1, is also called the mixing efficiency since it represents the ratio of the power expended in working against stratification to the total kinetic energy sink (and hence an upper limit for the total available for mixing). This quantity is shown in figure II.25. The maximum mixing efficiency is slightly lower than 0.2 in the highly stratified cases and does not appear to increase with Ri_τ beyond $Ri_\tau = 250$. As can be seen, the behavior is qualitatively different in the cases with smallest Ri_τ. When the flow is in the buoyancy dominated regime, the mixing efficiency appears to collapse to one function of z/h. Figure II.26(a) shows $B/(B+\epsilon)$ plotted as a function of the gradient Richardson number. It is evident that even when Ri_τ and

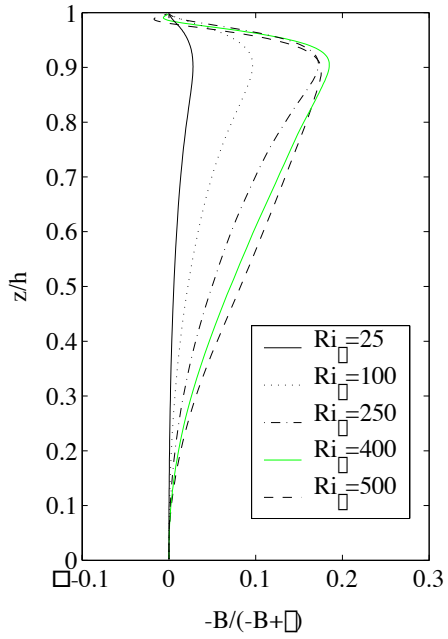

Figure II.25: Mixing efficiency, $-B/(-B+\epsilon)$

Ri_g are large, the mixing efficiency is not well described by a single function of Ri_g. A much better collapse is obtained by plotting the mixing efficiency as a function of the vertical Froude number. As a function of Fr_v, the largest stratification cases collapse quite well, except perhaps when Fr_v is small and the buoyancy flux becomes negative for $Ri_\tau = 400$ and 500.

The turbulent Prandtl number, defined as $Pr_T = \kappa_T/\nu_T$, where κ_T and ν_T are the turbulent diffusivity and turbulent viscosity, respectively, is shown in figure III.11. For $Ri_g < 0.25$, the value of Pr_t in all cases grows rapidly with Ri_g, but dependence on Ri_τ is non-monotone. For $0.25 < Ri_g < 1$, Pr_T and its growth rate decrease with Ri_τ. For even larger values of Ri_g, however, as seen in figure III.11(b), the cases with $Ri_\tau = 400$ and 500 begin to grow very rapidly before Pr_T becomes negative (the eddy diffusivity concept fails) when a countergradient buoyancy flux develops. This is qualitatively different from what is seen by Armenio and Sarkar (2002) (see their figure 17). For $Ri_g < 0.2$, they report that $Pr_T \approx 1$ and is nearly constant with Ri_g and $Ri_{\tau,\Delta}$. For $Ri_g > 0.2$,

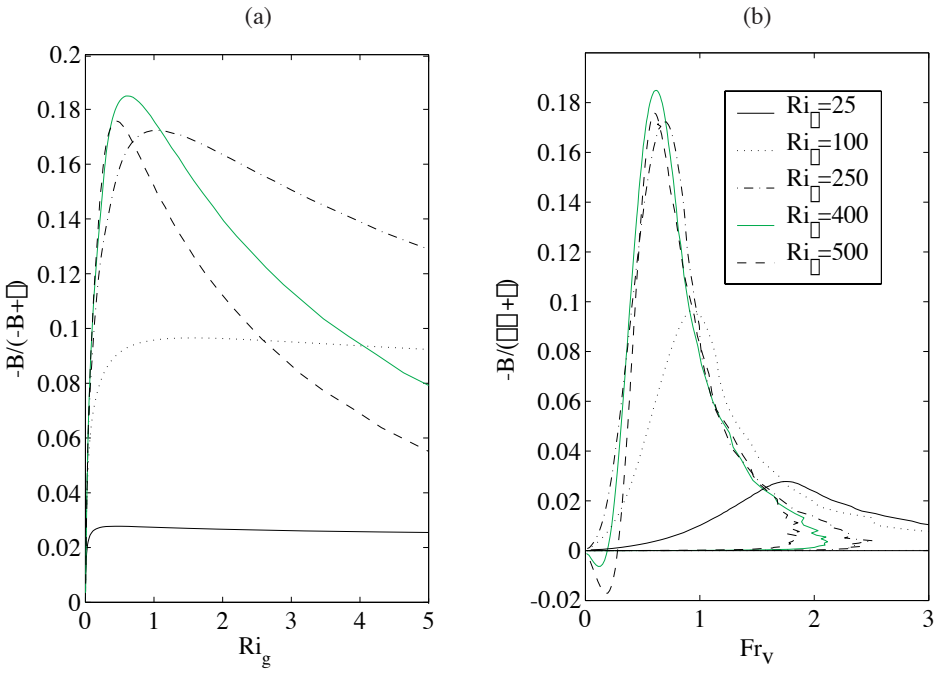

Figure II.26: Mixing efficiency, $-B/(-B+\epsilon)$ vs. (a) gradient Richardson number and (b) vertical Froude number

the less stratified cases continue growing slowly. When Ri_τ is large and $Ri_g > 0.2$, they report a very rapid increase of Pr_T, which eventually becomes negative when countergradient buoyancy fluxes are seen. This is similar to what is seen in the present study at much larger values of $Ri_g > 5$. It is difficult to draw a direct comparison since Armenio and Sarkar (2002) considered much larger values of $Ri_{\tau,\Delta}$ than are possible here. However, in their case 2, with $Ri_{\tau,\Delta} = 60$, they show that the buoyancy flux stays positive, and Pr_T grows slowly with Ri_g and doesn't become singular. In the present study, cases $Ri_\tau = 400$ and 500 correspond to $Ri_{\tau,\Delta} = 24.8$ and 39.4, yet both of these cases have a countergradient buoyancy flux and a singular turbulent Prandtl number.

Buoyancy effects on mixing are sometimes ascertained by examining the ratio of the Ozmidov to Ellison scales where the Ellison scale,

$$L_E = -\frac{\rho_{rms}}{d < \rho > /dz}, \tag{II.60}$$

is an indicator of the size of turbulent overturns. With increasing N the value

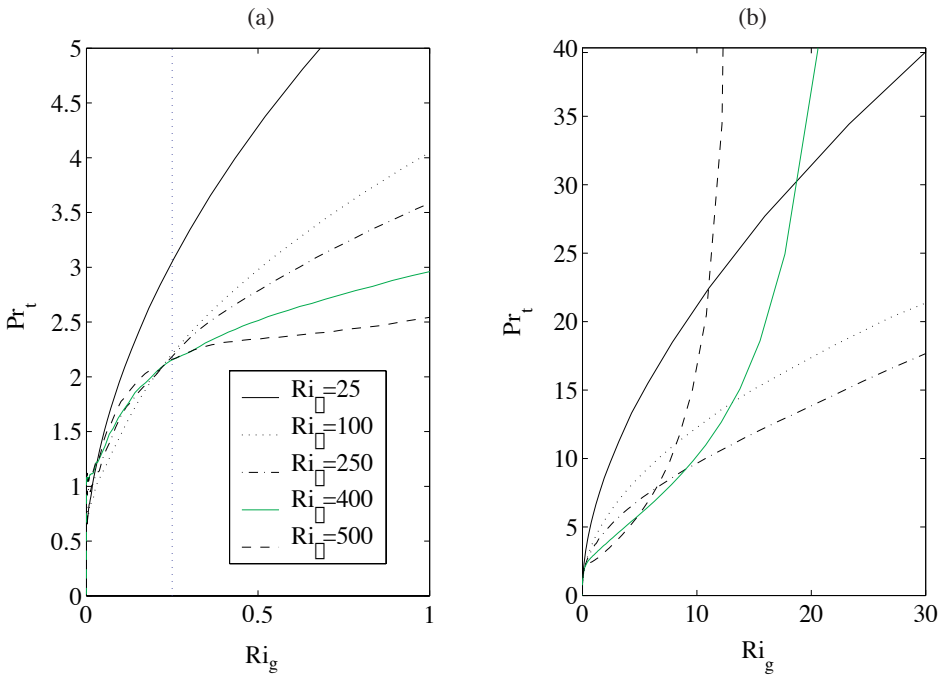

Figure II.27: Turbulent Prandtl number vs. Ri_g

of L_0 decreases, and when L_O becomes less than L_E stratification is expected to become dynamically important. The ratio of L_E/L_O is shown in figure II.18(a) as a function of z/h. Note that L_E is only an approximation to the turbulent overturning scale, and in particular will be an overestimate when internal waves are present and contribute to ρ_{rms}. The vertical profile maintains a similar shape, but increases in magnitude with Ri_τ. The maximum value occurs just above $z/h = 0.9$ and decreases close to the free surface. L_E/L_O is seen to vary significantly with Ri_τ even when plotted as a function of Ri_g in figure II.18(b), and the peak value varies from about 0.25 to 2.2 at $Ri_g \approx 1$. This is contrary to the results of multiple studies of stratified shear layers where it has been observed that for $Ri_g > 0.25$, L_E/L_O is maximum and remains constant with increasing Ri_g (Schumann and Gerz (1995)). The behavior seen here is qualitatively different since as the free surface is approached where $Ri_g >> 1$, L_E/L_O decreases to about 1, half of its maximum value. At a given Ri_g, L_E/L_O decreases with Ri_τ. As with the mixing efficiency and the buoyancy flux, the lengthscale ratio found here cannot be well

described by a single function of Ri_g.

II.4.G Comparison to Armenio and Sarkar (2002)

In order to put the present results on stratification effects in perspective, it is helpful to make a brief direct comparison with the stratified channel flow simulation of Armenio and Sarkar (2002). Among the differences between the two studies are the following features of the current study: addition of the free surface, a larger Reynolds number (increased to 400 from 180), a larger Prandtl number (5 vs. 1), and the thermal boundary conditions (zero heat flux at the bottom and imposed heat flux at the top instead of imposed bottom and top temperatures). The primary goal of this paper was to examine how the change in thermal boundary conditions, and equivalently the manner by which stratification is imposed, affected the turbulence and its interaction with the temperature field. As was mentioned in the introduction, this should provide some insight to the difference between an oceanic bottom boundary layer with no heat flux at the seafloor and a stable atmospheric boundary layer where the ground cools the surrounding air. While many features of a true oceanic boundary layer such as rotation, bottom roughness, and oscillatory forcing have not been considered here, any insights could be significant since the benthic boundary layer is notoriously difficult to observe in the field, and often parameterizations are developed by borrowing from knowledge of turbulence in the atmosphere.

It has been shown that the difference between the choice of boundary conditions has a very significant impact on the physics of the turbulence and mixing of the density field. In the present study, the near wall region where production is large remains unstratified for all cases considered. This is also true in the benthic boundary layer where a well mixed boundary layer of variable thickness is nearly ubiquitous (Armi and Millard (1976); D'Asaro (1982); Garrett et al. (1993)). That the dominant region of turbulence production is relatively unaffected by stratification is why the gradient Richardson number, often used in parameterizations

of stratified turbulence, is less useful in the present study. Indeed, as has been shown, many turbulence and mixing quantities, when plotted as a function of Ri_g, do not show collapse between cases to an universal dependence on Ri_g observed in previous studies of flow with vertical shear. Instead, it has been argued that stratification has an additional effect that acts to limit the vertical transport of turbulent patches by imposing a potential energy barrier. The vertical Froude number, Fr_v, constructed by using the vertical *rms* velocity and the mean density gradient, is a better indicator of such a buoyancy effect on turbulent transport and, consequently, in the upper stratified region of the channel, Fr_v provides a better collapse of the mixing efficiency and buoyancy flux than Ri_g.

One consequence of the influence of stratification on turbulent production at the lower wall in the study by Armenio and Sarkar (2002) is that the skin friction coefficient decreases sharply with $Ri_{\tau,\Delta}$, much more so than in the present study where stratification does not significantly affect turbulent production at the lower wall. The reverse is seen, however, when considering the dependence of the buoyancy flux on $Ri_{\tau,\Delta}$. Here, the buoyancy flux becomes countergradient in the pycnocline when $Ri_\tau \geq 400$ which corresponds to $Ri_{\tau,\Delta} \geq 24.8$, while Armenio and Sarkar (2002) do not observe countergradient buoyancy fluxes in the steady state until $Ri_{\tau,\Delta} = 240$. The relatively strong sensitivity of the buoyancy flux to $Ri_{\tau,\Delta}$ in the present case is likely due to the fact that nearly all of the density change across the channel occurs in the pycnocline where the countergradient buoyancy fluxes are seen. Armenio and Sarkar (2002) also find the countergradient buoyancy flux near the channel centerline, but the mean density gradient is more uniformly distributed throughout the channel.

II.5 Conclusion

Turbulent open channel flow with an imposed density gradient at the free surface corresponding to surface heating and an adiabatic bottom boundary was

investigated and the effects of changing the friction Richardson number, Ri_τ, have been examined. In all cases, a stably stratified pycnocline overlies a lower region that is well mixed by turbulence generated at the lower wall. As Ri_τ is increased, the turbulence in the mixed region remains unchanged while the turbulence in the pycnocline is affected by buoyancy, but never completely suppressed. It is possible that by sufficiently increasing Ri_τ, the flow in the pycnocline could relaminarize, although this limit is not obtained here. It is observed that increasing Ri_τ results in an increase in the bulk Reynolds number, Re_b, and a deepening and strengthening of the pycnocline. The mean velocity deviates from the log law with the extent of the deviation systematically increasing with Ri_τ. Since the mean shear is too small in the pycnocline for local turbulent production, the influence of increasing the surface stratification can be explained by a potential energy barrier affecting the interaction of bottom boundary layer turbulence with the surface region. Visualizations and joint PDFs of ρ' and w show that upwelling of dense bottom fluid to the surface becomes rare in the large Ri_τ cases.

As has been shown in section IV (F), the gradient Richardson number is not enough to parameterize the buoyancy flux. Since this is contrary to some previous results, it warrants further discussion. Komori et al. (1983) found that Ri_g is the best parameter for describing the local effect of stratification in their heated, open channel experiments. Armenio and Sarkar (2002) reach the same conclusion in a closed channel with a fixed temperature difference between the walls. The important difference between these results and the present study is that the turbulence generation region remains unstratified in our case. The boundary conditions used here separate the influence of stratification near the free surface from the flow elsewhere. The previously observed dependence on Ri_g therefore seems to be due to the stratification of the near wall region where turbulence is produced, with this region in turn affecting the outer region. The vertical Froude number, a direct measure of the state of stratification of the turbulence, is found to be a better indicator of buoyancy effects on turbulent transport in the present

configuration. Another consequence of the difference in boundary conditions is that the decrease in skin friction with increasing $\Delta\rho$ observed here is significantly smaller than that observed with constant density boundaries. Finally, we have seen that even when the density gradient becomes very large, free surface turbulence is not well-represented by two-dimensional physics since terms involving vertical gradients remain important in the balance of turbulent kinetic energy.

II.6 Acknowledgments

The contents of this chapter is publised in *Physics of Fluids*, 2005, co-authored by Professors Sutanu Sarkar and Vincenzo Armenio. The stratified flow code used for numerical simulations was developed by Professor Vincenzo Armenio during his work with S. Sarkar at UCSD with modifications by Dr. Stefano Salon. The research was partially supported by NSF OCE-0411938 and ONR N00014-05-1-0334, and by a NDSEG fellowship to the author.

III Subgrid-scale Model Validation

III.1 Introduction

The goal of this chapter is to perform a suite of numerical simulations of a stratified bottom boundary layer in order to validate the modeling assumptions that will be used in later chapters. Since the role of stratification in the near-neutral case is significantly different from that in a stable boundary layer with a heat flux at the boundary, we have conducted a DNS in order to evaluate the performance of a resolved LES at the same Reynolds number. Once confidence in the LES model has been achieved through comparison with the DNS dataset, the resolution requirements can be examined by considering a low resolution NWM-LES. An accurate NWM-LES will allow simulations at a much larger Reynolds number, to more closely approximate the conditions in the ocean and atmosphere.

In order to consider a situation where the bottom boundary layer does not interact with the free surface, an open boundary condition is placed at the top of the computational domain. This boundary condition is designed to allow internal gravity waves to freely escape the computational domain so that a bottom boundary layer in deeper water can be effectively considered. The influence of the Earth's rotation is added and the outer layer flow is assumed to be in geostrophic balance. When the flow is unstratified, the height of a fully-developed rotating boundary layer, or Ekman layer, scales with $\delta = u_*/f$ where u_* is the friction

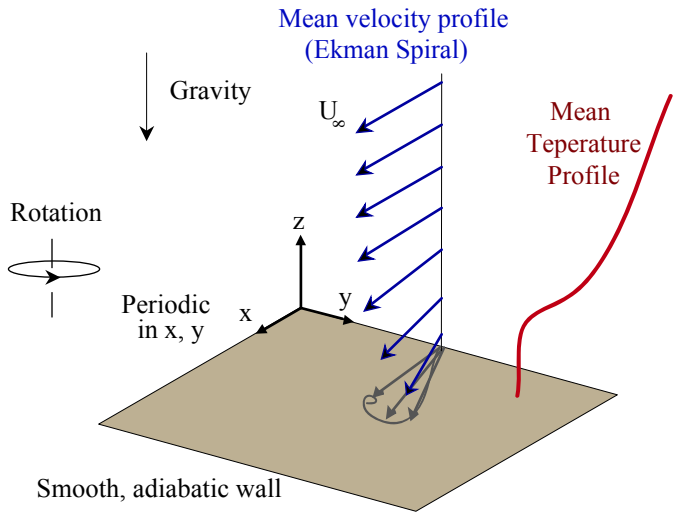

Figure III.1: Schematic: Benthic Ekman layer

velocity and f is the Coriolis parameter. Typically in the ocean $\delta = O(100m)$, but the observed boundary layer thickness is often $O(10m)$. This implies that the thickness of the oceanic bottom boundary layer is limited by the outer layer stratification.

III.2 Formulation

A schematic of a bottom Ekman layer is shown in Figure IV.1. The outer layer flow is assumed to be in geostrophic balance with a pressure gradient in the y-direction. The flow is bounded from below by a flat, no-slip, adiabatic surface and periodic boundary conditions are applied in the horizontal directions. Near the wall, as molecular and turbulent viscosity affects the momentum balance, the flow turns in the direction of the pressure gradient, forming a so-called Ekman spiral. Unlike a non-rotating boundary layer, the thickness of an Ekman layer is bounded and scales with $\delta = u_*/f$ when the flow is not stratified. This is an advantage computationally since it is possible to set the domain size to be larger than the boundary layer height, and the boundary layer achieves a statistically steady state.

When the outer layer flow is stratified, the boundary layer height will be further limited by the influence of stratification. An open boundary condition is applied at the top of the computational domain using a combination of a radiation condition and a Rayleigh damping region (Klemp and Durran (1983)). This combination has been shown to be effective in allowing turbulence-generated internal waves to freely leave the computational domain (Taylor and Sarkar (2007a)).

III.2.A Governing Equations

Using the friction velocity, u_*, the turbulent Ekman layer depth, $\delta = u_*/f$, and the outer layer temperature gradient, $d\theta/dz|_\infty$, the nondimensional, spatially filtered governing equations can be written:

$$\frac{\partial \overline{\mathbf{u}}}{\partial t} + \overline{\mathbf{u}} \cdot \nabla \overline{\mathbf{u}} = -\frac{1}{\rho_0}\nabla \overline{p'} + f\widehat{\mathbf{k}} \times (U_\infty \widehat{\mathbf{i}} - \overline{\mathbf{u}}) - Ri_* \overline{\theta'}\widehat{\mathbf{k}} + \frac{1}{Re_*}\nabla^2 \overline{\mathbf{u}} - \nabla \cdot \boldsymbol{\tau}, \quad \text{(III.1)}$$

$$\frac{\partial \overline{\theta'}}{\partial t} + \overline{\mathbf{u}} \cdot \nabla \overline{\theta'} = \frac{1}{Re_* Pr}\nabla^2 \overline{\theta'} - \nabla \cdot \boldsymbol{\lambda}, \quad \text{(III.2)}$$

$$\nabla \cdot \overline{\mathbf{u}} = 0, \quad \text{(III.3)}$$

where:

$$Re_* = \frac{u_* \delta}{\nu}, \quad Ri_* = -\alpha g \frac{d\theta}{dz}|_\infty \frac{\delta^2}{u_*^2} = \frac{N_\infty^2}{f^2}, \quad Pr = \frac{\nu}{\kappa}, \quad \text{(III.4)}$$

u_* is the friction velocity, ν is the molecular kinematic viscosity, κ is the molecular diffusivity, N_∞ is the outer layer buoyancy frequency, and $\boldsymbol{\tau}$ and $\boldsymbol{\lambda}$ are the subgrid-scale stress and density flux, respectively. The parameters considered in this study are listed in Table 1. Density changes are assumed to be caused by temperature variation in water, motivating the choice of Prandtl number, $Pr = 5$.

III.3 Numerical Method

Simulations have been performed using an algorithm described in detail in Bewley (2007). Since periodic boundary conditions are applied in the horizon-

tal directions, derivatives in these directions are treated with a pseudo-spectral method, while derivatives in the vertical direction are computed with second order finite differences. The low storage third-order Runge-Kutta-Wray method is used for time-stepping and viscous terms are treated implicitly with the Crank-Nicolson method. It can be shown that the numerical scheme ensures the discrete conservation of mass, momentum, and energy (Bewely (1999)). In order to prevent spurious aliasing due to nonlinear interactions between wavenumbers, the largest 1/3 of the horizontal wavenumbers are truncated using the 2/3 de-aliasing rule (Orszag (1971)).

The subgrid scale stress tensor, $\boldsymbol{\tau}$ in Eq. (IV.6) is evaluated using the dynamic mixed model (Zang et al. (1993); Vreman et al. (1997)), and a dynamic eddy diffusivity model is used for the subgrid scale density flux, $\boldsymbol{\lambda}$:

$$\tau_{ij} = -2C\overline{\Delta}^2|\overline{\mathbf{S}}|\overline{S_{ij}} + \widehat{\overline{u}_i\overline{u}_j} - \widehat{\overline{u}}_i\widehat{\overline{u}}_j, \tag{III.5}$$

and

$$\lambda_j = -2C_\theta\overline{\Delta}^2|\overline{\mathbf{S}}|\frac{\partial\overline{\theta}}{\partial x_j}. \tag{III.6}$$

The Smagorinsky coefficients, C and C_θ are evaluated using the dynamic procedure. This is useful since it avoids an empirical specification of the Smagoinsky coefficient and has been shown to perform well for wall-bounded and density stratified flows (Armenio and Sarkar (2002)). The coefficients are evaluated by applying a test filter to the resolved velocity field and using the resolved fields and the test-filtered fields together to estimate the subgrid-scale stress and buoyancy flux. Specifically

$$C = \frac{M_{ij}Lij - M_{ij}H_{ij}}{M_{kl}M_{kl}}, \tag{III.7}$$

where

$$L_{ij} = \widehat{\overline{u_iu_j}} - \widehat{\overline{u}}_i\widehat{\overline{u}}_j, \quad M_{ij} = 2\overline{\Delta}^2\widehat{|\overline{\mathbf{S}}|\overline{S}_{ij}} - 2\widehat{\overline{\Delta}}^2\widehat{|\overline{\mathbf{S}}|}\widehat{\overline{S}_{ij}}, \tag{III.8}$$

$$H_{ij} = \widehat{\widehat{\overline{u}}_i\widehat{\overline{u}}_j} - \widehat{\widehat{\overline{u}}}_i\widehat{\widehat{\overline{u}}}_j - \left(\widehat{\overline{\overline{u}_i\overline{u}_j}} - \widehat{\overline{\overline{u}}}_i\widehat{\overline{\overline{u}}}_j\right), \tag{III.9}$$

and

$$C_\theta = \frac{M_i^\theta L^\theta i}{M_j^\theta M_j^\theta}, \tag{III.10}$$

where

$$L_i^\theta = \widehat{\overline{\theta}\overline{u_i}} - \widehat{\overline{\theta}}\widehat{\overline{u_i}}, \quad M_i^\theta = 2\overline{\Delta}^2|\widehat{\overline{\mathbf{S}}}|\frac{\partial\overline{\theta}}{\partial x_i} - 2\widehat{\overline{\Delta}}^2\widehat{|\overline{\mathbf{S}}|}\frac{\widehat{\partial\theta}}{\partial x_i}, \tag{III.11}$$

The test filter, denoted by $\widehat{\cdot}$, is applied over the horizontal directions only using a trapezoidal rule on a five-point stencil.

A *resolved* LES is usually defined as a simulation that resolves at least 80% of the energy everywhere in the flow (Pope (2000)). Near solid boundaries, turbulent motions scale with the viscous scale, $\delta_\nu = \nu/u_*$. Away from boundaries, the largest turbulent eddies are constrained by the domain size, h. Therefore, the ratio of the filter size near the wall to that necessary in the outer layer scales with $\delta_\nu/h = \nu/(u_* h) = 1/Re_*$. Even when considering a stretched grid in the wall-normal direction, this places a strong constraint on the grid spacing for a resolved LES of wall-bounded flows at a large Reynolds number.

In order to ease the grid resolution requirement and allow simulations at a large Reynolds number, it is possible to use a near-wall model in conjunction with the LES. The model that we have used is a modification of that proposed by Schumann (1975), Grotzbach (1987), and Piomelli (1989), and modified slightly for a rotating boundary layer. This model uses an approximate boundary condition for the horizontal velocity near the wall by predicting the wall stress. Since a staggered grid is used in the vertical direction, the wall location is made coincident with the streamwise stress and the vertical velocity. The first horizontal velocity point away from the wall is located at $z^+(1) = 9.8$ in wall units, and the near-wall grid spacing is $\Delta z^+(1) = 19.2$. The first gridpoint is nearer to the wall than is common practice for near-wall models, and represents a tradeoff between near-wall grid spacing and resolution in the stratified boundary layer. If a grid spacing of 40^+ wall units were used, there would only be 5 gridpoints between the wall and the top of the stratified boundary layer at $z = 0.2\delta$. We have found that the location of the first gridpoint does not affect the ability of the NWM-LES to capture the expected log-law. Once the grid is determined, the plane average of the streamwise velocity at the first point away from the wall is used to estimate

Table III.1: Simulation Parameters

Type	Re_*	Ri_*	(L_x, L_y, L_z)	(N_x, N_y, N_z)	$min(\Delta_z^+)$	Δ_x^+, Δ_y^+
DNS	960	0, 1000	$(2\delta, 2\delta, 2.7\delta)$	$(192, 192, 192)$	1.4	10
LES	960	0, 1000	$(2\delta, 2\delta, 3\delta)$	$(96, 96, 96)$	1.8	20
NWM-LES	960	0, 1000	$(2\delta, 2\delta, 3\delta)$	$(48, 48, 48)$	19.2	40

the friction velocity by iteratively solving the expected mean logarithmic law:

$$\frac{\langle|\mathbf{u}|\rangle(1)}{u_*} = \frac{1}{\kappa} ln(\frac{z(1)u_*}{\nu}) + B, \tag{III.12}$$

where $\langle|\mathbf{u}|\rangle(1)$ is the plane averaged horizontal velocity magnitude evaluated at the first gridpoint away from the wall, and we have used $\kappa = 0.41$ and $B = 5.2$. Once the friction velocity is obtained, the components of the plane-averaged wall stress are estimated by specifying the angle α_0 between the wall-stress and the x-direction:

$$\langle\tau\rangle_{13} = \rho_0 u_*^2 cos(\alpha_0), \tag{III.13}$$

$$\langle\tau\rangle_{23} = \rho_0 u_*^2 sin(\alpha_0). \tag{III.14}$$

The surface stress angle α_0 is estimated using the finite Reynolds number theory of Spalart (1989) which gives $\alpha_0 = 20.6°$. The local wall stress is then estimated using fluctuations in the resolved horizontal velocity at the first gridpoint

$$\tau_{13}(x, y) = \frac{u(x, y, 1)}{\langle u\rangle(1)} \langle\tau\rangle_{13}, \tag{III.15}$$

$$\tau_{23}(x, y) = max\left(\frac{v(x, y, 1)}{\langle u\rangle(1)} \langle\tau\rangle_{13}, \frac{v(x, y, 1)}{\langle v\rangle(1)} \langle\tau\rangle_{23}\right) \tag{III.16}$$

The latter relation allows a smooth transition between the non-rotating case when the wall stress is dominated by the τ_{13} component and an Ekman layer where the mean velocity and wall stress in the spanwise direction are nonzero.

We have initialized each simulation with a steady-state temperature and velocity field from the large eddy simulations of Taylor and Sarkar (2007a) at the same Reynolds number. The temperature and velocity were interpolated onto

the appropriate grid for the DNS, resolved LES, and NWM-LES. Steady state fields have been used in order to focus on the characteristics of a fully-developed boundary layer as opposed to the boundary layer formation. Each simulation was continued for about $t = 3/f$ nondimensional time units which corresponds to about 8 hours at a latitude of 45°. Unless otherwise noted, a Reynolds average, denoted by $< \cdot >$ will be taken over horizontal planes and from $tf = 1.5 - 3$.

III.4 Results

III.4.A Velocity structure

Before examining the performance of the LES in simulating the thermal structure of the boundary layer, it is useful to examine the mean velocity profiles. In constructing the wall model for the NWM-LES, we have made the assumption that the stratified and unstratified simulations obey the same logarithmic law. Since gridpoints near the wall are within the well-mixed layer, this seems reasonable, but it should be confirmed using the DNS. Figure IV.8 shows the vertical shear normalized by the expected shear in the log-region:

$$\phi = \frac{\kappa z}{u_*} \left(\frac{d\langle u \rangle}{dz}^2 + \frac{d\langle v \rangle}{dz}^2 \right)^{1/2} . \tag{III.17}$$

Based on this definition, when $\phi = 1$ the mean shear is in agreement with the expected value from the logarithmic law. As seen in Figure IV.8(a), the mean shear in the unstratified DNS follows the logarithmic law scaling for approximatley $0.05 \leq z/\delta \leq 0.4$ and the resolved LES and to a lesser extent the NWM-LES are able to reproduce this profile. It may be possible to improve the representation of the mean velocity profile in NWM-LES using the adaptive stochastic forcing technique described by Taylor and Sarkar (2007b).

Figure IV.8(b) shows that there is a small region, $0.05 < z/\delta < 0.1$, where the stratified Ekman layer also has $\phi \approx 1$. Therefore, the assumed form of the near-wall model is reasonable. It is also evident that the mean shear increases

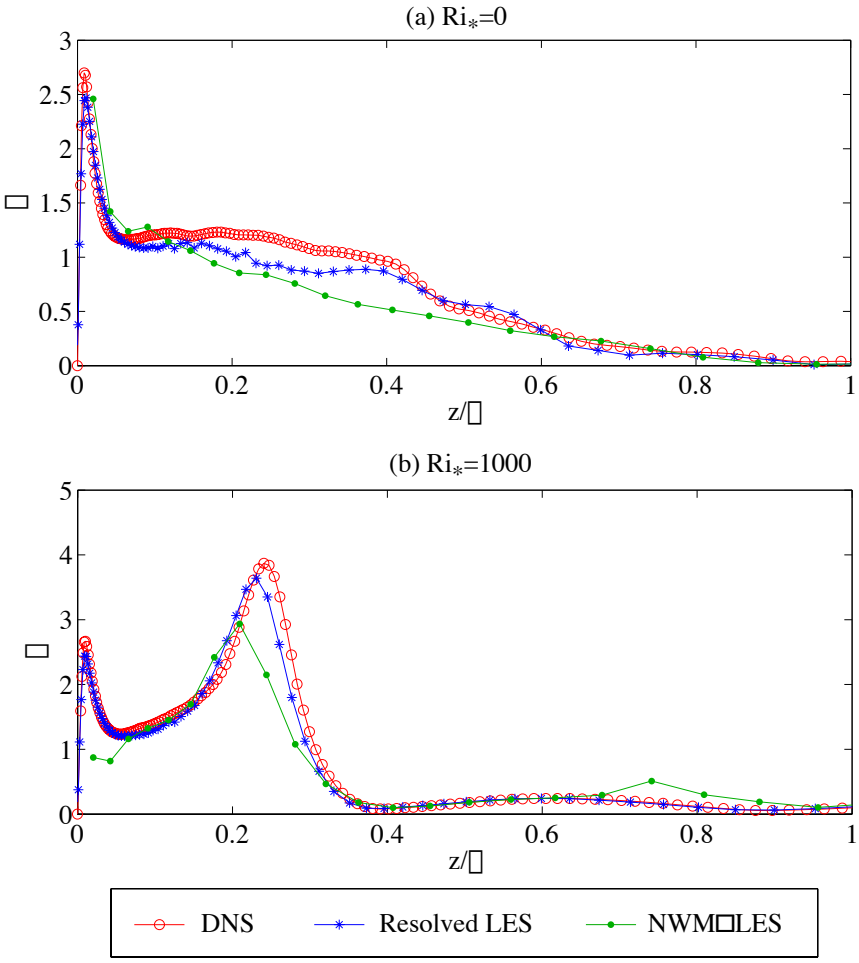

Figure III.2: Nondimensional shear, ϕ defined in Eq. (III.17)

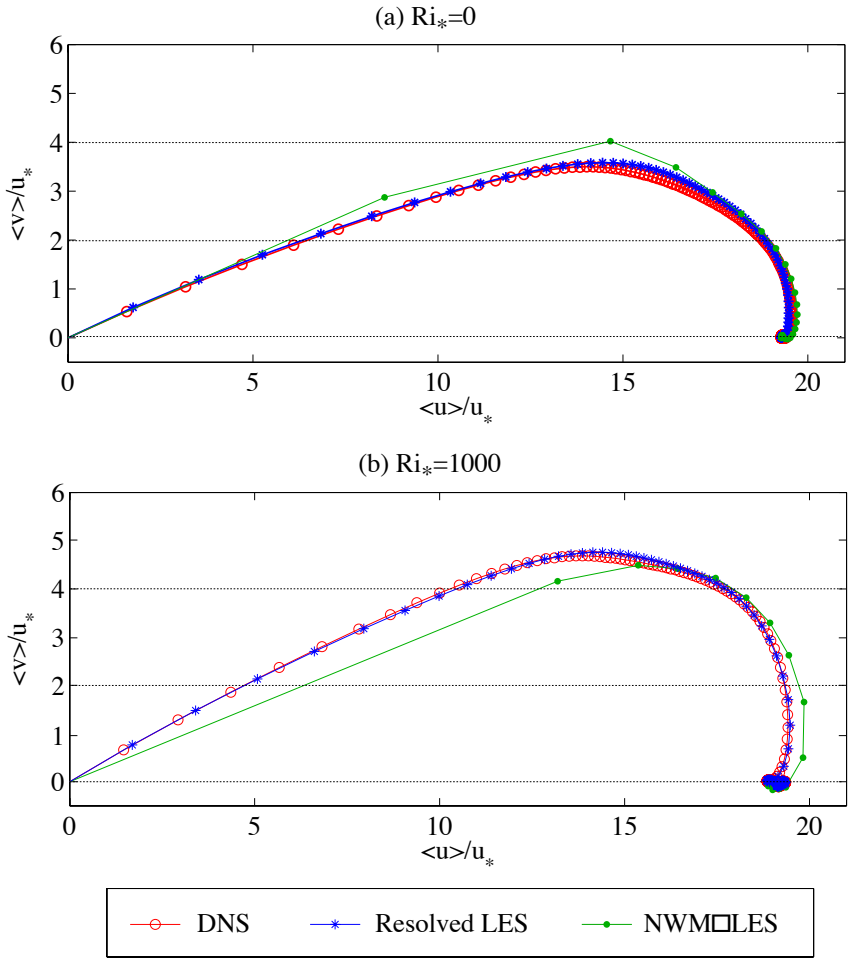

Figure III.3: Hodograph of the mean velocity

dramatically in the thermocline when $Ri_* = 1000$. The resolved LES is able to capture this increase, but the NWM-LES does not fully capture the maximum shear. This is not surprising since, as we will see, the NWM-LES also underestimates the temperature gradient in the thermocline.

The individual components of the mean horizontal velocity are shown in a hodograph in Figure IV.4. As has been observed for an Ekman layer with a stabilizing surface heat flux, the presence of an outer layer stratification acts to increase the cross-stream velocity. This can be seen by comparing Figure IV.4(a) and (b). It is interesting to note that the angle of the Ekman spiral increases near the wall where the mean temperature gradient is zero. Therefore, the effect of

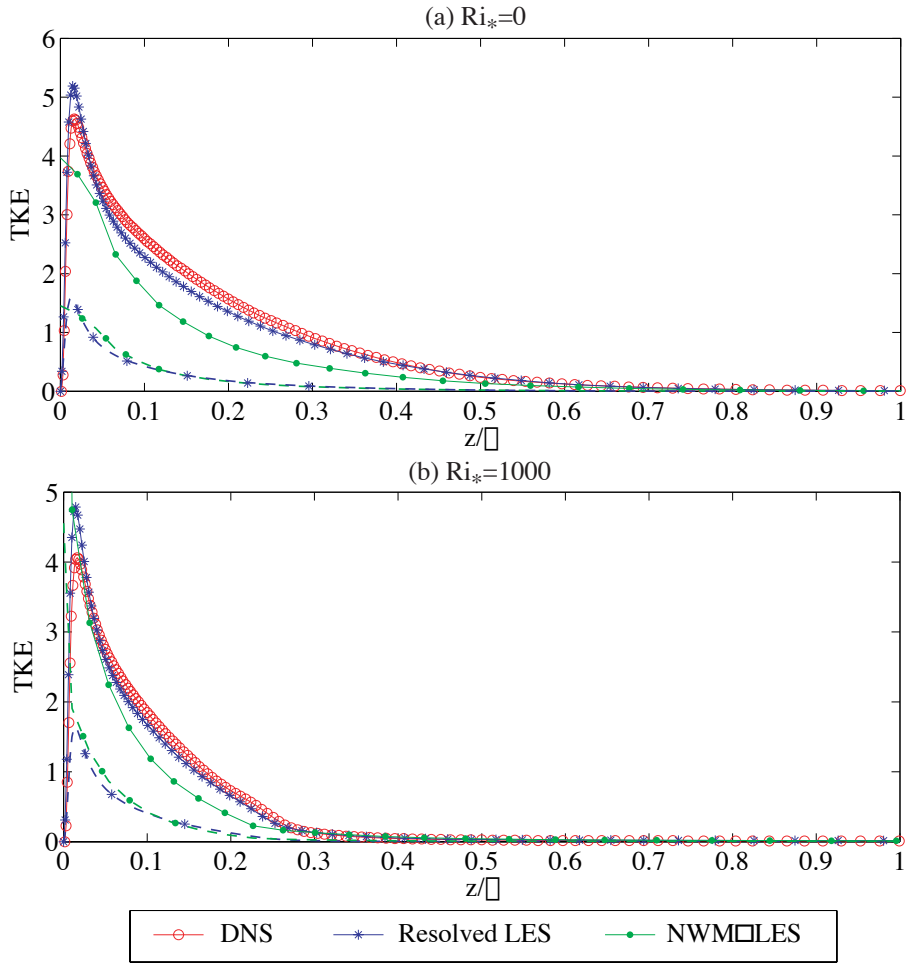

Figure III.4: Tubulent kinetic energy (TKE). Solid lines indicate the total TKE and dashed lines indicate the subgrid-scale component

stratification in this region appears to be non-local. The agreement between the resolved LES and DNS is excellent, and the NWM-LES is also able to generally capture the increase in the Ekman transport when the outer layer is stratified.

Although the resolution used by the LES is significantly lower than the DNS, the vertical profiles of turbulent kinetic energy (TKE) compare reasonable well between the simulations, as shown in Figure III.4. The NWM-LES tends to underestimate the TKE, particularly in the upper portion of the mixed layer. A significant fraction (30%) of the TKE near the wall is contained in the subgrid-scales (shown by dashed lines in Figure III.4).

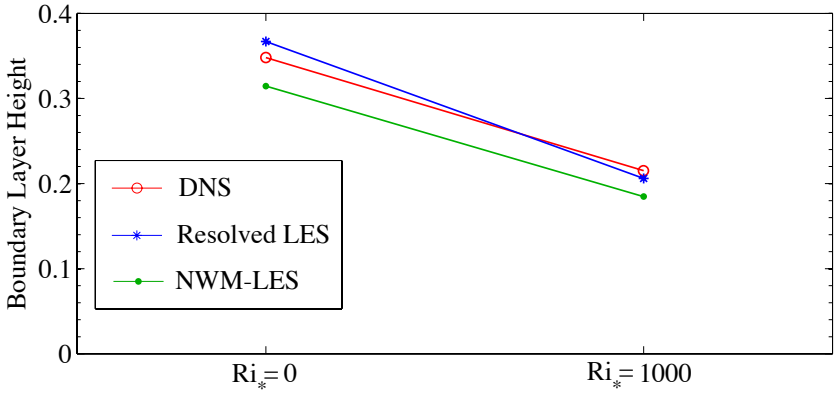

Figure III.5: Boundary layer height, defined as the location where the streamwise Reynolds stress, $\langle u'w' \rangle$ is 10% of its maximum value.

A useful definition for the height of a turbulent Ekman layer is the location where the streamwise Reynolds stress reaches 10% of its maximum value (Taylor and Sarkar (2007c)). The boundary layer height, defined using this criteria, is shown in Figure III.5. One of the primary effects of the outer layer stratification is to decrease the Ekman layer height, as seen in this Figure. Both the resolved and NWM-LES capture the decrease in boundary layer height with stratification reasonably well, although this is slightly overestimated in the resolved LES. The NWM-LES underestimates the boundary layer height, both with and without an external stratification.

III.4.B Thermal field

Since the lower wall is adiabatic and the molecular diffusion of heat is small, the heat content in the boundary layer is approximately conserved. In addition, at some location far enough from the boundary layer, the mean temperature profile is unchanged from its initial state. As a result, when the temperature profile mixes near the wall, the temperature gradient must increase above the mixed layer in order to return the temperature to the initial state. When the flow is strongly

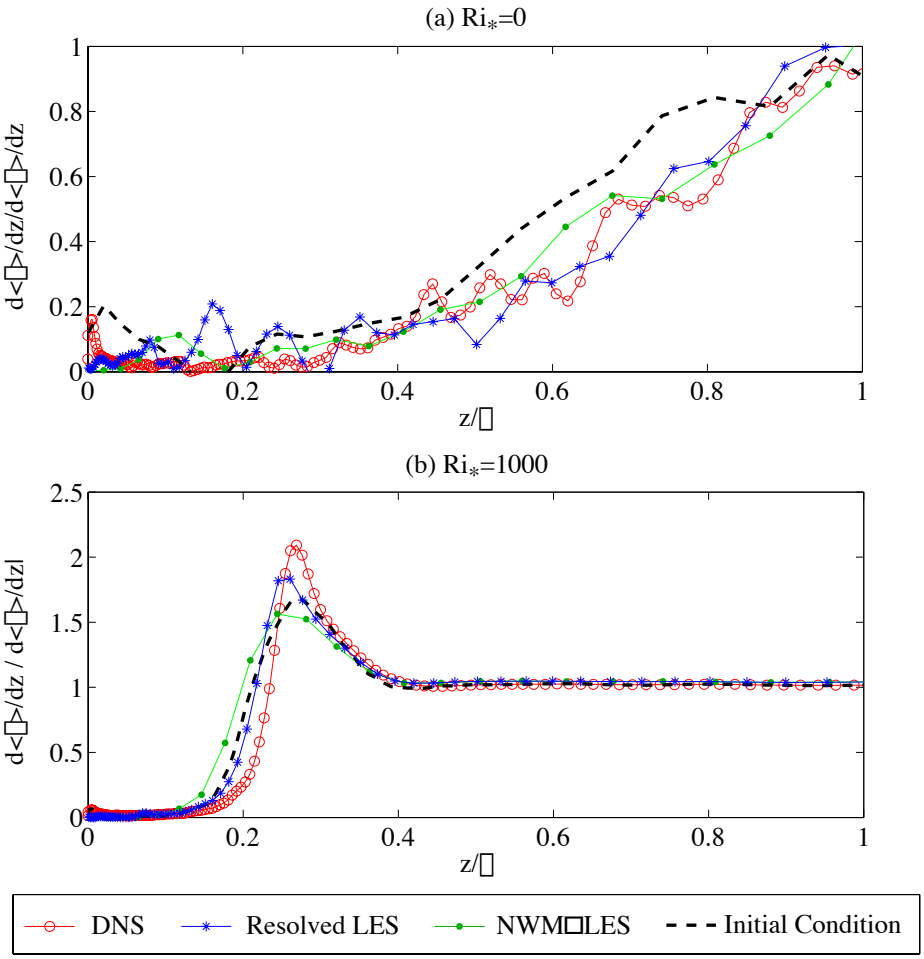

Figure III.6: Plane-averaged temperature gradient normalized by outer value, evaluated at $t = 3/f$.

stratified, the region with a nonzero turbulent heat flux is limited by stratification. In this case, the temperature gradient is very large in a thermocline above the mixed layer. The mean temperature field in the stratified boundary layer can then be characterized by a three-layer structure with a well-mixed region near the wall, a strongly stratified thermocline, and an outer layer were the temperature gradient is equal to the initial value. This structure can be seen in the plane-averaged temperature gradient at $t = 3/f$, shown in Figure III.6(b).

When $Ri_* = 0$, we still consider a uniform temperature gradient in the outer layer, but since the thermal and momentum equations become decoupled, the temperature is advected as a passive scalar. This allows us to evaluate the ability of the LES model to simulate both passive and active scalar mixing. The temperature profiles in both the resolved and NWM-LES compare well with the DNS when $Ri_* = 0$. Comparing Figs. III.6(a) and (b), it is evident that the mixed layer thickness is much smaller when $Ri_* = 1000$. In this case the mixed layer growth and the temperature gradient in the thermocline are underpredicted by the NWM-LES, and to a lesser extent by the resolved LES.

An important difference between the DNS and LES results is that both the resolved and the NWM-LES underestimate the rate of entrainment of outer layer fluid into the mixed layer. This can be quantified by comparing the rate of increase of the temperature of the mixed layer fluid. When the flow is strongly stratified and $Ri_* = 1000$, the rate of change of the mixed layer temperature is significantly understimated in the LES. Specifically, $d\langle\theta\rangle/dt$ in the mixed layer is $4.3 * 10^{-3}$, $3.3 * 10^{-3}$, and $2.1 * 10^{-3}$, in the DNS, resolved LES, and NWM-LES, respectively, in units of $d\langle\theta\rangle/dz|_\infty \delta^2 f$. When $Ri_* = 0$ and temperature acts as a passive scalar, the LES entrainment rate is in better agreement with the DNS.

The evolution of the mean temperature field can be written in terms of the molecular and turbulent heat flux:

$$\frac{\partial\langle\theta\rangle}{\partial t} = \frac{\partial}{\partial z}\left(\kappa\frac{\partial\langle\theta\rangle}{\partial z} - \langle\theta' w'\rangle\right). \tag{III.18}$$

The right hand side of Eq. (III.18) is dominated by the turbulent heat flux in

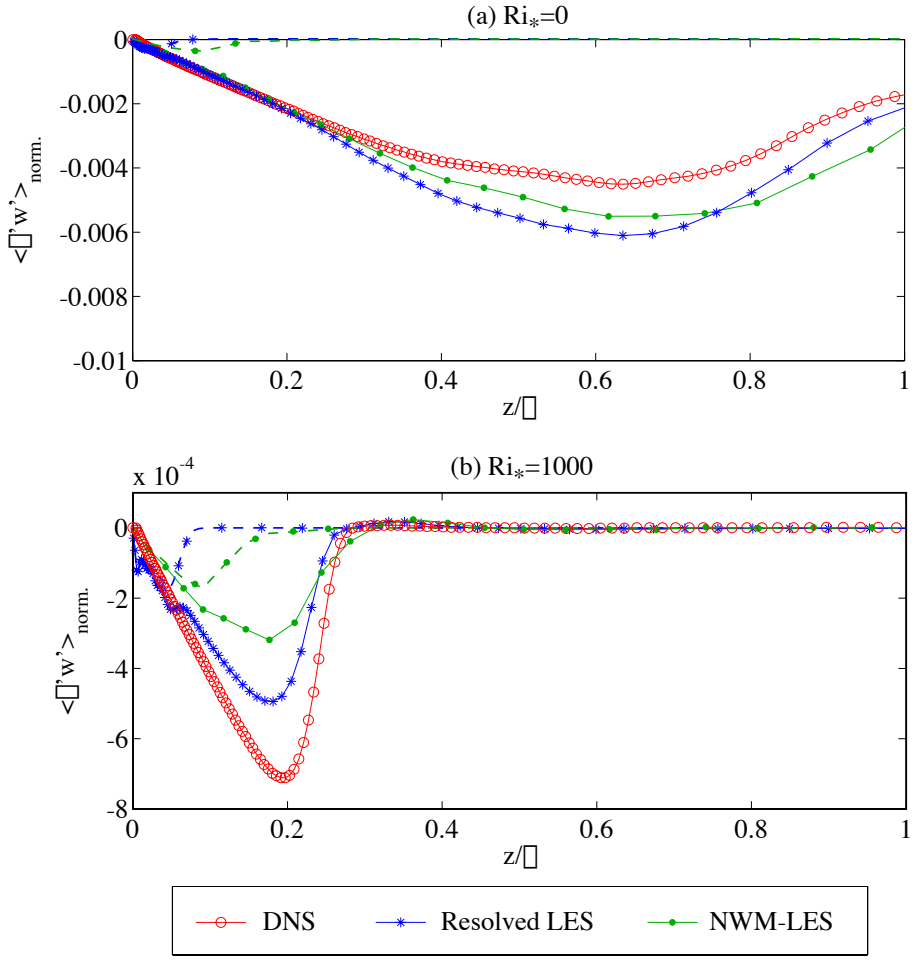

Figure III.7: Turbulent heat flux normalized by $d < \theta > /dz|_{\infty}\delta u_*$. Solid lines show the total heat flux, dashed lines show the subgrid-scale contribution.

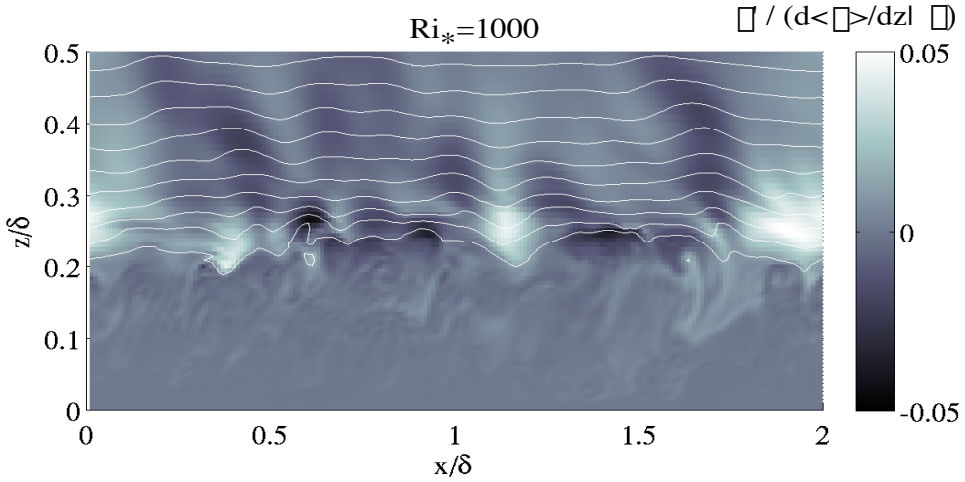

Figure III.8: Instantaneous visualization of the temperature field from DNS with $Ri_* = 1000$. Perturbations from the plane mean are shown in shades of gray, and white lines indicate isoterms.

the mixed layer and by the molecular heat flux above the thermocline. Since the heating of the mixed layer fluid is underpredicted by each LES when $Ri_* = 1000$, it follows that the estimate of the turbulent heat flux is also low. This is verified in Figure III.7. In both cases, the subgrid-scale contribution is shown by a dashed line. When $Ri_* = 0$ nearly all of the heat flux is accounted for by the resolved scales, while the subgrid-scale heat flux is more significant when $Ri_* = 1000$, particularly in the lower half of the mixed layer.

A visualization of the temperature field from the DNS with $Ri_* = 1000$ is shown in Figure III.8. In the mixed layer, small scale overturns and filaments are visible. For comparison, at $z = 0.2\delta$ the vertical grid spacing in the DNS, resolved LES, and NWM-LES is 0.0058δ, 0.012δ, and 0.034δ, respecitvely. Since the vertical grid spacing in the NWM-LES at the top of the mixed layer is quite large, many of the small scale features that are visible will not be resolved. Outside of the mixed layer, however, the characteristic scale of the temperature fluctuations increases dramatically. In the outer layer, stratification is strong enough to suppress turbulence, and temperature fluctuations are associated with internal wave field that is induced by eddies in the boundary layer.

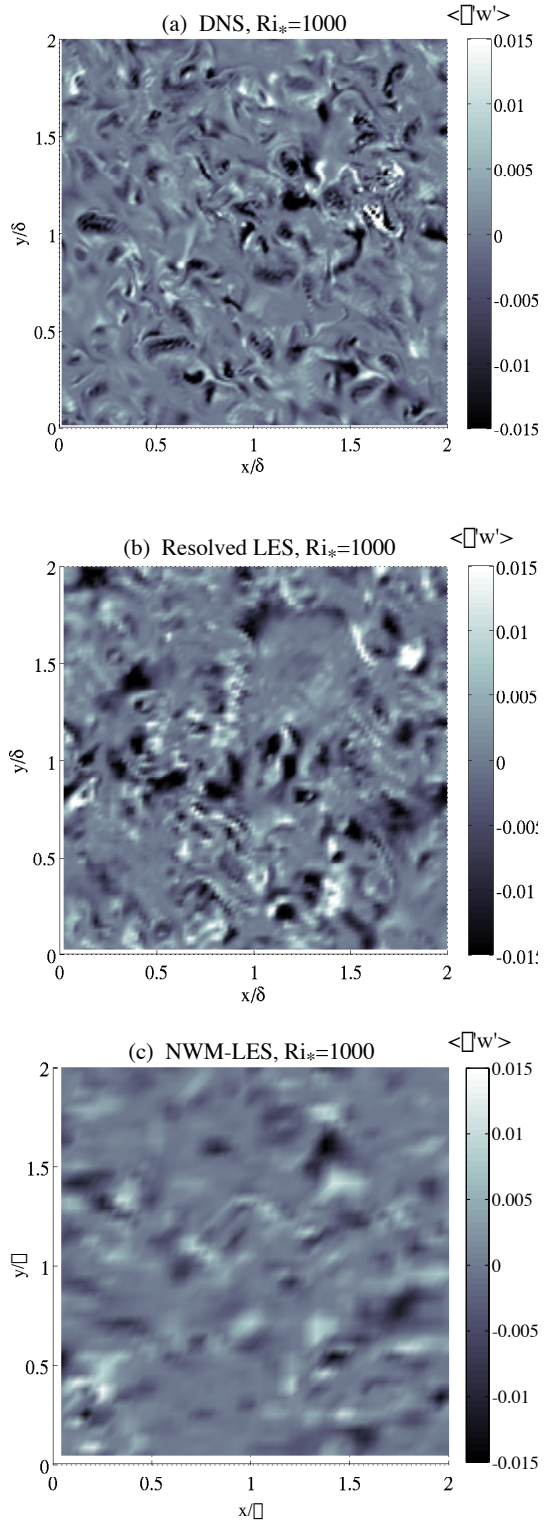

Figure III.9: Instantaneous visualization of the turbulent heat flux at $z/\delta = 0.2$, $Ri_* = 1000$

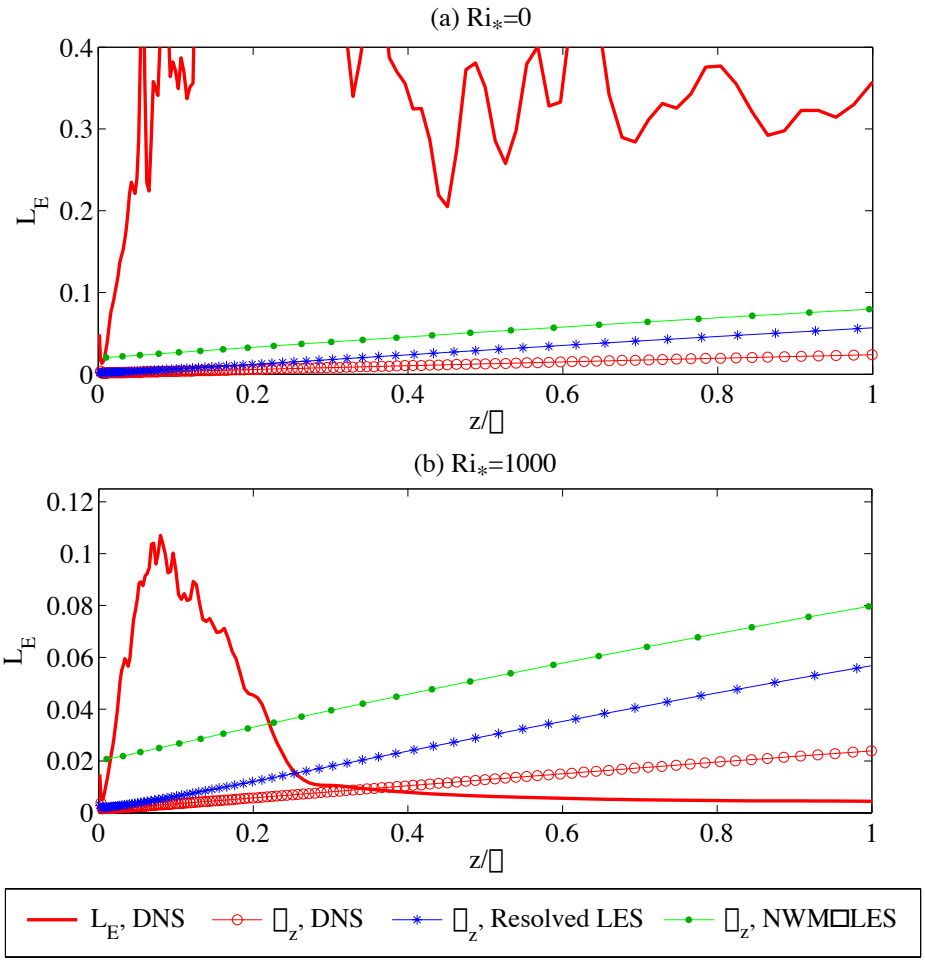

Figure III.10: Vertical grid spacing and Ellison scale

The horizontal scales in the $\langle \theta' w' \rangle$ field are visualized in Figure III.9 using a horizontal slice through $z = 0.2\delta$ (the location of maximum turbulent heat flux). At this location, $\langle \theta'^2 \rangle$ and $\langle w'^2 \rangle$ from the resolved and NWM-LES compare well with the DNS (not shown). As we have seen, however, the magnitude of $< \theta' w' >$ is underpredicted by the LES. In Figure III.9, it is apparent that many of the small scale features that are seen in the DNS are not present in the resolved or NWM-LES. Since the LES is unable to resolve all of the scales, and the subgrid-scale heat flux is negligible at this height, the plane averaged turbulent heat flux is underestimated.

Since the turbulent heat flux is significantly under-represented by the

LES, it seems likely that small scale motions contribute significantly to the turbulent heat flux at the top of the boundary layer. The length scale associated with density overturns can be estimated by the Ellison scale,

$$L_E = \frac{(\theta'^2)^{1/2}}{d\langle\theta\rangle/dz}. \tag{III.19}$$

The Ellison scale from the DNS, along with the vertical grid spacing in each simulation are shown in Figure III.10. When $Ri_* = 1000$, density stratification limits the scale of turbulent overturns, resulting in a much smaller Ellison scale compared to that when $Ri_* = 0$. In the DNS at $Ri_* = 1000$, at $z = 0.2\delta$, the Ellison scale is $L_E \simeq 0.03\delta$. At this location, the gridspacing in the NWM-LES is $(\Delta_x, \Delta_y, \Delta_z) = (0.04\delta, 0.04\delta, 0.03\delta)$ which clearly is not sufficiently to resolve the density overturns. The gridspacing in the resolved LES, at the same location, is roughly half of the Ellison scale. Therefore, the resolved LES is also not able to fully capture turbulent eddies at the Ellison scale.

The turbulent Prandtl number, defined as the ratio of the turbulent viscosity and diffusivity can be written:

$$Pr_T = \frac{\nu_T}{\kappa_T} = \frac{\left(\langle u'w'\rangle^2 + \langle v'w'\rangle^2\right)^{1/2}}{-\langle\theta'w'\rangle} \frac{d\langle\theta\rangle/dz}{d\langle u\rangle/dz}. \tag{III.20}$$

In both the stratified and unstratified DNS, the mixed region is characterized by $Pr_T \approx 1$ as has been previously reported for turbulence in a low stratification environment (Schumann and Gerz (1995)). The low value of the turbulent Prandtl number near the wall in the LES is directly related to an underestimate of the mean temperature gradient. In the DNS, the temperature gradient only vanishes in a thin viscous layer near the wall. In the each LES, the temperature gradient is much smaller near the wall. Specifically, at $z/\delta = 0.05$ when $Ri_* = 1000$, the temperature gradient normalized by the outer layer value is 0.0136, 0.0029, and 0.00094 in the DNS, resolved LES, and NWM-LES, respectively.

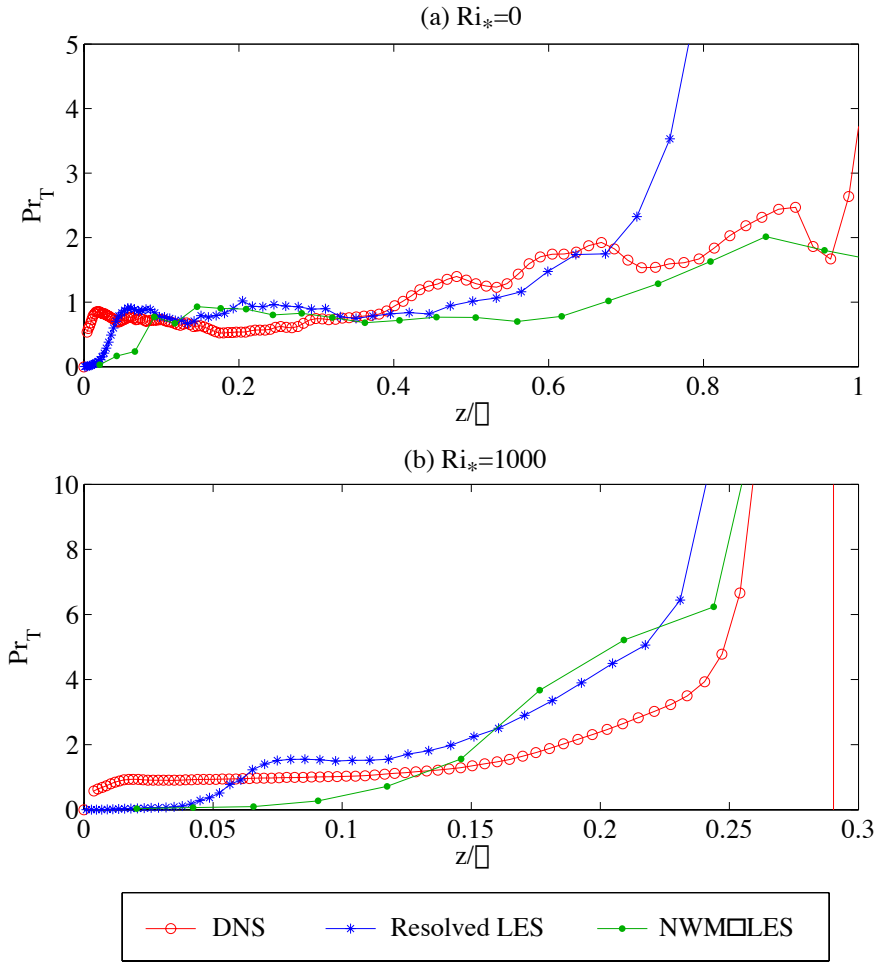

Figure III.11: Turbulent Prandtl number

III.5 Discussion

Thus far, we have considered nondimensional quantities. It is useful to estimate relevant dimensional parameters for a typical oceanic bottom boundary layer. If the free stream velocity is taken to be $U_\infty = 5cm/s$ and with $u_*/U_\infty = 0.05$, $f = 10^{-4}s^{-1}$, and $\nu = 10^{-6}m^2/s$, gives $\delta = 25m$ and $Re_* = 62,500$. Clearly this Reynolds number is much larger than what we have considered here. Since u_*/U_∞ does not depend strongly on the Reynolds number, if we keep the viscosity and the Coriolis parameter constant, $Re_* = 960$ is equivalent to a free stream velocity of $U_\infty = 0.077cm/s$. The Richardson number $Ri_* = 1000$ implies that $N/f = 31.6$ so that the free stream buoyancy frequency is 1.86 $cycles/hour$. With a thermal expansion coefficient of $\alpha = 10^{-4}\ ^\circ C^{-1}$, this implies that the background temperature gradient is $0.01^\circ C/m$. Although this temperature gradient is much smaller than is typically seen in engineering flows, buoyancy effects are still very important since the length scales are typically much larger in geophysical flows. In the deep ocean, buoyancy effects are significant since the velocities tend to be very low while the dynamical length-scales are large.

III.6 Conclusions

We have conducted simulations of an Ekman layer formed when a steady, linearly stratified fluid flows over a smooth boundary in the absence of a surface heat flux. The boundary layer thickness is strongly limited by the outer layer density stratification. A DNS was used to examine evaluate LES at two different resolutions with an emphasis placed on the thermal structure of the boundary layer. We have found that when the temperature is treated as a passive scalar, both low and high resolution LES compare well with the DNS. However, when the outer layer is stratified, the turbulent heat flux in the boundary layer is significantly underpredicted by the LES. Flow visualizations revealed that small scale motions that are not resolved by the LES or represented in the subgrid-scale model are

responsible for the entrainment of fluid into the boundary layer in the DNS. The Ellison scale provides a good estimate for the turbulent scales responsible for the entrainment and indicates that the entrainment motions are much smaller when the flow is stably stratified.

III.7 Acknowledgments

The contents of this chapter have been submitted to the *International Journal of Heat and Fluid Flow*, co-authored by Professor Sutanu Sarkar. The support of grant N00014-05-1-0334 from ONR Physical Oceanography, program manager Dr. Scott Harper, is gratefully acknowledged.

IV Stratification Effects in a Bottom Ekman Layer

IV.1 Introduction

The surface wind-driven Ekman layer forms when frictional terms contribute to the leading order momentum balance, leading to an ageostrophic flow. Since the velocity gradients, and hence the size of the viscous stresses are strongest at the sea surface, the ageostrophic component of the flow decreases with depth, leading to a turning of the mean velocity profile known as the Ekman spiral. The bottom Ekman layer, formed as a mean current flows over the seafloor, is directly analogous to the surface wind-driven Ekman layer. In a surface Ekman layer, the Ekman transport (the vertical integral of the Ekman layer velocity) is directed 90^o to the right of the wind stress in the northern hemisphere. In a bottom Ekman layer the Ekman transport is also directed to the right of the bottom stress. However, since the stress at the seafloor is in the opposite direction of the geostrophic current, the Ekman transport in the bottom boundary layer is 90^o to the *left* of the geostrophic current, and the Ekman spiral turns counter-clockwise with increasing depth in the northern Hemisphere. Also like the surface mixed layer, the bottom boundary layer is a site of intense turbulent dissipation and mixing (Garrett and Laurent (2002); Thorpe (2001)). Together with the surface mixed layer, the bottom boundary layer is a major 'hotspot' for diapycnal mixing in the ocean (Thorpe (2001)). It has long been hypothesized that mixing of the density field in bottom

boundary layers may be important to abyssal mixing through along-isopycnal advection out of the boundary layer and boundary layer detachment (Munk (1966); Armi (1978)). In addition, through frictional loss and Ekman pumping, the bottom boundary layer provides an important momentum sink for deep currents and mesoscale eddies.

Three-dimensional numerical simulations of stratified bottom Ekman layers have been described previously by several authors, but in all cases, stratification was applied with a cooling heat flux at the lower wall, akin to the stable atmospheric boundary layer. Coleman et al. (1992) performed a direct numerical simulation (DNS) of a turbulent Ekman layer with a friction Reynolds number of $Re_* = 340$ and a constant heat flux at a smooth, no-slip lower wall. They compared the stratified Ekman layer to a previous study of an unstratified Ekman layer (Coleman et al. (1990)) and found that the surface heat flux limits the transport of turbulent kinetic energy into the outer layer and broadens the Ekman spiral. Shingai and Kawamura (2002) (2002) considered the same flow at a friction Reynolds number $Re_* = 428.6$. They found that the boundary layer thickness defined in terms of either the momentum or buoyancy flux decreases sharply with the application of a surface heat flux. In general, these studies imply that when a strong stable stratification is applied to the wall under an Ekman layer, stratification acts to suppress the turbulent production in the boundary layer, increasing the turning angle and decreasing the boundary layer height.

In the ocean, with the exception of isolated hotspots, the seafloor can be assumed to be adiabatic. Changes in density then affect the Ekman layer through the stratification associated with the ambient water. Since a mixed layer can be found near the seafloor throughout most of the ocean, stratification can be expected to affect the boundary layer in a much different manner than in a typical stable atmospheric boundary layer where a heat flux is often present at the ground. By comparing the expected unstratified turbulent Ekman layer depth to the thickness of bottom mixed layers in field data, it is apparent that stratification often limits

the boundary layer height. In an unstratified Ekman layer, the boundary layer height is expected to be approximately $h = 0.5u_*/f$ where u_* is the friction velocity and f is the Coriolis parameter. Typical mid-latitude values, say $u_* = 1cm/s$ and $f = 10^{-4}s^{-1}$, imply an unstratified Ekman layer depth of about $h = 50m$. In many cases, especially in a coastal environment where the stratification is typically large, the observed mixed layer heights are often much smaller. For example, Perlin et al. (2007) observed a mixed layer thickness of about $10m$ in an Ekman layer over the Oregon shelf. It is not fully clear how the Ekman layer structure changes when the Ekman layer height is limited by stratification, and this will be one focus of the present study.

The bottom boundary layer plays an important role in the drag induced on mean currents and mesoscale eddies. In order to obtain an accurate prediction of the ocean state, numerical ocean models must represent this loss of momentum. However, due to computational restrictions on the grid size, this is not straightforward. To accurately apply the no-slip boundary condition at the seafloor, a numerical model must resolve the viscous sub-layer. Since the viscous sub-layer in the ocean is thin, $O(0.1 - 10cm)$ (Caldwell and Chriss (1979)), numerical models are clearly unable to resolve this region, and an approximate boundary condition must be used. It is common practice to model the seafloor stress which then provides a Neumann boundary condition for the horizontal momentum equations. For example, the Regional Ocean Modeling System (ROMS) provides three methods for modeling the bottom stress based on the velocity at the lowermost grid cell: linear and quadratic drag coefficients, and a law-of-the-wall using a specified bottom roughness. A general form for the bottom stress using the linear drag coefficient γ_1 and the quadratic drag coefficient γ_2 is

$$\frac{\tau_{w,x}}{\rho_0} = \left(\gamma_1 + \gamma_2\sqrt{u^2+v^2}\right)u \quad , \quad \frac{\tau_{w,y}}{\rho_0} = \left(\gamma_1 + \gamma_2\sqrt{u^2+v^2}\right)v, \tag{IV.1}$$

where $\tau_{w,x}$ and $\tau_{w,y}$ are the zonal and meridional components of the bottom stress, respectively. Typical values of the bottom stress coefficients are $\gamma_1 = 2 * 10^{-4}m/s$ and $\gamma_2 = 0$ for linear bottom drag, and $\gamma_1 = 0$ and $\gamma_2 = 2 * 10^{-3}$ for quadratic

bottom drag (Haidvogel and Beckmann (2000)).

The friction velocity, $u_* = \sqrt{\tau_w/\rho_0}$, is often used in scaling arguments for both bulk and turbulent properties such as the boundary layer height, turbulent dissipation, Reynolds stresses, etc. Despite its first order relevance, there remains some uncertainty about how to estimate the wall stress from observational data, especially when the velocity profile is affected by wall roughness and stratification. A common method used to evaluate the friction velocity is the so-called "profile method" (Jones (1989)) which utilizes the classical law-of-the-wall (see e.g. Pope (2000)). Using this method, the friction velocity and wall roughness, z_0, are determined by fitting the observed velocity profile to the logarithmic profile

$$|\mathbf{u}| = \frac{u_*}{\kappa} ln \left(\frac{z}{z_0} \right), \tag{IV.2}$$

where $|\mathbf{u}|$ is the horizontal velocity magnitude, and $\kappa = 0.41$ is von Karman's constant.

Johnson et al. (1994) applied this method to estimate the friction velocity at the bottom of the Mediterranean outfall plume. They found that estimates of the friction velocity depended on how far away from the bottom the fit was applied, even when restricted to the bottom mixed layer. This implies that the standard law-of-the-wall was not valid throughout the bottom mixed layer. Dewey et al. (1988) compared several method for estimating the bottom stress using microstructure profiles over a continental shelf. They found that the wall stress estimated using the profile method was a factor of 4.5 larger than that estimated using the dissipation method with the friction velocity given by

$$u_* = (\epsilon \kappa z)^{1/3} \tag{IV.3}$$

where again $\kappa = 0.41$ is von Karman's constant. The authors speculated that this discrepancy may be the result of form drag induced by local bedforms. Stahr and Sanford (1999) obtained velocity and dissipation measurements in the North Atlantic deep western boundary current and similarly found that the wall stress

estimated from the profile method was 3 times larger than the wall stress estimated using the dissipation method.

Perlin et al. (2005) also found that the profile method gave large values of the wall stress compared to the dissipation method and proposed that the elevated mean shear could be explained by the influence of stratification on the boundary layer structure. They proposed that when the local stratification is sufficiently large, stratification, not distance from the wall, limits the size of the largest turbulent eddies. In order to quantify this hypothesis, they used an empirical function involving the Ozmidov scale $L_{Oz} = (\epsilon/N^3)^{1/2}$ where ϵ is the turbulent dissipation rate. Estimates of the wall stress using this method, which will be referred to here as the "modified law-of-the-wall", gave much better agreement with the dissipation method. Since direct field observations of dissipation require instruments capable of capturing fine-scale velocity fluctuations, it would be desirable to have an accurate method for estimating the wall stress from more commonly observed quantities such as the velocity and density profiles.

Weatherly and Martin (1978) considered a stratified Ekman layer using a one-dimensional numerical model and the Mellor-Yamada level II closure to parameterize turbulent mixing. They assumed that the flow outside the boundary layer was uniformly stratified, steady, and in geostrophic balance; the same assumptions that will be made in the present study. Near the wall, a mixed layer formed, which was separated from the outer layer by a strongly stable pycnocline. They found that the thickness of the bottom Ekman layer was strongly limited by the presence of a stable stratification outside the boundary layer. When the outer layer buoyancy frequency was $N_\infty/f = 200$, they found that the angle made by the surface stress relative to the free stream velocity was $\alpha_0 = 27^o$, nearly twice the value in an unstratified boundary layer of $\alpha_0 = 15^o$. Most of the change in the turning angle was seen to occur in the pycnocline and the flow in the mixed layer was nearly unidirectional. Perlin et al. (2007) observed a lower turning angle of 15 ± 5^o in a stratified bottom Ekman layer over the Oregon shelf. In agreement

with the simulations by Weatherly and Martin (1978), they found that nearly all of the Ekman transport occurs in the relatively thin bottom mixed layer.

Weatherly and Martin (1978) proposed a scaling for the height of a stratified turbulent Ekman layer given by

$$h_{WM} = A\frac{u_*}{f}\left(1 + \frac{N_\infty^2}{f^2}\right)^{-1/4}, \tag{IV.4}$$

where $A \simeq 1.3$ as determined empirically by the one-dimensional model results. In the limit of an unstratified Ekman layer, Eq. (IV.4) gives a significantly larger height than the conventional value of $h = 0.4-0.5\delta$. This is a result of the choice by Weatherly and Martin to use the criteria that the turbulent kinetic energy becomes zero at the top of the boundary layer. Choosing the location where the velocity magnitude becomes equal to the free stream would have yielded a boundary layer height nearly a factor of three smaller than that obtained using the TKE criteria when the outer flow is unstratified. A somewhat different scaling law was proposed by Zilitinkevich and Esau (2002):

$$h_{ZE} = C_R\frac{u_*}{f}\left(1 + \frac{C_R^2 C_{uN}}{C_S^2}\frac{N_\infty}{f}\right)^{-1/2}, \tag{IV.5}$$

where the constants $C_R = 0.5$ and $C_{uN}/C_S^2 = 0.56$ were determined by fitting to data from large-eddy simulation. The functional form in Eq. (IV.5) was found to be an adequate fit to field observations by Zilitinkevich and Baklanov (2002).

When a stable stratification is found outside of a turbulent well-mixed region, internal waves generated by the interaction between the turbulent eddies and the stratification are possible. Turbulence-generated internal waves have been found in laboratory experiments and numerical simulations in a wide variety of flow: shear layers, gravity currents, boundary layers, etc. Taylor and Sarkar (2007a) observed turbulence-generated internal waves in numerical simulations of a stratified Ekman layer over a smooth wall at a modest Reynolds number. They found that the vertical energy flux associated with the upward-propagating internal waves was small compared to the integrated boundary layer dissipation, but

was of the same order as the integrated buoyancy flux. Since the buoyancy flux is responsible for the transfer of turbulent kinetic energy to the potential energy field, this implies that the energy radiated by internal waves is comparable to that used to mix the background density field. As in many previous studies, they found that the waves propagating through the outer layer were associated with a relatively narrow band of frequencies leading to vertical propagation angles between $30^o - 60^o$. Since the waves are generated in a turbulent region with a wide range of spatial and temporal scales, this result is remarkable. The authors described a model based on viscous ray-tracing that was used to predict the decay in amplitude of a wave packet after it had traveled a given distance from the source. They found that this relatively simple linear model was able to capture many characteristics of the observed frequency spectrum of the internal waves in the outer layer, including the range of dominant propagation angles.

This paper will be organized as follows: The governing equations and physical approximations are discussed in Section 2, and the numerical method used to evolve the governing equations is presented in Section 3. Results from the simulations will be separated into several sections: Evolution of the mean density and velocity profiles will be discussed in Section 4, boundary layer turbulence will be discussed in Section 5, methods for estimating the friction velocity from field data will be evaluated in Section 6, and turbulence-generated internal waves will be considered in Section 7.

IV.2 Formulation

The turbulent Ekman layer considered here is formed when a steady flow in geostrophic balance encounters a non-sloping, adiabatic lower wall, as is illustrated in Figure IV.1. The primary objective of this study is to consider a controlled environment where we can examine the influence of the outer layer stratification on a turbulent Ekman layer. Therefore, we will make several simplifying approx-

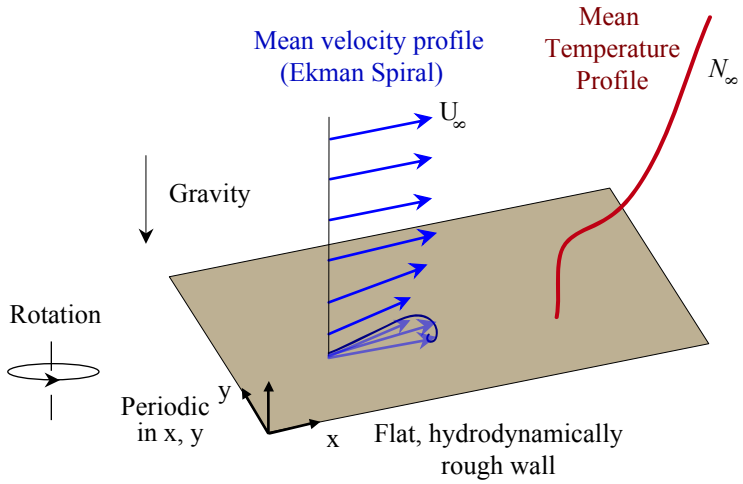

Figure IV.1: Schematic of computational model. Dimensional parameters can be obtained by assuming $U_\infty = 0.0674m/s$ and $f = 10^{-4}rad/s$. The domain size is $72.8m$ x $72.8m$ x $27.3m$. Three values of outer layer stratification are considered: N_∞/f =0, 31.6, and 75.

imations. The free stream will be assumed to be in geostrophic balance and will be aligned with the x-axis. The seafloor is represented by a non-sloping, rough surface. The roughness elements are too small to resolve directly by the grid, but their effect is parameterized through a near-wall model. The lateral boundaries are periodic which is consistent with the assumption that the flow is statistically homogeneous in the horizontal plane and that the domain is large enough so that the flow is de-correlated over a distance equal to the domain size. In outer units, $D = U_\infty/f$, the domain size is $0.108D$ x $0.108D$ x $0.0405D$ in the x, y, and z directions, respectively. If we assume that $U_\infty = 0.0674m/s$ and $f = 10^{-4}rad/s$, then $D = 674m$ and the domain size is $72.8m$ x $72.8m$ x $27.3m$. As a result of the horizontal periodicity, the mean vertical velocity must be zero. Therefore the features of oceanic boundary layers owing to Ekman pumping/suction driven by large scale horizontal gradients in the outer flow will not be present here.

The goal of a large-eddy simulation (LES) is to accurately solve a low-

pass filtered version of the Navier-Stokes equations. Since the filtered version of the nonlinear advection terms involves the total and filtered velocity fields, we are left with fewer equations than unknowns, the well-known turbulence closure problem. A model is then necessary to write the residual stresses in terms of the filtered quantities. After normalizing with the free stream velocity, U_∞, the lengthscale, $D = U_\infty/f$, and the outer layer density gradient, $d\rho/dz_\infty$, the LES filtered governing equations can be written

$$\frac{\partial \overline{\mathbf{u}}}{\partial t} + \overline{\mathbf{u}} \cdot \nabla \overline{\mathbf{u}} = -\frac{1}{\rho_0}\nabla \overline{p'} + f\hat{\mathbf{k}} \times (\hat{\mathbf{i}} - \overline{\mathbf{u}}) - Ri_\infty \frac{\overline{\rho'}}{\rho_0}\hat{\mathbf{k}} + \frac{1}{Re_\infty}\nabla^2 \overline{\mathbf{u}} - \nabla \cdot \boldsymbol{\tau}, \quad \text{(IV.6)}$$

$$\frac{\partial \overline{\rho'}}{\partial t} + \overline{\mathbf{u}} \cdot \nabla \overline{\rho'} = \frac{1}{Re_\infty Pr}\nabla^2 \overline{\rho'} - \nabla \cdot \boldsymbol{\lambda}, \quad \text{(IV.7)}$$

$$\nabla \cdot \overline{\mathbf{u}} = 0, \quad \text{(IV.8)}$$

where the Reynolds number, Richardson number, and Prandtl number are defined by

$$Re_\infty = \frac{U_\infty D}{\nu}, \quad Ri_\infty = -\frac{g}{\rho_0}\frac{d\rho}{dz}_\infty \frac{D^2}{U_\infty^2}, \quad Pr = \frac{\nu}{\kappa}, \quad \text{(IV.9)}$$

ρ_0 is the constant density used to define the momentum using the Boussinesq approximation, ν is the molecular kinematic viscosity, κ is the molecular diffusivity, and $\boldsymbol{\tau}$ and $\boldsymbol{\lambda}$ are the subgrid-scale stress and density flux, respectively. The density and pressure have been decomposed into a plane average plus a fluctuation, i.e. $\rho = \langle\rho\rangle + \rho'$. The hydrostatic pressure gradient and the plane averaged buoyancy force are in balance and do not appear in Eq. (IV.6). An alternative normalization can be carried out using the friction velocity $u_* = \sqrt{\tau_w/\rho_0}$. This leads to the friction Reynolds and Richardson numbers:

$$Re_* = \frac{u_*\delta}{\nu}, \quad Ri_* = -\frac{g}{\rho_0}\frac{d\rho}{dz}_\infty \frac{\delta^2}{u_*^2} = \frac{N_\infty^2}{f^2}, \quad \delta = \frac{u_*}{f}. \quad \text{(IV.10)}$$

Relevant input and output nondimensional parameters are listed in Table 1. The dimensional parameters U_∞, N_∞, f, ν and the roughness lengthscale z_0 are inputs to the simulations. Note that Re_∞ is the same for each simulation, but the drag coefficient depends on the outer layer stratification, and hence the friction

Table IV.1: Relevant physical parameters. Re_∞, N_∞/f, Pr and z_0 are input parameters and the other parameters are outputs of the numerical model.

Re_*	Ri_*	N_∞/f	Pr	u_*/U_∞	z_0/δ	α_0
$1.08 * 10^5$	0	0		0.0488	$4.80 * 10^{-5}$	15.4^o
$1.09 * 10^5$	1000	31.6	5-10	0.0490	$4.78 * 10^{-5}$	18.9^o
$1.12 * 10^5$	5625	75		0.0497	$4.71 * 10^{-5}$	24.8^o

Reynolds number varies between each case. We have performed simulations at three different values of Ri_*, equivalent to changing the free-stream density gradient. For comparison with oceanographic conditions, observations of the bottom boundary layer over the Oregon shelf by Perlin et al. (2007) provide estimates of $Re_* = 4 * 10^4 - 8 * 10^5$ and $N_\infty/f = 75$. Therefore, both the Reynolds numbers and stratification levels considered in the present study are comparable with the field data of Perlin et al. (2007). In order to provide dimensional scalings for our simulations, we will use $U_\infty = 0.0674m/s$, $f = 10^{-4}s^{-1}$, and $\nu = 10^{-6}m^2/s$ which, assuming that $u_*/U_\infty = 0.049$, yields $\delta = u_*/f \approx 33m$. The applied roughness lengthscale, $z_0 = 0.16cm$, is consistent with observations by Perlin et al. (2005) who found that $z_0 = 0.05$cm - 2 cm depending on the method used to infer the wall stress.

IV.3 Numerical Methods

Simulations have been performed using a computational fluid dynamics solver developed at the University of California, San Diego. The algorithm and numerical method are described in detail in Bewley (2007). Since periodic boundary conditions are applied in the horizontal directions, derivatives in these directions are computed using a pseudo-spectral method, while derivatives in the vertical direction are computed with second order finite differences. Time-stepping is accomplished with a mixed explicit/implicit scheme using third order Runge-Kutta and Crank-Nicolson. It can be shown that the numerical scheme ensures the dis-

crete conservation of mass, momentum, and energy (Bewely (1999)). In order to prevent spurious aliasing due to nonlinear interactions between wavenumbers, the largest 1/3 of the horizontal wavenumbers are set to zero, the so-called 2/3 de-aliasing rule (Orszag (1971)).

In order to prevent the formation of spurious energy near the grid scale, a low-pass spatial filter is applied to the velocity and temperature fields. A fourth order compact filter with a sharp wavenumber cutoff (Lele (1992)) is applied in the vertical direction every 10 time steps. An open boundary condition is implemented at the top of the computational domain in order to prevent spurious reflections of upward propagating internal gravity waves. The combination of a radiation boundary condition (Durran (1999)) and a sponge damping region that is used here was also used by Taylor and Sarkar (2007a) who found that only 6% of the wave energy was reflected back from the open boundary.

The subgrid-scale stress tensor, $\boldsymbol{\tau}$, and the subgrid-scale density flux, $\boldsymbol{\lambda}$, in Eqns. (IV.6) and (IV.7) are evaluated using the dynamic Smagorinsky model (Germano et al. (1991)). The Smagorinsky coefficients, C and C_ρ are evaluated using the dynamic procedure. This is useful since it avoids the empirical specification of the Smagorinsky coefficient and has been shown to perform well for wall-bounded and density stratified flows (Armenio and Sarkar (2002); Taylor et al. (2005)). Details of the basic LES model can be found in Germano (1991).

To ensure accuracy of the solution obtained using large-eddy simulation, it is generally necessary to resolve the turbulent scales responsible for a substantial portion, say $> 50\%$, of the turbulent kinetic energy. Near walls this criteria becomes increasingly stringent as the Reynolds number increases. To avoid the need to resolve the very small turbulent motions near the lower wall, we have used a near-wall model to estimate the wall stress based on the resolved velocity at the first gridpoint. We have used a model proposed by Marusic et al. (2001), that Stoll and Porte Agel (2006) found works well for high Reynolds number, rough wall boundary layers. In order to compensate for known deficiencies in the Smagorinsky

LES model at very large Reynolds numbers, the near-wall model was augmented by a novel adaptive stochastic forcing procedure. The forcing amplitude is small, less than 6% of $\partial w/\partial t$, and limited to the first nine grid points near the wall. This technique is described in detail and validated in Taylor and Sarkar (2007b).

In order to obtain an initial condition for the velocity field, a low Reynolds number, unstratified simulation was conducted until the flow reached a steady state. The velocity field from this simulation was then interpolated onto a finer grid and a simulation at a higher Reynolds number was continued until all transients had decayed. The stratified simulations were initialized using the steady-state unstratified velocity field and an undisturbed, piecewise-linear temperature profile. The initial temperature profile has a relatively thin mixed layer with a thickness of about $z \simeq 0.04\delta$. This was done so that the stochastic forcing, mentioned above, would not produce spurious internal waves by forcing a stratified region. For $z > 0.08\delta$, the temperature profile was set to $\Theta = zd\Theta/dz|_\infty$, and for $0.04 < z/\delta < 0.08$, a linear profile was used to make the integrated heat content over the domain the same as if $\Theta = zd\Theta/dz|_\infty$ everywhere. Each stratified simulation was run for about $tf = 1.5$ to allow the unstratified turbulence levels to adjust to the imposed stratification. This creates a better initial velocity field, and the temperature field was then reset to the piecewise linear profile. The time at which the temperature field was reset will be referred to as $t = 0$.

IV.4 Mean boundary layer structure

The time history of the plane averaged temperature gradient is shown in Figure V.2. After the flow is initialized, the mixed layer near the wall grows rapidly. As the flow develops, a strongly stratified pycnocline forms above the mixed layer. It can be shown that if there is no net heat flux into the domain (which is is a good approximation since the molecular heat flux through the top of the domain is small) then a pycnocline is necessary to maintain heat conservation after the

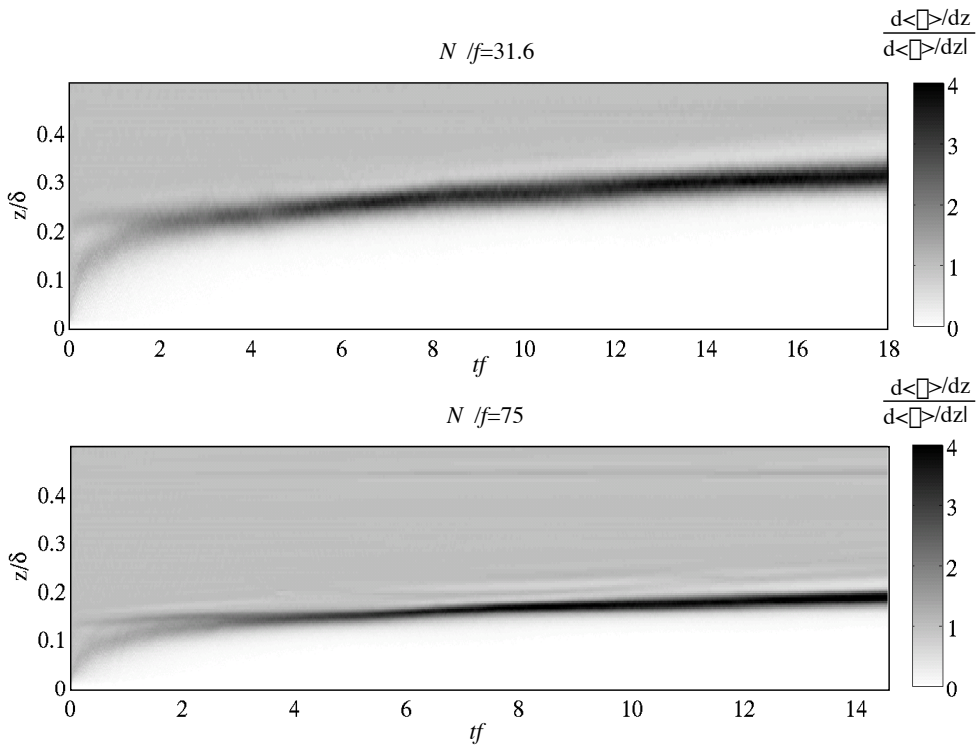

Figure IV.2: Evolution of the plane averaged temperature gradient

formation of a mixed layer. At the start of each stratified simulation, two distinct pycnoclines are visible for a short time, one above the bottom mixed layer, and another above a region where the residual motions from the initial velocity field mix the temperature field. Eventually these pycnoclines merge, and the resulting single pycnocline gradually moves away from the wall as the mixed layer grows. In the case with $N_\infty/f = 75$, the pycnocline has a larger stratification, four times the outer layer value, compared to the case with $N_\infty/f = 31.6$. After about $tf = 6$ the temperature fields in both stratified simulations reach a quasi-steady state where the temperature gradient in the pycnocline does not grow further, and the mixed layer growth becomes relatively slow.

Two averaging methods will be used for velocity and temperature dependent fields. The Reynolds average, denoted by $< \cdot >$ will be taken as an average over a horizontal plane and in time. In order to remove any bias due to inertial oscillations, averages are taken over one inertial period after the flow has reached

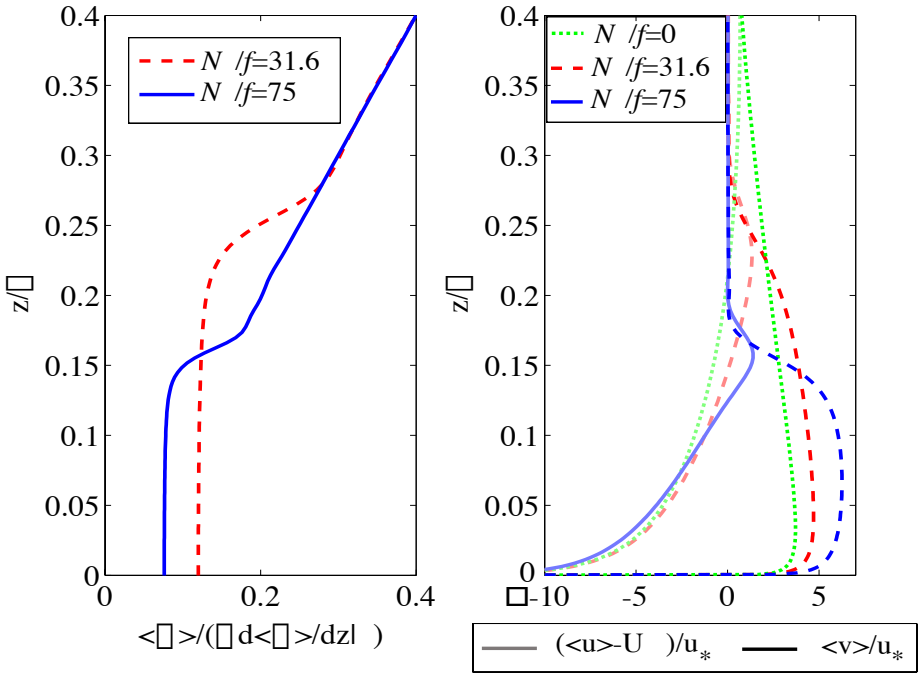

Figure IV.3: (a) Plane averaged temperature profiles, and (b) plane and time-averaged horizontal velocity components

quasi-steady state. However, since the mixed layer thickness continues to increase in time, albeit slowly, temporal averages are not appropriate for the thermal fields and would, for example, lead to a smearing out of the pycnocline. Temperature will therefore not be averaged in time, but the plane average of the temperature dependent fields will be taken at the time corresponding to the center of the Reynolds average window, unless otherwise noted.

The plane-averaged temperature profiles after the flow has reached quasi-steady state are shown in Figure IV.3(a). Both profiles correspond to a time $t = 9.4/f$ after initializing the temperature field. The components of the Reynolds averaged horizontal velocity are shown in Figure IV.3(b). Comparing with the temperature profiles, it is apparent that most of the Ekman transport is confined to the mixed layer. The increase in cross stream velocity results in a broadening of the Ekman spiral, as shown in Figure IV.4. It is interesting to note that although

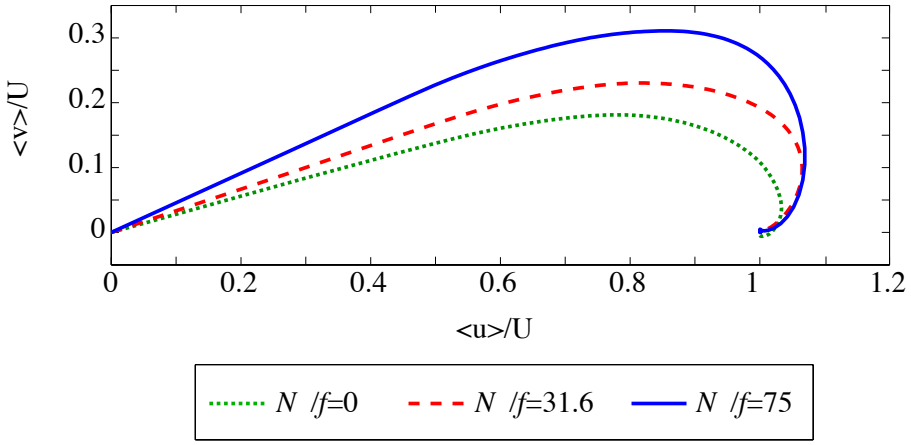

Figure IV.4: Mean velocity hodograph showing the Ekman spiral

the density gradient is zero near the lower wall, the surface turning angle $\alpha_0 = tan^{-1}(\tau_y/\tau_x)$ increases with the outer layer stratification, as listed in Table 1. The angle of Ekman veering, defined by

$$\alpha = tan^{-1}\left(\frac{< v >}{< u >}\right), \tag{IV.11}$$

is shown as a function of z/δ in Figure IV.5. When the flow is unstratified, the turning of the mean velocity occurs gradually throughout the boundary layer. The rate of turning in the mixed layer does not depend strongly on the outer layer stratification. Therefore, since the magnitude of the turning angle at the wall increases with the outer layer stratification, and the boundary layer height decreases significantly, the rate of turning, $d\alpha/dz$, becomes very large in the pycnocline.

Despite the fact that the boundary layer height changes significantly, the Ekman transport is nearly independent of the outer layer stratification. An expression for the Ekman transport can be found by integrating the mean streamwise momentum equation. Assuming that the mean flow is steady, and neglecting the molecular viscosity,

$$\int_0^\infty < v > dz = \frac{u_*^2}{f} cos(\alpha_0). \tag{IV.12}$$

As seen in Table VI.2, both u_*/U_∞ and α_0 increase with N_∞/f. Their effect

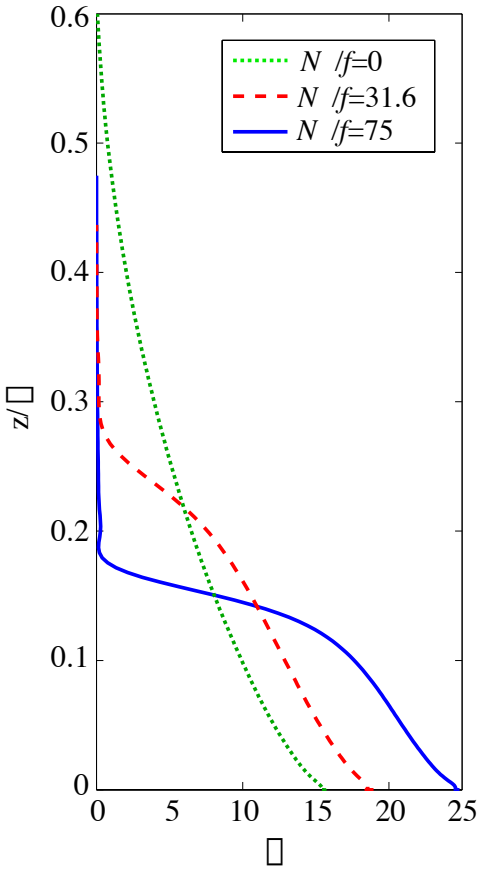

Figure IV.5: Ekman veering angle

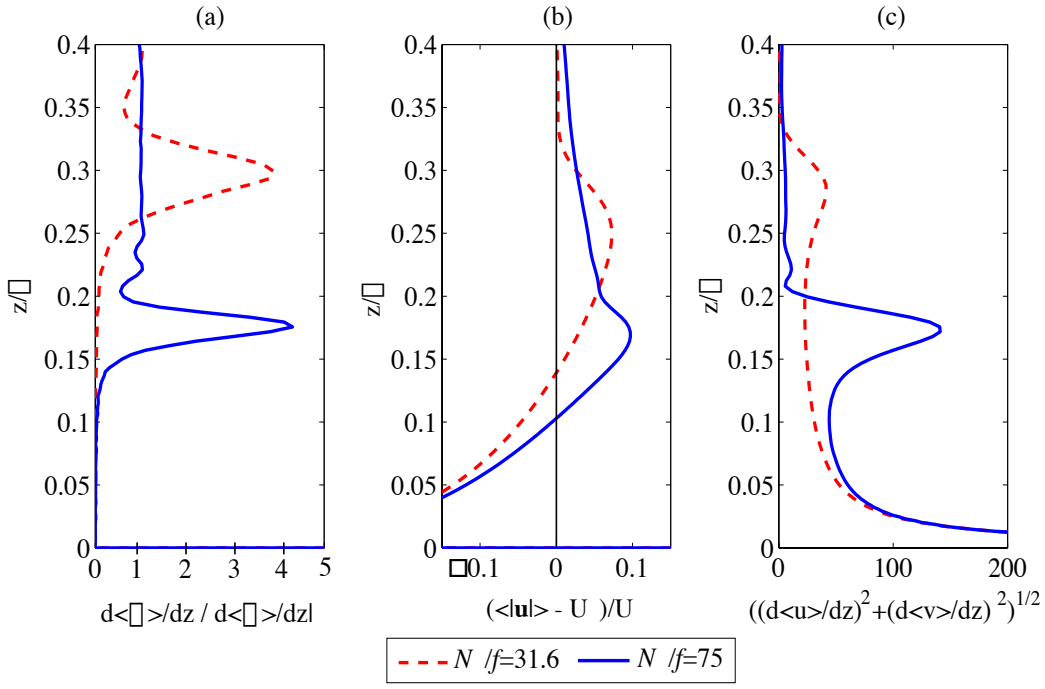

Figure IV.6: (a) Temperature gradient, (b) horizontal velocity magnitude (c) mean shear

partially cancels, so that the Ekman transport normalized by U_∞ and f is nearly independent of N_∞. Specifically, evaluation of Eq. (IV.12) yields a transport of $0.107m^2/s$, $0.105m^2/s$, and $0.101m^2/s$ for $N_\infty/f = 0$, 31.6, and 75, respectively, assuming that $U_\infty = 0.0674m/s$ and $f = 10^{-4}rad/s$. The same result could be obtained by numerically integrating the cross-stream velocity profiles.

As has been found in previous studies, the large density gradient at the top of the boundary layer coincides with an increase in the mean shear. The temperature gradient normalized by the outer layer value is shown in Figure IV.6(a), and the Reynolds averaged velocity and shear profiles are shown in Figure IV.6(b)-(c). A peculiar feature of the mean velocity profile when $N_\infty/f = 75$ is that the mean velocity and the mean shear are maximum at the *same* location near the center of the pycnocline. It can be shown that this is the result of the rapid rate of veering that occurs in the pycnocline in this case. Using the definition of the

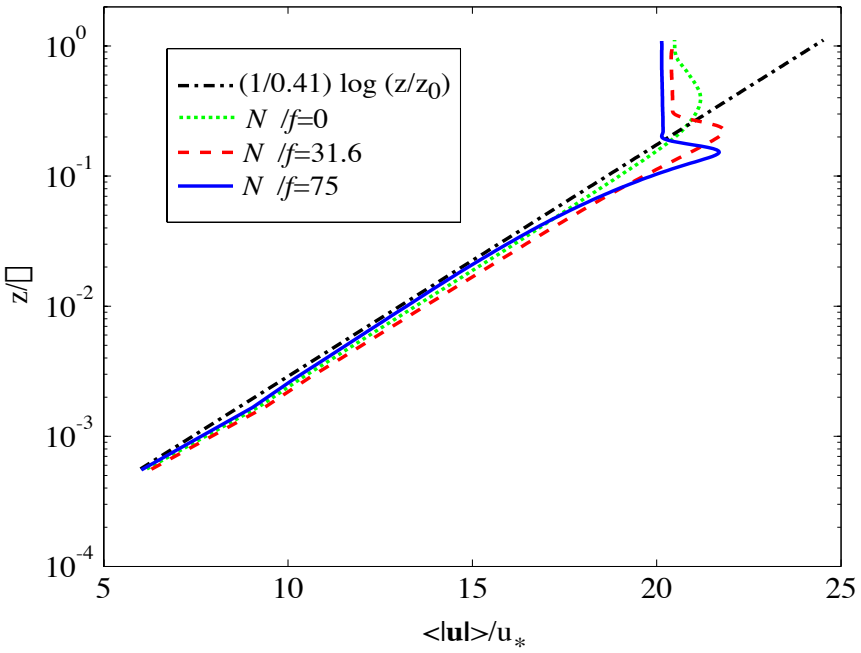

Figure IV.7: Reynolds averaged horizontal velocity magnitude

Ekman veering angle, the square of the mean shear can be written

$$\left(\frac{d\langle u\rangle}{dz}\right)^2+\left(\frac{d\langle v\rangle}{dz}\right)^2=\left(\frac{d\langle|\mathbf{u}|\rangle}{dz}\right)^2+\langle|\mathbf{u}|\rangle^2\left(\frac{d\alpha}{dz}\right)^2, \tag{IV.13}$$

where $|\mathbf{u}|=\sqrt{u^2+v^2}$. At the center of the pycnocline, the first term on the right hand size is zero since the velocity magnitude $|\mathbf{u}|$, is maximum at this location. However, since the Ekman veering rate is very large at this location, the second term leads to a local maximum of the mean shear in the pycnocline. Most of the enhanced shear in the lower portion of the pycnocline is due to the spanwise shear, while the streamwise shear dominates in the upper portion of the pycnocline.

Coleman (1999) showed that in an unstratified turbulent Ekman layer the mean velocity magnitude should follow the classical logarithmic law (or law-of-the-wall). The law-of-the-wall is expected to hold in a region far enough from the wall where viscosity can be neglected, but near enough to the wall so that the boundary layer depth is not felt. In this case, the only relevant lengthscale must

be the distance from the wall so that

$$\left|\frac{d<\mathbf{u}>}{dz}\right| = \frac{u_*}{l}, \tag{IV.14}$$

where $l = \kappa z$ and κ is the von Karman constant that is empirically found to be about 0.41. The Reynolds averaged horizontal velocity magnitude is plotted in Figure IV.7 on a semi-logarithmic scale. Very near the wall all cases are in reasonably good agreement with the unstratified logarithmic law. Deviations from the logarithmic velocity profile in the cases when stratification is present can be seen clearly by plotting the normalized velocity gradient

$$\Phi = \frac{\kappa z}{u_*}\left|\frac{d<\mathbf{u}>}{dz}\right|. \tag{IV.15}$$

The quantity Φ can be interpreted as the ratio of the observed mean velocity gradient to that expected from the logarithmic law and is shown in Figure IV.8. When the outer layer is stratified, the mean shear in the pycnocline increases significantly compared to the log-law value. It is worth noting that deviations from the law-of-the-wall begin well within the mixed layer. The consequences for this observation will be discussed in Section 7.

IV.5 Boundary Layer Turbulence

In order to understand the increase in mean velocity and mean shear in the pycnocline, it is necessary to consider the influence of stratification on the turbulent eddies. The turbulent kinetic energy in the mixed layer scales with the friction velocity u_* which, as we have seen, does not change significantly with the addition of an outer layer stratification. In addition, the density gradient in the pycnocline appears to scale with the outer layer stratification. Therefore, as the stratification in the outer layer increases, the kinetic energy associated with eddies at the top of the mixed layer remains about the same while the potential energy required for an eddy to overturn increases. Therefore, when the stratification

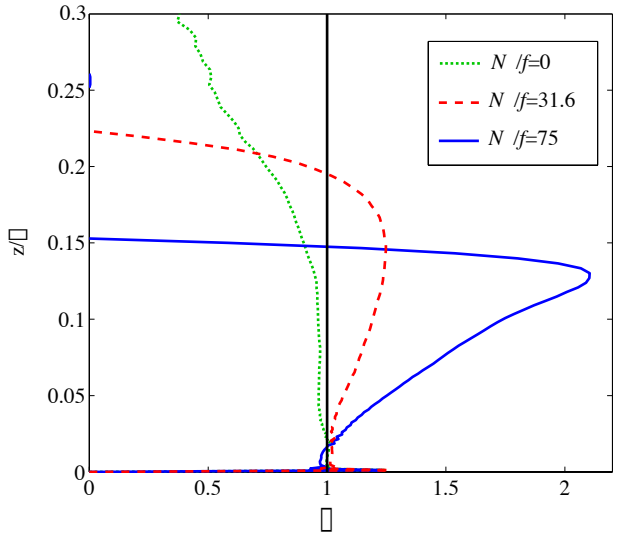

Figure IV.8: Nondimensional velocity gradient, $\Phi = (\kappa z/u_*)\, d < u > /dz$.

becomes large enough, turbulence is inhibited at the top of the boundary layer, and as a result the growth of the mixed layer is strongly limited.

One consequence of the damping of turbulence by stratification is a decrease in the turbulent stresses, $< u'w' >$ and $< v'w' >$. The decrease in boundary layer height with increasing stratification is very apparent from the Reynolds stress profiles shown in Figure IV.9. Here, the Reynolds stress includes both the resolved and subgrid-scale contributions. Note that above the boundary layer, the Reynolds stress approaches a small, nonzero value owing to the presence of turbulence-generated internal gravity waves. However, the Reynolds stress associated with the waves is much smaller than in the turbulent region, so this does not interfere with the definition of boundary layer height. It is evident from Figure IV.9 that the Reynolds stresses change more rapidly with height when the outer layer stratification is stronger. Changes in the Reynolds stress with height result in a momentum flux that must be balanced by other terms. The plane averaged horizontal momentum equations can be written

$$\frac{\partial \langle u \rangle}{\partial t} = -\frac{\partial \langle u'w' \rangle}{\partial z} + f \langle v \rangle + \nu \frac{\partial^2 \langle u \rangle}{dz^2}, \tag{IV.16}$$

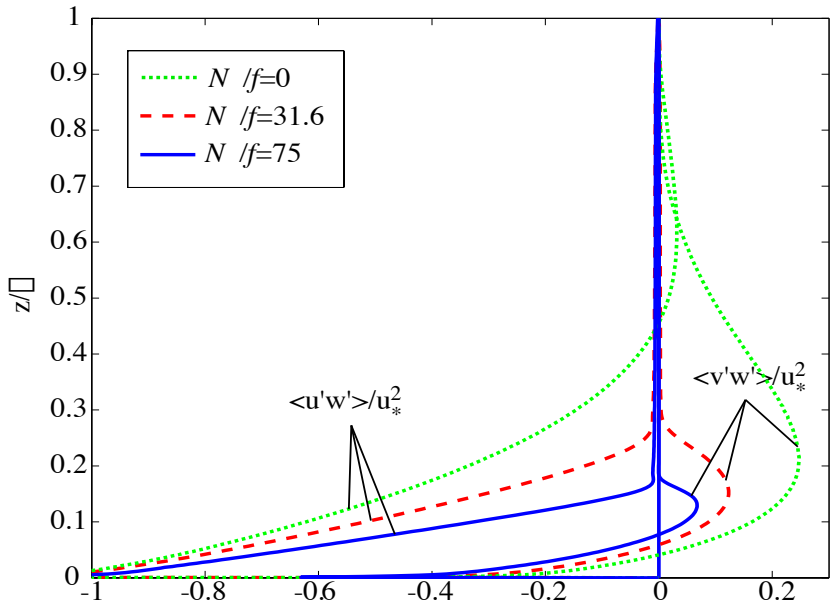

Figure IV.9: Reynolds stress profiles

$$\frac{\partial \langle v \rangle}{\partial t} = -\frac{\partial \langle v'w' \rangle}{\partial z} - f\left(\langle u \rangle - U_\infty\right) + \nu \frac{\partial^2 \langle v \rangle}{dz^2}. \tag{IV.17}$$

We have found that both streamwise and spanwise components of the eddy viscosity,

$$\nu_{T,x} = \frac{-\langle u'w' \rangle}{d\langle u \rangle / dz}, \qquad \nu_{T,y} = \frac{-\langle v'w' \rangle}{d\langle v \rangle / dz}, \tag{IV.18}$$

are positive, implying a co-gradient momentum flux. Therefore in the upper portion of the Ekman layer where $d\langle v \rangle / dz < 0$, the spanwise Reynolds stress is positive as evidenced in Figure IV.9. Since both components of the Reynolds stress become nearly zero in the outer layer, there must be a region near the top of the Ekman layer where $d\langle v'w' \rangle / dz < 0$. When the leading order y-momentum balance is between the Reynolds stress and Coriolis terms, the region with $d\langle v'w' \rangle / dz > 0$ leads to $\langle u \rangle > U_\infty$. Therefore, a zonal jet is an inherent feature of a steady-state turbulent Ekman layer.

The plane-averaged turbulent kinetic energy budget can be found by dot-

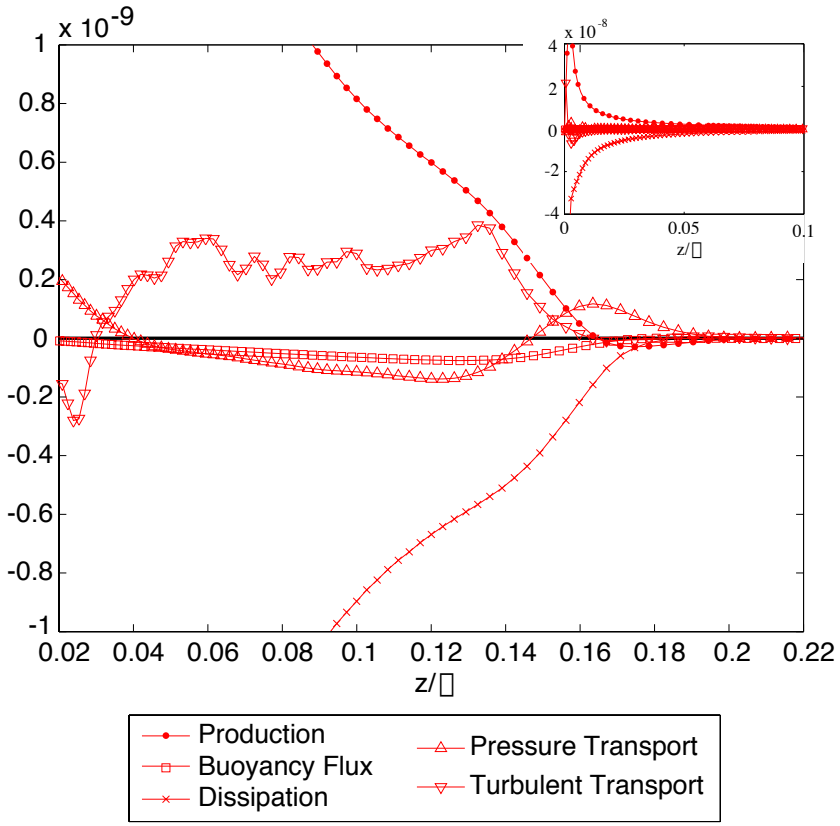

Figure IV.10: Turbulent kinetic energy budget at the top of the mixed layer and pycnocline for $N_\infty/f = 75$. Inset shows the TKE budget near the wall.

ting $\mathbf{u}'$ into the perturbation momentum equations, to give

$$\frac{\partial k}{\partial t} = -\frac{1}{2}\frac{\partial}{\partial z} < w'u_i'u_i' > -\frac{\partial}{\partial z}\frac{1}{\rho_0} < w'p' > +\frac{1}{Re_*}\frac{\partial^2 k}{\partial z^2} - < S_{ij} >< u_i'u_j' > \\ -\frac{1}{Re_*} < \frac{\partial u_i'}{\partial x_j}\frac{\partial u_i'}{\partial x_j} > -Ri_* < w'\rho' > -\frac{\partial}{\partial z} < u_i'\tau_{31} > + < \tau_{ji}\frac{\partial u_i'}{\partial x_j} >, \quad \text{(IV.19)}$$

where $k = \langle u_i'u_i' \rangle /2$ is the turbulent kinetic energy. Reading from left to right, the terms on the right hand side of Eq. (IV.19) can be identified as the turbulent transport, pressure transport, viscous diffusion, production, dissipation, buoyancy flux, subgrid transport and subgrid dissipation, respectively. The leading terms in the turbulent kinetic energy budget for $N_\infty/f = 75$ are shown in Figure IV.10. Near the wall, the leading order balance is between production and dissipation and does not differ significantly from the unstratified case as shown in the inset. In the upper portion of the mixed layer, the turbulent transport appears as a source term representing the advection of turbulent eddies towards the pycnocline. Pressure transport, buoyancy flux, and dissipation are the dominant energy sinks in the upper mixed layer. In the pycnocline, starting at about $z/\delta = 0.15$, the turbulent transport and buoyancy flux decrease as stratification suppresses turbulent motion while pressure transport becomes the dominant source term. When the pressure transport is positive the vertical energy flux, $< p'w' >$ increases with height, consistent with an internal wave field that is gaining energy. This is direct evidence of the generation of internal waves by the interaction between boundary layer turbulence and a stable stratification. The properties of these waves will be discussed in Section 6.

The instantaneous temperature field is shown for $N_\infty/f = 75$ in Figure IV.11 in a x-z plane at $t = 11.2/f$. Figure IV.11(b) shows an enlarged version of the box drawn in Figure IV.11(a). Isotherms are drawn every $0.025\delta d \langle \Theta \rangle /dz_\infty$. The mixed layer is very homogeneous with disturbances rarely exceeding the contour level. Turbulence-generated internal waves are visible as disturbances of the isotherms in the outer layer which is generally statically stable with the notable exception of the region just above the pycnocline. Density overturns are visible

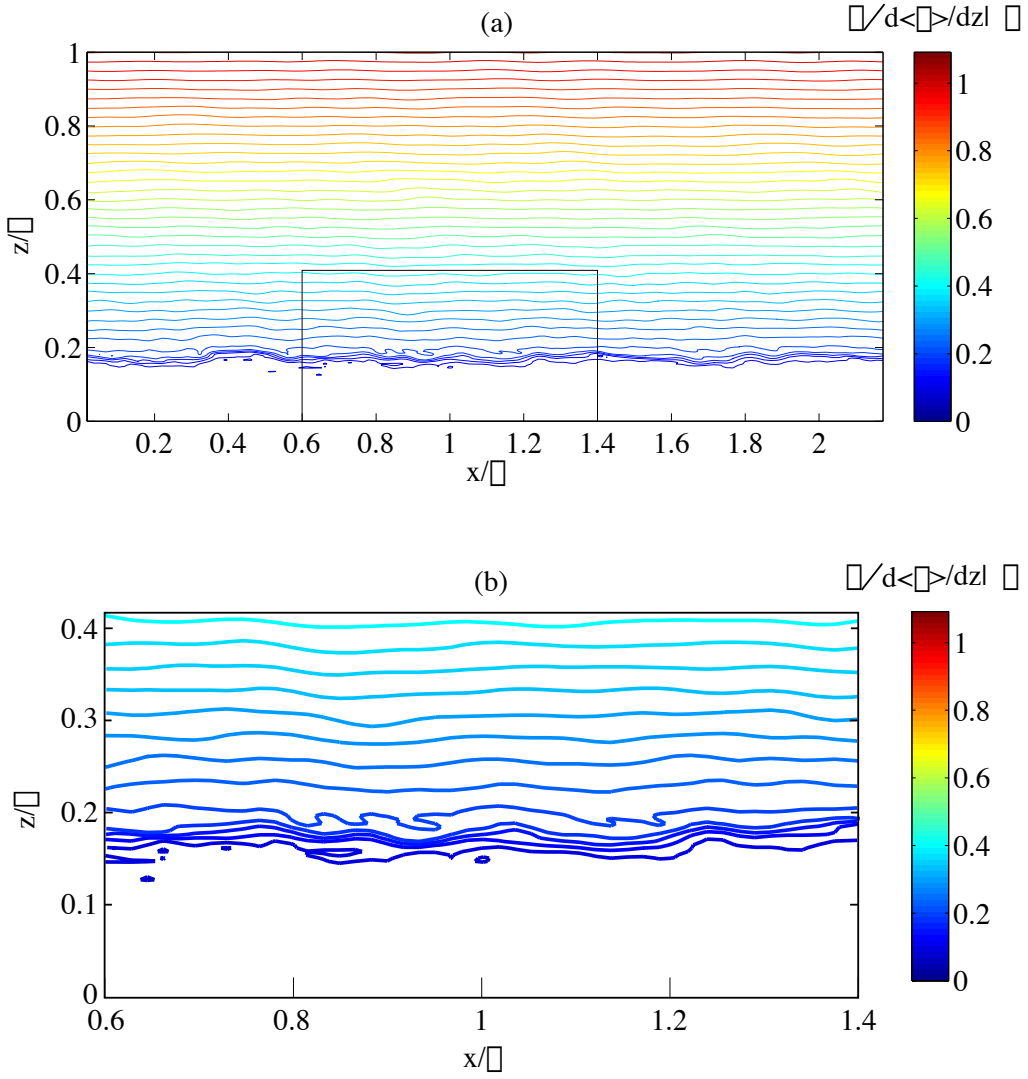

Figure IV.11: Isotherms projected onto an x-z plane for the case with $N_\infty/f = 75$ (a) full computational domain, (b) zoom of boxed region near the pycnocline.

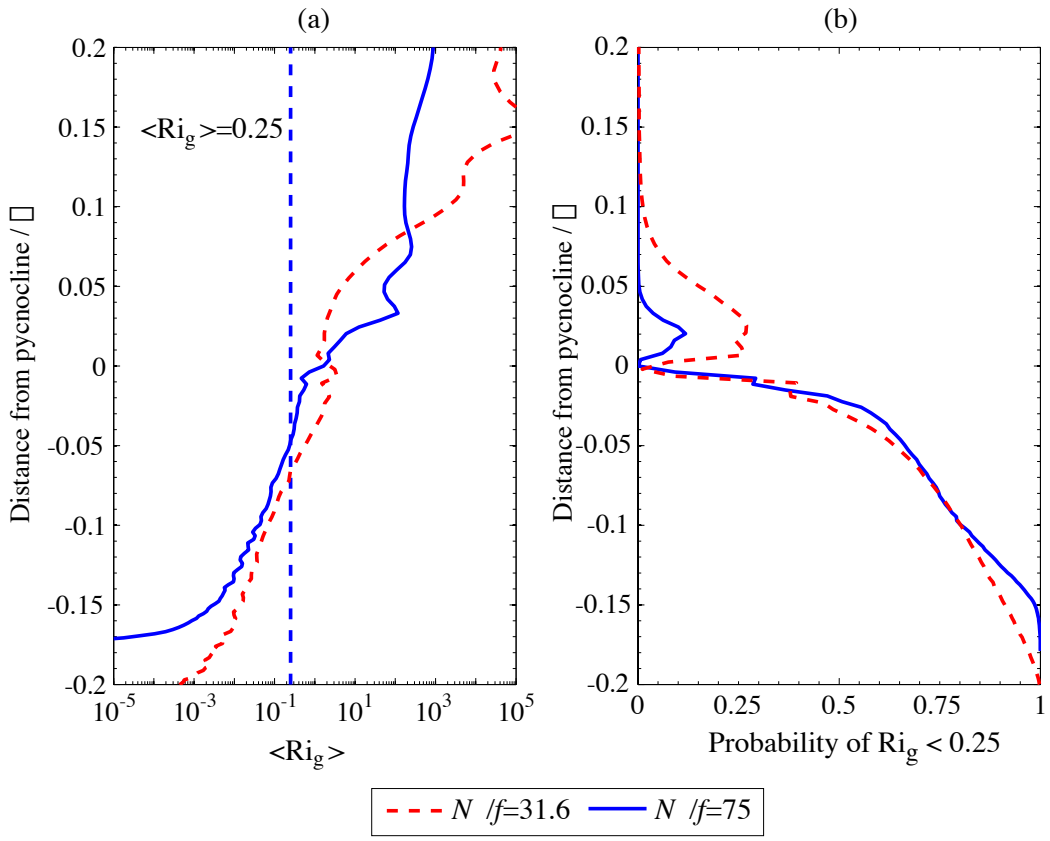

Figure IV.12: (a) Mean gradient Richardson number, $\langle Ri_g \rangle$, and (b) Probability of occurrences of the local $Ri_g < 0.25$. Vertical profiles have been averaged in terms of the distance from the maximum temperature gradient.

both below and *above* the pycnocline. As highlighted in Figure IV.11(b), the overturns above the pycnocline are reminiscent of Kelvin-Helmholtz billows associated with a negative mean shear. The irreversible mixing resulting from these overturns may be responsible for the reduced temperature gradient above the pycnocline as seen in Figure IV.6(a).

The stability of the shear above the pycnocline can be examined using the gradient Richardson number. The mean gradient Richardson number, defined as

$$\langle Ri_g \rangle = \frac{-\left(g/\rho_0\right) d\left\langle \Theta \right\rangle / dz}{\left(d\left\langle u \right\rangle / dz\right)^2 + \left(d\left\langle v \right\rangle / dz\right)^2} = \frac{\langle N^2 \rangle}{\langle S \rangle^2}, \tag{IV.20}$$

is shown in Figure IV.12(a). Heaving of the pycnocline, which is visible in Figure IV.11 causes significant variations in the pycnocline height. Since we are interested in the shear and stratification a small distance above the pycnocline, averaging over a constant height could be problematic. Therefore, the average operator in Eq. (IV.20) has been taken with respect to a constant distance from the center of the pycnocline (identified by the maximum temperature gradient). It has been shown that a stratified flow can develop linear shear instabilities if Ri_g is less than 0.25 somewhere in the flow (Miles (1961); Howard (1961)). In our simulations $\langle Ri_g \rangle < 0.25$ in the mixed layer, while $\langle Ri_g \rangle$ becomes very large in the outer layer where the stratification is large compared to the mean shear. Since $\langle Ri_g \rangle > 1$ above the pycnocline in both cases, it is perhaps surprising that *local* occurrences of $Ri_g < 0.25$ are not uncommon even above the pycnocline. Figure IV.12(b) shows the probability of the local $Ri_g < 0.25$. In the mixed layer (where the distance from the pycnocline is large and negative), the probability of $Ri_g < 0.25$ is very high, as expected. The probability of $Ri_g < 0.25$ drops to nearly zero in the pycnocline, but a local maximum in the probability occurs above the pycnocline. A coincident local maximum in the probability of local density overturns can also be seen above the pycnocline (not shown). About 70% of the overturns occurring above the pycnocline are associated with a local shear that is larger in magnitude than the plane-averaged value. This suggests that while the mean shear is not unstable based on the typical gradient Richardson number criteria, *local* shear instabilities may drive the overturns observed in this region.

In order to illustrate the appearance of overturns and unstable shear profiles in the region above the pycnocline, Figure IV.13 shows an instantaneous $x - z$ slice through a small section of the flow when $N_\infty/f = 75$. Color shading indicates du'/dz, lines show isotherms at an interval of $0.01\delta d < \Theta > /dz_\infty$, and circles indicate locations where $Ri_g < 0.25$. The perturbation shear appears to be closely associated with undulations in the pycnocline height. As we have seen, occurrences of $Ri_g < 0.25$ are common above and below the pycnocline. Most

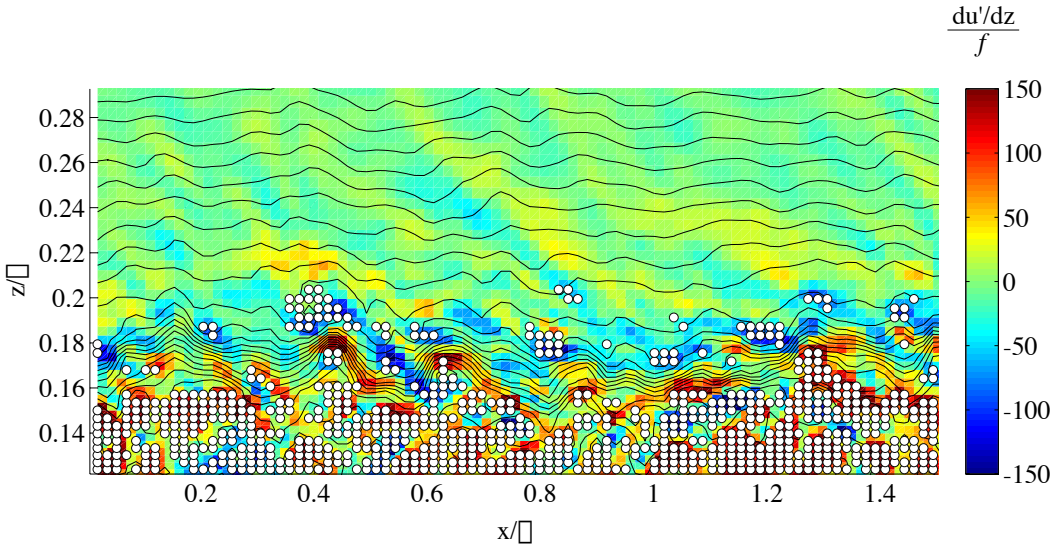

Figure IV.13: Instantaneous streamwise shear, du'/dz, with overlaid isopycnals for $N_\infty/f = 75$. Circles show where $Ri_g < 0.25$ locally.

of the regions with an unstable shear above the pycnocline are associated with a negative streamwise shear perturbations. It also appears that radiated internal waves (visible by phase lines of du'/dz that slope up and to the left) are sometimes associated with $Ri_g < 0.25$, but this only occurs near the pycnocline; in the outer layer, Ri_g is always large.

Since changes in the local shear and the local stratification can cause variations in Ri_g, it is of interest to examine the distribution of low Ri_g events. Figure IV.14 shows a scatter plot of the deviation of the local shear and buoyancy frequency from the background values, for events with $0 < Ri_g < 0.25$. Only one height is shown for clarity, $z/\delta = 0.195$, which corresponds to the secondary peak in Ri_g above the pynocline as shown in Figure IV.12(b). At this location, the mean buoyancy frequency is $73f$, and the mean gradient Richardson number is $Ri_g = \langle N^2 \rangle / \langle S \rangle^2 = 3.15$. Since the mean shear is dominated by the streamwise component at this location, only this component is considered. It is clear from Figure IV.14 that most of the occurrences of $Ri_g < 0.25$ occur when $du'/dz < 0$ and nearly all occurrences of $Ri_g < 0.25$ occur when the stratification is less then

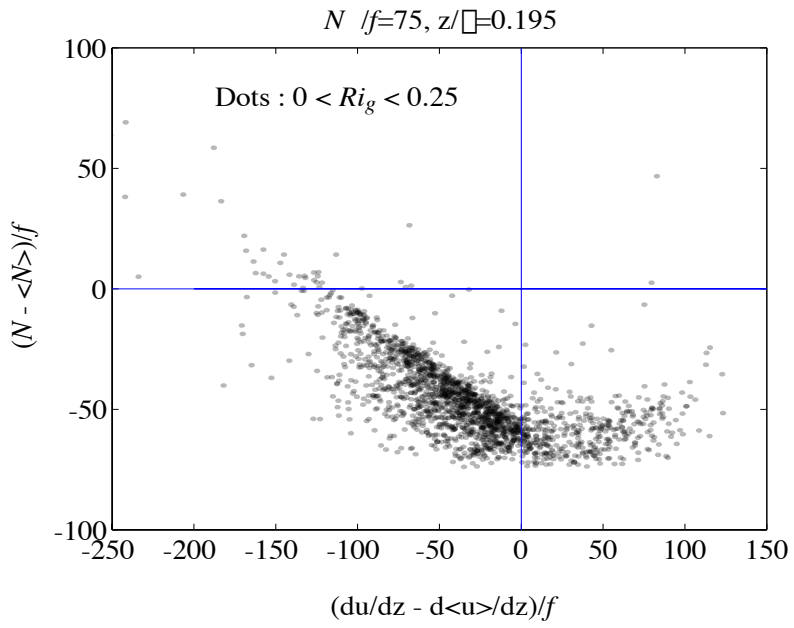

Figure IV.14: Perturbation streamwise shear and buoyancy frequency for events with $0 < Ri_g < 0.25$ at $z/\delta = 0.195$. The mean gradient Richardson number, $\langle Ri_g \rangle = 3.15$.

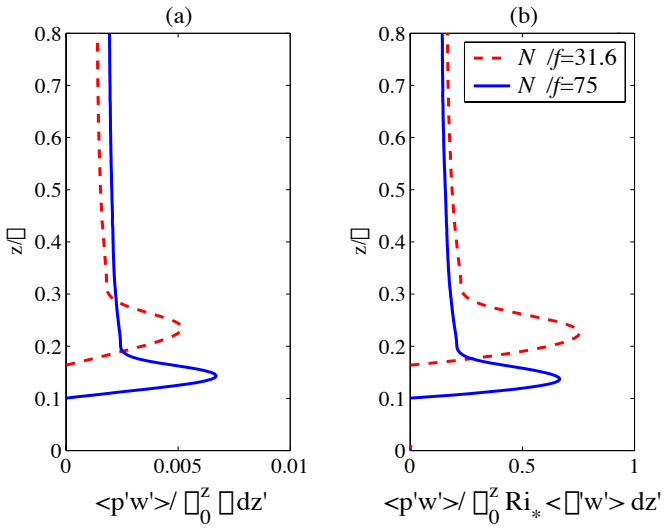

Figure IV.15: Vertical energy flux normalized by (a) the integrated turbulent dissipation, and (b) the integrated buoyancy flux.

its mean value. A notable exception is when the shear is very large and negative in which case $Ri_g < 0.25$ even though the local stratification is high.

IV.6 Turbulence-generated internal waves

In the outer layer above the pycnocline, vertically propagating internal waves can be observed. These waves, which are generated as turbulent eddies interact with the stratified ambient, were also observed at low Reynolds number and are described in detail by Taylor and Sarkar (2007a). The importance of radiated energy by turbulence-generated internal waves to the mixed layer growth has been discussed in several previous studies (Linden (1975); E and Hopfinger (1986)). Figure IV.15 shows the vertical energy flux, $\langle p'w' \rangle$ normalized by the integrated dissipation and the integrated buoyancy flux. Taylor and Sarkar (2007a) made a similar comparison for a lower Reynolds number boundary layer and found that the vertical energy flux was much smaller than the integrated dissipation, but

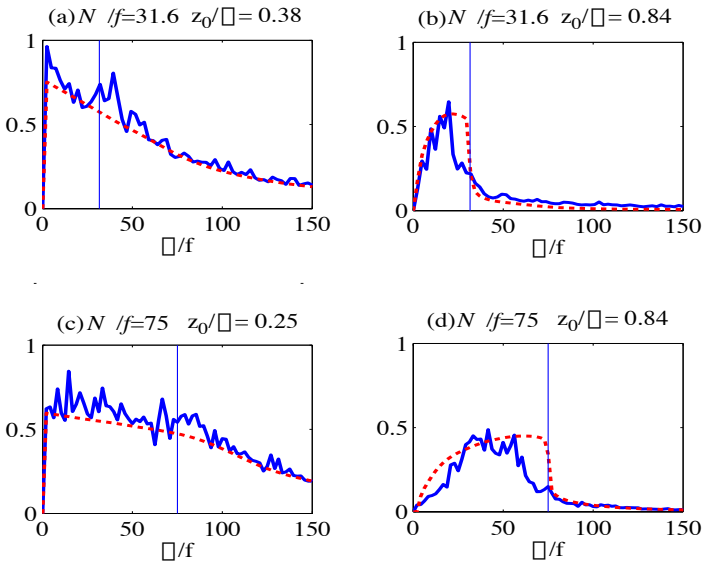

Figure IV.16: Vertical energy flux normalized by (a) the integrated turbulent dissipation, and (b) the integrated buoyancy flux. Vertical lines show N/f

the same order as the integrated buoyancy flux. Specifically, they found that the ratio of vertical energy flux to integrated dissipation at the top of the pynocline was between 0.01-0.03, while the ratio of the vertical energy flux to the integrated buoyancy flux at the same location was between 0.5-1. The present results are generally consistent with those of Taylor and Sarkar (2007a) but the vertical energy flux is about a factor of two smaller in the present study.

Taylor and Sarkar (2007a) found that the internal wave energy spectrum in the outer layer could be explained by damping of the waves based on the wavenumber and vertical propagation speed for a particular frequency. Given a turbulent spectrum that was assumed to be characteristic of the waves upon generation, they showed that the viscous decay term in the fully-nonlinear numerical simulations resulted in outer layer waves in a relatively narrow frequency range. Viscous ray-tracing was used to show that the vertical velocity amplitude for a

specific frequency and wavenumber can be written

$$A(k_h,\omega,z) = A_0(k_h,\omega,z_0)\frac{|\mathbf{k}_0|}{|\mathbf{k}|}\ exp\left[\frac{-\nu\omega}{k_h\left(\omega^2-f^2\right)^{1/2}}\int_{z_0}^{z}|\mathbf{k}|^4(N^2-\omega^2)^{-1/2}dz'\right], \tag{IV.21}$$

where k_0 and A_0 are the wavenumber and wave amplitude at $z = z_0$ in the generation region. Since the molecular viscosity and diffusivity used by Taylor and Sarkar were two orders of magnitude smaller than the present values, it is of interest to evaluate their viscous internal wave model using the present high Reynolds number simulations. The viscous decay model is compared to the observed frequency spectra of the outer layer waves in Figure IV.16. In order to compare the predicted wave amplitude to the simulations it is convenient to consider the spectral distribution of dw/dz which is estimated by multiplying $A(k_h,\omega,z)$ by the vertical wavenumber

$$m = -k_H[\frac{N^2-\omega^2}{\omega^2-f^2}]^{1/2}. \tag{IV.22}$$

Since the subgrid-scale eddy viscosity that is used as part of the LES model is not negligible compared to the molecular viscosity in the outer layer, we have used $\nu + \nu_{sgs}$ in Eq. (IV.21). Figure IV.16 shows the spectral amplitudes of $\partial w'/\partial z$ normalized by δ and u_*. In order to show the combined contributions of all values of k_H, the square root of the sum of the squared amplitudes of $\partial w'/\partial z$ is shown as a function of ω/f. The left panels show the observed spectra at $z = z_0$, corresponding to a location just above the pycnocline (solid line). The spectrum at $z = z_0$ was then smoothed and used as input (dashed line) to the viscous decay model. The viscous decay model predicts the amplitude of each frequency and wavenumber component after propagating a distance $z - z_0$. The predicted amplitude from the model is compared to the observed amplitudes from the numerical simulation in the panels on the right, corresponding to a location at the top of the computational domain. The qualitative agreement between the observed and predicted wave amplitudes is relatively good; in particular, the decrease in amplitude of the low frequency waves is captured well. At high frequencies, as $\omega \to N$, the observed wave amplitudes are significantly lower than the model prediction. It is possible

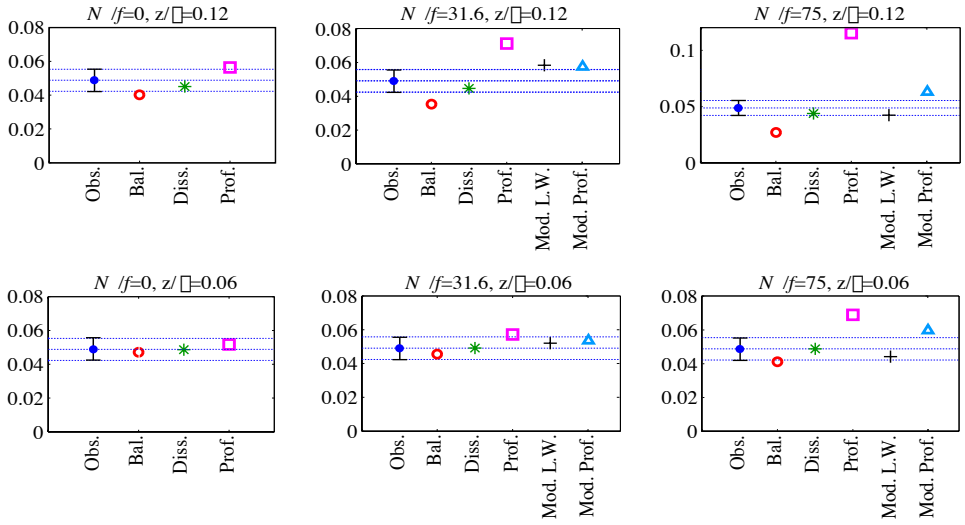

Figure IV.17: Estimates of the friction velocity using several different methods at two locations in the mixed layer. Horizontal lines show the friction velocity observed in the simulations and plus and minus one standard deviation of the timeseries. Models from left to right in each panel are: the balance method Eq. (IV.24), the dissipation method Eq. (IV.25), the profile method Eq. (IV.23), the modified law-of-the-wall Eq. (IV.26), and the modified profile method Eq. (IV.30). Note that when the flow is unstratified, the modified law-of-the-wall and the modified profile method are identical to the profile method.

that this is the result of nonlinear wave-wave and wave-mean flow interactions that are neglected in the linear viscous model.

IV.7 Evaluating methods for estimating the wall stress

Since we have high resolution velocity and density profiles through a steady Ekman layer, we are able to evaluate the performance of several methods for estimating the friction velocity from observational data under idealized conditions.

The profile method estimates the friction velocity by assuming that the mean shear follows the unstratified law-of-the-wall, to give

$$u_{*,p} = \kappa z \frac{d\langle u \rangle}{dz}. \tag{IV.23}$$

When the turbulent dissipation is measured, the friction velocity can be estimated by assuming a balance between the turbulent production and dissipation. As shown in the inset of Figure IV.10, the production and dissipation are in approximate balance throughout the mixed layer. The so-called balance method assumes a production and dissipation balance using the observed mean shear and disspation rate, so that the friction velocity is

$$u_{*,b} = \sqrt{\epsilon / \frac{d\langle u \rangle}{dz}}. \tag{IV.24}$$

A third method called the dissipation method can be formed through a combination of the profile and balance methods by using the production and dissipation balance and assuming that the mean shear follows the unstratified law-of-the-wall. The friction velocity predicted by this method takes the form

$$u_{*,\epsilon} = \langle \epsilon \kappa z \rangle^{1/3}. \tag{IV.25}$$

Estimates from these models are compared to the observed friction velocity in Figure IV.17. In order to illustrate the temporal variability in the friction velocity, plus and minus one standard deviation is also shown. As has been found by previous studies (Perlin et al. (2005); Johnson et al. (1994); Lien and Sanford (2004)), the performance of the friction velocity estimates depends on the location of the observed shear, and dissipation. Therefore, estimates of the friction velocity are shown using the mean shear and/or the dissipation rate at two heights, $z/\delta = 0.06$ and $z/\delta = 0.12$, which correspond to about 1.98 *mab* and 3.96 *mab*, respectively. When the outer flow is unstratified, as shown in the left column of Figure IV.17, all of the above methods provide a reasonable estimate of the friction velocity. However, when the outer layer is stratified, the profile method and to a lesser degree

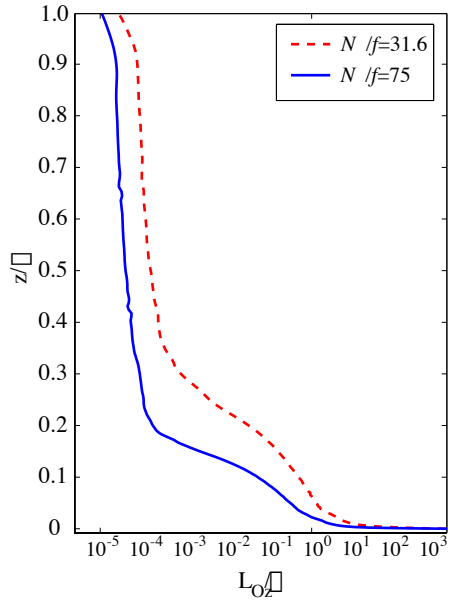

Figure IV.18: Ozmidov scale

the balance method do *not* provide accurate estimates for the friction velocity. The dissipation method appears to be the most accurate of the three methods in the mixed layer. However, since direct measurements of the dissipation rate are not always available from observations, it is desirable to have a method for estimating the friction velocity using more commonly measured quantities such as velocity and density profiles.

The error in the profile method is the result of the increase in the mean shear with stratification as was seen in Figure IV.8 that is not accounted for by the traditional law-of-the-wall. A modified law-of-the-wall that accounts for the increase in mean shear at the top of a stratified boundary layer was proposed by Perlin et al. (2005). They proposed that the mean velocity gradient could be modeled as

$$\frac{d < u >}{dz} = \frac{u_*}{l_p}, \tag{IV.26}$$

where

$$l_p = \kappa z(1 - z/h_d), \tag{IV.27}$$

and h_d is a measure of the boundary layer depth which is limited by stratification.

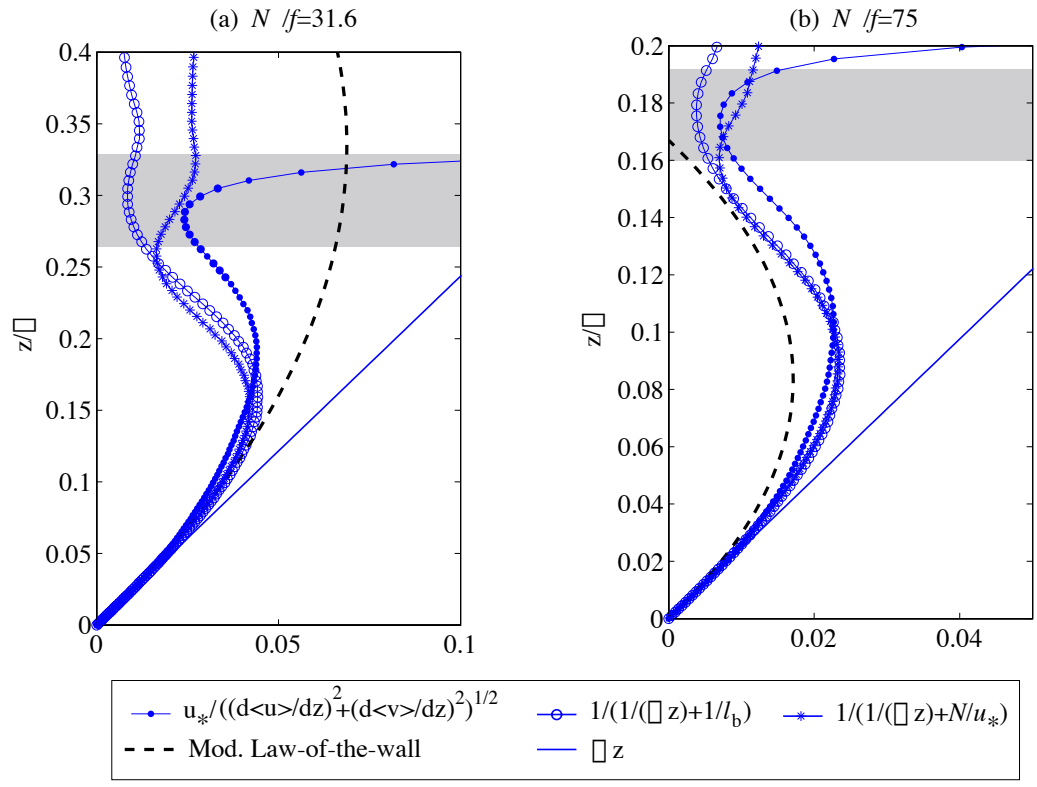

Figure IV.19: Lengthscale profile derived from the mean shear from the LES (line with filled circles) compared to several model profiles. Shaded regions show where $d\langle\rho\rangle/dz > d\langle\rho\rangle/dz_\infty$

In order to use Eq. (IV.26) to predict the friction velocity for a given velocity profile, an estimate for h_d must first be obtained. Perlin et al. (2005) proposed using the Ozmidov scale, $l_{Oz} = \sqrt{\epsilon/N^3}$, at the top of the mixed layer to set h_d. We have used a similar criteria to evaluate this method in Figure IV.17. Specifically the mixed layer height, d, is defined as the location where $\Delta\rho/d = 0.01 d\rho/dz_\infty$. Then h_d is set so that $l_p = l_{Oz}$ at $z = d$.

It is evident from Figure IV.17 that the modified law-of-the-wall provides a significant improvement over the profile method. However, as shown in Figure V.10, the Ozmidov scale varies very rapidly between the mixed layer and the pycnocline, so the estimate of h_d depends strongly on the definition of the mixed

layer depth. In the case when $N_\infty/f = 31.6$ the rapid change in the Ozmidov scale leads to $h_d = 0.67\delta$ which is significantly larger than the boundary layer height, $h = 0.215\delta$. As a result, l_p is significantly larger than the observed shear lengthscale as shown in Figure IV.19. An alternative method to account for the decrease in the lengthscale with stratification was proposed by Brost and Wyngaard (1978) and can be written

$$\frac{1}{l} = \frac{1}{\kappa z} + \frac{1}{l_b}, \tag{IV.28}$$

where $l_b = C_b \left\langle w'w' \right\rangle^{1/2} / N$ is a buoyancy lengthscale. Nieuwstadt (1984) suggested the value of $C_b = 1.69$ which was consistent with his local scaling theory. This lengthscale is shown in Figure IV.19 and compares favorably to the observed shear lengthscale below the center of the pycnocline. Practically, it is difficult to measure the vertical velocity, especially in the boundary layer where it cannot be deduced from isopycnal displacements. We have found that most of the decrease in the lengthscale with height is due to an increase in the local stratification rather than a change in the turbulent velocity. An alternative lengthscale can then be formed by replacing the vertical turbulent velocity with the friction velocity:

$$\frac{1}{l} = \frac{1}{\kappa z} + \frac{N}{C_b u_*}. \tag{IV.29}$$

This simplified form still provides a reasonable estimate for the shear lengthscale as shown in Figure IV.19. The friction velocity can then be recovered from the mean velocity and density profile without the need for direct turbulence measurements, specifically

$$u_{*,m-p} = \kappa z \left[\left(\left(\frac{d \left\langle u \right\rangle}{dz} \right)^2 + \left(\frac{d \left\langle v \right\rangle}{dz} \right)^2 \right)^{1/2} - N \right], \tag{IV.30}$$

where we have taken $C_b = 1$. In the limit of an unstratified boundary layer, this method becomes equivalent to the profile method, so we will refer to this as the modified profile (m-p) method. Estimates of the friction velocity based on Eq. (IV.30) are shown as triangles in Figure IV.17. While the estimated friction velocity is somewhat large, the modified profile method provides a significant

improvement over the profile method and is comparable to the modified law-of-the-wall. It is worth noting that since stratification effects enter into the modified law-of-the-wall through h_d in Eq. IV.27 which is independent of z, stratification effects are non-local in this model. By comparison, the modified profile method is the result of a local balance between shear and stratification.

IV.8 Conclusions

We have examined a benthic Ekman layer formed when a uniformly stratified, steady geostrophic flow encounters a flat, adiabatic seafloor. The thermal field rapidly develops a three-layer structure with a well-mixed region near the wall separated from the uniformly stratified outer layer by a pycnocline. The outer layer is populated by upward propagating internal waves that are generated by the boundary layer turbulence. After the initial spinup, a quasi-steady state is reached, characterized by a slow mixed layer growth and a nearly constant density gradient in the pycnocline. When the strength of the outer layer stratification is increased, the wall stress increases slightly, but the boundary layer thickness decreases significantly. The structure of the boundary layer is clearly confined by stratification as evidenced by the Reynolds stress, turbulent heat flux, and turning angle which all nearly vanish above the pycnocline. Since the Ekman transport balances the wall stress in the integrated streamwise momentum equation, and the wall stress remains relatively constant, the increase in outer layer stratification is accompanied by an increase in the magnitude of the cross-stream velocity.

The increased cross-stream velocity in the mixed layer leads to a broadening of the Ekman spiral. The rate of veering in the mixed layer is a function of z but does not depend strongly on the external stratification. When the stratification is increased and the boundary layer is thinner and the surface turning angle is larger, the amount of veering that occurs in the pycnocline increases. This finding is consistent with the results of Weatherly and Martin (1978) who found that most

of the veering occurred in the pycnocline using one-dimensional simulations. We have also found that when the outer layer stratification is large, the rapid rate of turning in the pycnocline causes the mean velocity and the mean shear to be maximum at the same location near the center of the pycnocline.

An interesting feature of the observed Ekman layer structure is the appearance of local shear instabilities above the pycnocline despite the fact that the mean shear is stable with respect to the local stratification. Between 10% and 25% of the vertical profiles exhibit a local gradient Richardson number less than 0.25. A similar observation has been made in terms of the occurrence of overturning events. Mixing during these events is significant and appears to cause a local minimum in the density gradient above the pycnocline. Analysis of events with $Ri_g < 0.25$ at a height above the pycnocline indicates that these events are more likely to be associated with a below average density gradient than an above average shear.

In the outer layer, turbulence-generated internal waves are observed radiating away from the boundary layer. The vertical energy flux associated with these waves is negligible compared to the turbulent dissipation integrated through the boundary layer. This is not surprising since most of the dissipation occurs near the seafloor where the flow is unstratified. However, the vertical energy flux at the top of the boundary layer is nearly half of the integrated buoyancy flux. This finding is consistent with a study at a lower Reynolds number by Taylor and Sarkar (2007a) and implies that the turbulence-generated internal waves may remove enough energy from the boundary layer to affect the growth rate of the mixed layer. The viscous internal wave model of Taylor and Sarkar (2007a) has been applied using the combined molecular and turbulent viscosity to estimate the decay rate of the turbulence-generated internal waves. The model qualitatively captures the decay of low frequency waves, but overestimates the amplitude of high frequency waves.

As was seen in previous studies (e.g. Perlin et al. (2005); Johnson et al. (1994)), an increase in the mean shear has been observed at the top of the mixed layer. The increase in mean shear with respect to an unstratified boundary layer

can lead to significant errors in the friction velocity estimated from observed velocity profiles using the profile method. It has been uncertain whether this increase in the mean shear could be explained in terms of the *local* stratification. Since the unstratified logarithmic law appears to hold very close to the wall, the profile method is adequate in principle if the mean velocity very near the wall can be obtained. However, this is often difficult or impossible in practice. We have evaluated the performance of a variety of techniques for estimating the friction velocity given mean quantities at various heights in the mixed layer. Since the turbulent production and dissipation are the dominant terms in the turbulent kinetic energy equation throughout the mixed layer, the dissipation method agrees very well with the observed friction velocity. The modified law-of-the-wall, proposed by Perlin et al. (2005) shows considerable improvement over the standard profile method, especially near the top of the mixed layer. However, like the balance and dissipation methods, the modified law-of-the-wall requires knowledge of the turbulent dissipation rate. Direct observation of the dissipation rate is difficult, especially in active turbulent regions since it involves small-scale velocity gradients. When such information is not available, it is desirable to have an alternative method for estimating the friction velocity. We have proposed a direct modification to the profile method based on the local stratification that shows significant improvement over the unstratified profile method.

IV.9 Acknowledgments

The support of grant N00014-05-1-0334 from ONR Physical Oceanography, program manager Dr. Scott Harper, is gratefully acknowledged.

V Turbulence-generated Internal Gravity Waves

V.1 Introduction

When turbulence is present in a stably stratified fluid, internal gravity waves are often created and radiate energy away from the source region. Turbulence-generated internal waves have been observed in a variety of flows: wakes (Bonneton et al. (1993); Gourlay et al. (2001); Spedding (2002); Diamessis et al. (2005)), shear layers (Sutherland and Linden (1998); Sutherland et al. (1994); Basak and Sarkar (2006)), in the lee of topography (Aguilar and Sutherland (2006)), grid-generated turbulence (Linden (1975); E and Hopfinger (1986); Dohan and Sutherland (2003, 2005)) and gravity currents (Flynn and Sutherland (2004)). The turbulence that generates the internal waves may be associated with an essentially well-mixed region (e.g. grid turbulence) or a stratified region (e.g. wakes and shear layers). This study will be focused on an example of the former case. Turbulence-generated internal waves may be important to the flow evolution since they are capable of extracting energy and momentum from a forced region, propagating to another nearby or remote location, and depositing their energy and momentum through a variety of possible mechanisms (e.g. wave breaking, wave/wave interactions, critical layer absorption, etc.)

In the ocean and in the atmosphere, one important site of intense turbulence is near boundaries. The problem of a turbulent region driven by internal

waves incident on a boundary has been considered in several studies (Slinn and Riley (1998); Thorpe (2001); D'Asaro (1982)), but it appears that the problem of internal waves generated by boundary layer turbulence has not been invesitgated. Since boundary regions are a hotspot of kinetic energy dissipation (Garrett and St. Laurent (2002); Gregg et al. (1999)), if the waves are able to extract even a fraction of the kinetic energy from near the boundary and transfer it to a less energetic region, they may play an important role in the global energy budget.

There is some suggestive evidence of turbulence-generated internal waves in the observations of Moum et al. (1992) from the upper equatorial ocean. A weakly stratified turbulent surface layer was diurnally forced by a combination of a wind stress and surface heat flux. Large amplitude internal waves were observed in the thermocline with a narrow range of wavenumbers. These waves were observed during times of strong wind and unstable convective forcing, suggesting that they may have been forced by turbulent motions near the sea surface. In addition, the turbulent dissipation rate in the thermocline was found to be correlated to the level of internal wave activity.

There is evidence that internal gravity waves are important to atmospheric dynamics, see Fritts and Alexander (2003) for a review. Gravity waves affect the large-scale dynamics in the mesosphere and stratosphere through the so-called "wave-drag" exerted on the mean flow (Holton and Alexander (2000)). Sources of turbulence-generated internal waves in the atmosphere include convective motions and shear instabilities (Fritts and Alexander (2003)). Buhler et al. (1999) and Buhler and McIntyre (1999) considered the generation of internal waves by an localized unstable shear layer at the top of the jet stream. They used ray tracing to estimate the transmission of waves into the mesosphere and concluded that these waves may be an important source term in the local momentum budget.

The importance of turbulence-generated internal waves to the growth of a mixed region was considered by Linden (1975). An oscillating grid was used to generate a turbulent mixed layer above a density stratified region. As the mixed

layer deepened, a pycnocline developed with a density gradient up to three times the value in the outer region. Internal waves were observed propagating away from the mixed region when the outer layer had a linear stratification instead of being homogeneous. The relative importance of the internal waves was quantified by comparing the rate of change of potential energy to the internal wave energy flux, and it was found that the presence of propagating internal waves may reduce the mixed layer growth by up to 50%. A different conclusion was reached by E and Hopfinger (1986) who also considered shear-free grid generated turbulence. With two initial conditions, a uniformly stratified fluid and a two-layer system, they found that the rate of mixed layer growth depends on the density jump at the interface, but not on the density structure away from the mixed region. Based on this observation, and an estimate of the internal wave energy flux relative to the turbulence flux, they concluded that radiated internal waves, which exist only in the continuously stratified case, do not significantly affect the growth of the mixed layer.

As a mixed region forms in a stratified fluid, it is common for a region of strong density gradient, or pycnocline, to form at the edge of the mixed layer. Since the density gradient in the pycnocline forms a local maximum, it is possible for high frequency waves to become isolated in this layer. Piat and Hopfinger (1981) considered a turbulent boundary layer in a fluid with a two-layer thermal structure. They found that the mean shear and *rms* velocity increased at the thermal interface. Internal waves traveling along the interface had a time-lag correlation between vertical velocity and temperature fluctuation that was 90^o out of phase. The authors reported that the waves occured in bursts generated by the interactions of turbulent eddies with the interface. The frequency of the observed waves was approximately equal to the buoyancy frequency at the interface.

Since the turbulent region that provides energy to the wave field is composed of many spatial and temporal scales, it is perhaps surprising that the turbulence-generated internal waves are often associated with a relatively nar-

row frequency range that is proportional to the local buoyancy frequency. The angle made by the group velocity vector and the vertical direction is set from the dispersion relation, which for non-rotating, linear internal gravity waves is $\omega = N cos\,\Theta$, where ω is the intrinsic frequency, N is the background buoyancy (or Brunt-Väisälä) frequency, and Θ is the angle made between the wavenumber vector and the horizontal axis. Therefore, waves with a particular frequency are also associated with a characteristic angle of propagation. Previous studies of turbulence-generated internal waves have generally found that $35^o < \Theta < 60^o$. Several explanations have been given for this frequency selection as discussed below.

Sutherland and Linden (1998) conducted a laboratory experiment with stratified fluid flowing over a vertical barrier. A turbulent shear layer formed in the wake of the barrier and internal waves were observed propagating away from the shear layer through the uniformly stratified surrounding fluid. The largest amplitude waves were associated with an angle of propagation in the range $45^o < \Theta < 60^o$. The authors noted that the vertical component of the group velocity is maximum for waves with $\Theta = 45^o$ (for a fixed wavelength) and suggested that if turbulence in the mixed region had a uniform frequency distribution, waves with this angle may optimally transport energy away from the mixed region. They also suggested that the radiated internal waves with $\Theta = 45^o$ may modify the mean flow so as to favor generation of waves with their own frequency.

An alternative hypothesis for the narrow frequency range observed in laboratory experiments was proposed by Sutherland (2001). He derived stability criteria for internal waves for two types of instabilities. For low frequency waves, convective overturning provides the most stringent stability criteria based on the wave amplitude. For high frequency waves the lowest critical wave amplitude is based on resonant interactions between the wave and its wave-induced mean flow, a process that steepens the waves until they become statically unstable. Based on the predicted stability criteria for these two mechanisms, it was shown

that the largest critical amplitude corresponds to waves propagating at $\Theta = 45^o$. Sutherland (2001) hypothesized that since other angles would become unstable at a lower amplitude, these instability mechanisms may explain the frequency selection observed in laboratory experiments.

Dohan and Sutherland (2003) described laboratory experiments using an oscillating grid to create a turbulent mixed region in a uniformly stratified tank. A novel visualization technique was used in order to examine the internal waves in detail. The background buoyancy frequency was varied by over a factor of 4 and in all cases the frequency of the waves was such that the vertical angle of propagation was between $42^o < \Theta < 55^o$. The authors explored two explanations for the narrow range of observed propagation angles. The first was that waves at frequencies other than those observed would become unstable through the mechanisms proposed by Sutherland (2001). Since the amplitudes of the waves was only about 25% of that predicted for instability, this explanation was deemed unlikely. They concluded that a better explanation was a resonant feedback between the waves and turbulence. Since waves at 35^o have a maximum vertical energy flux and waves at 45^o have a maximum momentum flux, they speculated that waves near these frequencies may extract energy from the turbulent region in an optimal way. Dohan and Sutherland (2005) compared a two-dimensional numerical simulation to laboratory experiments similar to their previous study. Turbulence in the simulations was generated by a small-scale forcing term with a randomized Gaussian spectrum in the horizontal and vertical directions, in addition to a large-scale counter-rotating vortex pair. The characteristic length scale of the turbulence-generated internal waves was between those associated with the large and small-scale forcing. The range of Θ in the simulations was similar to what had been observed in the laboratory experiments.

Keeler et al. (2005) reported surface manifestations of internal waves generated by turbulent motions above a submerged municipal wastewater outfall. Based on observations from previous laboratory experiments, the authors hypoth-

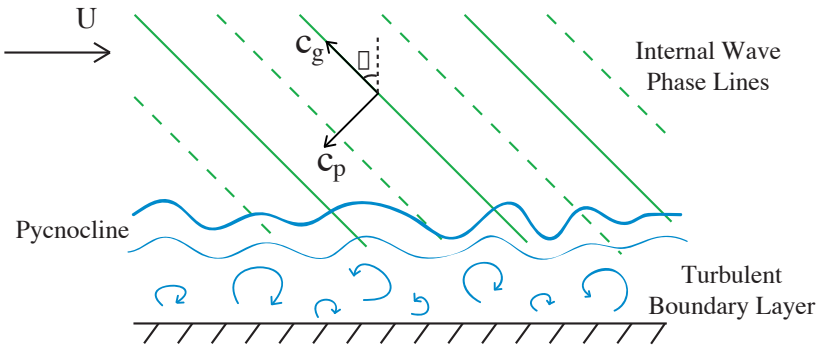

Figure V.1: Cartoon of internal wave exitation from a turbulent boundary layer. The group and phase velocity are shown relative to the free stream.

esized that the internal waves propagated upwards with $\Theta \approx 45^o$. Gibson et al. (2006) proposed an explanation for the selection of high-frequency waves. First, energy is transferred from turbulent motions to internal waves through fossilization at the buoyancy frequency. These waves do not propagate vertically since the vertical component of the group velocity for waves at $\omega = N$ vanishes. Frictional forces were then invoked to explain a reduction in the frequency of the waves which are then able to propagate vertically. The length scale associated with these waves was predicted to be proportional to the Ozmidov scale at the time of fossilization.

The present study is based on simulations of a bottom Ekman layer with a uniform density stratification outside the boundary layer as shown in the schematic of Figure V.1. The focus of this paper will be on the internal waves excited by turbulent motions in the bottom boundary layer. While previous laboratory and 2-D numerical studies have considered the generation of internal waves from a well-mixed turbulent region, this has not yet been examined in the case of boundary layers. The three-dimensional structure of the waves will be examined, and compared with the general characteristics of turbulence-generated internal waves previously observed in laboratory experiments. An attempt to explain the amplitude and frequency of the radiated waves in our simulations will be offered. The importance of the radiated internal waves to the dynamics of the boundary layer

will also be addressed by comparing the internal wave energy flux to the integrated turbulent dissipation rate and the integrated buoyancy flux.

V.2 Formulation

The turbulent boundary layer that is considered here is generated when a steady flow in geostrophic balance encounters a smooth, flat wall. Near the wall, where the turbulent viscosity contributes to the leading order momentum balance, the flow turns in the direction of the pressure gradient, forming the well-known Ekman spiral. A constant density gradient is applied as the upper boundary condition while the density gradient is set to zero at the wall. Since a large eddy simulation is used to examine this flow, the filtered governing equations are numerically integrated in time. Using the friction velocity, u_*, the turbulent Ekman layer depth, $\delta = u_*/f$, and the outer layer density gradient, $d\rho/dz_\infty$, the filtered nondimensional incompressible governing equations can be written:

$$\frac{\partial \overline{\mathbf{u}}}{\partial t} + \overline{\mathbf{u}} \cdot \nabla \overline{\mathbf{u}} = -\frac{1}{\rho_0}\nabla \overline{p'} + f\hat{\mathbf{k}} \times (U_\infty \hat{\mathbf{i}} - \overline{\mathbf{u}}) - Ri_* \frac{\overline{\rho'}}{\rho_0}\hat{\mathbf{k}} + \frac{1}{Re_*}\nabla^2 \overline{\mathbf{u}} - \nabla \cdot \boldsymbol{\tau}, \quad \text{(V.1)}$$

$$\frac{\partial \overline{\rho'}}{\partial t} + \overline{\mathbf{u}} \cdot \nabla \overline{\rho'} = \frac{1}{Re_* Pr}\nabla^2 \overline{\rho'} - \nabla \cdot \boldsymbol{\lambda}, \quad \text{(V.2)}$$

$$\nabla \cdot \overline{\mathbf{u}} = 0, \quad \text{(V.3)}$$

where

$$Re_* = \frac{u_* \delta}{\nu}, \quad Ri_* = -\frac{g}{\rho_0}\frac{d\rho}{dz}_\infty \frac{\delta^2}{u_*^2} = \frac{N_\infty^2}{f^2}, \quad Pr = \frac{\nu}{\kappa}. \quad \text{(V.4)}$$

Here, ρ_0 is the constant density which has been used to apply the Boussinesq approximation, ν is the molecular kinematic viscosity, κ is the molecular diffusivity, f is the Coriolis parameter, N_∞ is the free stream buoyancy frequency, and $\boldsymbol{\tau}$ and $\boldsymbol{\lambda}$ are the subgrid-scale stress and density flux, respectively. The parameters considered in this study are listed in Table 1. Density changes are assumed to be caused by temperature variation in water, motivating the choice of Prandtl number, $Pr = 5$. We have performed simulations at three different values of Ri_*,

Table V.1: Physical Parameters: Subscript h in the case number denotes a higher Reynolds number

Simulation	Ri_*	N_∞/f	Re_*	Pr
1	0	0	960	5
1_h	0	0	1920	
2	100	10	960	
2_h	100	10	1920	
3	1000	31.6	960	
3_h	1000	31.6	1920	

equivalent to changing the free-stream temperature gradient, and at two Reynolds numbers. For the cases with $Ri_* = 0$ the temperature acts like a passive scalar since the temperature and momentum equations are decoupled. For comparison with oceanographic conditions, observations of the bottom boundary layer over the Oregon shelf by Perlin et al. (2007) provide estimates of $Re_* = 60,000$ and $N_\infty/f = 75$. Therefore, the Reynolds number considered in the present study is much smaller than that found in the ocean while the stratification levels are comparable.

The vertical domain size is 8δ, significantly larger than the boundary layer thickness which is about 0.5δ for an unstratified turbulent Ekman layer (Coleman et al. (1990)). The large vertical domain provides a region above the boundary layer where the internal wave propagation can be examined. In order to allow waves to freely exit the top of the domain, an open boundary condition has been used with a combination of a sponge layer and a radiation condition (Klemp and Durran (1983)). The horizontal boundaries are periodic, which is consistent with the assumption that the flow is statistically homogeneous in the horizontal plane. A horizontal domain size of 4δ has been chosen to be sufficiently large so that the autocorrelation in the turbulent boundary layer is small at the scale of the domain size, limiting the energy in spurious box modes.

In order to simulate this flow at larger Reynolds numbers than would otherwise be possible, a near-wall model large eddy simulation (NWM-LES) has been used. The LES is based on a mixed model that consists of eddy viscosity and scale-similar components, and uses the dynamic procedure of Germano et al. (1991) to evaluate the Smagorinsky coefficient. This subgrid-scale model has been shown to perform well for stratified flow (Armenio and Sarkar (2002); Taylor et al. (2005)). The near-wall model alleviates the need to resolve the viscous scales near the wall, allowing a coarser grid than would otherwise be possible. The near-wall model that is used here is similar to that developed by Schumann (1975), Grotzbach (1987), and Piomelli et al. (1989), but has been modified for rotating flow. It assumes that the magnitude of the horizontal velocity near the wall follows a logarithmic law which has been confirmed by the authors using direct numerical simulation (DNS). We have found that the near-wall model performs well at the Reynolds numbers listed in Table 1, but does not adequately capture the mean velocity profile for simulations at a very large, geophysically relevant Reynolds number on a coarse grid. Spectral collocation is used in the horizontal directions, while a 2nd-order finite difference method on a staggered grid is used in the vertical direction. The grid that has been used for these simulations is 96 x 96 x 112 cells for a domain size of 4δ x 4δ x 8δ in the x, y, and z directions respectively, and 16 grid points dedicated to the sponge region from $8\delta - 10\delta$. The simulations are continued for about $tf = 30$ time units, and the time-step is $tf = 10^{-3}$, so that the integration time is quite long, about 30,000 time-steps. The integration time in buoyancy time units corresponds to $Nt = 300$ when $Ri_* = 100$, and $Nt = 950$ when $Ri_* = 1000$.

V.3 Summary of the boundary layer evolution

In order to initialize each case, a simulation of an unstratified turbulent Ekman layer was conducted until the mean velocity profile reached a steady

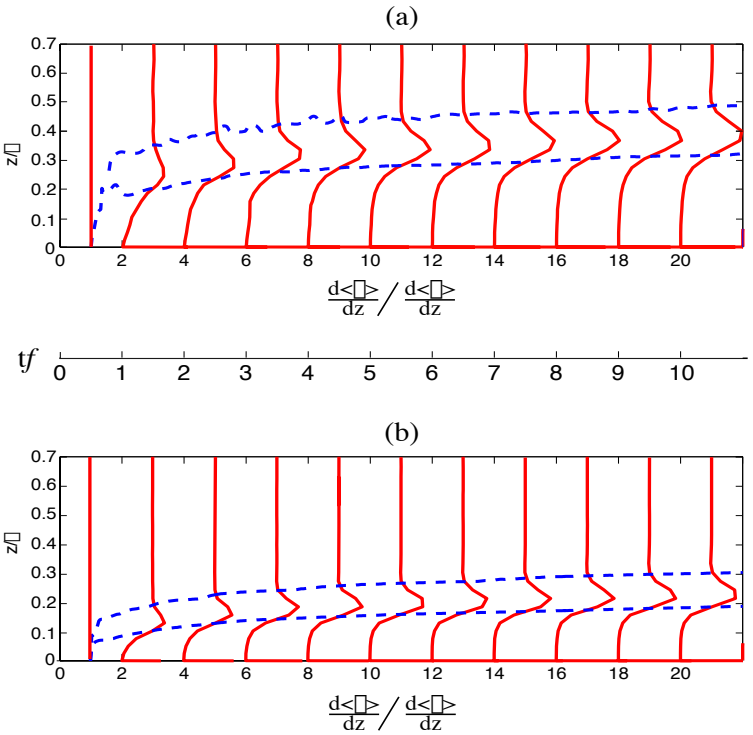

Figure V.2: Spinup of the plane averaged temperature gradient for $Re_* = 960$ (a) $Ri_* = 100$, (b)$Ri_* = 1000$. Profiles of the temperature gradient are shown every $tf = 1$ and offset by 2 * $d\langle\theta\rangle/dz_\infty$. Dashed lines show the locations where $d\langle\theta\rangle/dz = 1$ representing the edges of the pycnocline.

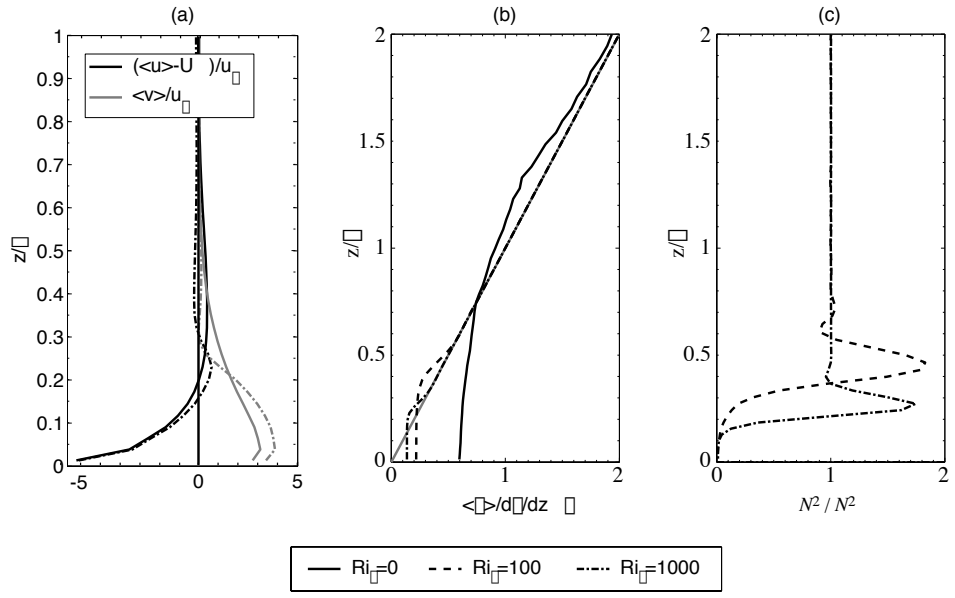

Figure V.3: Plane averaged profiles at $tf = 20$ and $Re_* = 960$: (a) velocity, (b) temperature, and (c) square of buoyancy frequency. For clarity, the $Ri_* = 100$ profile is not shown in part (a). The gray line in (b) shows the initial linear temperature profile.

state. The three-dimensional velocity field from the unstratified simulation was then used as the initial velocity field in the stratified simulations, while the temperature field was initialized with a linear, undisturbed profile. In each case the temperature profile in the boundary layer is mixed rapidly during the initial stage, and the thickness of the boundary layer is strongly influenced by the strength of the imposed statification. The development of the temperature gradient is shown in Figure V.2 where angled brackets denote an average over the horizontal plane. As the mixed layer grows in time, a pycnocline forms above the boundary layer with a mean temperature gradient up to twice the initial value. Dashed lines in Figure V.2 show the location where the temperature gradient is equal to the outer value, thereby illustrating the upper and lower bounds of the pycnocline.

After about $tf = 6$ time units, each case reaches a quasi-steady state where the mean velocity profile is steady, and the mixed layer grows slowly in

time. This slow growth of the temperature field is persistent even at late times. Figure V.3 shows the plane averaged velocity and temperature profiles at $tf = 20$. Only simulations with $Re_* = 960$ are shown, but these profiles are similar at the larger Reynolds number. The thickness of the bottom mixed layer decreases with increasing Ri_*, as the amount of energy required to mix the profile to a given height increases. The velocity profiles are also affected by Ri_*. The mean velocity gradient in the pycnocline increases with increasing stratification and most of the Ekman transport ($\int \langle v \rangle \, dz'$) occurs in the mixed layer. It can be shown that the Ekman transport balances the streamwise wall stress in the vertically integrated momentum equation. Therefore, if the wall stress is constant (which it is in our simulations) but the Ekman layer depth decreases, the magnitude of $\langle v \rangle$ should increase accordingly.

V.4 Observations of turbulence generated internal waves

The internal wave field generated by the boundary layer at quasi-steady state is shown through instantaneous x-z slices of w' and $\partial w'/\partial z$ in Figure V.4 for simulation 3. We have found that the vertical velocity field contains a significant non-propagating component in the outer layer and that $\partial w'/\partial z$ more clearly shows the phase lines of the propagating waves which slant up and to the left. For internal waves, the group velocity, $\mathbf{c}_g$, is perpendicular to the wavenumber vector and parallel to the phase lines. Note that the direction of the phase lines is the same as would be seen for topographically generated waves with a flow in the positive x-direction. It is visually evident from Figure V.4(b) that just above the pycnocline, for $0.5 < z/\delta < 1.5$, there are internal waves with phase lines forming a larger angle with the vertical direction. Since the dispersion relation for linear internal waves is $\omega = N cos\Theta$, these waves have a lower frequency.

Since the only source of internal wave generation is the turbulent bound-

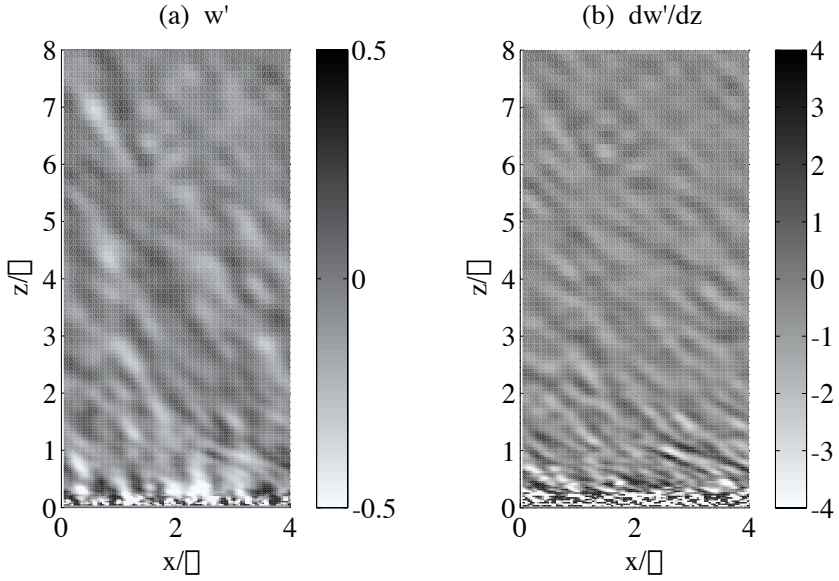

Figure V.4: Instantaneous vertical velocity, $Ri_* = 1000$, $Re_* = 960$, $tf = 20$. At this time, the maximum temperature gradient in the pycnocline occurs at about 0.275 δ.

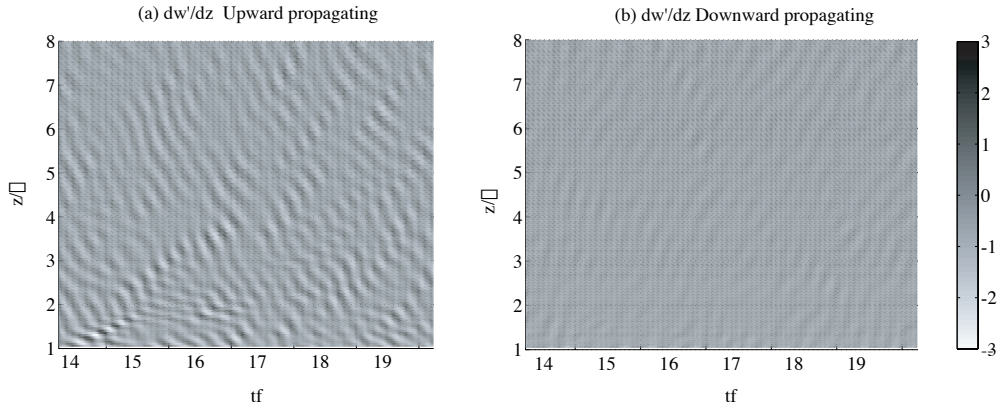

Figure V.5: Upward and downward propagating wave components in a frame moving with U_∞, for $Ri_* = 1000$ and $Re_* = 960$

ary layer, any waves external to the boundary layer and with a downward group velocity must be due to spurious reflections. The level of energy reflected from the upper boundary can be quantified by decomposing the spectrum into upward and downward propagating parts. This is done here by observing $\partial w'/\partial z$ in a coordinate frame moving with U_∞ and transforming the timeseries for $1 < z/\delta < 8$ into frequency and wavenumber space. Since internal waves with an upward propagating group velocity are associated with downward pointing phase lines, the amplitudes in quadrants II and IV of frequency, vertical wavenumber space (with $\omega > 0$, $m < 0$, and $\omega < 0$, $m > 0$ respectively) are retained for the upward propagating part. An inverse Fourier transform then yields the timeseries in physical space for internal waves with upward energy propagation (Pinkel (2005)). To obtain the reflected waves, the procedure is the same with quadrants I and III kept. The decomposition into waves with upward and downward propagating energy is shown in Figure V.5 for simulation 3. About 3% of the total $(\partial w'/\partial z)^2$ field consists of downward propagating waves. A similar decomposition for the w' field (not shown) demonstrates that about 6% of the vertical kinetic energy $(1/2w'^2)$ is associated with downward energy propagation. This demonstrates that the open boundary condition used at the top of the domain performs well.

The most energetic waves observed in the pycnocline and the outer layer are qualitatively different. We can examine the contributions to the internal wave energy flux by considering the phase angle of the p', w' co-spectrum. With the co-spectrum, $C_{p'w'}(k,z,t)$ and quadrature spectrum, $Q_{p'w'}(k,z,t)$ defined as the real and imaginary parts, respectively, of

$$\sum_l \hat{w}'(k,l,z,t)\hat{p}'^*(k,l,z,t), \tag{V.5}$$

the phase angle, $\gamma(k,z,t)$ can be defined by

$$tan(\gamma) = \frac{Q_{p'w'}}{C_{p'w'}}. \tag{V.6}$$

Here, k and l are the wavenumbers in the x and y directions and $*$ denotes the complex conjugate. The absolute value of the phase angle is shown for simulation 3

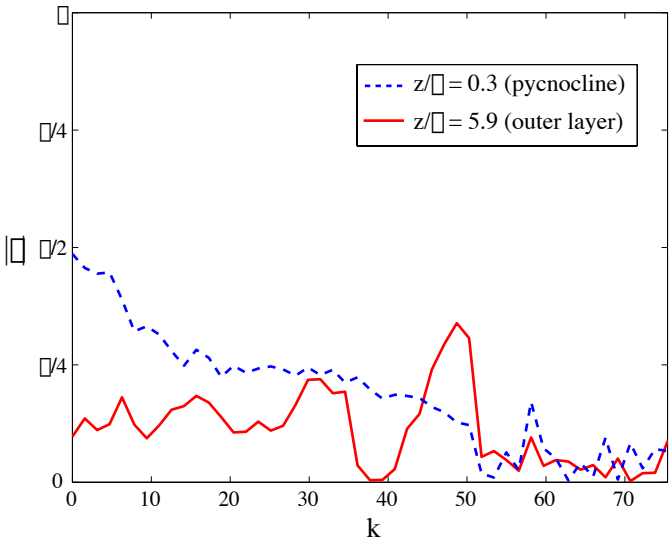

Figure V.6: Phase angle of the w' and p' cospectrum for $Ri_* = 1000$, $Re_* = 960$.

in Figure V.6. The phase angle is averaged over data at several times and linearly weighted by the absolute value of the energy at the corresponding k and t,

$$E_{p'w'}(k,z,t) = \sum_l \hat{p}'\hat{w}'^* + \hat{p}'^*\hat{w}'. \tag{V.7}$$

The energy flux is dominated by the low wavenumbers (not shown). When $|\gamma| = 0$, p' and w' are exactly in phase, while the energy flux, $\langle p'w' \rangle$ is directed upward for $0 \leq |\gamma| < \pi/2$ and downward for $\pi/2 < |\gamma| \leq \pi$. Figure V.6 shows that $|\gamma|$ is generally small in the outer layer. In the pycnocline, the most energetic modes with low wavenumbers have $|\gamma| \approx \pi/2$, so that p' and w' are about 90^o out of phase and the vertical energy flux is small. The phase lag observed in the pycnocline is consistent with horizontally propagating interfacial waves. In laboratory experiments of a turbulent boundary layer capped by a temperature interface, Piat and Hopfinger (1981) observed a 90^o phase lag between the vertical velocity and temperature at the interface, which is consistent with the present results if the waves are hydrostatic.

Frequency spectra obtained from the time history have been examined for dynamcial coupling between different regions in the flow. Figure V.7 shows

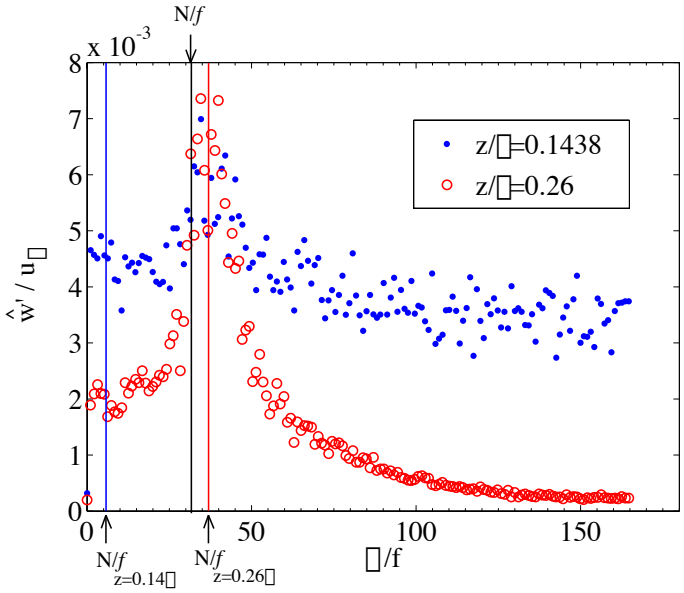

Figure V.7: Spectral amplitudes of the vertical velocity in the pycnocline and in the boundary layer, $Ri_* = 1000$, $Re_* = 960$.

the spectum for simulation 3 at two vertical locations: at $z/\delta = 0.14$ in the upper portion of the mixed layer where $N/f = 5.7$, and at $z/\delta = 0.26$ in the pycnocline where $N/f = 36.9$. The spectra were obtained using a timeseries in a coordinate frame moving with the local mean flow and the spectral amplitudes were averaged over the horizontal plane. The energy is large over a wide range of frequencies at the lower location, signifying broad-band turbulence. *Both* spectra have a maximum amplitude at frequencies near the buoyancy frequency in the pycnocline. At $z/\delta = 0.14$, this peak frequency lies outside the frequency band, $f < \omega < N$, for locally propagating internal waves. Since we expect nonlinear interactions between different frequencies to be strong in the turbulent boundary layer, the dynamics of turbulence in the mixed layer may be directly influenced by fluctuations in the pycnocline.

It is desirable to determine the relative importance of the radiated internal waves to the energetics of the turbulent boundary layer. We can assess this by

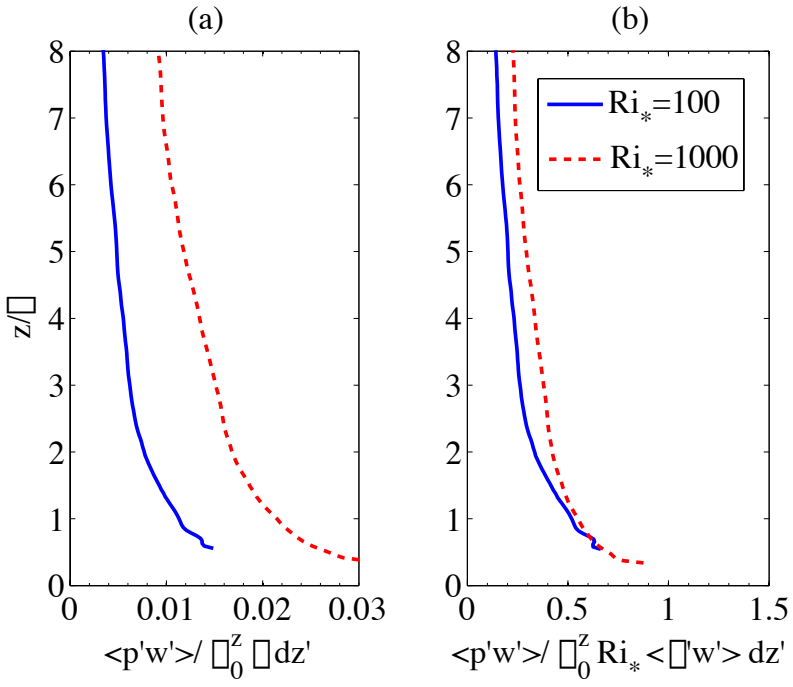

Figure V.8: Vertical energy flux normalized by (a) the integrated dissipation, and (b) the integrated buoyancy flux with $Re_* = 960$. In order to ensure that assumptions made to derive Eq. (V.8) hold, the first height shown is at the top of the pycnocline where $d\langle\rho\rangle/dz = d\rho/dz_\infty$.

comparing the size of the terms in the turbulent kinetic energy budget. At steady state, the turbulent kinetic energy budget integrated to a height z outside the boundary layer is:

$$\int_0^z P dz' - \int_0^z \epsilon dz' - \langle p'w' \rangle - Ri_* \int_0^z \langle w'\rho' \rangle \, dz' = 0, \tag{V.8}$$

where P and ϵ are the production and dissipation, respectively, and it has been assumed that z is sufficiently large so that the turbulent transport and the viscous diffusion are negligible. Here $< \cdot >$ denotes an average over a horizontal plane and time, during a period when the fluctuations are quasi-steady. Figure V.8(a) shows that the third term in Eq. (V.8), the vertical energy flux, is on the order of 1% of the integrated dissipation. Therefore, the energy radiated away from the boundary layer in the form of internal waves is negligible compared to the total energy extracted from the mean flow.

While the energy flux associated with radiated waves may be small compared to the integrated turbulent dissipation, the waves may still extract enough energy from the boundary layer to affect the evolution of the background potential energy. Since the kinetic energy is transferred to potential energy through the buoyancy flux, it is useful to compare the internal wave energy flux to the integrated buoyancy flux as shown in Figure V.8(b). In both cases, the outgoing energy flux at the top of the boundary layer is of the same order and the same sign as the buoyancy flux. The integrated turbulent kinetic energy budget therefore consists of the production term balanced to within a few percent by the dissipation. The rest of the energy extracted from the mean flow is either radiated away from the boundary layer by internal waves, or is transferred to mean potential energy.

The turbulence-generated internal waves in the simulations exhibit a characteristic propagation angle in the horizontal and vertical directions. This is illustrated for simulations 2 and 3 in Figure V.9. Part (a) shows the horizontal wavenumbers corresponding to the maximum amplitude of $\partial w'/\partial z$, and part (b) shows the corresponding azimuthal angle, ϕ made by the wavenumber vector and the x-axis. The dominant streamwise wavenumber in the outer layer increases with

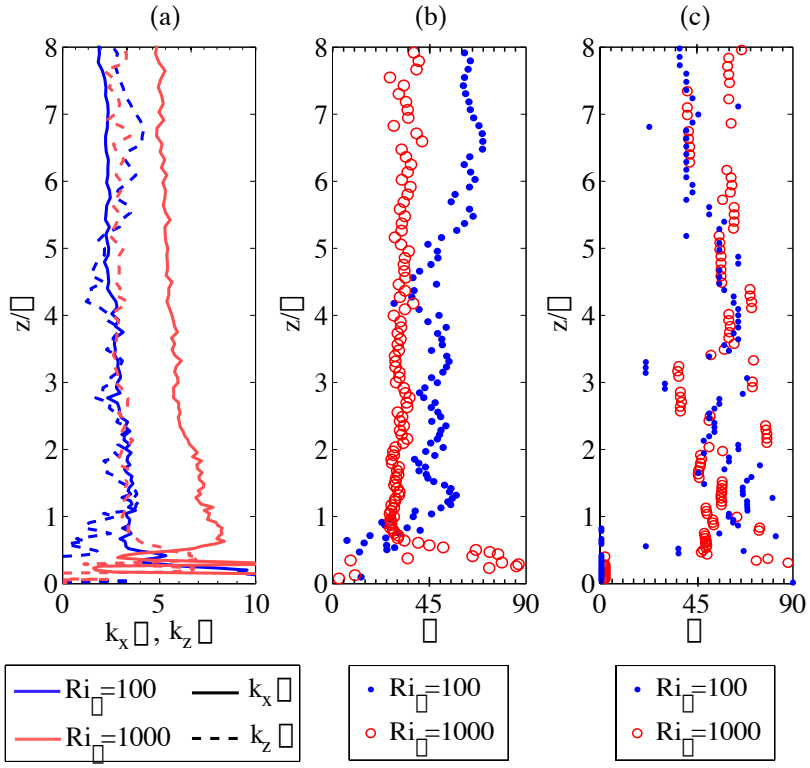

Figure V.9: Characteristics of waves with the largest amplitude of $\partial w'/\partial z$ for $Re_* = 960$. Here ϕ is the azimuthal angle and Θ is the polar angle.

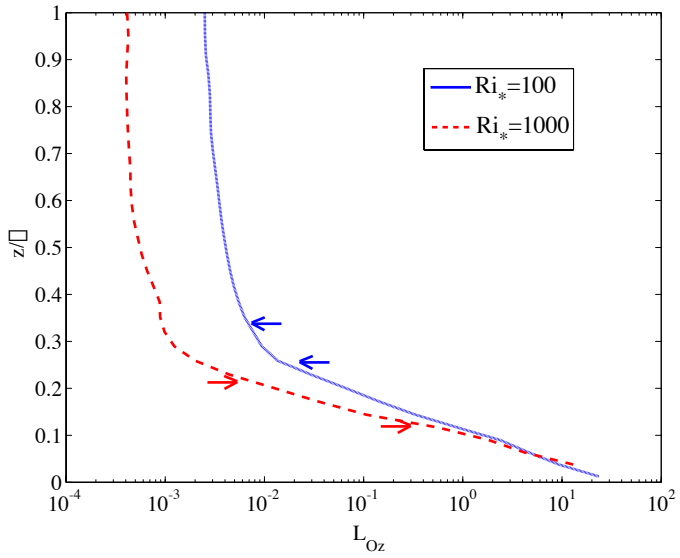

Figure V.10: Ozmidov scale for $Re_* = 1920$ and $tf = 20$. Arrows mark the region where $\langle p'w' \rangle$ and $d\langle p'w' \rangle / dz$ are positive.

stratification. Part (c) shows the polar angle, Θ made by the wavenumber vector and the horizontal plane, based on the linear dispersion relation using the dominant frequency of $\partial w'/\partial z$. Since the calculation of Θ assumes that the internal waves are linear, it will be accurate only where the flow consists of small amplitude waves, which is generally true here for $z/\delta > 1$. Since they are generated by a three-dimensional turbulent flow, it is remarkable that the internal waves with the largest $\partial w'/\partial z$ are associated with a definite structure, namely azimuthal and polar angles approximately $35-60^o$ under both stratifications considered here.

We have been unable to determine any connection between the wavelength of the most dominant propagating waves and the Ozmidov scale in the boundary layer as proposed by Gibson et al. (2006). The Ozmidov scale, $L_{Oz} = \sqrt{\epsilon/N^3}$, provides an estimate for the smallest scale eddies that are still affected by the presence of stratification (Itsweire et al. (1993)), and is shown in Figure V.10. In both cases, L_{Oz} is large in the turbulent mixed layer and becomes very small in the outer layer where stratification plays a dominant role. In an attempt to

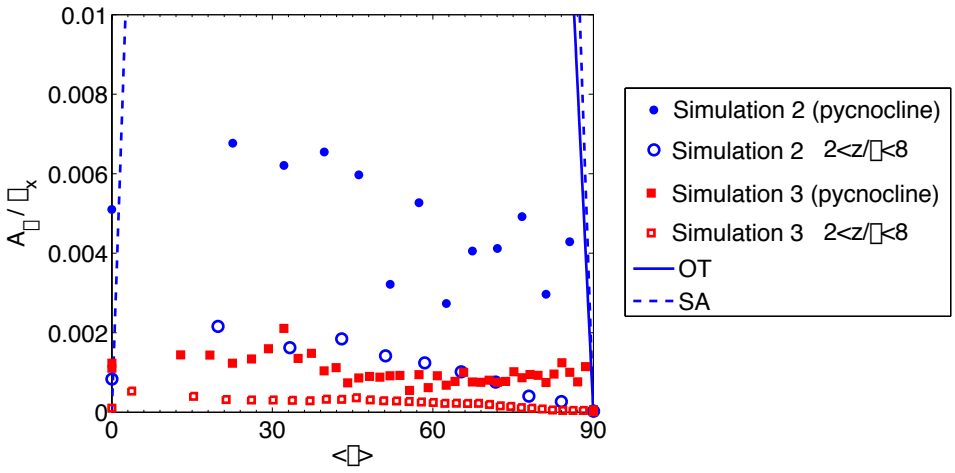

Figure V.11: Internal wave stability estimated from the ratio of the displacement amplitude to the horizontal wavelength, $Re_* = 960$. For each frequency, the wavenumber corresponding to the largest slope is shown. OT and SA show the critical amplitude ratios for overturning and self-advection instabilities, respectively.

estimate the region where internal waves are generated, the arrows in Figure V.10 mark the region where $\langle p'w' \rangle$ and $d \langle p'w' \rangle / dz$ are positive; that is the energy flux is upward and increasing in strength. Since L_{Oz} varies rapidly between the mixed layer and the pycnocline, it encompasses a large range of scales in the estimated internal wave generation region. This is especially true when $Ri_* = 1000$, and L_{Oz} varies by more than an order of magnitude in this region. We have been unable to determine a rigorous scaling of dominant wavelength observed in the outer layer, but it appears to be set through a combination of the mixed layer depth and the pycnocline thickness.

The stability of the internal waves can be evaluated by considering the ratio of the displacement amplitude to the horizontal wavelength. As shown by Sutherland (2001), plane waves will be unstable to density overturns if

$$\frac{A_\xi}{\lambda_x} > \frac{1}{2\pi} cot\Theta, \tag{V.9}$$

where $A_\xi = \Theta'/d\langle\Theta\rangle/dz$ is the approximate isopycnal displacement, λ_x is the horizontal wavelength, and Θ is the angle made by the wave number vector and the horizontal plane. When Θ is small, the internal wave motion is predominately in the vertical direction, so the amplitude of the waves must become very large in order to overturn. In these cases, specifically when $\Theta < 57.2^o$, Sutherland (2001) predicts that a more restrictive criteria on the wave amplitude is based on the resonant interaction between the wave and its wave-induced mean flow. The criteria for instability due to this resonant interaction is, Sutherland (2001),

$$\frac{A_\xi}{\lambda_x} = \frac{1}{2\pi\sqrt{2}} sin(2\Theta). \tag{V.10}$$

The ratio of the internal wave amplitude to the horizontal wavelength is shown in Figure V.11. Only the cases with $Re_* = 960$ are shown here, but the result does not significantly depend on Reynolds number. The internal waves are most unstable in the pycnocline and when Ri_* is small, but in all cases, the amplitude of the internal waves is sufficiently small so that they should be stable. The amplitude ratio observed here is significantly smaller than observed by Dohan and Sutherland (2003) who observed a ratio about 0.025 at $\Theta = 45^o$, which is nevertheless still predicted to be stable.

The relative sizes of the nonlinear and viscous terms can be estimated through the turbulent Reynolds number, defined as:

$$Re_T = \frac{\langle u_i' u_i' \rangle^{1/2} (2\pi/k_H)}{\nu}, \tag{V.11}$$

where k_H is the horizontal wavenumber associated with the maximum turbulent kinetic energy, and $< \cdot >$ denotes an average over horizontal planes and time. The turbulent Reynolds number is shown in Figure V.12 for simulations 2 and 3. As expected, Re_T is maximum in the turbulent boundary layer. A sharp decrease occurs in the pycnocline (delimited by arrows in Figure V.12) indicating that turbulence is suppressed by the strong stratification in this region. In the outer layer the turbulent Reynolds number approaches a relatively constant value between 200 and 300 and does not depend strongly on the Richardson number.

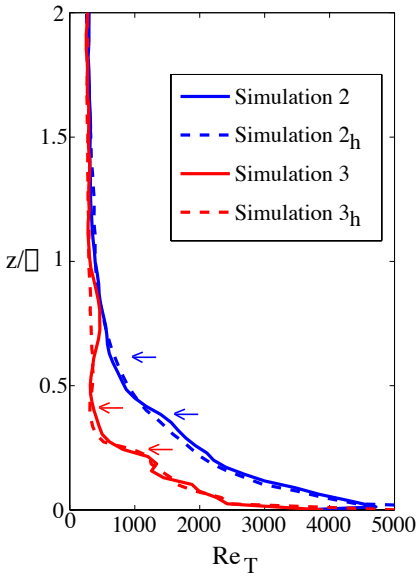

Figure V.12: Turbulent Reynolds number. Arrows show the upper and lower bounds of the pycnocline where $d\langle\Theta\rangle/dz > 1$.

Since we have seen in Figure V.9 that the dominant horizontal wavenumber in the outer layer is larger when $Ri_* = 1000$, the kinetic energy carried by the waves must also be larger in this case. Below the top of the pycnocline, however, the turbulent Reynolds number decreases with increasing stratification, even in the boundary layer where the temperature gradient is negligible. It is possible that this is a result of the reduced boundary layer thickness which limits the size of the energy containing scales.

V.5 Viscous Internal Wave Model

Although the generation of internal waves occurs in a region where non-linear effects are important, the selection of a dominant range of frequencies for the internal waves propagating in the outer region can be explained by a simple, linear model. It is expected that the viscous damping of internal waves should depend on the wavenumber with small scale waves decaying more rapidly. In addition, waves with high and low frequencies are associated with a small vertical group

velocity. Since they take longer to travel a given distance, they are therefore more susceptible to viscous decay. Starting with a known wave amplitude as a function of frequency and wavenumber at some initial location z_0, the wave amplitude at an arbitrary height z can be predicted based on the expected vertical propagation speed and viscous decay rate.

The linearized equations describing the evolution of a small perturbation from the background flow in a coordinate frame moving with the mean velocity can be written

$$\frac{\partial u'}{\partial t} + \langle \mathbf{u} \rangle \cdot \nabla u' + w' \frac{d \langle u \rangle}{dz} - f v' = -\frac{1}{\rho_0} \frac{\partial p'}{\partial x} + \nu \nabla^2 u', \tag{V.12}$$

$$\frac{\partial v'}{\partial t} + \langle \mathbf{u} \rangle \cdot \nabla v' + w' \frac{d \langle v \rangle}{dz} + f u' = -\frac{1}{\rho_0} \frac{\partial p'}{\partial y} + \nu \nabla^2 v', \tag{V.13}$$

$$\frac{\partial w'}{\partial t} + \langle \mathbf{u} \rangle \cdot \nabla w' = -\frac{1}{\rho_0} \frac{\partial p'}{\partial z} - \frac{\rho'}{\rho_0} g + \nu \nabla^2 w', \tag{V.14}$$

$$\frac{\partial \rho'}{\partial t} + w' \frac{d \langle \rho \rangle}{dz} = \kappa \nabla^2 \rho'. \tag{V.15}$$

Taking the dot product of $\mathbf{u}'$ and the momentum equations, and taking the horizontal plane-average, denoted by $< \cdot >$, gives

$$\begin{aligned} \frac{\partial K}{\partial t} + \langle \mathbf{u} \rangle \cdot \nabla K = \quad & - \langle u' w' \rangle \frac{\partial \langle u \rangle}{\partial z} - \langle v' w' \rangle \frac{\partial \langle v \rangle}{\partial z} \\ & - \frac{1}{\rho_0} \nabla \cdot \langle \mathbf{u}' p' \rangle - \frac{g}{\rho_0} \langle \rho' w' \rangle + \nu \nabla^2 K - \nu \left\langle \frac{\partial u_i'}{\partial x_j} \frac{\partial u_i'}{\partial x_j} \right\rangle, \end{aligned} \tag{V.16}$$

where $K = \langle u_i' u_i' \rangle / 2$ is the perturbation kinetic energy. Since K is only a function of z and t, and $\langle w \rangle = 0$, the convective term $\langle \mathbf{u} \rangle \cdot \nabla K = 0$. When Eq. (V.16) is taken to apply away from the boundary layer where $\partial \langle u \rangle / \partial z \approx 0$ and $\partial \langle v \rangle / \partial z \approx 0$, it simplifies to

$$\frac{\partial K}{\partial t} = -\frac{1}{\rho_0} \nabla \cdot \langle \mathbf{u}' p' \rangle - \frac{g}{\rho_0} \langle \rho' w' \rangle + \nu \frac{\partial^2 K}{\partial z^2} - \nu \left\langle \frac{\partial u_i'}{\partial x_j} \frac{\partial u_i'}{\partial x_j} \right\rangle, \tag{V.17}$$

Similarly, multiplying Eq. (V.15) by ρ' and taking the plane average gives

$$\frac{\partial P}{\partial t} = \frac{g}{\rho_0} \langle \rho' w' \rangle + \kappa \frac{\partial^2 P}{\partial z^2} - \frac{g}{\rho_0 \partial \langle \rho \rangle / \partial z} \kappa \left\langle \frac{\partial \rho'}{\partial x_j} \frac{\partial \rho'}{\partial x_j} \right\rangle, \tag{V.18}$$

where the perturbation potential energy is defined by

$$P = \frac{-g\left\langle \rho'^2 \right\rangle}{2\rho_0 \frac{d\langle\rho\rangle}{dz}}. \tag{V.19}$$

Using the general form for a plane wave, $u_i' = \hat{u}_i exp[i(\mathbf{k}\cdot\mathbf{x} - \omega t)]$, the kinetic and potential energy dissipation can be written as

$$\epsilon = -\nu \left\langle \frac{\partial u_i'}{\partial x_j}\frac{\partial u_i'}{\partial x_j} \right\rangle = -\nu|\mathbf{k}|^2 \left\langle u_i' u_i' \right\rangle, \tag{V.20}$$

$$\epsilon_\rho = -\kappa \left\langle \frac{\partial \rho'}{\partial x_j}\frac{\partial \rho'}{\partial x_j} \right\rangle = -\kappa|\mathbf{k}|^2 \left\langle \rho'\rho' \right\rangle. \tag{V.21}$$

An equation for the wave energy, $W = \rho_0(P + K)$ can be found by summing Eqs. (V.17) and (V.18). If $Pr = 1$, the wave energy then satisfies

$$\frac{\partial W}{\partial t} + \nabla\cdot(W\mathbf{c}_g) = \nu\frac{\partial^2 W}{\partial z^2} - 2\nu|\mathbf{k}|^2 W, \tag{V.22}$$

where we have used the result that the energy flux $\langle p'\mathbf{u}'\rangle = \mathbf{c}_g W$ where $\mathbf{c}_g$ denotes the group velocity vector. If we make the approximation that the mean wave energy and the background stratification vary slowly in z, then viscous dissipation dominates the diffusion term, and the previous equation can be re-written

$$\frac{DW}{Dt} = -2\nu|\mathbf{k}|^2 W - W\nabla\cdot\mathbf{c}_g, \tag{V.23}$$

where D/Dt denotes a derivative following the group velocity of the wave. For waves in a slowly varying medium, $\nabla\cdot\mathbf{c}_g \approx 0$ so that with this approximation

$$\frac{DW}{Dt} = -2\nu|\mathbf{k}|^2 W. \tag{V.24}$$

For convenience, we can recast Eq. (V.24) in terms of the vertical velocity. For a plane wave with an unknown z-dependence, the vertical velocity can be expressed as

$$w = A(z,t)exp[i(kx + ly - \omega t + \theta(z)], \tag{V.25}$$

By inserting equations of this form into Eqs. (V.12-V.15), the wave energy can be expressed in terms of the vertical velocity amplitude

$$W = \frac{1}{2}\rho_0 A^2 \frac{|\mathbf{k}|^2}{k_h^2}. \tag{V.26}$$

Again, assuming that the background density gradient and the wave amplitude vary on scales larger than the wavelength, and since k_h and ω are constant following internal wave rays (Luyten et al. (1983)), Eq. (V.24) simplifies to

$$\frac{D}{Dt}(|\mathbf{k}|^2 A^2) = -2\nu|\mathbf{k}|^4 A^2. \tag{V.27}$$

In a coordinate frame moving with the group velocity, Eq. (V.27) can be integrated to give

$$A^2(z,t) = A_0^2 \frac{|\mathbf{k}_0|^2}{|\mathbf{k}|^2} exp(\int_0^t -2\nu|\mathbf{k}|^2 dt), \tag{V.28}$$

or

$$A(z,t) = A_0 \frac{|\mathbf{k}_0|}{|\mathbf{k}|} exp(\int_0^t -\nu|\mathbf{k}|^2 dt) \tag{V.29}$$

We can obtain an expression for the expected vertical velocity amplitude as a function of z in a stationary reference frame by using the vertical component of the group velocity for a rotating internal wave (Luyten et al. (1983))

$$c_{gz} = \frac{\partial\omega}{\partial m} = -\frac{m}{\omega}\frac{\omega^2 - f^2}{|\mathbf{k}|^2} = \frac{k_h}{\omega|\mathbf{k}|^2}(\omega^2 - f^2)^{1/2}(N^2 - \omega^2)^{1/2} = \frac{dz}{dt}, \tag{V.30}$$

which makes use of the dispersion relation for internal waves with rotation

$$m = -k_H[\frac{N^2 - \omega^2}{\omega^2 - f^2}]^{1/2}. \tag{V.31}$$

The negative branch of m has been chosen since we are interested in waves with an energy flux directed upward. The expected amplitude for a given frequency and horizontal wavenumber, expressed as a function of z in an Eulerian frame is then

$$A(z) = A_0 \frac{|\mathbf{k}_0|}{|\mathbf{k}|} \; exp\left[\frac{-\nu\omega}{k_h}(\omega^2 - f^2)^{-1/2}\int_{z_0}^{z} |\mathbf{k}|^4 (N^2 - \omega^2)^{-1/2} dz'\right]. \tag{V.32}$$

From Eq. (V.30), it is clear that for low and high frequency waves ($\omega = f$ and $\omega = N(z)$, respectively) the vertical component of the group velocity vanishes. It also follows from Eq. (V.32) that when the frequency is near these limits, the wave amplitude decays rapidly as a function of z. For a fixed horizontal wavenumber, it can be shown that the vertical component of the group velocity is maximum for waves with $\omega^2 = (2/3)N^2$, which propagate at $\theta = 35^o$. (Note that

when the magnitude of the wavenumber vector, $|\mathbf{k}|$ is held constant, the group velocity maximum is at $\theta = 45^o$, see Gill (1982)). It is of interest to find the frequency that is associated with the smallest rate of viscous decay. For a fixed horizontal wavenumber and a constant background stratification, the minimum rate of decay, determined from Eq. (V.32), occurs at $\omega = \sqrt{4/5}N$, or $\theta = 26.6^o$. Note that while waves at this frequency are expected to decay the slowest, the amplitude at a given height is strongly dependent on the distribution of the *initial* wave amplitude $A_0(k_h, \omega)$.

The proposed model for the propagation of internal waves then proceeds as follows. Start with an initial estimate for the internal wave amplitude $A_0(k_H, \omega)$ at a height z_0. Then use the expression for $m(z)$ given by Eq. (V.31) for a given $N(z)$ profile, to numerically integrate Eq. (V.32) for every value of k_H and ω. The performance of the viscous internal wave model has been evaluated by using the observed internal wave spectrum from the simulations at the bottom of the pycnocline. The location z_0 is chosen in each case by using two conditions. First, z_0 should be above the height where $\langle p'w' \rangle$ is maximum, with the expectation that most of the waves have been generated below this level. In addition, z_0 should be chosen so that $N(z_0) \geq N_\infty$ to ensure that all frequencies $f < \omega < N_\infty$ correspond to vertically propagating waves.

The viscosity that appears in Eq. (V.32) is taken to be the molecular value. In our simulations, since the perturbation amplitude in the outer layer is small, the eddy viscosity in this region is zero, so this is the proper choice. In a situation where an eddy viscosity is present in the outer layer, it would be possible to re-derive Eq. (V.32) with $\nu_T(z)$. We have derived the model equations with a Prandtl number of unity, but altering the viscosity in Eq. (V.32) by a small fraction does not qualitatively affect the results. It is important to note that this model is linear and neglects the turbulent production and assumes that the background flow is slowly varying.

In order to estimate $A_0(k_H, \omega)$, the frequency/wavenumber spectrum for

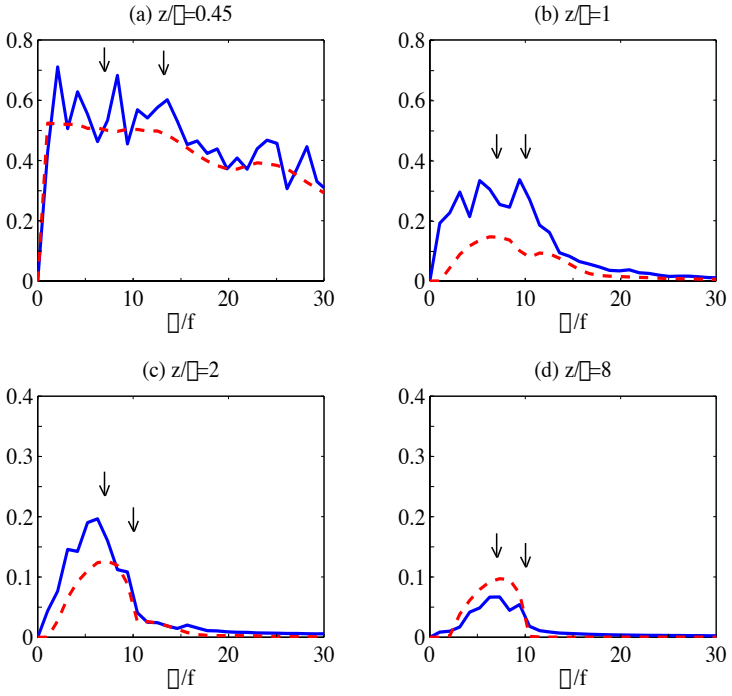

Figure V.13: Comparison between observed and predicted spectra of $\partial w'/\partial z$ using a viscous internal wave model for $Ri_* = 100$, $Re_* = 960$. Arrows show $N_\infty/(\sqrt{2}f)$ (left) and $N(z)/f$ (right). Note that the upper and lower sets of panels have different y-axis scales.

$\partial w'/\partial z$ in a reference frame moving with the plane-averaged horizontal velocity is divided by $m(z_0)$ as estimated from Eq. (V.31). This effectively filters out the high frequency waves in the pycnocline that do not propagate vertically. The spectral amplitudes are then smoothed in frequency space to obtain $A_0(k_H, \omega)$ used in Eq. (V.32). Frequencies with $\omega > N(z)$ are allowed to decay exponentially in the vertical direction, representing evanescent modes with $A = A_0 exp[im(z - z_0)]$ where m, calculated using Eq. (V.31), is imaginary.

The estimate of the spectrum of $\partial w'/\partial z$ from the viscous decay model is compared with the corresponding spectrum from the simulations in Figures V.13 and V.14. In order to show the combined contributions of all values of k_H, the square root of the sum of the squared amplitudes of $\partial w'/\partial z$ are shown as a function of ω/f in these figures. The initial spectrum at z_0, shown in panel (a)

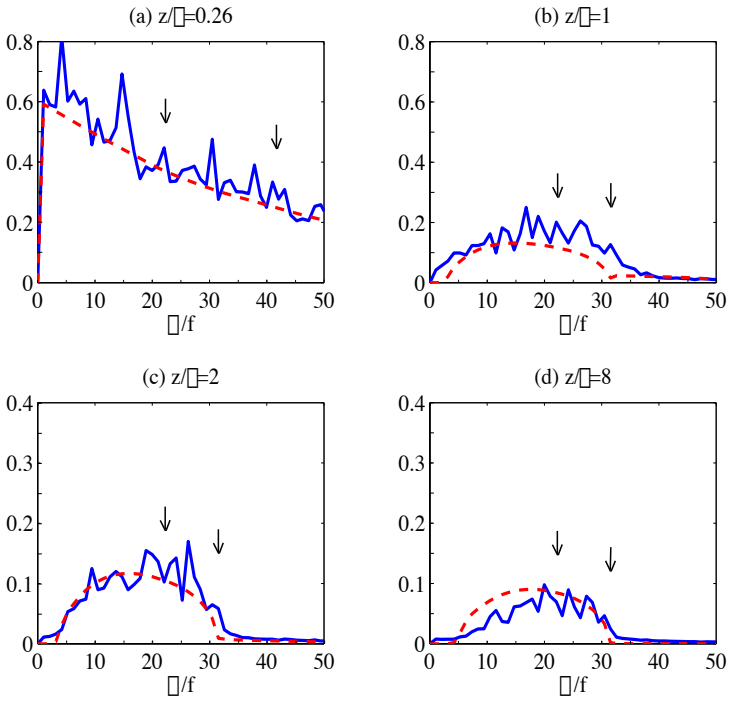

Figure V.14: Comparison between observed and predicted spectra of $\partial w'/\partial z$ using a viscous internal wave model for $Ri_* = 1000$, $Re_* = 960$. Arrows show $N_\infty/(\sqrt{2}f)$ (left) and $N(z)/f$ (right). Note that the upper and lower sets of panels have different y-axis scales.

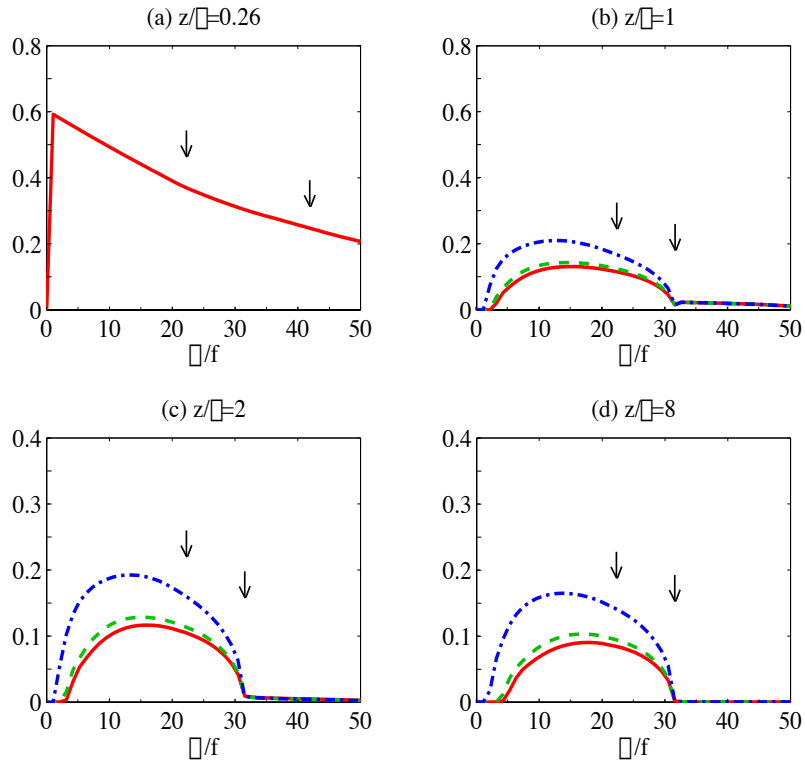

Figure V.15: Predicted spectrum of $\partial w'/\partial z$ for $Ri_* = 1000$ and various Reynolds numbers. Arrows show $N_\infty/(\sqrt{2}f)$ (left) and $N(z)/f$ (right). Note that the upper and lower sets of panels have different y-axis scales.

in both figures, peaks at low frequencies. Arrows indicate the local values of N/f and $N_\infty/(\sqrt{2}f)$. As they propagate vertically, the waves with large and small frequencies decay leaving a central peak. Generally, the viscous internal wave model predicts the decay of the wave magnitude well. However, the model tends to overestimate the decay rate for $z < \delta$, especially for the low stratification case. This may be due to a combination of the neglect of the turbulent production, the presence of non-propagating modes, and a breakdown of the WKB assumption of a slowly varying background state. Nevertheless, in the outer layer the shape of the spectrum and the frequency associated with the largest amplitude are generally captured by this simple model, both for moderate ($Ri_* = 100$) and large ($Ri_* = 1000$) stratification.

The dependence of the viscous internal wave model on the Reynolds number is examined in Figure V.15 for $Ri_* = 1000$. Here, the spectra at z_0 are assumed to be independent of Reynolds number. This assumption is made in order to proceed to high Reynolds numbers beyond the available simulation data. Comparison of the data at $Re_* = 960$ and $Re_* = 1920$ shows that the turbulence spectra for $\omega < N$ are not significantly different, but future simulations of high Reynolds number boundary layers are necessary to obtain the appropriate Reynolds number scaling. The model prediction using the molecular viscosity corresponding to both Reynolds numbers considered here are shown, together with a much larger Reynolds number, $Re_* = 60,000$, that would be typical of oceanic conditions. Even at the large Reynolds number, the viscous model predicts that the high and low frequencies decay sufficiently to create a central spectral peak. It is possible that nonlinear effects could become important at a large Reynolds number, or that the generated wave spectrum could change. Simulations or experiments at a larger Reynolds number should be carried out in the future to test the viscous decay mechanism in this situation.

It is of interest to determine the influence of the initial amplitude distribution, $A_0(k_h, \omega)$, on the model results. Figure V.16 compares the model predictions when A_0 is taken from the LES data to a case where the initial amplitude is independent of k_h and ω. In order to isolate the influence of the initial amplitude and to compare to the predicted decay in a uniform background flow, the initial height is set to $z_0 = 2\delta$. At this location, the mean density gradient is equal to the free stream value. Figure V.16(b) shows that when starting from a uniform initial amplitude (with A_0 independent of k_h and ω) the maximum amplitude of the propagating waves occurs at $\omega = \sqrt{4/5}N$. It can be shown analytically that this frequency corresponds to the minimum rate of decay as predicted by the viscous decay model. It is interesting to note that when using the simulation data to set $A_0(k_h, \omega)$ as shown in Figure V.16(a), the frequency associated with the maximum wave amplitude increases with z, but does so very slowly. Even at a height of

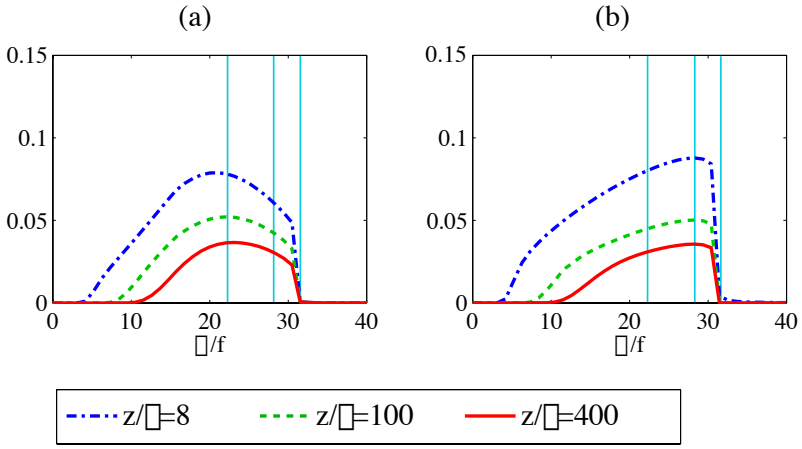

Figure V.16: Predicted spectrum of $\partial w'/\partial z$ for $Ri_* = 1000$ at various heights for (a) Initial amplitude distribution $A_0(k_h, \omega)$ taken from simulation data and (b) Uniform initial amplitude, A_0 independent of ω and k_h. In both cases, the initial height $z_0 = 2\delta$. Vertical lines show $N_\infty/(\sqrt{2}f)$ (left), $\sqrt{4/5}N_\infty/f$ (center), and N_∞/f (right).

$z/\delta = 400$, the maximum wave amplitude occurs at a frequency less than $\sqrt{4/5}N$. If $\delta = u_*/f = 25m$, as roughly estimated from the data of Perlin et al. (2007), then $z = 400\delta = 10km$! This implies that the initial amplitude distribution set-up by the turbulent generation process may affect the distribution of wave amplitudes very far from the source.

V.6 Discussion of the internal wave model

While a differential viscous decay explains the amplitude and spectral shape of the turbulence-generated internal waves observed in our simulations, it remains to be determined if this mechanism can explain the results of other experiments, particularly in those cases with larger amplitude waves. This should be possible to test, particularly from other numerical simulations. The observed amplitude of w' as a function of ω and k_H just beyond the wave-generation site can be used in Eq. (V.32) to obtain the predicted amplitude $A(\omega, k_H, z)$ which can

then be compared to the observed wave field.

The differential viscous decay mechanism was considered by Dohan and Sutherland (2005). They rejected this explanation partly because they expected that it would yield waves at the frequency associated with the maximum vertical group velocity, $\Theta \approx 35^o$, while they observed $\Theta \approx 45^o$. As we have shown, differential viscous decay is able to produce waves near 45^o since the distribution of initial wave amplitudes is shifted towards low frequencies and therefore larger angles of vertical propagation and since ω depends on $|\mathbf{k}|$ through the dispersion relation. Sutherland and Linden (1998) hypothesized that the narrow frequency band that they observed for turbulence-generated internal waves was due to nonlinear interactions between the waves and turbulence. Since we have seen that the local Reynolds number in the region of internal wave production is large, this mechanism cannot be ruled out and warrants further investigation. However, as we have shown, a simpler mechanism of viscous decay is capable of capturing many of the features of the observed frequency spectrum.

V.7 Conclusions

We have conducted simulations of a turbulent Ekman layer over a flat wall. A uniform stratification was applied initially and maintained as the upper boundary condition, and the temperature gradient was set to zero at the lower wall. As the flow developed, a well-mixed, turbulent region formed near the wall, capped by a strongly stratified pycnocline. It has been established that turbulence in a bottom Ekman layer, when subject to an overlying stratification, radiates internal waves. The primary focus of this paper was an analysis of this internal wave field. It is worth noting that the internal waves are radiated by turbulence in a well-mixed region in this problem in contrast to the stratified turbulence that is often seen in wakes and shear layers.

Two types of internal waves were observed in the simulations. The first

type of waves have frequencies larger than the outer layer buoyancy frequency and were observed in the pycnocline. The pressure perturbation and the vertical velocity of these waves are nearly 90^o out of phase, indicating horizontally propagating waves associated with a small vertical energy flux. Above the boundary layer, these waves decay as evanescent modes since their frequency is not between f and N. In the boundary layer, the turbulent spectrum exhibits a peak at the same frequency observed for waves in the pycnocline, which indicates the potential for nonlinear interactions between the boundary layer turbulence and the pycnocline waves. Since regions of strong density gradient are commonly observed above turbulent boundary layers in both the ocean and atmosphere, investigating the influence of the pycnocline waves on the boundary layer turbulence would be an important topic for further study.

The second type of waves that were observed here are associated with frequencies $f < \omega < N_\infty$ and therefore able to propagate in the outer layer. Considering that they were excited from a turbulent region with a broad range of frequencies and scales, it is remarkable that these waves are associated with a distinct peak in frequency and wavenumber space. The vertical angle of propagation of these waves is between $35-60^o$, which is consistent with several previous studies of turbulence-generated internal waves. As we have shown, the decay in amplitude and the formation of a spectral peak is consistent with a linear viscous decay. Although the mechanism that we have proposed to explain the propagation angle observed for waves propagating in the outer layer relies on the effects of molecular viscosity, our model indicates that the formation of a distinct spectral peak is possible even at a realistically large oceanic Reynolds number.

It can be shown that the viscous model presented here predicts that waves propagating at $\Theta = 26.6^o$ have the slowest rate of decay. Nevertheless, when starting with initial wave amplitudes weighted towards low frequencies as observed in the simulations, the observed and predicted waves show a maximum amplitude at larger angles. Using the model prediction, we have shown that the

initial distribution of wave amplitudes affects the wave field at very large distances away from the boundary layer. This implies that knowledge of the boundary layer turbulence is important to predicting the amplitude and spectral content of turbulence-generated internal waves far from the generation site.

The importance of the internal wave energy flux to the boundary layer energetics has been estimated by comparing the magnitudes of the terms in the vertically integrated turbulent kinetic energy equation. It was found that the dominant balance is between production and dissipation in the boundary layer and that the vertical energy flux is only a few percent of these terms. However, most of the production and dissipation occurs in the mixed region where stratification effects are not directly felt. We have found that the internal wave energy flux and the integrated buoyancy flux are the same order in the pycnocline. Since the buoyancy flux is a measure of the energy transferred from kinetic to potential, if all of the energy radiated away from the boundary layer as internal waves were instead present as an additional buoyancy flux, the evolution of the local mean temperature profile in the pycnocline would be significantly affected.

V.8 Acknowledgments

This chapter has been published in the *Journal of Fluid Mechanics*, 2007, co-authored by Professor Sutanu Sarkar. The support of grant N00014-05-1-0334 from ONR Physical Oceanography, program manager Dr. Scott Harper, and an NDSEG fellowship is gratefully acknowledged.

VI Numerical Methods

VI.1 Development of an Open-Source CFD Solver

One of the general goals of computational fluid dynamics (CFD) is to accurately solve the Navier-Stokes equations. For incompressible flow, these equations can be written:

$$\frac{\partial u_i}{\partial t} + \frac{\partial u_j u_i}{\partial x_j} - \nu \frac{\partial^2 u_i}{\partial x_j^2} + \frac{\partial p}{\partial x_i} = -\delta_{1i} P_x(\mathbf{x}, t) + f_i,$$

$$\frac{\partial u_j}{\partial x_j} = 0,$$

where f_i is a body force exerted on the fluid. To solve this problem numerically, the continuous flow field must be approximated on a discrete set of points in space. Further, the resulting approximate equation on this finite set of points must be advanced in time using discrete time steps. To minimize the expense of the computation, one desires to use as few spatial points as possible with large time steps while maintaining the accuracy (in both space and time) and stability of the simulation. With a particular spatial discretization, some terms of the governing equation will impose a more stringent time step limitation than other terms. Generally, the most restrictive terms should be treated implicitly to increase numerical stability, while other less restrictive terms may be taken explicitly. These issues guide the choice of spatial and temporal discretizations of the current problem, which are discussed in detail below.

Diablo is an open-source CFD solver designed by Professor Thomas Bewley. The channel flow solver, scalar advection, and geophysical forcing terms were

written by the author with guidance from Professors Bewley and Sarkar. Extra features such as the inclusion of a Darcy force for porous media and immersed obstacles are being added by other students at UCSD. The goal of Diablo is to provide an efficient and easy to use solver for incompressible, three-dimesional turbulent flows in simple geometries. The code has been designed to allow the choice of one, two, or three periodic directions, although only those cases with two or three periodic directions are fully functional at this time. When a given direction is periodic, all derivatives in that direction are computed in Fourier space. This improves the accuracy of the algorithm and minimizes the numerical dissipation. When a given direction is not periodic, second-order finite differences are used. The formulation has been designed to ensure discrete conservation of mass, momentum, and energy while allowing for a wide range of possible boundary conditions.

Time stepping in Diablo uses a combination of the explicit third-order Runge-Kutta and the implicit Crank Nicolson schemes. In order for the time-stepping of diffusion problems to be stable when using the Runge-Kutta or other explicit methods, the condition of stability requires that the diffusion number defined as $D = \nu\Delta t/\Delta x^2$ be less than some constant. For a given grid spacing this places a condition on the size of Δt. Since the grid spacing must scale inversely with the Reynolds number this can place a severe limitation on the allowable time-step. The Crank-Nicolson scheme, however, is unconditionally stable for the pure diffusion problem. For wall bounded flows, the minimum grid spacing generally occurs in the wall-bounded direction and near the wall which motivates the choice of treating the diffusion terms with Crank-Nicolson.

The Runge-Kutta method evaluates the right hand side multiple times for each timestep and uses these "trial" steps to improve the accuracy of the scheme. See Press et al. (1992) or Bewley (2007) for an introduction to the method. Since RAM may be a limiting factor for the problem size in some applications, the low-storage Runge-Kutta-Wray algorithm is used here. The algorithm can be written

(Bewely (2007))

$$k_1 = f(y_n, t_n), \tag{VI.1}$$

$$k_2 = f(y_n + \beta_1 h k_1, t_n + \alpha_1 h), \tag{VI.2}$$

$$k_3 = f(y_n + \beta_2 h k_1 + \beta_3 h k_2, t_n + \alpha_2 h), \tag{VI.3}$$

$$y_{n+1} = y_n + h(\gamma_1 k_1 + \gamma_2 k_2 + \gamma_3 k_3), \tag{VI.4}$$

where

$$\beta_1 = 8/15, \quad \beta_2 = 1/4, \quad \beta_3 = 5/12,$$

$$\alpha_1 = 8/15, \quad \alpha_2 = 2/3,$$

$$\gamma_1 = 1/4, \quad \gamma_2 = 0, \quad \gamma_3 = 3/4.$$

Although there are four equations, when the algorithm is ordered carefully only two storage variables are needed.

In order to ensure that the velocity field is divergence free as required by mass conservation under the Boussinesq approximation, the fractional step method is used. First, at each Runge-Kutta substep (rk=1,2,3), time-marching produces an intermediate velocity field $\hat{u_i}^j$ that may not be solenoidal. The second step of the fractional step method then uses the pressure gradient to ensure that the velocity is divergence free. If the corrected velocity field is denoted u_i^j:

$$u_i^j = \hat{u_i}^j - h_j \frac{\partial \phi}{\partial x_i}, \tag{VI.5}$$

where $\phi = p^{j+1} - p^j$ is the pressure adjustment between successive Runge-Kutta substeps and $\overline{h}_j$ is proportional to the timestep and for the RKW3 scheme is:

$$h_1 = \frac{8}{15}\Delta t \tag{VI.6}$$

$$h_2 = \frac{2}{15}\Delta t$$

$$h_3 = \frac{5}{15}\Delta t.$$

Taking the divergence of Eq. VI.5 gives a Poisson equation for ϕ involving only the known $\hat{u_i}^j$ since, by definition, u_i^j is divergence free:

$$\nabla^2\phi = \frac{1}{h_j}\nabla \cdot \hat{u_i}^j. \tag{VI.7}$$

When this equation is solved in Fourier space with second order finite differences in one direction, we obtain a tridiagonal system of equations for the discrete ϕ. After solving the Poisson equation, ϕ is used to update the pressure and the velocity through Eq. VI.5. In order to ensure that the discrete continuity equation is satisfied at the walls, homogeneous Neumann boundary conditions are applied to ϕ. Notice that with these boundary condtions, the value of ϕ is undetermined by an additive constant. In order to make the Poisson equation well-posed we arbitrarily set the mean pressure at the lower boundary to be zero.

The computational domain is discretized in the horizontal directions with a uniform grid-spacing and co-located variables, allowing these directions to be transformed efficiently to and from Fourier space. The discrete Fourier transforms are calculated using the freely available FFTW software (see www.fftw.org or Frigo and Johnson (2005)). This software is one of the fastest publicly available discrete Fourier transform algorithms. While some machine-specific algorithms may be slightly faster, the advantage of FFTW is that it can self-optimize on a variety of computer architectures, allowing the efficiency of Diablo to be portable. The speed of FFTW is achieved by creating an adaptive plan utilizing a selection of FFT solvers determined at runtime which is optimized for the problem size and local architecture (Frigo and Johnson (2005)).

The Fourier transform of a discrete field f_j defined on the grid $j = 1...N$ will be denoted by $\hat{f}_k$ where the discrete wavenumbers are $k = -N/2, ..., 0, ..., N/2$. Since we are interested in real functions in physical space, when f is real $\hat{f}_k = \hat{f}^*_{-k}$ where * denotes the complex conjugate. Since $\hat{f}_0$ is real, we only need to keep $1, ..., N/2$ complex numbers. The Nyquist frequency, $k = \pm N/2$ presents problems when considering an odd number of spectral derivatives, so the coefficients $\hat{f}_{N/2}$ and $\hat{f}_{-N/2}$ are set to zero (Bewely (2007)). Other high wavenumbers also

present a problem in spectral methods. The nonlinear term in the momentum equation can transfer energy from low to high-wavenumers. If two relatively large wavenumber modes interact through the nonlinear term, they can produce energy to wavenumbers larger than the Nyquist (Bewely (2007)). The resulting wavenumbers, $|k| > N/2$ cannot be represented with a discrete Fourier series and will be aliased to lower wavenumbers. This occurs since the k Fourier mode and the $k + mN$ mode look the same on when represented by $k = -N/2...0...N/2$ where m is a positive or negative integer (Canuto et al. (1988)). It is therefore possible for high wavenumers to feed spurious energy to low wavenumber modes, contaminating the solution. In order to remedy this, the Orszag 2/3 de-aliasing method is used (see Canuto et al. (1988) for a description). In Diablo, this is done by zeroing all Fourier modes with wavenumbers $k > N/3$ before transforming to physical space.

Evaluation of the nonlinear term in the Navier-Stokes equations in a spectral code is not straightforward. For the terms that involve a horizontal derivative, we would like to evaluate the derivate in Fourier space to get spectral accuracy. However, since these terms involve a product, evaluating it in Fourier space would require computing a discrete convolution sum which requires $O(N^2)$ operations where N is the number of gridpoints in *one* direction. For large problems, this will become very computationally costly. Instead, we use the so-called pseudo-spectral method where the nonlinear term is first written in conservation form:

$$\frac{\partial}{\partial x_j}(u_i u_j). \tag{VI.8}$$

The product in parentheses is computed in physical space, requiring $O(N)$ operations. This is then transformed into Fourier space requiring $O(N\log(N))$ operations using the FFT algorithm, and the derivatives are taken in Fourier space, requiring an additional $O(N)$ operations. This method of computing the nonlinear term is then $O(N\log(N))$ instead of $O(N^2)$.

In the wall-bounded finite difference directions, Diablo uses a staggered grid with vertical velocity located at "G" nodes and the horizontal velocity, pres-

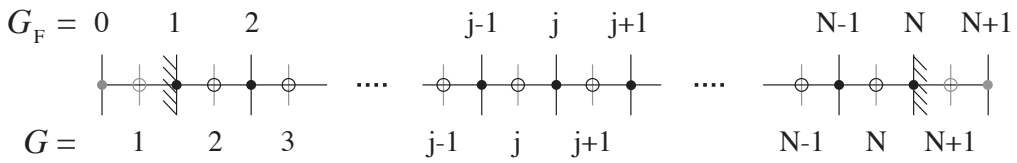

Figure VI.1: Grid layout of Diablo in the wall-normal directions. The wall-normal velocity is stored at G points (open circles), all other variables are stored at G_F points (closed circles). Note that G here stands for G_X, G_Y, and/or, G_Z, depending on which directions are wall-bounded.

sure, and scalars defined at "$G_{1/2}$" nodes, see figure VI.1. Grid stretching is used in the wall-bounded directions in order to resolve small-scale turbulence near the wall. The $G_{1/2}$ cells are located exactly halfway between neighboring G points. The staggering is done so that neighboring pressure values are coupled. If central finite differences were used on a collocated grid, neighboring pressure values would be coupled only through the viscous term, and so for large Reynolds numbers oscillatory solutions may arise (Fletcher (1991)). The location of the walls (marked by cross-hatching in Figure VI.1) are chosen to coincide with wall-parallel velocity points. Interpolation from the G grid to the $G_{1/2}$ grid is then accomplished by taking the average of neighboring values which is second-order accurate. In order to interpolate a quantity f from the $G_{1/2}$ to the G grid with second order accuracy, the following formula is used:

$$f(G^j_{1/2}) = \frac{1}{2\Delta G^j}(\Delta G^{j-1}_{1/2} f(G^j_{1/2}) + \Delta G^j_{1/2} f(G^{j-1}_{1/2})). \tag{VI.9}$$

This equation is not always used for interpolation, and is substituted for less accurate interpolation schemes where necessary to ensure discrete mass, momentum, and energy conservation as derived by Bewley (1999).

In the finite difference directions, boundary conditions are applied using ghost cells as depicted by gray circles in Figure VI.1. The boundary conditions can be either Neumann or Dirichlet with the gradient or boundary value specified, respectively. Since a staggered grid is used, the boundary conditions are not always

applied exactly at the wall locations, but it is ensured that the discrete conservation properties are satisfied. Since the grid spacing near the wall is small, this should not significantly affect the results. When Neumann boundary conditions are specified for the wall-parallel velocity or the scalars, the value of the ghost cell at $G_{1/2} = 0$ and $G_{1/2} = N+1$ is set so that the wall-normal derivative at $G = 1$ and $G = N+1$ is the specified value. Since the wall-normal velocity is offset from the wall, its gradient can easily be specified exactly at the wall. When Dirichlet boundary conditions are used, the wall-parallel velocity and scalars are prescribed at the wall locations, while the wall-normal velocity is specified at the $G = 2$ and $G = N$ points.

In addition to solving the momentum equations, Diablo has the capacity for timestepping the scalar advection-diffusion equation. Any number of scalars can be considered (including zero) and memory is allocated accordingly. The timestepping for the scalar equations is done using the same scheme as the momentum equations. Each scalar is associated with a unique Prandtl and Richardson number, enabling the consideration of multiple active scalars such as temperature and salinity or passive scalars to simulate a dye release. The updating of the scalars and velocity is offset so that the scalars at the $k+1$ step are found using the velocity at the k step, then the velocity is updated with the buoyancy term evaluated at $k+1$. The scalars coincide with the wall-parallel velocity points on the staggered grid.

In order to simulate model problems of interest for geophysical applications, additional terms are included to account for a rotating coordinate frame. One term, the centripetal acceleration, is conservative and can be expressed as the gradient of a potential and absorbed into the definition of the pressure. The second term, the Coriolis acceleration represents a new term in the equations of motion. For convenience, a background pressure gradient used to force the flow is written in terms of a geostrophic wind, U_G, and included in the Coriolis term. The x-axis is chosen to be aligned with the geostrophic wind, not necessarily in the east-west

direction. When placed on the right hand side of the momentum equations, the Coriolis term is:

$$\begin{aligned} &(\frac{-\cos(\phi)\sin(\gamma)}{\sin(\phi)}w + v)\hat{i} \\ &(\frac{\cos(\phi)\cos(\gamma)}{\sin(\phi)}w - u + U_G)\hat{j} \\ &(-\frac{\cos(\phi)\cos(\gamma)}{\sin(\phi)}v + \frac{\cos(\phi)\sin(\gamma)}{\sin(\phi)(u - U_G)})\hat{k}. \end{aligned} \tag{VI.10}$$

In deriving this term, we have not assumed that the rotational vector is aligned with the vertical direction as is done in many ocean models (and called the 'traditional approximation'). Instead, ϕ is the latitude, and γ is the angle made between the geostrophic velocity and a northward heading.

VI.2 Large Eddy Simulation

A direct numerical simulation (DNS) involves solving the Navier-Stokes equations with specified initial and boundary conditions where the viscosity and diffusivity are the molecular values. In order to guarantee accuracy, a DNS must resolve nearly all scales of motion. The smallest scale that a turbulent eddy can take before being damped out by viscosity is estimated by the Kolmogorov scale, η defined as:

$$\eta = (\frac{\nu^3}{\epsilon})^{1/4}. \tag{VI.11}$$

An estimate of the range of scales that must be considered by a DNS can be obtained by dividing the Kolmogorov scale by the scale of the largest eddies, h.

$$\frac{\eta}{h} = \nu^{3/4}\epsilon^{-1/4}h^{-1} = Re_o^{-3/4}(\frac{h\epsilon}{U_o^3})^{-1/4}, \tag{VI.12}$$

where $Re_o = U_o h/\nu$, and U_o is the velocity scale associated with the large-scale motions. The last term in parentheses is the dissipation normalized by the large scale velocity and length. According to Kolmogorov's hypothesis, dissipation is driven by the large scales of motion, independent of viscosity, which implies that this last term should be independent of Reynolds number. Since a DNS must

resolve the all scales of motion, the number of gridpoints needed in each direction will scale with h/η, which we see from Eq. VI.12 is $O(Re_o^{3/4})$. The total number of gridpoints for a three-dimensional simulation will thus scale with $Re_o^{9/4}$, so a doubling of the outer Reynolds number requires nearly a five-fold increase in the number of points used. This requirement is made even more severe since the size of the timestep that is taken must decrease with the gridspacing, and it can be shown (Pope (2000)) that the total computational cost scales with Re_o^3.

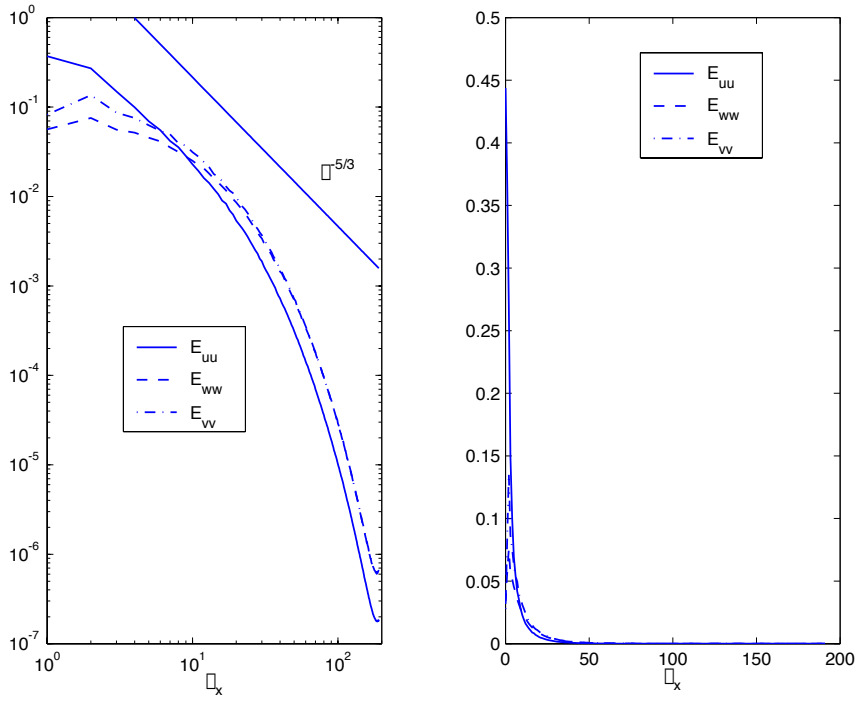

Figure VI.2: One-dimensional energy spectra for turbulent channel flow at $Re_\tau = 590$ at $z^+ = 298$ from the data of Moser et al. (1999)

Most of the energy in a turbulent flow is contained in its largest scales of motion. This is illustrated in Figure VI.2, which shows the one dimensional velocity spectra from the DNS of turbulent channel flow of Moser et al. (1999) at $Re_\tau = 590$ taken at a height of $z^+ = 298$. The panel on the left of Figure VI.2 shows the spectra as they are traditionally plotted with logarithmic axes

with the Kolmogorov inertial subrange model spectrum for reference. The panel on the right shows the same spectra on linear axes. It is clear that most of the wavenumbers considered by the DNS carried a very small amount of energy. This does not imply that these scales are not important to the simulations since they play an important role in the turbulent energy cascade. Still this gives hope that an adequate representation of the flow may be obtained by directly solving for the velocity by resolving only the low wavenumbers.

A large eddy simulation (LES) explicitly solves the largest scales of motion and models the influence of the smaller scales. Specifically, the equations of motion are filtered in space; when the incompressible, Boussinesq form is used we get:

$$\frac{\partial \overline{u_i}}{\partial t} + \frac{\partial \overline{u}_j \overline{u}_i}{\partial x_j} = -\frac{\partial \overline{p'}}{\partial x_i} - Ri_\tau \overline{\rho'}\hat{\mathbf{k}} + \frac{1}{Re_\tau}\frac{\partial}{\partial x_j}\frac{\partial \overline{u_i}}{\partial x_j} - \frac{\partial \tau_{ij}}{\partial x_j}, \tag{VI.13}$$

$$\frac{\partial \overline{\rho}}{\partial t} + \frac{\partial \overline{u}_j \overline{\rho}}{\partial x_j} = \frac{1}{Re_\tau Pr}\frac{\partial}{\partial x_j}\frac{\partial \overline{\rho}}{\partial x_j} - \frac{\partial \lambda_j}{\partial x_j}, \tag{VI.14}$$

$$\frac{\partial u_i}{\partial x_i} = 0, \tag{VI.15}$$

where $\overline{u_i}$ denotes the filtered velocity field. The last terms in Eqns. VI.13 and VI.14 represent the effect of the sub-filter scales on the filtered velocity and density. Since the LES solves only for the filtered velocity, the sub-filter contributions must be modeled. The residual stress tensor as it appears in equation VI.13 is then: (Pope (2000))

$$\tau_{ij} = \overline{u_i u_j} - \overline{u}_i \overline{u}_j. \tag{VI.16}$$

There are many possible choices of models for the sub-filter momentum stress and buoyancy flux. Here we chose to implement the dynamic Smagorinsky method with an optional scale-similar part. In the dynamic Smagorinsky model, first proposed by Germano et al. (1991), the deviatoric part of the sub-filter stress and buoyancy flux are modeled as

$$\tau_{ij} = -2\nu_{sgs}\overline{S_{ij}}, \qquad \lambda_i = -\kappa_{sgs}|\frac{\partial \overline{\rho}}{\partial x_i}, \tag{VI.17}$$

where $\overline{\Delta}$ is the filter width, $\overline{S_{ij}}$ is the resolved rate of strain tensor, and C_M and C_ρ are the dynamic coefficients that will be set using the dynamic procedure. The

subgrid-scale eddy viscosity and eddy diffusivity are given by

$$\nu_{sgs} = C_M \overline{\Delta}^2 |\overline{\mathbf{S}}|, \qquad \kappa_{sgs} = C_\rho \overline{Delta}^2 |\overline{\mathbf{S}}|.$$

The dynamic coefficients, C_M and C_ρ are determined by applying a test filter to the LES filtered field. $\hat{\bar{f}}$ denotes a field, f, that has been filtered first by the LES filter and subsequently by the test filter. The scales between the LES and test filter widths are used to estimate the dynamic coefficients. Specifically, the dynamic procedure is:

$$C_M = -\frac{1}{2}\frac{< L_{ij} M_{ij} >}{< M_{ij} M_{ij} >}, \tag{VI.18}$$

where

$$L_{ij} = \widehat{\overline{u}_i \overline{u}_j} - \widehat{\overline{u}}_i \widehat{\overline{u}}_j, \tag{VI.19}$$

$$M_{ij} = \widehat{\overline{\Delta}}^2 \widehat{\overline{|S|}\,\overline{S_{ij}}} - \widehat{\overline{\Delta}^2 \overline{|S|} \overline{S_{ij}}}. \tag{VI.20}$$

The dynamic coefficient for the sub-filter buoyancy flux is determined in a similar way:

$$C_\rho = -\frac{1}{2}\frac{< L_i M_i >}{< M_j M_j >}, \tag{VI.21}$$

where now

$$L_i = \widehat{\overline{\rho u_i}} - \widehat{\overline{\rho}}\widehat{\overline{u}_i}, \quad M_i = \widehat{\overline{\Delta}}^2 \widehat{\overline{|S|}\frac{\partial \overline{\rho}}{\partial x_i}} - \widehat{\overline{\Delta}^2 \overline{|S|}\frac{\partial \overline{\rho}}{\partial x_i}}. \tag{VI.22}$$

Since the dynamic model estimates the sub-filter stress and buoyancy flux by applying a second 'test' filter, the choice of the filter width is the *only tunable* parameter in the dynamic model given the definition of $\overline{\Delta}$ in terms of Δ_g. Here, the test filter can be applied in either physical or Fourier space. Unless otherwise noted, all applications described here will apply a filter based on an explict five-point trapezoidal rule in the wall-parallel directions only. The ratio of the LES to grid filter widths is taken to be $\overline{\Delta}/\Delta_g = 3$. This is consistent with the pseudo-spectral method used here. Since we have applied the 2/3 de-aliasing rule, the smallest resolved wavelength is $3\Delta_g$, which therefore corresponds to the lengthscale associated with the implicit LES filter. The ratio of the test to LES filter is taken to be $\hat{\overline{\Delta}}/\overline{\Delta} = 4$. It is our experience that $\hat{\overline{\Delta}}/\overline{\Delta} = 2$, the common

choice for finite difference codes, is not the optimal choice here. Unlike when a filter is applied in Fourier space, the test filter used here does not have a well-defined width, and the specified width was found to be optimal based on trial and error. Although the grid size and the LES filter width are not equal, the terms sub-filter and sub-grid scale will be used interchangeably to refer to scales unresolved by the LES.

One advantage of the dynamic model is that it contains few adjustable parameters and can be used in a variety of flow regimes. For example, for wall-bounded flows the dynamic coefficient adjusts so that the length scale associated with the Smagorinsky coefficient and the filter width, $l = (C_M\overline{\Delta}^2)^{1/2}$ decreases near the wall without the use of a prescribed damping function (Piomelli (1993)). Piomelli and Liu (1995) considered rotating channel flow and found that the dynamic model LES performed well compared to a DNS. The dynamic model (with a scale-similar part to be described below) has been used successfully in many previous studies including lid-driven cavity flow (Zang et al. (1994)), stratified channel flow (Armenio and Sarkar (2002); Taylor et al. (2005)), and a rotating, tidally-driven boundary layer (Salon (2004)).

For stratified flow, Armenio and Sarkar (2002) found that although stratification is not explicitly represented in the LES model, the dynamic coefficient adjusted in a reasonable manner. For example, Figure VI.3 shows that the sub-grid turbulent Prandtl number increased with the gradient Richardson number in their simulations of stratified channel flow. While the exact dependence of the turbulent Prandtl number on the gradient Richardson number is problem specific, many previous studies show a positive correlation. Figure VI.4 shows the dependence for a variety of numerical studies, field data, and proposed models including results of the stratified open channel flow presented earlier. While the data varies significantly, each study shows an increase in the turbulent Prandtl number with gradient Richardson number, a feature that is automatically picked up by the dynamic Smagorinsky model.

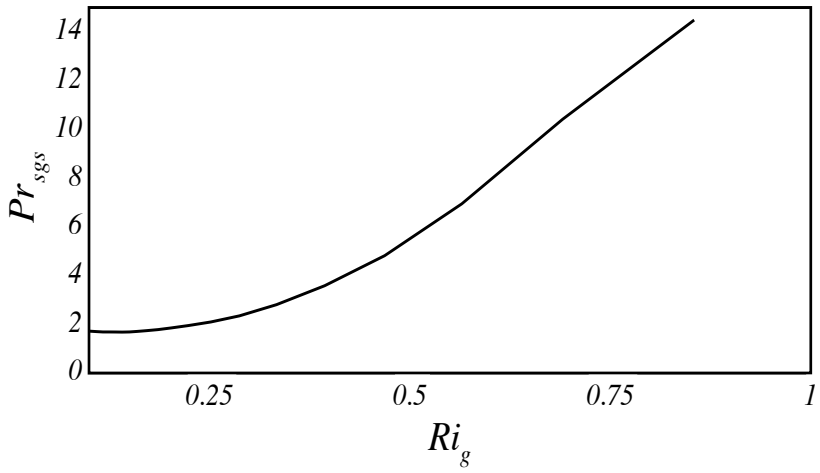

Figure VI.3: Subgrid turbulent Prandtl number and gradient Richardson number from Armenio and Sarkar(2002)

The primary disadvantage of the dynamic model is the computational cost. The algorithm that has been written for Diablo seeks to minimize the computational cost (flops) at the expense of added memory allocation. For example, $\overline{S_{ij}}$, $\overline{|S|}$, and $\hat{\overline{u_i}}$ are computed at every point in space and placed in storage arrays at start of the dynamic procedure since each are needed in multiple places in the algorithm. Since a LES with the dynamic model is significantly more expensive than a DNS for the same number of gridpoints, it is unlikely that available memory will be a limiting factor for a LES. A measure of the computational load can be estimated by considering the number of FFT calls, the most expensive operation in the algorithm. In an unstratified DNS of channel flow, Diablo requires 14 calls to the FFT algorithm (including both forward and inverse transforms) for each Runge-Kutta substep, as shown later in Section VI.5. The dynamic procedure adds 12 FFT calls, which are requried to transform the six unique components of the $\overline{S_{ij}}$ tensor to physical space where products are computed and to transform the sub-filter stress-tensor to Fourier space since derivatives in the wall-parallel directions are needed for the contribution to the momentum equations. For an

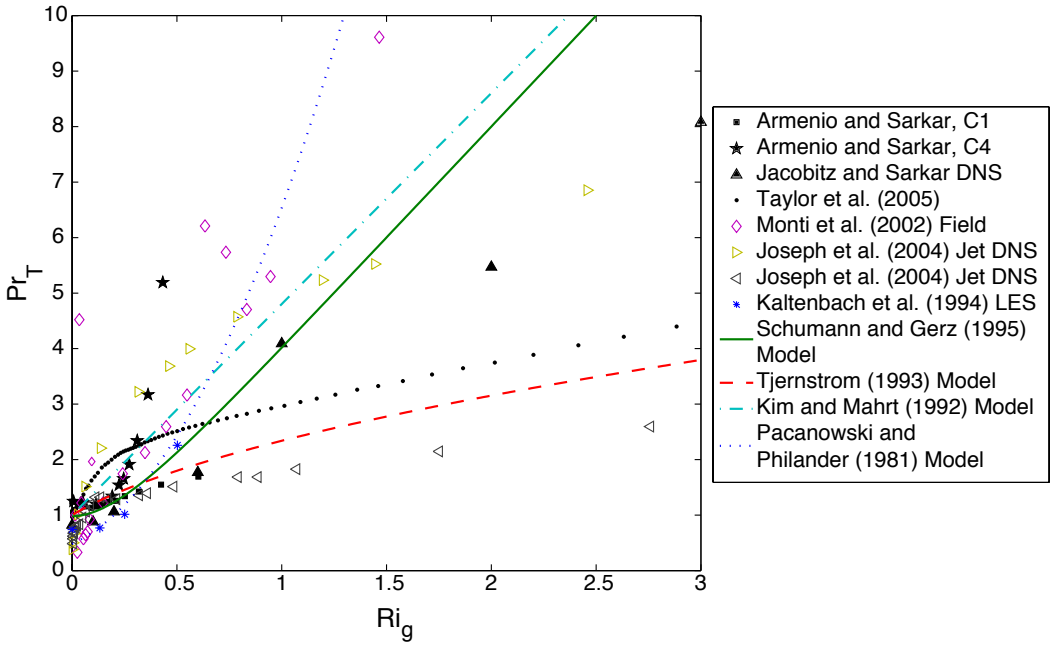

Figure VI.4: Dependence of the turbulent Prandtl number on the gradient Richardson number

unstratified DNS of channel flow, Diablo requires 11 three-dimensional storage arrays. The dynamic mixed subgrid-scale model used for the LES more than doubles the memory requirement by requiring an additional 19 three-dimensional storage arrays. The LES algorithm has been designed to save commonly used quantities, such as the test-filtered velocity fields and the strain rate tensor which are needed at multiple steps in the algorithm. This effectively sacrifices extra storage in order to minimize the computational cost. Since an LES with the dynamic model is typically much slower than a DNS for the same number of grid points, the limiting factor is often the computational cost, and not the memory storage.

In the above equations for the dynamic model coefficients, $< \cdot >$ denotes an averaging operator. This was introduced by Germano et al. (1991) in a channel flow application where the average was taken over the planes parallel to the walls. Since it is possible for M_{ij} to be zero, Germano introduces the averaging operator to keep C_M well-conditioned. When C_M is positive, the model is purely dissipative;

that is the subgrid-scale model acts as a sink for the resolved turbulent kinetic energy. If C_M were less than zero than the opposite would be true and energy would be transferred from the subgrid to the resolved scale motions, a process known as backscatter. By considering the interactions of various Fourier modes through the nonlinear term in the momentum equations, it can be shown that backscatter is theoretically possible and may sometimes be expected locally in physical space (Pope (2000)). In practice, however, it is found that negative values of C_M lead to numerical instabilities and, therefore, when this occurs C_M is set to zero (Meneveau and Katz (2000)). In this study, since all problems of interest are statistically homogeneous in the wall-parallel directions, C_M and C_ρ are always averaged over wall-parallel planes and set to zero if they ever become negative. For flows that are not statistically homogeneous, local averaging techniques have been proposed such as the Lagrangian averaging method of Meneveau et al. (1996).

The assumption that the subgrid stress tensor is aligned with the strain rate tensor and that the subgrid is purely dissipative can be relaxed by including an addition term in the subgrid model. Bardina et al. (1980) proposed a scale-similar model, in which it is assumed that the unresolved stress is proportional to the sub test-filter stress:

$$\tau_{ij} = \widehat{\overline{u_i}\overline{u_j}} - \widehat{\overline{u}_i}\widehat{\overline{u}_j}. \tag{VI.23}$$

Since $\overline{u_i}$ is known, we can then compute the sub test-filter stress directly. This model does allow energy transfer from the unresolved to the resolved scales, but it is generally not dissipative enough and Bardina (1980) proposed combining it with an eddy viscosity model. Zang et al. (1994) was the first to combine the scale similar model with a dynamic eddy viscosity model to form the so-called dynamic mixed model (DMM). This model has been implemented in Diablo and it has been shown to perform very well in a variety of situations (Meneveau and Katz (2000)). With the DMM, the subgrid scale stress tensor is:

$$\tau_{ij} = (\widehat{\overline{u}_i\overline{u}_j} - \hat{\overline{u}}_i\hat{\overline{u}}_j) - 2C_M\overline{\Delta}^2\overline{|\mathbf{S}|}\overline{S}_{ij}, \tag{VI.24}$$

and the equation for the dynamic coefficient has an extra term:

$$C_M = -\frac{1}{2}\frac{< L_{ij}M_{ij} > - < N_{ij}M_{ij} >}{< M_{ij}M_{ij} >}, \tag{VI.25}$$

where

$$N_{ij} = (\widehat{\overline{\widehat{u}_i}\overline{\widehat{u}_j}} - \widehat{\overline{\widehat{u}}_i}\widehat{\overline{\widehat{u}}_j}) - (\widehat{\overline{u_i}\overline{u_j}} - \widehat{\overline{u}_i}\widehat{\overline{u}_j}). \tag{VI.26}$$

Note that the scale-similar part is considered only for the momentum equation; the subgrid buoyancy flux is modeled as in Eq. VI.21 with a dynamic eddy viscosity model. The most expensive part of the dynamic algorithm are the many filtering operations that are performed. When the filtering is done in Fourier space and multiplication operations are done in physical space, many discrete Fourier transforms need to be added at each time-step. Decreasing the number of required Fourier transforms and thereby decreasing the computational load is one motivation for the choice of filtering in physical space that has been made in the studies reported here.

VI.3 Open Boundary Conditions

In order to approximate an unbounded domain in the vertical, an open boundary condition is employed. This is accomplished through a combination of a Rayleigh damping or 'sponge' layer and a radiation condition. An introduction to both types of boundary conditions can be found in Durran (1999).

The concept behind the sponge layer is simple: in a region at the top of the computational domain, the velocity and scalar fields are relaxed towards a specified background state. Sponge layers can be very effective at eliminating reflections if the damping region is large enough so that the strength of the damping increases gradually. An illustration of the effectiveness of a sponge layer is seen in Fig. VI.5. Here, oscillatory vertical forcing is applied to a small region in an otherwise quiescent background with a uniform stratification, and contours of the horizontal velocity are plotted. The forcing creates beams of internal waves radiating away

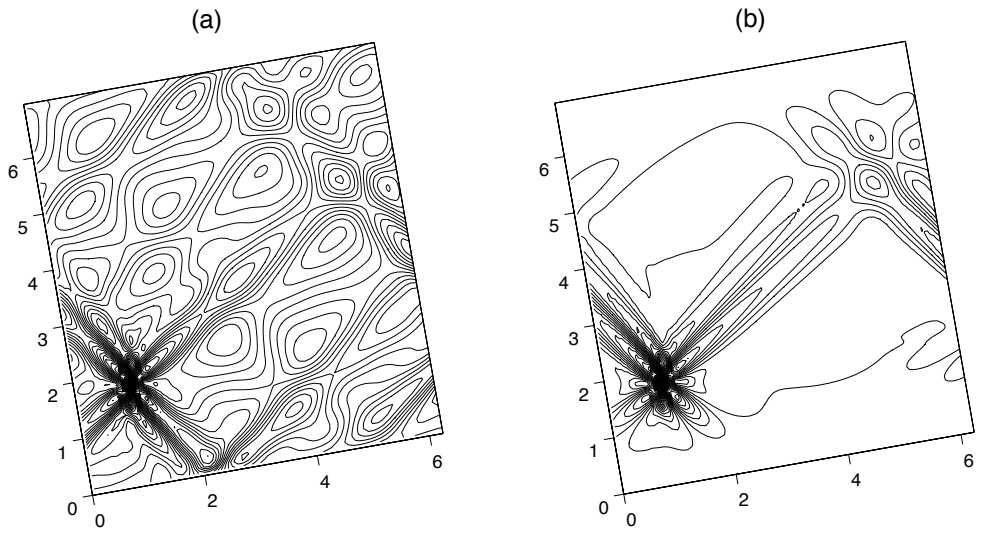

Figure VI.5: Test of the sponge layer

at angles that depend on the forcing frequency and the background buoyancy frequency. The entire domain is tilted at an angle of 10^o to the horizontal so that the waves produced intersect the boundary at two different angles. In Fig. VI.5(a) the boundary condition at the top and bottom walls are free-slip and constant density gradient and the horizontal directions are periodic. The simulation has been run for a sufficiently long time to fill the domain with internal waves. Figure VI.5(b) is the same test but with sponge regions placed near the upper and lower walls, and most of the reflections are eliminated.

The radiation boundary condition involves constructing a linearized wave using the instantaneous velocity, density, and pressure at the boundary and setting the downward propagating part to zero. This boundary condition was developed by Klemp and Durran (1983) and is summarized in Durran (1999). When solving the incompressible Boussinesq equations, this boundary condition takes the form of a Dirichlet boundary condition on the Fourier coefficients of the pressure. The procedure to obtain the appropriate boundary condition in three dimensions is a

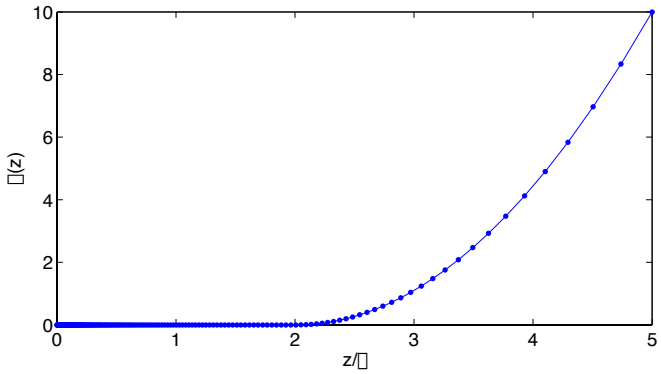

Figure VI.6: Sponge layer damping coefficient

generalization of that found for the two-dimensional problem found in Klemp and Durran (1983). Start with the nonrotating, hydrostatic equations, linearized about a constant mean flow aligned with the x-direction:

$$\frac{\partial u}{\partial t} + U\frac{\partial u}{\partial x} + \frac{\partial p}{\partial x} = 0 \tag{VI.27}$$

$$\frac{\partial v}{\partial t} + U\frac{\partial v}{\partial x} + \frac{\partial p}{\partial y} = 0 \tag{VI.28}$$

$$\frac{\partial \rho}{\partial t} + U\frac{\partial \rho}{\partial x} + \frac{d\overline{\rho}}{dz}w = 0 \tag{VI.29}$$

$$\frac{\partial p}{\partial z} - g\frac{\rho}{\rho_0} = 0 \tag{VI.30}$$

$$\frac{\partial u}{\partial x} + \frac{\partial v}{\partial y} + \frac{\partial w}{\partial z} = 0 \tag{VI.31}$$

Inserting into these equations the form of a linear plane wave: $u = \hat{u}\,\exp[i(kx + ly - \omega t)]$ . . . gives:

$$-\omega\hat{u} + kU\hat{u} + k\hat{p} = 0 \tag{VI.32}$$

$$-\omega\hat{v} + kU\hat{v} + l\hat{p} = 0 \tag{VI.33}$$

$$-\omega\hat{\rho} + kU\hat{\rho} - i\hat{w}\frac{d\overline{\rho}}{dz} = 0 \tag{VI.34}$$

$$\frac{\partial \hat{p}}{\partial z} - g\frac{\hat{\rho}}{\rho_0} = 0 \tag{VI.35}$$

$$ik\hat{u} + il\hat{v} + \frac{\partial \hat{w}}{\partial z} = 0 \tag{VI.36}$$

Eliminating all variables from the above set of equations except for $\hat{w}$ yields:

$$N^2 \frac{k^2 + l^2}{(Uk - \omega)^2} \hat{w} + \frac{\partial^2 \hat{w}}{\partial z^2} = 0 \tag{VI.37}$$

Solutions to this equation are of the form:

$$\hat{w} = Aexp(\frac{iN(k^2 + l^2)^{1/2} z}{Uk - \omega}) + Bexp(-\frac{iN(k^2 + l^2)^{1/2} z}{Uk - \omega}). \tag{VI.38}$$

Since the second term corresponds to waves with upward propagating energy, set $B = 0$. Then it follows that

$$\frac{\partial \hat{w}}{\partial z} = iN \frac{(k^2 + l^2)^{1/2}}{Uk - \omega} \hat{w}. \tag{VI.39}$$

An equation relating the pressure to the vertical velocity can be found using the horizontal momentum and continuity equations:

$$\frac{\partial \hat{w}}{\partial z} = i\hat{\phi} \frac{k^2 + l^2}{Uk - \omega}. \tag{VI.40}$$

Finally, combining the final two equations gives a relation between the pressure and vertical velocity:

$$\hat{\phi} = \frac{N}{(k^2 + l^2)^{1/2}} \hat{w}. \tag{VI.41}$$

This equation is very easy to implement in the code used here since the Fourier modes of the vertical velocity are already known. The equations used above to obtain the boundary conditions were simplified from the rotating, nonhydrostatic equations simulated in our DNS and LES studies. Klemp and Durran (1983) give the result of the derivation starting with the linearized rotating non-hydrostatic equations, in which case Eq. (VI.42) becomes

$$\hat{\phi} = \frac{N}{(k^2 + l^2)^{1/2}} \hat{w} \left[1 - \frac{(Uk + Vl - \omega)^2}{N^2} \right]^{1/2} \left[1 - \frac{f^2}{(Uk + Vl - \omega)^2} \right]^{1/2}. \tag{VI.42}$$

Note that the non-hydrostatic and rotating corrections involve the frequency of the wave, ω. Since the frequency of the waves is not known from the instantaneous fields, applying these corrections requires storing the boundary data in time (Bennett (1976)). Klemp and Durran (1983) report adequate results using the boundary

condition given in Eq. VI.42 even when the flow is rotating and nonhydrostatic as long as the scales considered are not too large (less than the Rossby radius). Since our domain is small compared to the Rossby radius and since we also consider a sponge region, the simplified radiation condition in Eq. VI.42 should suffice.

VI.4 Wall Model

Near walls the turbulent motions scale with the viscous scale, $\delta_\nu = \nu/u_\tau$. In order to resolve the energy containing scales near the wall, the LES filter lengthscale and hence the gridspacing need to scale with δ_ν. In the outer region the energy containing scales are much larger, on the order of order δ, which is defined by the geometry of the problem. The ratio of these lengthscales is $\delta_\nu/\delta = \nu/(u_\tau\delta) = 1/Re_\tau$. Most CFD codes, including Diablo, are forced to have a grid spacing in the x and y directions (in the plane of the wall) that do not vary as a function of z (the wall-normal direction). With this requirement and the need to resolve the near wall viscous scale, the x and y grid spacing must be proportional to δ_ν even in the outer region. When large Reynolds numbers need to be considered, such as in geophysical applications, this limitation is prohibitive.

In order to consider large Reynolds number wall bounded flows, a near-wall model is introduced. The model is only active near the wall, and provides a boundary condition for the LES which is free to scale with the outer flow. A variety of near-wall models exist in the engineering and atmospheric science literature. Constructing a near-wall model for the benthic boundary layer is significantly easier than in the atmospheric case since we do not need to model surface heat flux effects since, as we have seen from the DNS and resolved LES, the near wall region remains unstratified. Recall also from the DNS of the benthic Ekman layer that the magnitude of the horizontal velocity follows a logarithmic law. This inspires the use of a model type first proposed by Schumann (1975) and later modified by Grotzbach (1987) in which it is assumed that the instantaneous plane-averaged

velocity obeys a prescribed logarithmic law.

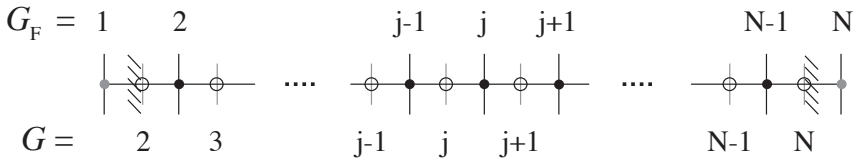

Figure VI.7: Grid layout of Diablo with a near-wall model. The wall-normal velocity is defined at G nodes (open circles) and all other components are defined at $G_{1/2}$ nodes (closed circles).

The near-wall model of Schumann (1975) proceeds as follows. For Poiseuille flow, the steady state wall stress is known *a priori* by integrating the streamwise momentum equation over the wall-normal coordinate. At steady state the wall stress must balance the applied pressure forcing. The wall stress can then be used to estimate the plane averaged velocity at some location in the region where the log law is expected, say at $z^+ = 40$.

$$U(z^+ = 40) = u_\tau(\frac{1}{\kappa} ln(z^+ = 40) + B). \tag{VI.43}$$

Recall that the friction velocity is related to the wall stress by $u_\tau = \sqrt{\tau_w/\rho}$. The first LES gridpoint is then placed at this location, $z^+ = 40$, and the boundary condition supplied from the near-wall model is the local wall stress estimated by assuming that the ratio of the local stress and velocity is equal to the ratio of the corresponding plane averages:

$$\tau_{13}(z = 0)(x, y) = \frac{u(x, y, 1)}{U(1)} < \tau_w > . \tag{VI.44}$$

The local spanwise wall stress is assumed to be proportional to the local spanwise velocity:

$$\tau_{23}(z = 0)(x, y) = \frac{2}{Re_\tau} \frac{v(x, y, 1)}{z(1)}. \tag{VI.45}$$

When a staggered grid is used in the vertical direction, the most natural grid with this wall-model is with a vertical velocity point and the horizontal momentum

flux defined at the wall. The wall stress is then specified according to Eq. VI.44 and used as a boundary condition for the first gridpoint away from the wall. In addition, the wall-normal velocity, the subgrid stress, and the buoyancy flux are set to zero at the wall. Diablo has been written such that when the wall-model is selected, the location of the wall shifts to the wall-normal velocity points as illustrated in Figure VI.7.

We are interested in problems where the wall stress is not known *a priori*, such as a boundary layer with an oscillating free stream velocity. An extension of Schumann's model without a prescribed wall stress was proposed by Grotzbach (1987). Here the first gridpoint of the LES model is placed at $z(1)/\delta$ where the *expected* corresponding location in wall units lies within the logarithmic region. Then the plane average of the streamwise velocity at this location from the LES is used to estimate the friction velocity by iteratively solving

$$\frac{U(1)}{u_\tau} = \frac{1}{\kappa} ln(\frac{z(1)}{\delta}\frac{u_\tau \delta}{\nu}) + B. \tag{VI.46}$$

The local wall stress is then estimated using the friction velocity and the LES velocity:

$$\tau_{13}(z=0) = \frac{u(x,y,1)}{U(1)} u_\tau^2 \rho, \tag{VI.47}$$

$$\tau_{23}(z=0) = \frac{v(x,y,1)}{U(1)} u_\tau^2 \rho. \tag{VI.48}$$

The latter relation was suggested by Piomelli et al. (1989). In steady channel flow, the plane averaged wall stress estimated by this method will necessarily be the same as that prescribed by the Schumann model since the same momentum balance must be satisfied.

The Schumann-Grotzbach near-wall model described above has been implemented in Diablo and tested for unstratified closed channel flow. Closed channel flow was chosen for validation since it is a well-studied problem and DNS results are available for comparison. Note that while it is standard for y to be assigned to the wall-normal direction in the engineering literature, here we will use z to stay

consistent with the geophysical studies in the rest of the thesis. The first horizontal velocity point of the LES is placed at $z^+ = 20$ with a constant wall-normal grid spacing throughout the domain $\Delta z^+ = 40$. We have considered a friction Reynolds number of $Re_\tau = 2000$. After de-aliasing, 48 Fourier modes remain in the horizontal directions which have lengths of $L_x = 2 * \pi * \delta$, and $L_y = \pi * \delta$. Using the number of de-alised modes, the horizontal grid spacing in wall units is then $\Delta x^+ = 262$ and $\Delta y^+ = 131$. The total number of points used after dealiasing is 48 x 48 x 100 in the x, y, and z directions respectively. *By comparision, a DNS at this Reynolds number by Hoyas and Jimenez (2006) used grid of 6144 x 633 x 4608, or nearly 18 billion gridpoints!* The total number of gridpoints used for this near-wall model test is then 6500 times fewer than needed for a DNS done at the same domain size.

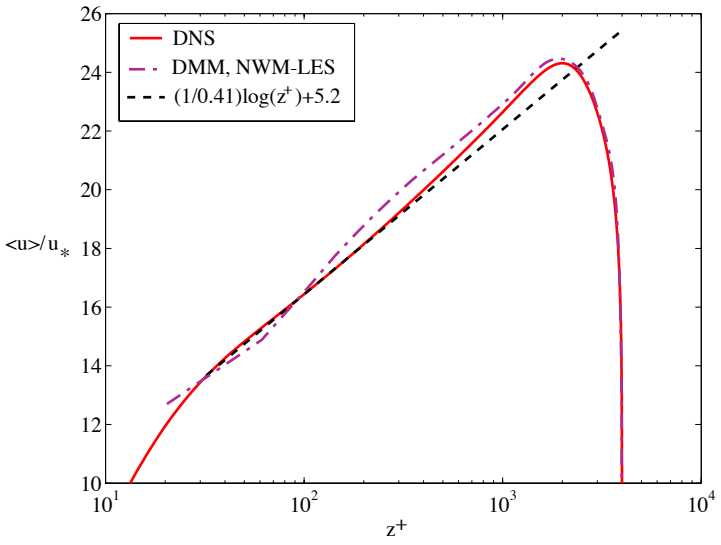

Figure VI.8: Mean velocity profile for near-wall model LES test for closed channel flow, $Re_\tau = u_\tau h/\nu = 2000$, $Re_\infty = U_\infty h/\nu = 49000$

Results from the near-wall model test at a large Reynolds number, $Re_\tau = 2000$, are shown in Figures VI.8 and VI.9. Figure VI.8 shows the streamwise velocity profile plotted as a function of the distance from the lower wall in wall units. Also shown is the expected logarithmic law and DNS results at the same

Reynolds number by Hoyas and Jimenez (2006). The agreement between the mean velocity using the near-wall model, the expected log law, and the DNS is excellent. Notably, the near-wall model LES is able to accurately capture the deviation from the log law near the centerline compared to the DNS. Figure VI.9 shows profiles of the rms velocity and the Reynolds stress averaged over horizontal planes and time at steady state. These turbulent profiles include both the resolved and subgrid-scale components. The dynamic mixed model (DMM) was chosen since it gave a better mean velocity profile than the dynamic eddy viscosity model (DEVM). We found that the DMM predicted a larger total turbulent kinetic energy than the DEVM, and it appears from Figure VI.9 that the energy is larger than might be expected from a DNS. In addition, the peaks in the rms velocities are too far from the wall; the peak u_{rms} velocity for example is at the second gridpoint at $z^+ = 60$ whereas DNS studies indicate that it should be near $z^+ = 15$. Since the peak in turbulent production occurs in the buffer layer (Pope (2000)), these differences in the near-wall turbulence intensities are not unexpected for a near-wall model simulation with such a coarse grid. The rms velocity profiles using the near-wall model at a lower Reynolds number of $Re_\tau = 400$ in open channel flow are compared directly to DNS and resolved LES with a dynamic eddy viscosity subgrid model in Figure VI.10. Here, the peak in the turbulent profiles is underpredicted and slightly too far away from the wall, but the general agreement is quite good. This test at $Re_\tau = 400$ used 32 uniformly spaced points in the vertical direction for the wall-model simulation compared to 128 and 192 for the resolved LES and DNS, respectively.

Since the previous relations assumed that the wall stress is aligned with the outer flow, they cannot be directly applied to the Ekman layer. Instead, for the results presented in Chapter III, we modify the model of Grotzbach (1987) as follows. First, the friction velocity and the magnitude of the wall stress are found by applying the logarithmic law to the *magnitude* of the horizontal velocity at the first LES gridpoint as in Eq. VI.46. Then the plane average wall stresses in the

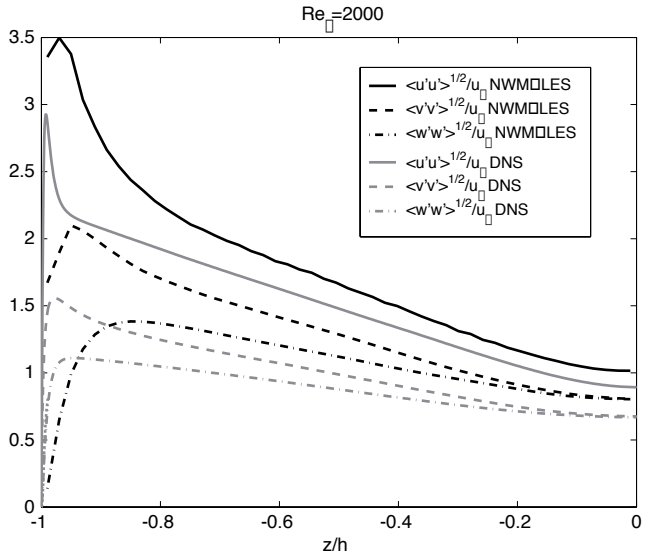

Figure VI.9: Turbulent profiles for near-wall model LES test for closed channel flow using the dynamic mixed subgrid-scale model, $Re_\tau = 2000$, $Re_\infty = 49000$

streamwise (x) and cross-stream (y) directions are found by specifying the angle α_0 between the free stream and the wall stress:

$$< \tau_{13} >= |\tau_w| cos(\alpha_0), \quad < \tau_{23} >= |\tau_w| sin(\alpha_0). \tag{VI.49}$$

Then, the x-z component of the local stress is found from:

$$\tau_{13}(x, y) = u(x, y, 1) \frac{< \tau_{13} >}{U(1)}, \tag{VI.50}$$

and the local y-z stress is estimated by taking taking the local maximum of the following expressions:

$$\tau_{23}(x, y) = v(x, y, 1) \frac{< \tau_{23} >}{V(1)}, \tag{VI.51}$$

$$\tau_{23}(x, y) = v(x, y, 1) \frac{< \tau_{13} >}{U(1)}. \tag{VI.52}$$

The maximum of these two expression is chosen to prevent the spanwise stress from becoming too small when the mean spanwise stress is small. Equations VI.50 - VI.52 are then used as the boundary condition on the LES velocity field.

An alternative near-wall model formulation for geophysical boundary layers was proposed by Marusic et al. (2001) which will be referred to as the MKP

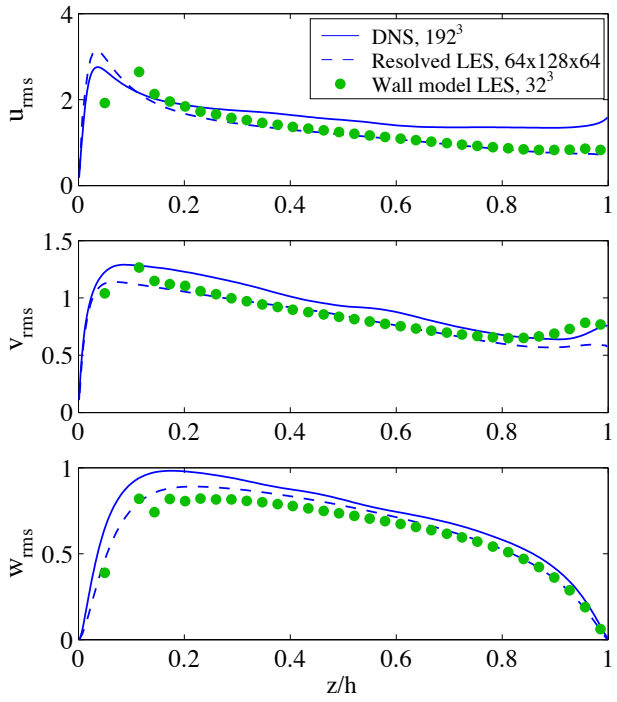

Figure VI.10: Turbulent profiles for open channel flow, $Re_\tau = 400$ using the dynamic eddy-viscosity subgrid-scale model

model. The model was formulated as an attempt to improve on the SG models by increasing the level of fluctuations in the local wall stress and to improve the velocity spectra in the logarithmic region (Marusic et al. (2001)). This model has another advantage that it works for both rotating and non-rotating flows and does not require the specification of the wall-stress angle, α_0. This model is formulated as:

$$\tau_{i,3}(x,y) = U_i(z(1))\frac{|\tau_w|}{(U(z(1))^2 + V(z(1))^2)^{1/2})} - \alpha u_*[u_i(x+\delta_d, y, z(1) - U_i(z(1))]. \tag{VI.53}$$

Marusic et al. (2001) hypothesized that the constant α should be universal, and is empirically determined to be 0.10. It can be shown (R.Stoll and Porte-Agel (2006)) that the MKP model is identical to the shifted SG model if

$$\alpha = \frac{\kappa}{ln(z(1)/z_0)}. \tag{VI.54}$$

However, Marusic et al. (2001) hypothesize that α should not depend on either the roughness or the grid-spacing. Indeed, a better agreement with similarity theory and experimental observations has been obtained with the MKP model compared to the MKP model for rough wall boundary layers (R.Stoll and Porte-Agel (2006)). The MKP model has been used in the NWM-LES presented in Chapter IV.

VI.5 Algorithm: Channel Geometry

Here, we will present the algorithm that Diablo uses for channel flow with periodic boundary conditions on the velocity in the x_1 (x) and x_3 (z) directions and walls bounding the flow in the x_2 (y) direction. Wall-normal derivatives are treated with second order, central finite differences, while the x_1 (x) and x_3 (z) directions are treated with a pseudo-spectral method. Time-stepping is accomplished with a mixed implicit/explicit strategy with all terms involving wall-normal derivatives stepped with Crank-Nicolson and all other terms treated with a low storage 3rd order Runge-Kutta method. The right hand side of the momentum equations $\partial u_i/\partial t = ...$ are stored in R_i while the Runge-Kutta terms will be stored in F_i and saved for the next R-K substep. $\widehat{u}_i$, $\widehat{R}_i$, etc. denote the Fourier space representations. Care has been taken to order the algorithm so that the physical and Fourier space arrays can occupy the same location in memory. In order to clarify the operations, the intermediate and final velocity will both be denoted by u_i. It is implied that each step is done over all gridpoints in physical space or modes in Fourier space. For notational simplicity, only those steps which depend on neighboring points are explicitly indexed.

Below is an algorithm based on the above choices that has been carefully ordered in order to minimize the number of storage variables and FFT calls.

For $t = 1 \ldots$ (# of time steps)
For $rk = 1 \ldots 3$

1. Start building the right hand side array with the previous velocity in Fourier space ($\widehat{u}_i$)
   $\widehat{R}_i = \widehat{u}_i,$

2. If ($rk > 1$) then add the term from the previous rk step
   $\widehat{R}_i = \widehat{R}_i + \overline{\zeta}_{rk}\overline{\beta}_{rk}\widehat{F}_i$

3. Add the pressure gradient to the RHS
   $\widehat{R}_1 = \widehat{R}_1 - \overline{h}_{rk}\hat{\imath}k_x\widehat{P}$
   $\widehat{R}_2(k_x, k_z, j) = \widehat{R}_2(k_x, k_z, j) - \overline{h}_{rk}\frac{\widehat{P}(k_x,k_z,j)-\widehat{P}(k_x,k_z,j-1)}{\Delta Y(j)}$
   $\widehat{R}_3 = \widehat{R}_3 - \overline{h}_{rk}\hat{\imath}k_z\widehat{P}$

4. Add P_x, the background pressure gradient that drives the flow
   $\widehat{R}_1(k_x = 0, k_z = 0, j) = \widehat{R}_1(k_x = 0, k_z = 0, j) - \overline{h}_{rk}P_x$

5. Create a storage variable F that will contain all Runge-Kutta terms and start with the viscous terms involving horizontal derivatives.
   $\widehat{F}_i = -\nu(k_x^2 + k_z^2)\widehat{u}_i,$

6. Convert the velocity to physical space
   $\widehat{u}_i \rightarrow u_i$

7. Add the nonlinear terms involving horizontal derivatives to $\widehat{F}$
   $\widehat{F}_1 = \widehat{F}_1 - \hat{\imath}k_x\widehat{u_1u_1} - \hat{\imath}k_z\widehat{u_1u_3}$
   $\widehat{F}_2 = \widehat{F}_2 - \hat{\imath}k_x\widehat{u_1u_2} - \hat{\imath}k_z\widehat{u_3u_2}$
   $\widehat{F}_3 = \widehat{F}_3 - \hat{\imath}k_x\widehat{u_1u_3} - \hat{\imath}k_z\widehat{u_3u_3}$
   (Note that we need 5 independent FFTs here)

8. Now, we are done building the Runge-Kutta terms, add to the right hand side. We will need to keep $\widehat{F}_i$ for the next rk step, so it should not be overwritten below this point.
   $\widehat{R}_i = \widehat{R}_i + \overline{\beta}_{rk}\overline{h}_{rk}\widehat{F}_i$

9. Convert the right hand side arrays to physical space
   $\widehat{R}_i \rightarrow R_i$,

10. Compute the vertical viscous terms and add to the RHS as the explicit part of Crank-Nicolson.

$$R_1(i,j,k) = R_1(i,j,k) + \frac{\nu\overline{h}_{rk}}{2\Delta Y_F(j)}\left(\frac{u_1(i,j+1,k)-u_1(i,j,k)}{\Delta Y(j+1)}\right) - \frac{\nu\overline{h}_{rk}}{2\Delta Y_F(j)}\left(\frac{u_1(i,j,k)-u_1(i,j-1,k)}{\Delta Y(j)}\right)$$

$$R_2(i,j,k) = R_2(i,j,k) + \frac{\nu\overline{h}_{rk}}{2\Delta Y(j)}\left(\frac{u_2(i,j+1,k)-u_2(i,j,k)}{\Delta Y_F(j)}\right) - \frac{\nu\overline{h}_{rk}}{2\Delta Y(j)}\left(\frac{u_2(i,j,k)-u_2(i,j-1,k)}{\Delta Y_F(j-1)}\right)$$

$$R_3(i,j,k) = R_3(i,j,k) + \frac{\nu\overline{h}_{rk}}{2\Delta Y_F(j)}\left(\frac{u_3(i,j+1,k)-u_3(i,j,k)}{\Delta Y(j+1)}\right) - \frac{\nu\overline{h}_{rk}}{2\Delta Y_F(j)}\left(\frac{u_3(i,j,k)-u_3(i,j-1,k)}{\Delta Y(j)}\right)$$

11. Compute the nonlinear terms involving vertical derivatives and add to the RHS as the explicit part of Crank-Nicolson.

$S_1 = \overline{u}_1 * u_2$

$R_1(i,j,k) = R_1(i,j,k) - \frac{\overline{h}_{rk}}{2}(S_1(i,j+1,k) - S_1(i,j,k))/\Delta Y_F(j)$

$S_1 = \overline{u}_3 * u_2$

$R_3(i,j,k) = R_3(i,j,k) - \frac{\overline{h}_{rk}}{2}(S_1(i,j+1,k) - S_1(i,j,k))/\Delta Y_F(j)$

12. Solve the tridiagonal system for the intermediate wall-normal velocity for each i,j:

$$v_2(i,j,k) - \frac{\nu\overline{h}_{rk}}{2}\left(\frac{v_2(i,j+1,k)-v_2(i,j,k)}{\Delta Y_F(j)} - \frac{vv_2(i,j,k)-v_2(i,j-1,k)}{\Delta Y_F(j-1)}\right)/\Delta Y(j) + \overline{h}_{rk}\left(\overline{v}_2(i,j,k)\overline{u}_2(i,j,k) - \overline{v}_2(i,j-1,k)\overline{u}_2(i,j-1,k)\right)/\Delta Y(j) = R_2(i,j,k)$$

13. Now that we have the new intermediate wall-normal velocity, v_2, solve the tridiagonal system for the intermediate v_1 and v_3 using this new velocity.

$$
\begin{aligned}
& v_1(i,j,k) \\
& - \frac{\nu \overline{h}_{rk}}{2} \left(\frac{v_1(i,j+1,k) - v_1(i,j,k)}{\Delta Y(j+1)} - \frac{v_1(i,j,k) - v_1(i,j-1,k)}{\Delta Y(j)} \right) / \Delta Y_F(j) \\
& + \overline{h}_{rk} \left(\overline{v}_1(i,j+1,k) v_2(i,j+1,k) - \overline{v}_1(i,j,k) v_2(i,j,k) \right) / \Delta Y_F(j) \\
& = R_1(i,j,k)
\end{aligned}
$$

$$
\begin{aligned}
& v_3(i,j,k) \\
& - \frac{\nu \overline{h}_{rk}}{2} \left(\frac{v_3(i,j+1,k) - v_3(i,j,k)}{\Delta Y(j+1)} - \frac{v_3(i,j,k) - v_3(i,j-1,k)}{\Delta Y(j)} \right) / \Delta Y_F(j) \\
& + \overline{h}_{rk} \left(\overline{v}_3(i,j+1,k) v_2(i,j+1,k) - \overline{v}_3(i,j,k) v_2(i,j,k) \right) / \Delta Y_F(j) \\
& = R_3(i,j,k)
\end{aligned}
$$

14. Convert the intermediate velocity to Fourier space

$v_i \rightarrow \widehat{v}_i$

15. Solve the tridiagonal system for the pressure correction:

$$
\begin{aligned}
& -(k_x^2 + k_z^2) \widehat{\phi}(k_x, k_z, j) + \left(\frac{\widehat{\phi}(k_x,k_z,j+1) - \widehat{\phi}(k_x,k_z,j)}{\Delta Y(j+1)} - \frac{\widehat{\phi}(k_x,k_z,j) - \widehat{\phi}(k_x,k_z,j-1)}{\Delta Y(j)} \right) / \Delta Y_F(j) \\
& = \hat{i} k_x \widehat{v}_1(k_x,k_z,j) + \hat{i} k_z \widehat{v}_3(k_x,k_z,j) + (\widehat{v}_2(k_x,k_z,j+1) - \widehat{v}_2(k_x,k_z,j)) / \Delta Y_F(j)
\end{aligned}
$$

(Note that in order to avoid an extra storage array, we can store ϕ in R_1 which is no longer needed for this rk step. Also notice that a factor of $\overline{h}_{rk}$ has been absorbed into ϕ)

16. Now, use the gradient of the pressure correction to obtain a divergence-free velocity field.

$\widehat{u}_1^{rk+1} = \widehat{v}_1 - \hat{i} k_x \widehat{\phi}$

$\widehat{u}_2^{rk+1}(k_x, k_z, j) = \widehat{v}_2(k_x, k_z, j) - (\widehat{\phi}(k_x, k_z, j) - \widehat{\phi}(k_x, k_z, j-1))/\Delta Y(j)$
$\widehat{u}_3^{rk+1}\widehat{v}_3 - \hat{i}k_z\widehat{\phi}$

(In order to avoid an extra storage array, only one set of velocity arrays are defined, and this update is done in place.)

17. Finally, update the pressure field using ϕ
$\widehat{P} = \widehat{P} + \widehat{\phi}/\overline{h}_{rk}$

(We need to divide by $\overline{h}_{rk}$ since this constant had been absorbed into $\overline{\phi}$ in the steps above.)

In all, we have 14 FFT calls per Runge-Kutta substep, and 11 full-sized storage arrays.

In the above algorithm, the base grid (G in Fig. VI.7) is denoted by Y) and the fractional grid ($G_{1/2}$ in Fig. VI.7) is denoted by Y_F. The grid spacing centered at the base and fractional grids are denoted by ΔY and ΔY_F, respectively, where

$$\Delta Y(j) = Y_F(j) - Y_F(j-1), \Delta Y_F(j) = Y(j+1) - Y(j). \tag{VI.55}$$

Interpolation of the horizontal velocity components to the base grid is given by

$$\overline{u}_1(i,j,k) = \frac{1}{2}\left(u_1(i,j,k) + u_1(i,j-1,k)\right), \tag{VI.56}$$

$$\check{u}_1(i,j,k) = \frac{1}{2\Delta Y(j)}\left(\Delta Y_F(j)u_1(i,j,k) + \Delta Y_F(j-1)u_1(i,j-1,k)\right), \tag{VI.57}$$

where the choice of interpolation has been made in order to ensure discrete conservation of mass, momentum, and energy (Bewely (2007)).

The parameters used in the third order Runge-Kutta algorithm given above are:

Table VI.1: Runge-Kutta parameters

R-K Step	$\overline{h}$	$\overline{\beta}$	$\overline{\zeta}$
1	8/15 Δt	1	0
2	2/15 Δt	25/8	-17/8
3	1/3 Δt	9/4	-5/4

VI.6 Algorithm: Triply periodic flow

The following is a description of the algorithm that Diablo uses for triply periodic flow. The right hand side of the momentum equations $\partial u_i/\partial t = ...$ will be stored in R_i while the Runge-Kutta terms will be stored in F_i and saved for the next R-K substep. $\widehat{u}_i$, $\widehat{R}_i$, $\widehat{F}_i$, etc. denote the Fourier space representations of U_i, R_i, F_i, etc. An extra storage array called S is also defined. Care has been taken to order the algorithm so that the physical and Fourier space arrays can occupy the same location in memory. One Runge-Kutta substep solving for U_{rk+1} proceeds as follows:

1. Add U_{rk} and the explicit part of the C-N viscous term to $\widehat{R}_i$
   $\widehat{R}_i = \left\{1 - \frac{\nu}{2}\overline{h}_{rk}(k_x^2 + k_y^2 + k_z^2)\right\}\widehat{u}_i$

2. Add the pressure gradient as Explicit Euler
   $\widehat{R}_i = \widehat{R}_i - \overline{h}_{rk} k_i CP$

3. Add the R-K terms from the previous timestep, stored in $\widehat{F}_i$
   If $(rk > 1)$ then $\widehat{R}_i = \widehat{R}_i + \overline{\zeta}_{rk}\widehat{F}_i$

4. Convert the velocity to physical space
   $\widehat{u}_i \rightarrow U_i$

5. Calculate the nonlinear terms and store in $\widehat{F}_i$
   Note that while there are 9 nonlinear terms, the ordering used here requires only 6 FFT calls.

(a) $F_1 = U1 * U1$
(b) $F_2 = U1 * U2$
(c) $F_3 = U1 * U3$
(d) $S = U2 * U2$
(e) $F_1 \rightarrow \widehat{F}_1$
(f) $F_2 \rightarrow \widehat{F}_2$
(g) $F_3 \rightarrow \widehat{F}_3$
(h) $S \rightarrow \widehat{S}$
(i) $\widehat{F}_1 = -\hat{i}k_x\widehat{F}_1 - \hat{i}k_y\widehat{F}_2 - \hat{i}k_z\widehat{F}_3$
(j) $\widehat{F}_2 = -\hat{i}k_x\widehat{F}_2 - \hat{i}k_y\widehat{S}$
(k) $\widehat{F}_3 = -\hat{i}k_x\widehat{F}_3$
(l) $S = U_2 * U_3$
(m) $S \rightarrow \widehat{S}$
(o) $\widehat{F}_2 = \widehat{F}_2 - \hat{i}k_z\widehat{S}$
(p) $\widehat{F}_3 = \widehat{F}_3 - \hat{i}k_y\widehat{S}$
(q) $S = U_3 * U_3$
(r) $S \rightarrow \widehat{S}$
(s) $\widehat{F}_3 = \widehat{F}_3 - \hat{i}k_z\widehat{S}$

6. Add the Runge-Kutta term to the right hand side
   $\widehat{R}_i = \widehat{R}_i + \overline{\beta}_{rk}\overline{h}_{rk}\widehat{F}_i$

7. Solve for the intermediate velocity. Since the system is diagonal, this is easy.
   $\widehat{u}_i = \widehat{R}_i/\{1 + \frac{\nu}{2}\overline{h}_{rk}(k_x^2 + k_y^2 + k_z^2)\}$

8. Calculate the pressure update ϕ that will make the velocity divergence free
   $\widehat{\phi} = -\hat{i}k_i\widehat{u}_i/(k_x^2 + k_y^2 + k_z^2)$

9. Project the velocity to get a divergence free field
   $\widehat{u}_i = \widehat{u}_i - \hat{i}k_i\widehat{\phi}$

10. Finally, update the pressure field using ϕ
    $\widehat{p} = \widehat{p} + \widehat{\phi}/\overline{h}_{rk}$

In all, we have 9 FFT calls per Runge-Kutta substep, and 11 full-sized storage arrays.

VI.7 Parallel Computing for CFD

The basic goal of parallel computing for fluid dynamics is to allow us to solve larger problems on several computers (or several processors within one computer) more quickly than would be possible on a single computer. For direct

numerical simulations (DNS) at large Reynolds numbers, parallel computation often becomes a necessity owing both to speed and memory limitations. Solving the Navier-Stokes equations involves performing the same set of operations at a large number of gridpoints, an indication that parallel computing may be effective for this problem. There are two basic approaches to parallel programming depending on the type of hardware that is being used, specifically whether memory is shared or distributed among the processors. It is now becoming common for new PCs to use CPUs with multiple cores on a single silicon chip, or to have multiple CPUs within one computer. These are examples of shared memory systems. It has become less common for supercomputers to share memory among all processors, but often processors within a single node are able to share memory. An example of a distributed memory system would be a cluster of PCs connected via a network, or separate nodes of a supercomputer. The task of programming to take advantage of shared and distributed memory systems is quite different and will be discussed below.

For *shared memory* systems, a set of tasks is split into multiple *threads* each of which is able to access all of the address space. This effectively eliminates the need for communication between threads. The main task of the programmer is then to distribute the computational tasks among the threads with the goal of achieving an adequate load balance and minimizing the amount of time that any thread must wait for the others to complete a task. Since the threads utilize the same address space, it is important to ensure that they do not interfere with each other. In order to prevent this from occuring, synchronization (or barrier) commmands are used to make sure that all threads have reached the specified point before proceeding further. A standard low-level set of thread commands is known as POSIX. This is commonly used in system-level programming and gives the programmer full control over the threads, but also requires significant modifications to a serial code.

The OpenMP standard provides a higher-level set of constructs for pro-

```
! The first block of code will be executed by a single thread only

!$OMP PARALLEL
    !Any code here will be executed by all threads

!$OMP BARRIER
    ! This statement tells threads to wait here until all threads have reac
hed this point

!$OMP END PARALLEL
    !The threads will wait at the end parallel section before proceeding

! Subsequent code will be executed by a single thread until the next OMP
directive is reached

! Here is an example of a loop parallelized with OpenMP:
! On an OpenMP compatible compiler, the DO I loop will be distributed among
the active threads
!$OMP DO
      DO I=1,NX
         ! Stuff
      END DO
!$OMP END DO
```

Figure VI.11: Example of a Fortran code parallelized with OpenMP for shared memory systems

graming in a shared memory environment. An OpenMP compiler translates a set of compiler directives (which are ignored as comments to a serial compiler) into POSIX thread commands. This process is analogous to a high level programming language such as Fortran translating a program into assembly language. An example of how to implement OpenMP compiler directives is shown in Figure VI.11. See Chandra et al. (Chandra et al. (2000)) for an introduction to parallel computing with OpenMP.

On *distributed memory* systems, memory is local to each process and other processes are unable to access it directly. An example of this type of system is a so-called 'beowulf cluster' which consists of a number of personal computers connected through a network. Many modern supercomputers use a combination of distributed and shared memory with memory distributed over a number of nodes each consisting of several processors in a shared memory configuration. There are several models for parallel computing on distributed memory systems. Three

examples are the manager/worker, distributed data, and the pipeline models.

A manager/worker model assigns one process to be the manager which delegates tasks to the worker processes. This model works well on unbalanced systems where some processes are much faster than others. The fast processes may finish a job, return the data, and be assigned a new task before the slower processes finish. In addition, if all data is stored on the manager process, this model can be used on unreliable networks. If one process goes offline before it has completed its job, the manager can then redirect the job to another process. However, for large simulations in CFD, it is often not possible to store the full flow domain in memory on a single process.

The distributed data model is useful when the same set of operations are to be performed on a large block of data, as is generally the case in CFD. With this model it is not necessary to ever store all of the data on one process and each process is treated equally. Typically a single source code is copied to all processes and excecuted locally on a set of data. Whenever data is required from a remote process, the execution of the code must halt until the appropriate data is recieved. Load balancing is important for this model in order to minimize the wait time necessary before a synchronized communication. In addition, since communication tends to be the most time-intensive step in a parallel algorithm, it is important to minimize the amount of data sent between processes.

The third model, the pipeline approach, is required when one piece of data must be operated on by all processes. In the limit when each process must wait until receiving data from its neighbor, this model becomes even worse than a serial algorithm (the speedup factor becomes less than one) since the communication takes some amount of time. Because of this, it is important to structure the algorithm so that as many processes as possible are active at a given time. This model has been used in the parallel channel flow Diablo for the solve of a tridiagonal system using the Thomas algorithm. This will be discussed in more detail below.

The most common programming construct for distributed memory sys-

Table VI.2: Essential MPI routines

MPI_INIT	Initialize MPI
MPI_COMM_SIZE	Get the total number of processes
MPI_COMM_RANK	Obtain the rank of the current process
MPI_SEND	Send data to one other process
MPI_RECV	Recieve data from another process
MPI_FINALIZE	Terminate MPI

tems is the Message Passing Interface (MPI) which is a standardized library of subroutines that allow the user to direct the communication between processes (Gropp et al. (1999)). While the MPI standard contains many subroutines, only six routines are essential (Grama et al. (2003)) as listed in Table 1. In fact, these are the only MPI routines that are used in the MPI implementation of Diablo for the channel geometry. The other non-essential MPI routines can be useful in some applications to simplify the parallel programing. Unlike OpenMP where compiler directives look like comments to a serial compiler, compiling an MPI program requires that the MPI libraries are installed on the local system. In order to allow a single source code to run on serial and parallel systems, Diablo has been written with all subroutines that use the MPI libraries in a separate file from the serial code. The Makefile then determines if MPI will be used, and if not substitutes an empty set of subroutines in place of the MPI calls.

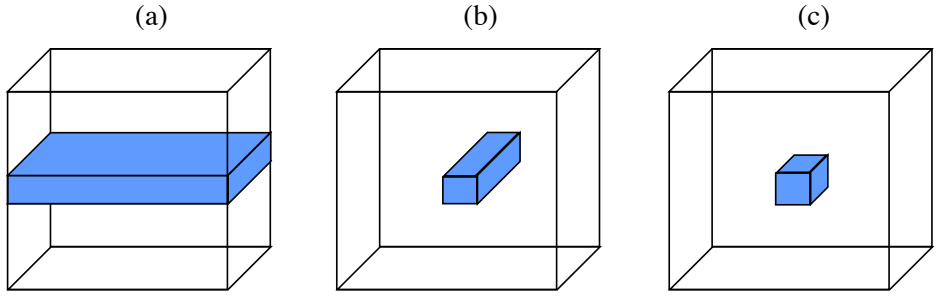

Figure VI.12: Domain decomposition options, splitting the domain along (a) one axis, (b) two axes, and (c) three axes

An important step when writing a distributed memory parallel algorithm is to decide how to distribute the data among the processes. A schematic of the three possible choices is shown in Figure VI.12. By decomposing the domain along one, two, or three axes, the data contained by a single process can be described as a plane, pencil, or cube. Decomposing in one direction only, as shown in Figure VI.12(a) is easier to program and minimizes the number of connections that must be made between processes. However, more data must be shared with this choice than the others. For example, consider decomposing a domain of size N^3 into eight processes. With domain decomposition in one direction, 7 connections between processes must be made, and the amound of data shared scales as $7N^2$. For a three dimensional decomposition with eight processes (with each dimension split into two subdomains), 12 connections between processes must be made, while the amount of data shared is $3N^2$. Based primarily on the ease of implementation, one-dimensional decomposition has been used in the parallelization of Diablo.

The communication time on distributed memory systems is often the most limiting process and should be minimized for an efficient parallel algorithm. The total time requried to send a message can be separated into three parts:

$$t = t_b + t_l + t_s. \tag{VI.58}$$

t_b is the 'buffer time', or the time it takes for the sending process to pack the message into a buffer array including the header and trailer that are used to help direct the message. t_l is the 'node latency' (or per-hop) time, that is the time required for the routing switch to establish a connection between two nodes. This can be measured as the time needed to send a message of zero size (consisting of only the header and trailer) between two processes. Finally, t_s is the time required to send the packet of data. On large networks, it becomes too expensive to form direct connections between all nodes, so that depending on the topology of the network, a message must be passed along to intermediate nodes like a game of telephone. In this case, the communication time scales like: $t = t_b + L(t_l + t_s)$ where L is the number of intermediate steps required to connect the two nodes.

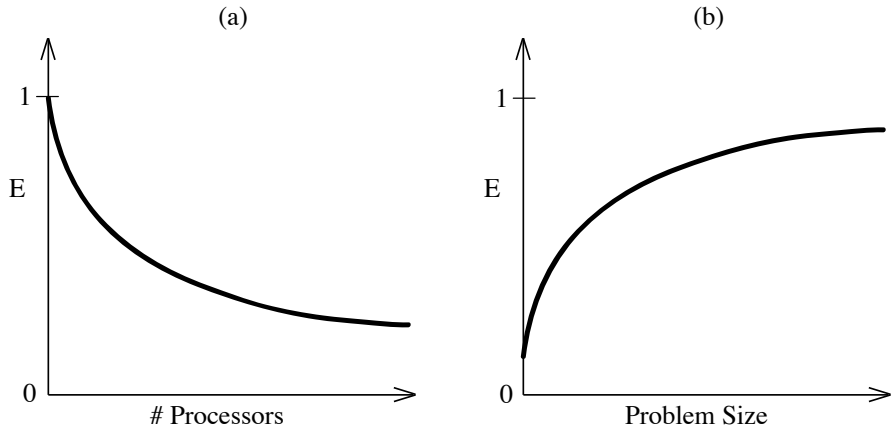

Figure VI.13: Parallel efficiency for (a) a fixed problem size as a function of the number of processing elements and (b) for a fixed number of processing elements as a function of problem size (After Grama et al. (Grama et al. (2003))).

Several metrics are commonly used to measure the efficiency of a parallel algorithm. The parallel speedup is defined as the ratio of the serial runtime to the parallel runtime where both are measured based on the wall clock time elapsed between the start and end of the algorithm. The parallel efficiency is the ratio of the speedup to the number of processing elements (Grama et al. (2003)):

$$E = \frac{T_S}{pT_p}, \tag{VI.59}$$

where T_S is the serial runtime, T_p is the parallel runtime, and p is the number of processing elements. The parallel efficiency is a good measure of the performance of a parallel algorithm, but it also strongly depends on the problem size and the number of processing elements. For a given problem size, increasing the number of processors decreases the computational load on each element while increasing the amount of data that must be shared. As a result, for a given algorithm and a fixed problem size, increasing the number of processors results in a decreased efficiency. Conversely, maintaining a fixed number of processors and increasing the problem size increases the relative time spent performing computations and results in an increase in efficiency. This behavior is shown in Figure VI.13.

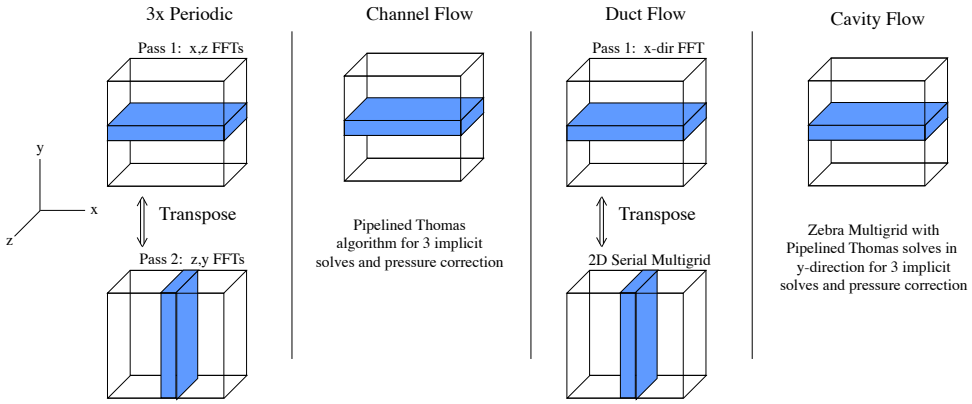

Figure VI.14: Proposed domain decomposition for MPI version of Diablo

A strategy for writing a parallel version of Diablo illustrated in Figure VI.14. In order to keep data local for any FFT calls and the implicit solves, and to make the programming easier, we propose one-dimensional domain decomposition in all cases. With this choice, all parallel communication can be broken down into three subroutines: ghost cell communication, a parallel data transpose, and a pipelined Thomas algorithm.

In the case of triply periodic flow, FFTs are needed in all three directions, and the right hand side of the momentum equation is computed in Fourier space. When computing nonlinear terms, the pseudo-spectral method is used by transforming the velocity to physical space, computing the nonlinear product, and transforming the result back to Fourier space. The Fourier transform is a notoriously difficult algorithm to parallelize since it requires a large amount of non-local communication. In order to avoid a parallel FFT call, each Runge-Kutta substep can be divided into a two-pass structure. Linear terms are computed during the first pass with the domain decomposed across wavenumbers in the y-direction. The velocity is then partially transformed to physical space by taking an inverse FFT in the $x - z$ plane. Before taking the inverse FFT in the z-direction, the data must be made local in the z-direction. This can be accomplished by an MPI

all-to-all transpose to distribute the data in $y - z$ planes. At this point, the velocity is in physical space and nonlinear products can be computed. The process then proceeds in reverse to transform the velocity to Fourier space involving one more data transpose. Therefore, the triply periodic algorithm without any scalar advection requires 6 all-to-all transpose operations per Runge-Kutta step (two for each velocity component). It is expected that the transpose operations will be the most costly step in this algorithm.

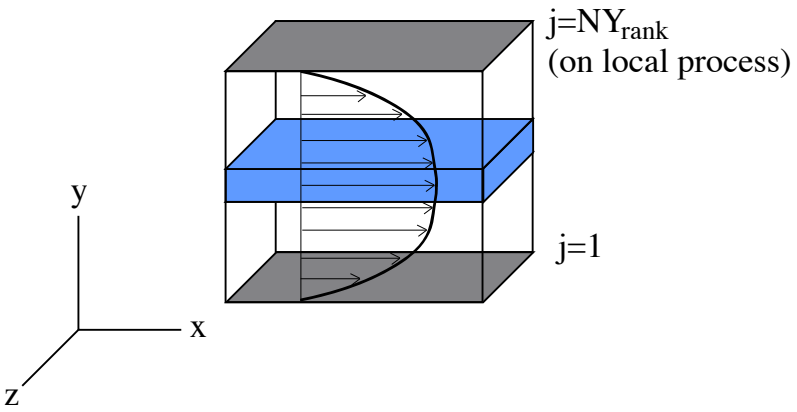

Figure VI.15: Domain decomposition for the MPI version of channel flow in Diablo

For channel flow a different strategy is implemented. Since FFTs are only needed in the x and z directions in this case, the domain is decomposed into $x - z$ slabs as shown in Figure VI.15. Indexing of the grid on each processor is chosen so that the momentum equations are time-stepped on interior nodes between $j = 2$ and $j = NY$ on both the fractional and base grids. By changing a starting and ending index, the same code can be used for serial and parallel computation. The grid indexing is shown in Figure VI.19. At the start of each Runge-Kutta substep the ghost cells on interior nodes are filled by obtaining data from the neighboring nodes. Then, the right hand side of the momentum equations is calculated just as in the serial algorithm. Solving for the intermediate velocity involves solving a

tridiagonal system in the y-direction at each x and z location. Since the data is decomposed along the y-axis, this solve is nonlocal and must be parallelized.

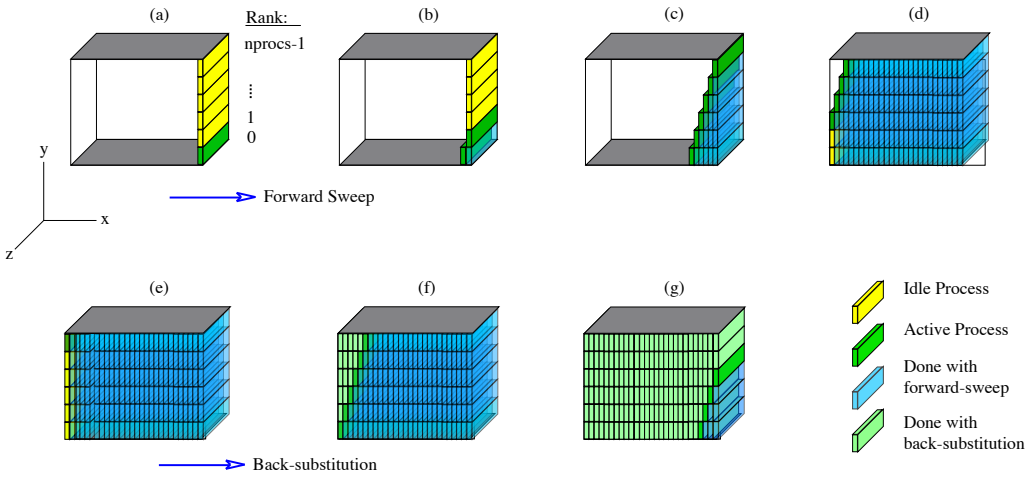

Figure VI.16: Illustration of a pipelined Thomas algorithm with the forward sweep in (a)-(d) and back substitution in (e)-(g). Note that this choice requires storage of the tridiagonal matrix and unknown vector at each gridpoint in three dimensions.

By its nature, the parallel Thomas algorithm requires a pipelined approach as mentioned above. During both the forward and backward sweeps, information is passed up or down the system so that only one row can be operated on at a given time. With only one process operating at a given time, a parallel algorithm would be even slower than the serial version since there is additional communication overhead. However, we can limit the amount of idle time spent by the processes by leveraging the fact that we need to do $NX * NZ$ tridiagonal solves. One approach is to separate the Thomas algorithm into separate forward and backward sweeps. After the first process finishes the forward sweep for one i, k and passes data to its neighbor, it is free to proceed to the forward sweep at the next column. One problem with this approach is that many communications with small messages are required. Since each send/recieve requires some overhead time owing to data buffering and switch latency. In order to reduce the number

of communication required, during each forward or backward sweep, each process can finish the sweep in one coordinate direction, say the k direction, before passing the data. This algorithm is illustrated in Figure VI.16.

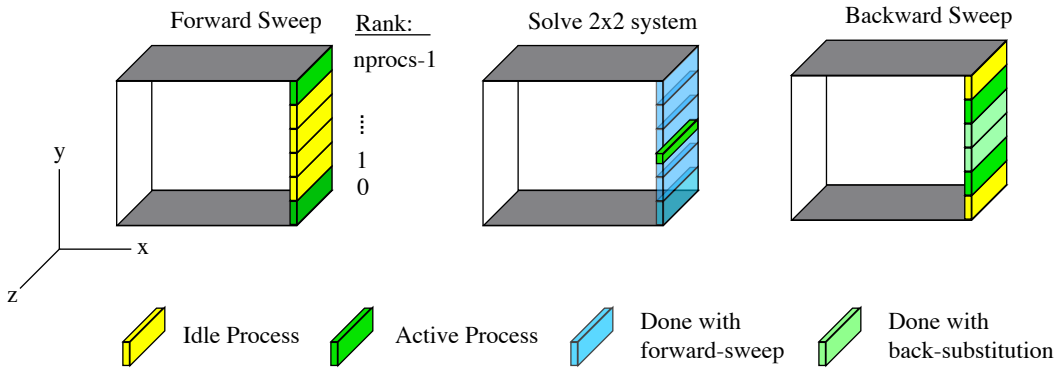

Figure VI.17: Illustration of a pipelined Thomas algorithm with reduced wait-time using bi-directional solves.

Separating the forward and backward sweeps necessarily requires storing the components of the tridiagonal matrix and the solution vector. The above algorithm therefore requires storage of four three-dimensional arrays. Since memory requirements can become restrictive for large arrays, this can be a severe limitation. In order to reduce the storage, we can do the forward and backward sweeps over the $x-y$ axis before moving to the next z-location. This reduces the storage requirement from 3d arrays to 2d arrays at the expense of added wait time. A code written in Fortran using MPI for a pipelined Thomas algorithm with storage in $x-y$ planes is given in Figures VI.20 and VI.21.

A further improvement on this algorithm can be made by starting 'forward' sweeps at both the uppermost and lowermost process eliminating the lower and upper diagonal components respectively. Then at the center of the domain where these solves meet a 2x2 system can be solved quickly on the center process and back-substitution can again proceed in two directions. This modification to the Thomas algorithm for a single tridiagonal system is shown in Figure VI.18. The computational load for this algorithm is illustrated in Figure VI.17 which

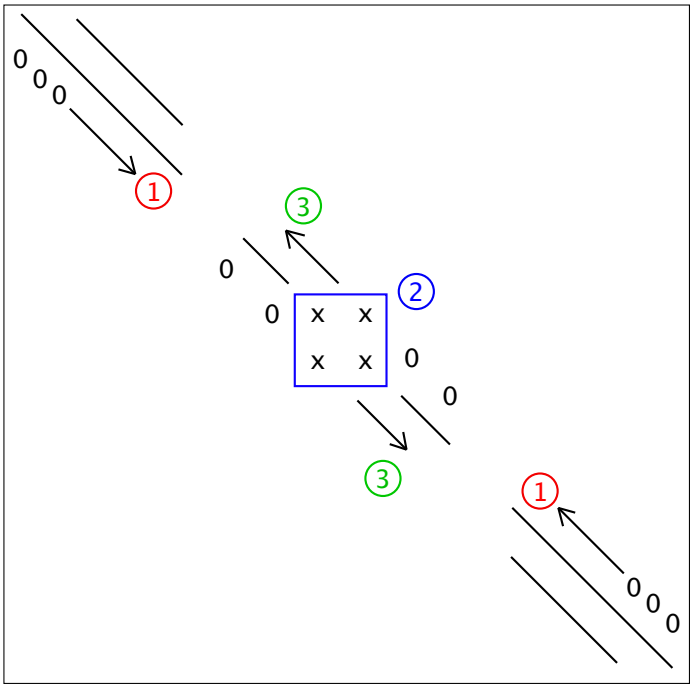

Figure VI.18: Solution of a tridiagonal system using a modified Thomas algorithm with bi-directional solves for improved parallel performance. Step 1: Start with the lower and upper process and eliminate the upper and lower diagonals, respectively. Step 2: When the two 'forward' sweeps meet at the center, solve the resulting 2x2 system. Step 3: Perform 'back-substitution' in the opposite directions as the 'forward' sweeps.

demonstrates that the wait time is reduced by a factor of two.

The duct and cavity flow version of Diablo can largely leverage the MPI routines that were described above. For duct flow (with the x-derivatives treated with the psuedo-spectral method), four Helmholtz equations are solved with a two-dimensional multigrid routine for the implicit solves for the three velocity components and the pressure correction. Since the grid and smoothing operations in multigrid are communication intensive, it is desirable to keep this operation location on each process which implies that data should be decomposed in the

$y-z$ plane. Since it is also important to keep the FFTs in the x-direction local this suggests that a two-pass algorithm similar to what was proposed above for the triply periodic case. For the cavity flow case with finite differences used in all three directions, there is no clear benefit from a two-pass algorithm. Instead, an algorithm may be used similar to that used in channel flow with ghost cell communication on each interior node. Then, a parallel version of the three-dimension multigrid routine will be needed for the velocity and pressure correction solves. One solution would be to use a zebra variant of multigrid. Smoothing and grid refinement would then be replaced by a direct tridiagonal solve in one direction for which we already have a parallel algorithm shown above.

VI.8 Acknowledgments

The material in this chapter was developed after many insightful discussions with Professors Thomas Bewley and Sutanu Sarkar. Robert Martin is also gratefully acknowledged for developing the first pipelined Thomas algorithm and the ghost cell communication algorithm.

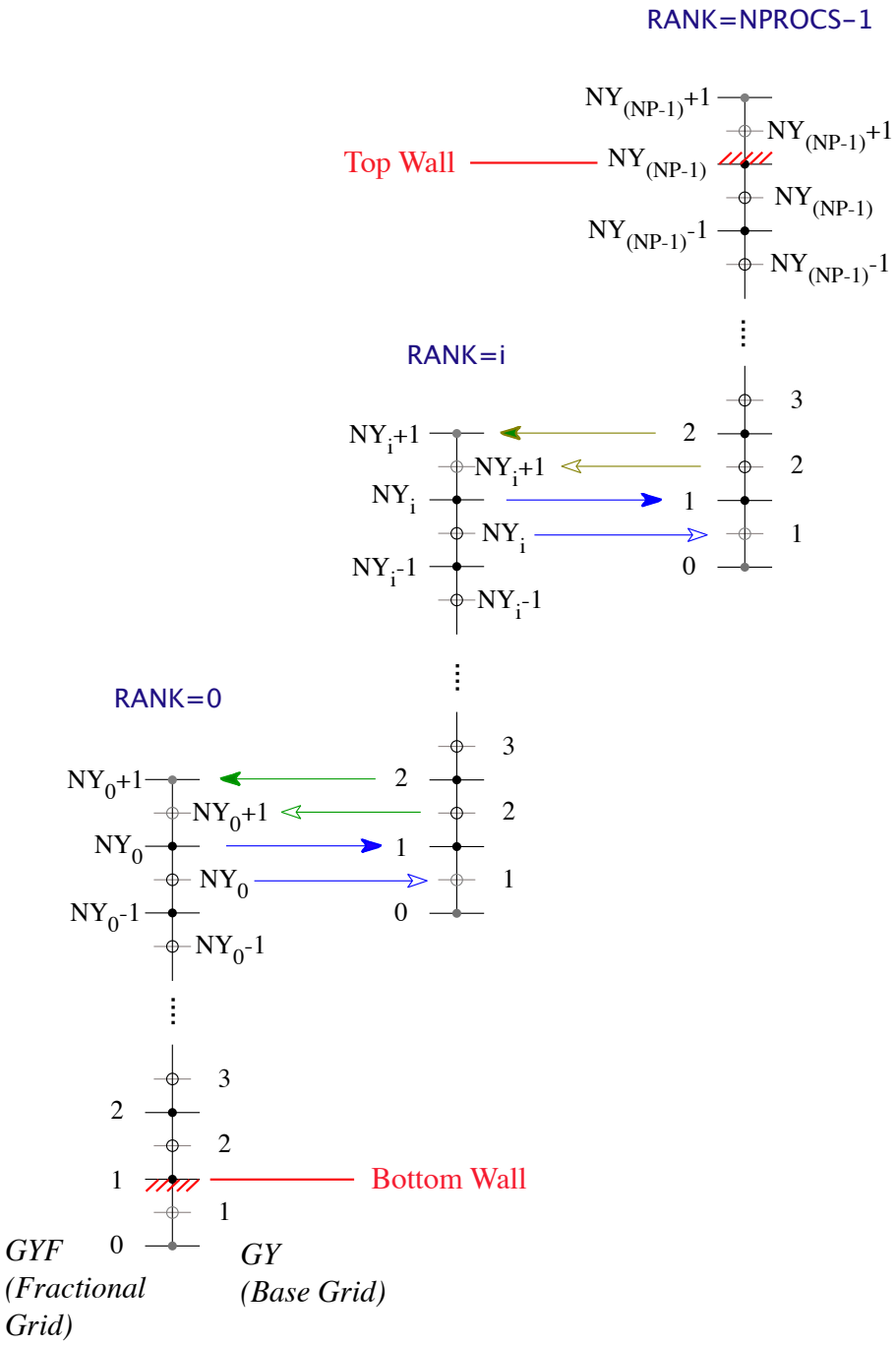

Figure VI.19: Grid indexing with ghost cell communication for the Diablo MPI channel flow algorithm

```
C----*|--.---------.---------.---------.---------.---------.---------.
      SUBROUTINE THOMAS_FORWARD_REAL_MPI(A,B,C,G,NY,NX)
C----*|--.---------.---------.---------.---------.---------.---------.

C This subroutine performs the backward sweep of the Thomas algorithm
C Input lower, main, and upper diagonals, A, B, C, and rhs G
C Returns solution in G
C The tridiagonal system is written:
C [ b1  c1   0   0   0 ...
C [ a2  b2  c2   0   0 ...
C [  0  a3  b3   c3  0 ...
      INCLUDE 'mpif.h'
      INCLUDE 'header_mpi'

      INTEGER I,J,NY
      REAL*8 A(0:NX,0:NY), B(0:NX,0:NY), C(0:NX,0:NY), G(0:NX,0:NY)
C The following arrays are used to pack data for MPI SEND/RECV
      REAL*8 OCPACK(3),ICPACK(3)

      DO I=0,NXM
      IF (RANK.NE.0) THEN
C If we aren't the lowest process, then wait for data
        CALL MPI_RECV(OCPACK,3,MPI_DOUBLE_PRECISION,RANK-1,1
     &               ,MPI_COMM_WORLD,status,ierror)
C Unpack the data
        B(I,0)=OCPACK(1)
        C(I,0)=OCPACK(2)
        G(I,0)=OCPACK(3)
      END IF
      DO J=0,NY-1
        A(I,J+1)=-A(I,J+1)/B(I,J)
        B(I,J+1)=B(I,J+1)+A(I,J+1)*C(I,J)
        G(I,J+1)=G(I,J+1)+A(I,J+1)*G(I,J)
      END DO
      IF (RANK.NE.NPROCS) THEN
        ICPACK(1)=B(I,NY)
        ICPACK(2)=C(I,NY)
        ICPACK(3)=G(I,NY)
        CALL MPI_SEND(ICPACK,3,MPI_DOUBLE_PRECISION,RANK+1,1
     &               ,MPI_COMM_WORLD,ierror)
      END IF
      END DO
```

Figure VI.20: Source code in Fortran for the forward sweep of a pipelined Thomas algorithm using MPI.

```
C----*|--.---------.---------.---------.---------.---------.---------.
      SUBROUTINE THOMAS_BACKWARD_REAL_MPI(A,B,C,G,NY,NX)
C----*|--.---------.---------.---------.---------.---------.---------.

C This subroutine performs the backward sweep of the Thomas algorithm

      INCLUDE 'mpif.h'
      INCLUDE 'header_mpi'

      INTEGER I,J,NY
      REAL*8 A(0:NX,0:NY), B(0:NX,0:NY), C(0:NX,0:NY), G(0:NX,0:NY)

      DO I=0,NX
      IF (RANK.NE.NPROCS) THEN
C If we aren't the highest process, then wait for data
        CALL MPI_RECV(G(I,NY),1,MPI_DOUBLE_PRECISION,RANK+1
     &               ,MPI_COMM_WORLD,status,ierror)
      ELSE
C Else, if we are the highest process, then compute the solution at j=NY
        G(I,NY)=G(I,NY)/B(I,NY)
      END IF
      DO J=NY-1,0,-1
        G(I,J)=(G(I,J)-C(I,J)*G(I,J+1))/B(I,J)
      END DO
      IF (RANK.NE.0) THEN
        CALL MPI_SEND(G(I,0),1,MPI_DOUBLE_PRECISION,RANK-1,1
     &               ,MPI_COMM_WORLD,ierror)
      END IF
      END DO

      RETURN
      END
```

Figure VI.21: Source code in Fortran for the back substitution of a pipelined Thomas algorithm using MPI.

VII Conclusions

A suite of numerical simulations has been examined in an attempt to improve our understanding of some fundamental physical properties of the stratified oceanic bottom boundary layer. A few of the important conclusions from these studies are summarized here.

Stratified open channel flow was studied in Chapter II. Stable stratification was applied with an adiabatic lower wall and a uniform heat flux applied at the free surface. The thermal boundary conditions were chosen to produce a density profile that qualitatively matches the oceanic bottom boundary layer where a mixed layer forms beneath a stable density gradient. Although the geometry of this flow is idealized, this problem allowed us to isolate the influence of the thermal boundary conditions on the turbulent flow structure. The geometry also allowed a direct comparison with previous studies of channel flow with a stabilizing heat flux at the boundaries. This comparison has shed some light on differences in stratification effects in the stable atmospheric and oceanic boundary layers.

Contrary to previous observations of channel flow stratified with a heat flux at the walls, near-wall turbulent production was unaffected by the imposed free surface stratification. A well-mixed region was found near the wall even when the surface heat flux was large, and stratification effects were limited to a relatively thin region near the free surface. Nevertheless, when the surface heat flux was sufficiently large, stratification suppressed the turbulent upwellings of low-speed fluid to the free surface that were observed in the unstratified simulations. The corresponding reduction in the Reynolds stress near the free surface in the stratified

simulations led to an increase in the mean shear. A counter-gradient buoyancy flux was also observed in the stratified region near the free surface, an indication that potential energy was transferred to kinetic energy on average.

The buoyancy scale is traditionally used to give an estimate of how far a fluid parcel can be moved in the vertical direction if all of the local turbulent kinetic energy is transferred to potential energy. However the buoyancy scale is defined with the *local* kinetic energy levels and the *local* density gradient. For the stratified open channel flow that we have considered, this lengthscale is of limited use since turbulent bursts form near the lower wall where the density gradient is negligible. In order to quantify the affect of stratification on turbulent transport, we have proposed considering the ratio of the potential energy needed to lift a local fluid parcel to the free surface to the local vertical turbulent kinetic energy. When this ratio is larger than one throughout the channel, stratification has a strong influence on the flow near the free surface .

Previous studies of stratified wall-bounded flows with a stabilizing heat flux at the wall have found found that stratification effects could be well-described by the local gradient Richardson number (Komori et al. (1983); Armenio and Sarkar (2002)). By comparing results from our simulations with various levels of the imposed surface heat flux, we have found that the local effects of stratification cannot be adequately described by the gradient Richardson number. This can be explained by the observation that stratification can additionally affect the turbulent motions in a non-local sense by reducing the turbulent transport. This is an important conclusion since many turbulence parameterizations used in ocean models (such as the Mellor-Yamada closure) use the gradient Richardson number to quantify the influence of stratification. Many of these closures have been developed using data from stratified shear layers where stratification may affect the turbulence levels in a local sense. However, when the primary influence of stratification is to limit turbulent transport from one region to another, stratification effects are inherently non-local. The influence of stratification on turbulent trans-

port can be characterized by the vertical Froude number more effectively than the gradient Richardson number.

The simulations described in Chapter II in an idealized geometry provided some insight into the effects of an external stratification on a turbulent boundary layer. However, the direct application of this study was limited to shallow water since stratification effects were strongly felt only near the free surface. Most of the bottom boundary layer is deep enough that it does not directly interact with the surface of the ocean. To extend the applicability to deeper seas, subsequent chapters considered a turbulent boundary layer above a flat surface, driven by a steady geostrophic flow. The influence of the free surface was removed by applying an open boundary condition at the top of the computational domain to effectively consider a small domain near the seafloor. The outer flow was assumed to be uniformly stratified and the bottom boundary was adiabatic. In addition, we considered flow in a rotating coordinate frame with the outer flow in geostrophic balance and the mean velocity following the familiar Ekman spiral. Since unstratified boundary layers will grow indefinitely in time, the presence of the Coriolis term has the advantage of bounding the momentum boundary layer thickness so that it can be encompased inside the computational domain even at long times.

Since these were the first turbulence-resolving simulations of a bottom Ekman layer, it was not clear how well large-eddy simulations (LES) would perform in this context. In order to validate the large-eddy simulation, a direct numerical simulation (DNS) was conducted and described in Chapter III. Based on the DNS/LES comparison, it was found that an additional resolution constraint owing to the stable stratification must be satisfied for an accurate LES of this flow. Specifically, the turbulent overturns responsible for the entrainment of fluid into the mixed layer must be adequately resolved since their effects are not be captured by the Smagorinsky-type models used here. It was found that these overturns scale with the local Ellison scale which provides a good criteria for evaluating the LES resolution. When the Ellison scale is not adequately resolved, the turbulent heat

flux in the LES is significantly underestimated.

The simulations that were considered in Chapter II can be classified as *resolved* LES since a majority of the energy containing scales was captured by the simulation everywhere in the flow. Near the wall this requires a much higher resolution than in the outer layer since the energy containing eddies scale with the distance from the wall. As the Reynolds number is increased, a resolved LES quickly becomes very computationally costly since the viscous sublayer becomes thinner. In order to extend our simulations to realistic geophysical Reynolds numbers, a near-wall model can be introduced, and simulations of this type are referred to as NWM-LES. Fortunately, we have learned from our DNS and resolved LES that the near-wall region is not affected by stratification, so that unlike most atmospheric models, our near-wall model does not need to directly account for density stratification.

We have found that when using previously formulated near-wall models in conjunction with the dynamic Smagorinsky model at very large Reynolds numbers, the Reynolds stress is under-predicted near the wall, leading to an overestimate in the mean shear. In order to improve the performance of the NWM-LES, we have developed a novel adaptive stochastic forcing procedure. This forcing is not described here in detail, instead the reader is referred to Taylor and Sarkar (2007b). The performance of the NWM-LES at relatively low Reynolds numbers has been compared to DNS and resolved LES in Chapter III. We have found that with stochastic forcing the NWM-LES was able to capture the logarithmic behavior of the mean velocity even at very high Reynolds numbers.

Chapter IV described a study of a stratified bottom Ekman layer using the NWM-LES that was validated in the previous chapter. The Reynolds and Richardson numbers were selected to match field observations. In order to focus on the effect of stratification on the boundary layer structure, and to reduce the parameter space, some simplifying assumptions have been made. Notably, the outer layer flow was assumed to be steady in time, and the bottom slope was taken

to be zero (although realistic small-scale roughness was added through the near-wall model.) As the flow developed from an intially linear temperature profile, a turbulent bottom mixed layer developed which was separated from the outer layer by a strongly stable pycnocline.

One important finding presented in Chapter IV was that the bottom drag coefficient was nearly independent of the outer layer stratification. In contrast, it has been found that the drag coefficient is strongly dependent on the surface heat flux in an atmospheric Ekman layer (Shingai and Kawamura (2002)). It may then be a good approximation to neglect the influence of stratification when parameterizing the bottom drag over a non-sloping seafloor. It is important to note that the bottom drag will likely depend on stratification in a stratified Ekman layer over a *sloping* bottom where Ekman tranport can induce upwelling or downwelling (Garrett et al. (1993)). Although the drag coefficient remains nearly constant in a non-sloping bottom boundary layer, stratification does have important affects on the boundary layer structure. Specifically, the mixed layer height is strongly limited by the outer layer stratification, and the magnitude of the cross-stream velocity increases when the outer layer is stably stratified.

Another important influence of stratification on the bottom boundary layer is to increase the mean shear near the top of the mixed layer. When the outer layer was strongly stratified, the mean shear in the pycnocline increased by more than an a factor of two compared to the unstratified case. This can have very important consequences for interpreting field data. Since it is difficult to measure the very thin viscous sublayer near the seafloor, it is common to infer the bottom stress from the observed mean velocity profiles by assuming that the flow follows the classical law-of-the-wall. This is known as the 'profile method' and it was shown by Perlin et al. (2005) and Johnson et al. (1994) that when the boundary layer is limited by stratification, this method tends to overestimate the wall stress. Since the wall stress inferred from the profile method scales with the square of the shear, overestimating the shear by a factor of two will lead to a wall stress that is four

times too large. Furthermore, since the bottom boundary layer is often affected by stratification, this error could be systematic throughout existing datasets. Perlin et al. (2005) proposed an alternative method for inferring the wall stress from field observations. However, their method may not always be straightforward to apply since it requries direct observation of the dissipation rate and resolution of the density profile in the boundary layer. When such microstructure data is not available, we proposed a simple modification to the profile method using the local density gradient. This modified profile method performed adequately when applied to the simulation data.

Chapter V considered the internal gravity waves that are generated by the interaction between the boundary layer turbulence and the stable outer layer stratification. Several previous studies have considered internal gravity waves generated by turbulence for a variety of flow types including shear layers, gravity currents, and stratified wakes. Many of these studies reported that the frequency and angle of propagation associated with the turbulence-generated internal gravity waves were confined to a relatively narrow range. A similar observation was made in the present study where the turbulence-generated internal waves in the outer layer were associated with angles of propagation between $30^\circ < \Theta < 60^\circ$. Since these waves originated from the turbulent region with a broad range of frequencies, the narrow range of frequencies seen here and in previous studies was counterintuitive.

An explanation for the narrow frequency range was proposed in Chapter V by invoking viscous decay of the wave amplitude. This mechanism can be understood by considering a wave packet associated with a fixed frequency and wavenumber. Ray theory states that the frequency and horizontal wavenumber associated with an internal gravity wave remain fixed as the wave propagates through a slowly varying background medium. The wave energy propagates at an angle Θ formed between the group velocity vector and the vertical axis. This angle is related to the wave frequency through the dispersion relation, which for waves in

a non-rotating reference frame is $\omega = Ncos(\Theta)$. As a given wave packet travels, its amplitude will decrease in time due to molecular viscosity at a rate dependent on the wavenumber. That is, small scale waves are more strongly influenced by viscosity than large waves. The vertical group velocity of the wave packet is given by the vertical component of the group velocity which depends on both the frequency and wavenumber associated with the packet. Using the rate of decay of the wave amplitude and the vertical propagation speed, an equation can be written for the wave amplitude as a function of the vertical coordinate z. This expression depends on the frequency and wavenumber of the packet, reflecting the fact that some waves propagate slowly in the vertical direction and therefore have more time to decay before reaching a given height. By starting with an observed spectrum in the turbulent region, the viscous decay model captures both the rate of decay of the wave amplitude, and the narrow range of frequencies and propagation angles of the turbulence-generated internal waves.

Chapter VI described the computational fluid dynamics code that was developed as part of this thesis. The numerical algorithm was developed in collaboration with Prof. Thomas Bewley, with coding help from other graduate students at UCSD. Considerable effort has gone into making this code easy to understand while retaining advanced features that allow it to be generally useful. The code has been made freely available under an open-source license and has already been successfully used in a variety of research projects including magnetohydrodynamics, sediment transport, gravity currents, channel flow, and boundary layers. The code includes advanced turbulence models for large-eddy simulation, passive and/or active scalar advection, and has been parallelized using MPI.

References

Aguilar, D., and Sutherland, B., 2006: Internal wave generation from rough topography. *Physics of Fluids*, **18**(066603), 1–9.

Armenio, V., and Piomelli, U., 2000: A Lagrangian mixed subgrid-scale model in generalized coordinates. *Flow Turbulence and Combustion*, **65**, 51–81.

Armenio, V., and Sarkar, S., 2002: An investigation of stably-stratified turbulent channel flow using large eddy simulation. *J. Fluid Mech.*, **459**, 1–42.

Armi, L., 1978: Some evidence for boundary mixing in the deep oean. *J. Geophys. Res.*, **83**(C4), 1971–1979.

Armi, L., and Millard, R., 1976: Bottom boundary-layer of the deep ocean. *Journal of Geophysical Research - Oceans and Atmospheres*, **81**, 4983–4991.

Bardina, J., Ferziger, J., and Reynolds, W., 1980: Improved subgrid models for large eddy simulation. *AIAA*, **80-1357**.

Basak, S., and Sarkar, S., 2006: Dynamics of a stratified shear layer with horizontal shear. *J. Fluid Mech.*, **568**, 19–54.

Batchelor, G., 1959: *The theory of homogeneous turbulence*. Cambridge University Press, London.

Bennett, A., 1976: Open boundary conditions for dispersive waves. *J. Atmos. Sci.*, **33**, 176–182.

Bewely, T., 1999: *Optimal and robust control and estimation of transition, convection, and turbulence*. Ph.D. thesis, Stanford University.

Bewely, T., 2007: *Numerical methods for simulation, optimization, and control*.

Bonneton, P., Chomaz, J., and Hopfinger, E., 1993: Internal waves produced by the turbulent wake of a sphere moving horizontally in a stratified fluid. *J. Fluid Mech.*, **254**, 23–40.

Brost, R., and Wyngaard, J., 1978: A model study of the stably stratified planetary boundary layer. *J. Atmos. Sci.*, **35**(8), 1427–1440.

Buhler, O., and McIntyre, M., 1999: On shear-generated gravity waves that reach the mesosphere. part II: Wave propagation. *J. Atmos. Sci.*, **56**, 3764–3773.

Buhler, O., McIntyre, M., and Scinocca, J., 1999: On shear-generated gravity waves that reach the mesosphere. part I: Wave generation. *J. Atmos. Sci.*, **56**, 3749–3763.

Caldwell, D., and Chriss, T., 1979: The viscous sublayer at the sea floor. *Science*, **205**(4411), 1131–1132.

Calhoun, R. J., and Street, R. L., 2002: Patterns on a free surface caused by underwater topography: a laboratory-scale study. *International Journal of Remote Sensing*, **23**, 1609–1620.

Calmet, I., and Magnaudet, J., 2003: Statistical structure of high Reynolds-number turbulence close to the free surface of an open-channel flow. *Journal of Fluid Mechanics*, **474**, 355–378.

Canuto, C., Hussaini, M., Quarteroni, A., and Zang, T., 1988: *Spectral methods in fluid dynamics*. Springer-Verlag.

Chandra, R., Menon, R., Dagum, L., Kohr, D., Mavdan, D., and McDonald, J., 2000: *Parallel Programming in OpenMP*. Morgan Kaufmann.

Coleman, G., 1999: Similarity statistics from a direct numerical simulation of the neutrally stratified planetary boundary layer. *J. Atmos. Sci.*, **56**(6), 891–900.

Coleman, G., Ferziger, J., and Spalart, P., 1990: A numerical study of the turbulent Ekman layer. *J. Fluid Mech.*, **213**, 313–348.

Coleman, G., Ferziger, J., and Spalart, P., 1992: Direct simulation of the stably stratified turbulent Ekman layer. *J. Fluid Mech.*, **244**, 677–712.

D'Asaro, E., 1982: Velocity structure of the benthic ocean. *Journal of Physical Oceanography*, **12**, 313–322.

Dewey, R., Leblond, P., and Crawford, W., 1988: The turbulent bottom boundary layer and its influence on local dynamics over the continental shelf. *Dynamics of Atmospheres and Oceans*, **12**(2), 143–172.

Diamessis, P., Domaradzki, J., and Hesthaven, J., 2005: A spectral multidomain penalty method model for the simulation of high Reynolds number localized incompressible stratified turbulence. *Journal of Computational Physics*, **202**(1), 298–322.

Dohan, K., and Sutherland, B., 2003: Internal waves generated from a turbulent mixed region. *Physics of Fluids*, **15**(2), 488–498.

Dohan, K., and Sutherland, B., 2005: Numerical and laboratory generation of internal waves from turbulence. *Dynamics of Atmospheres and Oceans*, **40**, 43–56.

Durran, D., 1999: *Numerical methods for wave equations in geophysical fluid dynamics: With applications in geophysics*. Springer-Verlag.

E, X., and Hopfinger, E., 1986: On mixing across an interface in stably stratified fluid. *J. Fluid Mech.*, **166**, 227–244.

Fletcher, C., 1991: *Computational Techniques for Fluid Dynamics, Volume 2*. Springer-Verlag, second edition.

Flynn, M., and Sutherland, B., 2004: Intrusive gravity currents and internal gravity wave generation in stratified fluid. *J. Fluid Mech.*, **514**, 355–383.

Frigo, M., and Johnson, S., 2005: The design and implementation of fftw3. *Proceedings of the IEEE*, **93**, 216–231.

Fritts, D., and Alexander, M., 2003: Gravity wave dynamics and effects in the middle atmosphere. *Reviews of Geophysics*, **41**(1003), doi:10.1029/2001RG000106.

Garg, R., Ferziger, J., Monismith, S., and Koseff, J., 2000: Stably stratified turbulent channel flows. I. Stratification regimes and turbulence suppression mechanism. *Phys. Fluids A*, **12**, 2569–2594.

Garrett, C., and Laurent, L. S., 2002: Aspects of deep ocean mixing. *Journal of Oceanography*, **58**, 11–24.

Garrett, C., MacCready, P., and Rhines, P., 1993: Boundary mixing and arrested Ekman layers: Rotating stratified flow near a sloping boundary. *Annual Rev. Fluid Mech.*, **25**, 291–323.

Garrett, C., and St. Laurent, L., 2002: Aspects of deep ocean mixing. *Journal of Oceanography*, **58**, 11–24.

Germano, M., Piomelli, U., Moin, P., and Cabot, W., 1991: A dynamic subgrid-scale eddy viscosity model. *Phys. Fluids A*, **3**(7), 1760–1765.

Gibson, C., Bondur, V., Keeler, R., and Leung, P., 2006: Energetics of the beamed zombie turbulence maser action mechanism for remote detection of submerged oceanic turbulence. *manuscript in prep.*, 1–36.

Gill, A., 1982: *Atmosphere-Ocean Dynamics*. Academic Press.

Gourlay, M., Arendt, S., Fritts, D., and Werne, J., 2001: Numerical modeling of initially turbulent wakes with net momentum. *Physics of Fluids*, **13**(12), 3783–3802.

Grama, A., Karypis, G., Kumar, V., and Gupta, A., 2003: *An introduction to parallel computing: Design and analysis of algorithms*. Addison Wesley.

Gregg, M., Winkel, D., MacKinnon, J., and Lien, R., 1999: Mixing over shelves and slopes. In *Dynamics of oceanic internal gravity waves II, Proceedings, Hawaiian Winter Workshop*, editors P. Muller, and D. Henderson, 37–45.

Gropp, W., Lusk, E., and Skjellum, A., 1999: *Using MPI - 2nd Edition: Portable Parallel Programming with the Message Passing Interface (Scientific and Engineering Computation)*. The MIT Press.

Grotzbach, G., 1987: Direct numerical and large eddy simulation of turbulent channel flows. In *Encyclopedia of Fluid Mechanics*, editor N. Cheremisinoff, volume 6, 1337–1391. Gulf Publ., West Orange, NJ.

Haidvogel, D., and Beckmann, A., 2000: *Numerical ocean circulation modeling*. Imperial College Press, second edition.

Handler, R., Saylor, J., Leighton, R., and Rovelstad, A., 1999: Transport of a passive scalar at a shear-free boundary in fully developed turbulent open channel flow. *Phys. Fluids A*, **11**, 2607–2625.

Hofmeister, A., and Criss, R., 2005: Earth's heat flux revised and linked to chemistry. *Tectonophysics*, **395**, 159–177.

Holton, J., and Alexander, M., 2000: The role of waves in the transport circulation of the middle atmosphere. In *AGU Monograph: Science Across the Stratopause*, 21–35. American Geophysical Union.

Howard, L., 1961: Note on a paper of John W. Miles. *J. Fluid Mech.*, **10**, 509–512.

Hoyas, S., and Jimenez, J., 2006: Scaling off velocity fluctuations in turbulent channels up to $re_\tau = 2000$. *Phys. Fluids*, **18**, 011702.

Itsweire, E., Koseff, J., Briggs, D., and Ferziger, J., 1993: Turbulence in stratified shear flows: Implications for interpreting shear-induced mixing in the ocean. *Journal of Physical Oceanography*, **23**, 1508–1522.

Ivey, G., and Imberger, J., 1991: On the nature of turbulence in a stratified fluid. part i: The energetics of mixing. *Journal of Physical Oceanography*, **21**, 650–658.

Johnson, G., Sanford, T., and Baringer, M., 1994: Stress on the Mediterranean outflow plume: Part I. Velocity and water property measurements. *Journal of Physical Oceanography*, **24**(10), 2072–2083.

Jones, D., 1989: Velocity profiler (XCP) observations of a bottom boundary layer in the Strait of Juan de Fuca. *APL-UW TR*, **8927**, 209 pp.

Keeler, R., Bondur, V., and Gibson, C., 2005: Optical satellite imagery detection of internal wave effects from a submerged turbulent outfall in a stratified ocean. *Geophysical Research Letters*, **32**(L12610), 1–5.

Klemp, J., and Durran, D., 1983: An upper boundary condition permitting internal gravity wave radiation in numerical mesoscale models. *Monthly Weather Review*, **111**, 430–444.

Komori, S., Nagaosa, R., Murakami, Y., Chiba, S., Ishii, K., and Kuwahara, K., 1993: Direct numerical simulation of three-dimensional open-channel flow with zero-shear gas-liquid interface. *Phys. Fluids A*, **5**, 115–125.

Komori, S., Ueda, H., Ogino, F., and Mizushina, T., 1983: Turbulence structures in stably stratified open-channel flow. *J. Fluid Mech.*, **130**, 13–26.

Lele, S., 1992: Compact finite difference schemes with spectral-like resolution. *J. Comp. Phys.*, **103**(1), 16–42.

Lien, R., and Sanford, T., 2004: Turbulence spectra and local similarity scaling in a strongly stratified oceanic bottom boundary layer. *Continental Shelf Research*, **24**, 375–392.

Linden, P., 1975: The deepening of a mixed layer in a stratified fluid. *J. Fluid Mech.*, **71**, 385–405.

Luyten, J., Pedlosky, J., and Stommel, H., 1983: The ventilated thermocline. *J. Physical Oceanography*, **13**, 292–309.

Mahrt, L., 1999: Stratified atmospheric boundary layers. *Boundary-Layer Meteorology*, **90**, 375–396.

Marusic, I., Kunkel, G., and Porte-Agel, F., 2001: Experimental study of wall boundary conditions for large-eddy simulation. *J. Fluid Mech.*, **446**, 309–320.

Meneveau, C., and Katz, J., 2000: Scale-invariance and turbulence models for large-eddy simulation. *Ann. Rev. Fluid Mech.*, **32**, 1–32.

Meneveau, C., Lund, T., and Cabot, W., 1996: A lagrangian dynamic subgrid-scale model of turbulence. *J. Fluid Mech.*, **319**, 353–385.

Miles, J., 1961: On the stability of heterogeneous shear flows. *J. Fluid Mech.*, **10**, 496–508.

Moser, R., Kim, J., and Mansour, N., 1999: Direct numerical simulation of turbulent channel flow up to Re=590. *Phys. Fluids*, **11**, 943.

Moum, J., Herbert, D., Paulson, C., and Caldwell, D., 1992: Turbulence and internal waves at the equator. Part I: Statistics from towed thermistors and a microstructure profiler. *J. Physical Oceanography*, **22**, 1330–1345.

Munk, W., 1966: Abyssal recipes. *Deep-Sea Res.*, **13**, 707–730.

Nagaosa, R., 1999: Direct numerical simulation of vortex structures and turbulent scalar transfer across a free surface in fully developed turbulence. *Phys. Fluids A*, **11**, 1581–1595.

Nagaosa, R., and Saito, T., 1997: Turbulence structure and scalar transfer in stably stratified free-surface flows. *AIChE J.*, **43**, 2393.

Nieuwstadt, F., 1984: The turbulent structure of the stable, nocturnal boundary layer. *J. Atmos. Sci.*, **41**(14), 2202–2216.

Orszag, S., 1971: Numerical simulation of incompressible flows within simple boundaries. 1. Galerkin (spectral) representation. *Stud. Appl. Maths*, **L**, 293.

Pan, Y., and Banerjee, S., 1995: A numerical study of free-surface turbulence in channel flow. *Phys. Fluids*, **7**, 1649–1664.

Paulson, C., and Simpson, J., 1981: The temperature difference across the cool skin of the ocean. *Journal of Geophysical Research - Oceans and Atmospheres*, **86**, 1044–1054.

Perlin, A., Moum, J., Klymak, J., Levine, M., Boyd, T., and Kosro, P., 2005: A modified law-of-the-wall applied to oceanic bottom boundary layers. *J. Geophys. Res.*, **110**(C10S10 doi:10.1029/2004JC002310).

Perlin, A., Moum, J., Klymak, J., Levine, M., Boyd, T., and Kosro, P., 2007: Organization of stratification, turbulence, and veering in bottom Ekman layers. *J. Geophys. Res.*, **112**(C5, doi:10.1029/2004JC002641).

Perot, B., and Moin, P., 1995: Shear-free boundary layers: Part 1. Physical insights into near-wall turbulence. *J. Fluid Mech.*, **195**, 199.

Piat, J.-F., and Hopfinger, E., 1981: A boundary layer topped by a density interface. *J. Fluid Mech.*, **113**, 411–432.

Pinkel, R., 2005: Near-inertial wave propagation in the western Arctic. *Journal of Physical Oceanography*, **35**(5), 645–665.

Piomelli, U., 1993: High Reynolds number calculations using the dynamic subgrid-scale stress model. *Phys. Fluids*, **5**, 1484.

Piomelli, U., Ferziger, J., Moin, P., and Kim, J., 1989: New approximate boundary conditions for large eddy simulations of wall-bounded flows. *Phys. Fluids A*, **1**(6), 1061–1068.

Piomelli, U., and Liu, J., 1995: Large-eddy simulation of rotating channel flows using a localized dynamic model. *Phys. Fluids*, **7**, 839.

Pope, S., 2000: *Turbulent Flows*. Cambridge University Press, Cambridge.

Press, W., Teukolsky, S., Vetterling, W., and Flannery, B., 1992: *Numerical Recipes in C: the art of scientific computing*. Cambridge University Press, Cambridge, second edition.

R.Stoll, and Porte-Agel, F., 2006: Effect of roughness on surface boundary conditions for large-eddy simulation. *Boundary Layer Met.*, **118**, 169–187.

Salon, S., 2004: *Turbulent mixing in the Gulf of Trieste under critical conditions*. Ph.D. thesis, Universita degli studi di Trieste.

Salvetti, M., and Banerjee, S., 1995: *A priori* tests of a new dynamic subgrid-scale model for finite-difference large-eddy simulations. *Phys. Fluids*, **7**, 2831–2847.

Sanford, T., and Lien, R., 1999: Turbulent properties in a homogeneous tidal bottom boundary layer. *J. Geophys. Res.*, **104**(C1), 1245–1257.

Schumann, U., 1975: Subgrid-scale model for finite difference simulation of turbulent flows in plane channels and annuli. *J. Comp. Phys.*, **18**, 376–404.

Schumann, U., and Gerz, T., 1995: Turbulent mixing in stably stratified shear flows. *Journal of Applied Meteorology*, **34**, 33–48.

Shen, L., and Yue, D., 2001: Large-eddy simulation of free-surface turbulence. *J. Fluid Mech.*, **440**, 75–116.

Shingai, K., and Kawamura, H., 2002: Direct numerical simulation of turbulent heat transfer in the stably stratified Ekman layer. *Thermal Science and Engineering*, **10**, 25.

Slinn, D., and Riley, J., 1998: Turbulent dynamics of a critically reflecting internal gravity wave. *Theoret. Comput. Fluid Dynamics*, **11**, 281–303.

Spalart, P., 1989: Theoretical and numerical study of a three-dimensional turbulent boundary layer. *J. Fluid Mech.*, **205**, 319–340.

Spedding, G., 2002: Vertical structure in stratified wakes with high initial Froude number. *J. Fluid Mech.*, **454**, 71–112.

Stahr, F., and Sanford, T., 1999: Transport and bottom boundary layer observations of the North Atlantic Deep Western Boundary Current at the Blake Outer Ridge. *Deep Sea Res. II*, **46**(1), 205–243.

Sutherland, B., 2001: Finite-amplitude internal wavepacket dispersion and breaking. *J. Fluid Mech.*, **429**, 343–380.

Sutherland, B., Caulfield, C., and Peltier, W., 1994: Internal gravity wave generation and hydrodynamic instability. *J. Atmos. Sci.*, **51**(22), 3261–3280.

Sutherland, B., and Linden, P., 1998: Internal wave excitation from stratified flow over a thin barrier. *J. Fluid Mech.*, **377**, 223–252.

Taylor, J., and Sarkar, S., 2007a: Internal gravity waves generated by a turbulent bottom Ekman layer. *J. Fluid Mech.*, **590**(1), 331–354.

Taylor, J., and Sarkar, S., 2007b: Near-wall modeling for LES of an oceanic bottom boundary layer. *Proceedings of the Fifth International Symposium on Environmental Hydraulics*.

Taylor, J., and Sarkar, S., 2007c: Stratification effects in a bottom Ekman layer. *J. Phys. Oceanography*, (submitted).

Taylor, J., Sarkar, S., and Armenio, V., 2005: Large eddy simulation of stably stratified open channel flow. *Physics of Fluids*, **17**, 116602.

Thorpe, S., 2001: Internal wave reflection and scatter from sloping rough topography. *J. Physical Oceanography*, **31**, 537–553.

Vreman, B., Geurts, B., and Kuerten, H., 1997: Large-eddy simulation of the turbulent mixing layer. *J. Fluid Mech.*, **339**, 357–390.

Walker, D., Leighton, R., and Garza-Rios, L., 1996: Shear-free turbulence near a flat free surface. *J. Fluid Mech.*, **320**, 19–51.

Weatherly, G., and Martin, P., 1978: On the structure and dynamics of the oceanic bottom boundary layer. *Journal of Physical Oceanography*, **8**, 557–570.

Zang, Y., Street, R., and Koseff, R., 1993: A dynamic mixed subgrid-scale model and its application to turbulent recirculating flows. *Phys. Fluids A*, **5**(12), 3186–3196.

Zang, Y., Street, R., and Koseff, R., 1994: A non-staggered grid, fractional step method for time-dependent incompressible Navier-Stokes equations in curvilinear coordinates. *J. Comput. Physics*, **114**, 18–33.

Zilitinkevich, S., and Baklanov, A., 2002: Calculation of the height of the stable boundary layer in practical applications. *Boundary-Layer Meteorology*, **105**(3), 389–409.

Zilitinkevich, S., and Esau, I., 2002: On integral measures of the neutral barotropic planetary boundary layer. *Boundary-Layer Meteorology*, **104**(3), 371–379.